



Environmental Performance of Photocatalytic Materials for Energy Save

DIMITRA PAPADAKI

April 2017



Technical University of Crete
School of Environmental Engineering

DOCTORAL THESIS

Environmental Performance of
Photocatalytic Materials for Energy Save

Doctoral thesis of:
Dimitra Papadaki

Supervising Committee:

Professor Theocharis Tsoutsos

Professor George Kiriakidis

Associate Professor Noni- Pagona Maravelaki

April 2017

Scientific Board

Professor **Theocharis Tsoutsos**, Technical University of Crete

Professor **George Kiriakidis**, University of Crete, Foundation for Research and Technology, FORTH/IESL

Associate Professor **Noni- Pagona Maravelaki**, Technical University of Crete

Professor **Suprakas Sinha Ray**, Director at National Centre for Nanostructured Materials (SCIR, South Africa)

Associate Professor **Dionysia Kolokotsa**, Technical University of Crete

Assistant Professor **Nikolaos Xekoukoulotakis**, Technical University of Crete

Assistant Professor **Danae Venieri**, Technical University of Crete

Abstract

The incorporation of nanoparticles in the building industry is a further step towards green, efficient smart buildings. These applications can be found in building matrices, coatings or insulating applications. Nanostructured titanium dioxide (TiO_2), zinc (ZnO), and other oxides, can be used as photocatalytic products, antibacterial, self-cleaning and water or germ repellents. In the case of photocatalysis, these nanoparticles have been widely used for indoor air quality and urban air quality through their use inside building materials. The two nanomaterials, namely TiO_2 and ZnO , are studied in this PhD thesis. Different synthesis parameters like Temperature, Power, doping, oxygen vacancies enhancement via ammonia exposure, are investigated for their role in the photocatalytic performance of the nanoparticles. It has been proved that higher temperature and power leads to higher crystallinity, surface area and porosity, leading to higher photocatalytic activity. A nanomaterial with higher surface area therefore is also environmental friendlier as a small increase in temperature or power may enhance its activity as a photocatalyst. Specifically increasing the temperature has a positive effect on the ZnO nanostructures environmental sustainability, with 150 °C and 220 °C having a ~10% and ~41% lower total environmental footprint, compared to 90 °C. Also increased power has lower environmental footprint. Particularly the total environmental footprint of 310 W and 710 W is ~18% and ~27% lower than using 110 W.

Doping led to higher photocatalytic results also. Co doped ZnO showed a 10% photocatalytic behavior under visible light. In and Al doped TiO_2 samples had a good photocatalytic response (90% and 60%) under UV. Nanoparticles inside calcareous filler cement and cement paint were studied and high photocatalytic activity was found at the calcareous filler incorporating TiO_2 , specifically 12% degradation of HCHO under UV irradiation at Mn doped TiO_2 . Moreover cement and cement paint appeared to have a big adsorption of pollutants with cement having the lowest pollution rates. Organic compounds were found in calcareous building material and this decreased dramatically the performance of P25 inside this BM matrix. Nonetheless the highest photocatalytic results (12%) are achieved under calcareous fillers incorporating TCM. Therefore in construction industry, the choice of the matrix that will incorporate the photocatalytic nanomaterial is a crucial step.

Acknowledgements

This PhD thesis was conducted under a strong collaboration between FORTH/IESL and Technical University of Crete, from February 2013 until March 2017, under the supervision of Professor **Theocharis Tsoutsos**, Professor **George Kiriakidis** and Associate Professor **Noni- Pagona Maravelaki**. I am grateful for my supervisors to whom I would like to express my appreciation for all their help and understanding throughout the whole period. My supervisor, Prof. Theocharis Tsoutsos was great support for my PhD, to whom I would like to express my gratitude for the opportunity he gave me to gain knowledge and experience in the field of Environmental Studies and further develop my career in this highly emerging scientific field. The advices and knowledge I gained from him and all the School of Environmental Engineering and the high level of lectures, courses and scientific level of all the academic stuff I am very grateful for. Also, my supervisor, Noni Pagona Maravelaki was always a great mentor, always available for further recommendation and assistance and I would also like to thank.

The experimental procedure was carried out at the Foundation for Research and Technology Hellas, Institute of Electronic Structure and Lasers- Transparent Conductive Materials lab (TCM lab), of which Prof. George Kiriakidis is the team leader. I would like to express my sincere gratefulness to Prof. George Kiriakidis, who inspired me to return to Greece for my PhD, and has followed my daily work for the past four years providing me with the insights and the useful comments which were of major help for my research. I cannot but express the gratefulness I feel for his generosity first of all as a person, and as a supervisor and leader of the TCM lab, and his efforts to support me in any way he could. All people from TCM group are highly acknowledged and I feel grateful to be a part of this team, in which Prof. Kiriakidis has warmly welcomed me from day first. Lastly, his generosity on participating in a fellowship program and exchange experience with several highly qualified researchers around the world cannot be forgotten.

Also, the WIROX project (PIRSES-GA-2011-295216), a Marie Curie International Research Staff Exchange Scheme Fellowship within the 7th European Community Framework Programme is highly acknowledged. I would also like to express my gratitude for the experiments carried out at the Laboratory of Photochemistry and Kinetics, Department of Chemistry, University of Crete under the supervision and help of

Vassileios C. Papadimitriou and Dr. Spyros Fotinis, Renewable and Sustainable Energy Lab, Technical University of Crete for his great assistance.

At a personal and very important level, I thank gratefully my parents, for all their love, and the warm family they created, my sisters for their endless care, my friends who make me laugh and Frank for his major support and great understanding.

Dimitra G. Papadaki

Crete, April 2017

*Στην οικογένειά μου,
που με δίδαξε τα πιο σημαντικά.*

Table of Contents

Abstract	4
Acknowledgements.....	5
Table of Contents	8
Glossary of Terms.....	11
List of Images	12
List of Tables	12
List of Figures.....	13
List of Publications	16
Chapter I.....	17
Introduction	17
1.1 Research questions	18
1.2 Goal and Scope.....	18
1.3 Methods	19
1.4 Hosting Institutions – Fellowship programs.....	20
1.5 Thesis structure	21
Chapter II.....	22
Theoretical Background.....	22
2.1 Nanoparticle Technologies in the construction industry.....	22
2.1.1 Nanomaterials in building matrices	23
2.1.2 Energy saving nanomaterials in the building sector.....	26
2.2 Photocatalytic nanomaterials	28
2.2.1 Applications of photocatalytic nanomaterials	30

2.3 Semiconductors TiO ₂ – ZnO	34
2.4 Critical Process Parameters	36
2.5 Limitations, Challenges and Drawbacks in the construction industry.....	38
2.6 Nanotechnology and environmental assessment – Life Cycle Analysis	41
Chapter III.....	44
Experimental Procedure.....	44
3.1 Synthesis and Characterization Techniques.....	48
3.1.1. Microwave oven synthesized ZnO nanoparticles.....	48
3.1.2 Sol gel synthesized TiO ₂ nanoparticles.....	49
3.1.3 Incorporation of TiO ₂ in building matrices	51
3.2 Photocatalytic Performance experiments	54
3.2.1 Photochemical Static Reactor for Acetaldehyde degradation.....	54
3.2.2 Methylene Blue (MB) decolorization.....	54
3.2.3 Demo houses	55
3.2.4 Handmade Photocatalytic Apparatus.....	57
Chapter IV.....	59
Characterization Results.....	59
4.1 ZnO characterization results.....	59
4.1.1 The effect of different Temperature and Power	59
4.1.2 The morphological effect of different stirring time	65
4.1.3 The effect of doping in ZnO nanostructures.....	69
4.2 TiO ₂ characterization results	80
4.2.1 The effect of Ammonia exposure.....	80
4.2.2 The incorporation of TiO ₂ in Building Materials	86

Chapter V	104
Photocatalytic Performance Results	104
5.1 Indoor photocatalytic behavior of ZnO- Acetaldehyde degradation	104
5.2 The effect of Ammonia exposure for Methylene Blue (MB) degradation	106
5.3 Real time application Photocatalysis- Demo houses.....	109
5.4 Formaldehyde degradation in Photocatalytic Apparatus.....	112
Chapter VI.....	122
Environmental Performance	122
6.1 Life Cycle Analysis of ZnO Nanopowders.....	123
6.2 Novel isolative building materials in Demo houses- Environmental assessment and Energy Performance	130
Discussion.....	139
Conclusion & Recommendations	144
References.....	148
Appendix	156

Glossary of Terms

BET: Brunauer–Emmett–Teller

BMs: Building Materials

CH₃CHO: Acetaldehyde

FORTH/IESL: Foundation for Research and Technology Hellas, Institute of Electronic Structures and Laser

FIB- SEM: Focused ion beam scanning electron microscopy

HCHO: Formaldehyde

LCA: Life Cycle Analysis

LCI: Life Cycle Inventory

MB: Methylene Blue

NH₃: Ammonia

PL: Photoluminescence Spectroscopy

Room Temperature: RT

SEM: Scanning electron microscopy

TEM: Transmission electron microscope

TiO₂: Titanium Dioxide, or Titania

UV/Vis: Ultraviolet –visible Spectroscopy

VOCs: Volatile Organic Compounds

XPS: X-ray Photoelectron Spectroscopy

XRD: X-ray diffraction

ZnO: Zinc Oxide

List of Images

Image 1. X-ray Photoelectron Spectroscopy at INRS.....	19
Image 2. WIROX- Marie Curie Fellowship program collaborators.	20
Image 3. Queensland University of Technology (QUT)- Australia – XPS instrument.....	51
Image 4. Cement paint material.....	52
Image 5. Photocatalysis in dyes at FORTH/IESL	55
Image 6. Demo houses, stages of construction and photocatalytic plasterboards for testing process	56
Image 7. Handmade Photocatalytic Apparatus: Aluminum box, Pyrex chamber, BM samples with different coating, HCHO sensor, HCHO solution.....	57
Image 8. Schematic representation of handmade photocatalytic apparatus. Photocatalytic Reactor connected to HCHO mobile sensor.....	58
Image 9. Critical process parameters that affect the photocatalytic behavior.....	69
Image 10. FORTH/ ISPRA JRC results on TCM and P25	115
Image 11. a. FTIR of BMs, b. FTIR of BMs incorporating TCM and P25, c. Reference calcite FTIR acquired from RRUFF database	116

List of Tables

Table 1: Experimental Procedures, samples and techniques used.	46
Table 2: Samples tested in photocatalytic Apparatus	58
Table 3: Lattice parameters, crystallite size & surface area, from XRD & BET	64
Table 4: Summary of lattice parameters, optical band gap and surface area	71
Table 5: XPS details for binding energy and atomic concentration.....	76
Table 6: Crystallite sizes and Energy band gap of TiO ₂ doped samples	81
Table 7: XPS details for binding energy and atomic concentration.....	85
Table 8: Structural characteristics of bulk materials	92
Table 9: Surface Area, pore volume, and pore sizes as obtained from BET surface area analysis	93
Table 10: TEM results.....	94
Table 11: EDX analysis of all TiO ₂ samples.....	98
Table 12: Life Cycle Inventory for the two demo-houses.....	132
Table 13: Lattice /surface ratio calculated for most of the photocatalytic samples.....	141

List of Figures

Figure 1. Photocatalytic reactions process.....	29
Figure 2. Anatase, Brookite and Rutile phases of TiO ₂	35
Figure 3. XRD patterns of zinc oxide at different (a) temperature and (b) microwave power.	60
Figure 4: SEM images on different synthesis conditions: a.110 W –90 °C; b. 310 W –90 °C; c.710 W -90 °C; d.110 W –150 °C; and e.110 W –220 °C.....	62
Figure 5. UV-visible spectroscopy on different (a) power and (b) temperature.....	64
Figure 6. PL of zinc oxide with different (a) power and (b) temperature.....	64
Figure 7. ZnO microwave synthesized nanopowders with pH 7 - power 310 W.....	65
Figure 8. ZnO microwave synthesized nanopowders with pH 7 – power 510 W	66
Figure 9. ZnO microwave synthesized nanopowders with pH 7 –power 710 W	66
Figure 10. ZnO microwave synthesized nanopowders with pH 13 -power 110W.....	66
Figure 11. ZnO microwave synthesized nanopowders with pH 13 -power 310 W	67
Figure 12. ZnO microwave synthesized nanopowders with pH 13 - power 510 W	67
Figure 13. ZnO microwave synthesized nanopowders with pH 13 – power 710 W	68
Figure 14. XRD patterns of zinc oxide undoped and Cu, Co, Mn-doped	70
Figure 15. SEM images of ZnO samples doped with Co, Mn and Cu, at 200 nm.	72
Figure 16.(a) Reflectance spectra and (b) representation of Kubelka- Munk functions for ZnO samples ...	73
Figure 17. PL of zinc oxide doped with Cu, Mn and Co.....	75
Figure 19. XPS spectra for Zn 2p peaks.....	77
Figure 18: XPS spectra for O 1s Gaussian fitted peaks (a) pure (b) Co doped ZnO (c) Mn doped (d) Cu doped.....	78
Figure 20. XRD patterns of TiO ₂ doped with In, Al, Mn, Co and Fe; red: after Ammonia exposure, black: before Ammonia exposure.....	80
Figure 21. UV Vis spectra of TiO ₂ doped with In, Al, Mn, Co and Fe samples	81
Figure 22. SEM images of TiO ₂ doped with In, Al, Mn, Co and Fe.....	82
Figure 23. XPS spectra of In doped TiO ₂	82
Figure 24. XPS high resolution O1s spectra of In doped TiO ₂	83
Figure 25. XPS high resolution O1s spectra	84
Figure 26. XRD patterns of Titania samples and building materials	86
Figure 27. All TiO ₂ samples in different concentrations and T, inside calcareous filler, <i>a.</i> TCM, <i>b.</i> P25, <i>c.</i> Undoped, <i>d.</i> Crystal Global.....	88
Figure 28. XRD patterns of TCM, undoped, and cement paint. Also 2% TCM, and 2% undoped, inside cement paint, before and after calcination	89
Figure 29. XRD patterns of Crystal Global, P25, TCM, undoped, and cement	90
Figure 30. XRD patterns of cement, calcareous filler and cement paint with 2% TCM before and after calcination.....	91
Figure 31. Calcareous filler with 2% TCM not calcined	95
Figure 32. Calcareous filler with 2% TCM calcined at 700 °C.....	95

Figure 33. Calcareous filler with 2% P25, left image: not calcined and right image: calcined at 700 °C.....	96
Figure 34. Calcareous filler with 2% Crystal Global, left: not calcined, right: calcined -700 °C.....	96
Figure 35. TEM for TiO ₂ samples, TCM, P25, undoped, Crystal Global	97
Figure 36. a. Calcareous filler 2% TCM not calcined and b. Calcareous filler 2% TCM 700 °C.....	97
Figure 37. a. Calcareous filler not calcined and b. Calcareous filler calcined at 700 °C mixed with 2% Crystal Global.....	98
Figure 38. a. Cement paint not calcined and b. Cement paint calcined at 700 °C mixed with 2% P25	99
Figure 39. Cement not calcined.....	99
Figure 40. Cement calcined at 700 °C mixed with 2% TCM	99
Figure 41. XPS spectra of TiO ₂ , Crystal Global, undoped, P25 and TCM.....	101
Figure 42. XPS spectra of calcareous filler, cement paint and cement.	103
Figure 43. a. Acetaldehyde degradation of Co doped ZnO under UV b. Acetaldehyde degradation of Mn doped under UV c. Acetaldehyde degradation of Co doped ZnO under Visible light d. Kinetics of Co doped ZnO under visible	105
Figure 44. Decolorization under UV light a. before ammonia and b. after ammonia.....	106
Figure 45. Decolorization and Kinetics of In doped sample	107
Figure 46 Decolorization under visible light a. before ammonia and b. after ammonia.....	107
Figure 47. VOCs levels at 60% Rh without plaster boards, and with plasterboards.	109
Figure 48. Seasonal dependancy of VOCs level per month.....	110
Figure 49. VOCs levels before and after light exposure for 3h, 4h and 10h.....	111
Figure 51. BMs photocatalytic behavior. The section between the two lines crossing x-axis is the period when the lights were on, outside of that the lights were off.	112
Figure 52 Formaldehyde degradation with 2% TCM in calcareous filler, 2% P25 in calcareous filler and pure calcareous filler.....	113
Figure 53 Formaldehyde degradation with 2% TCM in cement, 2% P25 in cement and pure cement.....	114
Figure 54 Formaldehyde degradation with 2% TCM in cement paint, 2% P25 in cement paint and pure cement paint.....	115
Figure 55. TCM and P25 incorporated in different building materials	117
Figure 56. Pollution increase after the use of different building material, cement, cement paint, calcareous filler.....	118
Figure 57 Formaldehyde degradation with 2%, 1% and 0.2% TCM in calcareous filler	119
Figure 58. Formaldehyde degradation with 2% TCM in calcareous filler before calcination, and after, under 700 °C.....	119
Figure 59. Repeatability of 2% TCM in calcareous filler after three weeks	120
Figure 60 Impact categories for the fabrication of ZnO nanostructures (microwave power 110 W, temperature 90 °C).....	126
Figure 61. Comparative analysis of varying the microwave power (110 W, 310 W, 710 W at 90 °C temperature) on the environmental sustainability of ZnO nanostructures.....	127
Figure 62. Comparative analysis of varying synthesis temperatures (90 °C, 180 °C and 220 °C, at 110 W microwave power) on the environmental sustainability of ZnO nanostructures,.....	128
Figure 63. Comparative analysis of ZnO nanostructures by using different energy mixes.....	129

Figure 64. Temperature profile of the demo houses using only PCMs-23	133
Figure 65. Demo houses temperatures using PCMs-23 &VIPs	133
Figure 66. Normalized impact scores of the “red”(PCMs and VIPs) and “green” demo house;	134
Figure 67. LCA Severity of damage categories for the (a) “red” and (b) “green” house expressed in a single score	135
Figure 68. LCA Severity of damage categories for the construction and operation (i.e. energy required to maintain comfort) phase of the (a) “red” and (b) “green” house.	137

List of Publications

Peer reviewed Journal Publications

DE Motaung, I Kortidis, **D. Papadaki**, SS Nkosi, GH Mhlongo, J Wesley-Smith, GF Malgas, BW Mwakikunga, E Coetsee, HC Swart, G Kiriakidis, SS Ray. "Defect-induced magnetism in undoped and Mn-doped wide band gap zinc oxide grown by aerosol spray pyrolysis". **Journal Applied Surface Science**, 311(2014)14–26, Elsevier

D. Papadaki, S. Foteinis, G.H. Mhlongo, S.S. Nkosi, D.E. Motaung, S.S. Ray, T. Tsoutsos, and G. Kiriakidis. 2017. "Life Cycle Assessment of Facile Microwave-Assisted Zinc Oxide (ZnO) Nanostructures." **Science of the Total Environment**. Elsevier. doi:10.1016/j.scitotenv.2017.02.019.

Peer reviewed Book Chapter

D. Papadaki, G. Kiriakidis, T. Tsoutsos. **Book Chapter**. "Applications of nanoparticles Technologies in the construction industry. A step forward towards greener buildings". **Handbook of nanoparticles and architectural nanostructured materials**. Vol. 2: Emerging applications of nanoparticles and architecture nanostructures: current prospects and future trends, **Elsevier**.

Conference Proceedings

D. Papadaki, Binas V., Gupta B, Lipton-Duffin J., Motta N., Kiriakidis G., "Metal doped TiO₂: the effect of NH₃ exposure on structural and photocatalytic properties" 6th International Symposium on Transparent Conductive Materials 2016, Platanias Chania, **Oral presentation**

D. Papadaki, V. Binas, S. Foteinis, T. Tsoutsos, G. Kiriakidis. "Life cycle assessment for demo-houses utilizing phase change materials and vacuum insulation panels" 3rdInternational Exergy, Life Cycle Assessment, and Sustainability Workshop & Symposium, 2013, (ELCAS-3), **Oral presentation**

D. Papadaki, Mhlongo G. H, Papadimitriou V.C., Panagiotaki K., Nkosi S., Motaung D. E., Rosei F., Kiriakidis G. "Microwave Assisted Synthesis of Doped ZnO nanostructures for Photocatalytic Indoor Applications" 6th International Symposium on Transparent Conductive Materials 2016, Platanias Chania, **Poster presentation**

Chapter I

Introduction

Nanotechnology has been introduced in several industries, increasing daily life comfort. One of these industries is the building sector, where nanotechnology has offered several advantages on the enhancement of the characteristics, or by the addition of extra properties than the ones conventional building materials have. Building materials have rarely used innovation, but emerging technologies are necessary to be introduced there, for a further step towards greener, efficient and smart buildings. The applications can be met in cement or calcareous based construction materials, on building coating and windows facets, or on innovative isolative materials.

Titanium dioxide, and zinc oxide nanoparticles, can be used as photocatalytic products or coatings for air purification, antibacterial or self-cleaning. Moreover climate change and fossil fuel deficits lead to an increasing interest of highly energy consuming sectors, as building sector, to take advantage of the development of new materials and use them for energy savings or energy generating, taking zero energy buildings a step forward.

Overall new, air purifying, energy efficient materials in a highly energy consumed industry must be an integral part of the construction. Important steps of this procedure are the hidden potential environmental or health risks of nanomaterials during their synthesis, application or recycle phase. Thus Life Cycle Analysis (LCA) studies must be conducted and assessed, as part of a holistic approach.

1.1 Research questions

In this PhD thesis, synthesis and characterization of photocatalytic nanoparticles took place, followed by the assessment of their photocatalytic effectiveness as pure nanoparticles or inside several building matrices, and their overall environmental assessment. The main research questions that have been addressed during this study are:

- i. How can we synthesize a high performance photocatalyst with low environmental impacts?
- ii. Is the use of nanomaterials in the building sector environmental friendly and contributing to energy savings?
- iii. What are the parameters highly affecting a photocatalyst and its behavior as a nanomaterial?
- iv. Which building materials can be used as a matrix and what is their behavior when incorporated with the photocatalyst?
- v. Which process can this new photocatalytic building material undergo for photocatalytic enhancement?
- vi. Are there environmental hotspots when synthesizing photocatalytic nanomaterials, which could ideally be bypassed?

1.2 Goal and Scope

This PhD aims at shedding light on nanomaterials' structural, photocatalytic and environmental behavior and makes a step towards the fabrication of building materials (BMs) enhanced with high performance photocatalyst with the minimum environmental risks. This is achieved by investigating the role of different photocatalysts and different synthesis parameters, like different temperature, a different dopant that affects their structural behavior and photocatalytic performance. It also aims at analyzing structurally and photocatalytically the incorporation of nanomaterials in several building matrices for direct application in the building industry. Furthermore, the aim of this study is achieved by investigating on the role of external conditions (the presence of ammonia, humidity, temperature rise etc.) on photocatalytic behavior and structural analysis. Generally, with several parameters differentiation, it aims at exploring the circumstances under which the photocatalyst is highly active and the parameters that affect its performance. Lastly, the goal is concluded by the investigation of the embodied risks of nanomaterials and possible energy savings from their use. This is an innovative research since it combines materials science with environmental science and through this further knowledge has

been gained for the synthesis of sustainable nanomaterials used as high functioning photocatalyst for Indoor or Outdoor Air Quality. The environmental risks of the synthesis of nanomaterials is assessed for the first time and steps with high environmental risks are analyzed; while future replacing steps could lead to sustainable synthesis of these nanomaterials. Moreover, this thesis offers further expertise on the incorporation of nanomaterials in the construction industry and the limitations and benefits gained after this incorporation, under several different construction materials widely applicable to the construction industry.

1.3 Methods

Throughout the whole PhD study, several methods for achieving the aforementioned goals were used. The synthesis of TiO₂ nanoparticles was conducted with Sol-Gel method at TCM lab at FORTH/IESL and the synthesis of ZnO via microwave oven at CSIR/ South Africa. Several characterization techniques have been used. X-Ray Diffraction (XRD), Focused Ion Beam Scanning Electron Microscopy (FIB- SEM), Scanning Electron Microscopy (SEM), Transmission Electron Microscope (TEM), UV/Vis Spectroscopy, Photoluminescence Spectroscopy (PL) and for the investigation of the surface area porosity the Brunauer–Emmett–Teller (BET) analysis. All these characterization techniques took place at CSIR, S. Africa. Optical measurements were conducted also at FORTH/IESL.

Moreover, X-ray Photoelectron Spectroscopy (XPS) analysis was conducted at INRS, Canada and QUT, Australia where the introduction of NH₃ gas in situ was conducted for the first time inside the chamber of the XPS. Photocatalysis was conducted at FORTH/IESL under Methylene blue and under formaldehyde inside a photocatalytic apparatus. Also, measurements of degradation of gaseous acetaldehyde were conducted at the Laboratory of Photochemistry and Kinetics, Department of



Image 1. X-ray Photoelectron Spectroscopy at INRS

Chemistry, University of Crete. Real time photocatalysis at a bigger scale was conducted at FORTH/IESL at the Demo houses of TCM laboratory group. For the LCA the software package SimaPro 8.0.3 was used at Technical University of Crete, School of Environmental Engineering.

1.4 Hosting Institutions – Fellowship programs

This PhD program started in February 2013, with the immediate collaboration between two Institutes; the **Foundation for Research and Technology Hellas, Institute of Electronic Structure and Lasers- Transparent Conductive Materials lab (TCM lab)** together with the **Technical University of Crete**, School of Environmental Engineering, Renewable and Sustainable Energy Lab and lasted for 4 years. During this period the PhD candidate participated at the Exchange Research program- *Marie Curie FP7-PEOPLE-2011-IRSES 2012-2015 No: IRSES-GA-2011-295216*, “WIROX” and worked for four months at **CSIR –Council of Science and Industrial Research/Nano sciences and Nanostructures Department in South Africa**, where the traineeship involved synthesis and characterization. Four months at **QUT-Queensland University of Technology**, Brisbane Australia where the fellow was trained on XPS analysis and three months at **INRS- Institute National de la Recherché Scientifique** in Montreal, Canada for a full operation training on XPS.



Image 2. WIROX- Marie Curie Fellowship program collaborators.

1.5 Thesis structure

This PhD consists of six chapters. Initially, in this first chapter, some basic information regarding the thesis are presented, i.e. research methods, goals and scope, techniques used, programs involved and thesis structure.

In the second chapter, a theoretical background is being presented. In that chapter, the nanomaterials used in the construction industry are analyzed through application necessities, novelties and future trends. Photocatalysis is explained and basic information about the two studied photocatalysts, TiO_2 and ZnO , is given. An introduction to the environmental assessment of nanomaterials via LCA tools and necessities is further explained. Also, critical process parameters and limitations of the use of nanomaterials in the construction industry are being analyzed.

Next, the experimental part is presented. In this chapter, the experimental procedures are explained, together with materials and methods used, techniques and instrumentations, as well as further understanding on the choices of the further analyzed samples.

Then the results are presented and analyzed in the next chapter. The results from the characterization of photocatalysts TiO_2 and ZnO takes place. As regard to the ZnO , the effect of synthesis temperature, doping and effect of microwave power on the structural characteristics is analyzed. For the TiO_2 nanoparticles the effect of Ammonia exposure and the incorporation of Titania samples inside building matrices are also investigated.

In the fifth chapter the photocatalytic activity of the nanoparticles takes place. Firstly the ZnO performance under acetaldehyde degradation, and then TiO_2 exposed on Ammonia are studied under Methylene blue decolorization. The photocatalytic activity of Titania mixed with BMs is assessed through their performance inside Demo houses and lastly inside a photocatalytic apparatus under gaseous formaldehyde.

In the last chapter two Life Cycle Analyses are presented for the assessment of the synthesis procedure of nanoparticles and for the use of further innovative materials in the building sector, contributing to the thermal efficiency of the house. Then Discussion follows and Conclusion remarks and Recommendations are presented.

Chapter II

Theoretical Background

2.1 Nanoparticle Technologies in the construction industry

Nanotechnology has been introduced in several industries, contributing to an improved living environment and comfort on a daily base. Some of these industries associate with the building sector, where nanotechnology is offering several advantages either by enhancement of material and components characteristics, or by the introduction of additional properties for a number of conventional building elements. Such an interaction may promote the building industry into a sector where nanostructures are widely applied.

Traditionally the building sector has not been very open to innovation and change. However, over the last decades, new emerging technologies are introduced and are successfully integrated as a decisive step towards greener, more efficient and smart buildings. The incorporation of novel technologies may associate with cement or calcareous-based construction materials, plasters or building coating, windows facets, or innovative isolation materials.

Nanoparticles can be used in concrete binders to enhance performance. A range of nanoparticles can also be used for repair mortars or future self-healing applications. Others may be used for air purification or self-cleaning surfaces. Materials synthesized as water or germ repellents, anti -mosses, -mold, -graffiti can be selected for their properties by the building industry.

On the other hand, nanomaterials can be used in order to increase strength and durability of cement composites, pollution reduction and corrosion-free steel products. They can be used for the production of thermal insulation materials with 10 times higher performance ([Pacheco-Torgal & Jalali, 2011](#)), self-cleaning or self-color change thin films, nanosensors and self-repairing materials.

From an environmental perspective, climate change and fossil fuel deficits lead to an increasing interest by high energy consuming sectors, such as the building sector and a readiness to take advantage of new developments and novel materials aiming to use them for air quality enhancement or energy savings or even energy production. Overall more and more new, light, self-cleaning, energy efficient materials in the highly energy consuming industries are developed and applied effectively. Important steps of this procedure are the hidden potential environmental or health risks of nanomaterials during their synthesis, application or recycle phase. Therefore Life Cycle Analysis studies on nanomaterials generally or specifically on their application in the building sector must be conducted and assessed. Research and development should also contribute to their cost effectiveness. Future trends are undoubtedly leading towards greener, lighter, low health risk, minimum environmental impact, stronger, cleaner and more energy-efficient nanomaterials.

2.1.1 Nanomaterials in building matrices

The most studied materials so far are cementitious materials, and knowledge on the nanoscale level of cement materials is available by several studies bringing light to basic knowledge and understanding of structural and mechanical properties ([Kurapati, 2014](#)).

From a bottom-up perspective, concrete is a composite material in which molecular surfaces and chemical bonds interact with chemical reactions, intermolecular forces, and intraphase diffusion. At the nanoscale, processes within the material are defined by the interactions between particles and phases, while at a macroscale the effects of working loads and the surrounding environment are dominating ([Sanchez & Sobolev, 2010](#)). Nanoscience and nanoengineering of concrete are sometimes called nanomodification an area that meets lots of attention in recent years. Nanoengineering is the technique of

manipulating the nanostructures to develop a new generation of multifunctional materials with extra high mechanical performances and durability ([Sanchez & Sobolev, 2010](#)). Some of these multifunctional materials could be cementitious or calcareous materials with enhanced mechanical performance and durability, with a series of properties like self-cleaning, self-healing, crack control and sensing. Widely used nanomaterials inside a matrix of building materials are Titanium dioxide (TiO_2), Nanosilica (SiO_2), Alumina (Al_2O_3), ZrO_2 , Carbon nanotubes (CNTs), Carbon nanofibers (CNFs), nanoclay, etc. ([Kurapati, 2014](#)).

Nanoscience focuses on the synthesis and characterization at the nano and micro scale of material structures leading to the understanding of their structure and analyzing their performances at a macroscale level as studied only through advanced characterization techniques at atomic or molecular level. Nanomaterials are characterized by a high surface area to volume ratio, making them suitable for chemical reactions ([Sanchez & Sobolev, 2010](#)).

Hereby several additional nanomaterials commonly induced in cementitious matrices, and concrete, are presented. Nanosilica (Nano- SiO_2) is one of the most commonly used additives in building materials matrices. Nano- SiO_2 concrete increases resistance to water penetration, workability and strength. It accelerates hydration reactions. Very important role plays, the dispersion in the paste of cement and the molar ratios of reagents, the reaction media, and the duration of the reaction while synthesis ([Sanchez & Sobolev, 2010](#)). Nanosilica particles may increase the strength of cement, particularly as much as 15-20%. It is widely accepted that nanosilica improves the performance of sludge/ clay mixtures also for tile production. Other nanoparticles like nanotubes, nanofibers, and nanoclay are also responsible for a high hydration of cement, as long as high nanoparticles dispersion can be achieved, which is a crucial step in this process ([Pacheco-Torgal & Jalali, 2011](#)). Nanoclay materials are also promising additives for enhancing the mechanical performance, the resistance to chloride penetration and reducing permeability and shrinkage. Clay particles are hydrophilic therefore attention should be given to the control of water requirements in clay-cement composites ([Sanchez & Sobolev, 2010](#)). In other studies cement based mortars have been proven to accelerate damage, therefore, they have been replaced with original mortars containing magnesium lime ([Maravelaki-Kalaitzaki et al., 2005](#)). On the other hand, Carbon nanotubes (CNTs) and nanofibers (CNFs) exhibit extraordinary strength and tensile strength in the range of GPa, and they

have unique electronic and chemical properties ([Sanchez & Sobolev, 2010](#)) along with high electrical and thermal conductivity ([Mudimela et al., 2009](#)). Moreover, carbon nanotubes based polymer composites are poised to exhibit exceptional mechanical, thermal and electrical properties ([Ray & Bousmina, 2005](#)). Single wall is composed of single graphene cylinders and multi walls by multiple concentric graphene cylinders co-axially arranged around a hollow core. It should be noticed that CNFs have lower production cost (100 times lower than single wall CNTs, SWCNTs) ([Sanchez & Sobolev, 2010](#)). However, the main challenge, also in these materials, remains the appropriate dispersion of CNTs/ CNFs in building pastes. In a cement matrix, the CNT tend to agglomerate and therefore cannot be homogeneously dispersed by a simple mixing procedure ([Mudimela et al., 2009](#)). Moreover, the role of Alumina, (Al_2O_3) induced cementitious materials, is mainly on increasing the mechanical properties of cement. Zirconium dioxide has also been studied in building matrices as it forms more hydrated products and improves the pore structure. The addition of the nanoparticles decreased also the fluidity and increased the water demand for normal consistency ([Kurapati, 2014](#)). Lastly, Nanoferous Oxide provides concrete with self-sensing abilities and improves compressive and flexural strength ([Sanchez & Sobolev, 2010](#)).

Crack Recovery and Acid resistance

In nanoconcrete industry, a current trend is a span around the self-healing process. When concrete cracks, embedded microcapsules release a healing agent into the region that has been damaged, by capillary action. This healing agent contacts an embedded catalyst, polymerizing, to bind the crack face close-by. The recovery via this mechanism is 75 percent of the original strength. This means that the life of crack recovering in concrete can increase by 2 or 3 times ([Kurapati, 2014](#)). In the case of acid attack on cement, the consequences can be minimized by investigating into the concrete's porosity. The smaller the porosity, the smaller the chances of an acid attack on concrete are. High-performance concrete, with the use of nanomaterials, is effective in this category. Nonetheless, materials with high strength are associated with high density and lead to increased weight of the structure ([Kurapati, 2014](#)).

2.1.2 Energy saving nanomaterials in the building sector

The building sector contributes largely in the total energy consumption and CO₂ emissions and it accounts for the 40% of the energy consumed in Europe (Bernardo et al., 2016; Stephan & Stephan 2016; Gobakis et al., 2013) while been responsible for around 36% of CO₂ emissions (Nolte & Strong, 2011). Meeting the commitments addressed by the Kyoto protocol for lowering the CO₂ and greenhouse gas emission, Europe has to take drastic initiatives for improving the energy-efficiency of buildings. According to European Union Directive on Energy Performance of Buildings (Directive 2010/31/EU, “Recast”) the implementation of energy efficiency legislations for buildings, focusing on reduced energy consumption and CO₂emissions while minimization of waste is a necessity (EU, 2010).

Urban heat island and global warming increase the urban ambient temperature, leading to tremendously higher energy demand for cooling, and total energy demand (Kolokotsa 2017; IPCC 2014), Taking into account building and district level, energy efficient technologies the zero energy buildings are a necessity while climate change is putting pressure in the urban thermal environment (Kolokotsa et al., 2011; Kolokotsa et al 2012). The possibility of near zero energy buildings is mainly studied lately and new technologies in the building industry are investigated in order to reduce the big energy consumption and CO₂ emissions. All new buildings constructed in the European Union after 2020 should meet the near zero energy building target. All Member States have to draw up national plans and policies to increase the number of these buildings (Tsoutsos et al., 2013).

Smart Windows Technologies

Vanadium dioxide is a material that undergoes a metal to insulator (MIT) transition when heated over the critical temperature of 68°C and belongs to the general family of “photochromic” materials which may undergo changes in their transmission under a stimulus such as temperature, light or current (Gagaoudakis et al., 2016; Smith & Granqvist, 2010). VO₂ is considered as a promising oxide for smart windows applications. In detail, this means a coated window that can regulate the internal temperature of the building via the variation of solar IR transmittance thus contributing

to energy efficient buildings and indoor comfort. Such a coating is called thermochromic and is expected to increase in the market, rapidly ([Gagaoudakis et al., 2016](#); [Panagopoulou et al., 2016](#)) due its function, avoiding excessive solar heating while taking advantage of that solar heating on demand ([Granqvist et al., 2007](#)).

Quantum Dot third generation photovoltaics

These nanocrystals have attracted interest in the field of solar photo conversion devices. QD devices used as photovoltaic cells constitute the basis for the next generation of photovoltaics. The concept for the use of quantization effects in semiconductors in order to increase solar photo conversion efficiency is now the base of these third generation PVs, originates in the late 1970s. Such inexpensive materials may be incorporated into devices with higher potential efficiency ([Nozik et al., 2010](#)) and can be applied for solar energy generation in building sector contributing to further energy savings.

Phase Change Materials (PCM) and Vacuum Insulation Panels (VIPs)

The high costs and associated environmental impact of fossil fuel consumption for space heating and cooling have raised awareness on thermal energy storage. Focus has been given on building materials that can successfully store sufficient energy during the daytime, while releasing excess heat during night time, when extra heat is required during lower temperatures. Unlike conventional storage materials, PCMs are proved to store more heat per volume unit, while heat storage and recovery occur isothermally, making them ideal for thermal applications ([Tyagi & Buddhi, 2007](#)).

Currently, there is a lack of sufficient thermal envelope insulation in building stocks in southern European countries, while cooling (mainly air conditioning) is an important contributor to the overall energy consumption ([Nolte & Strong, 2011](#)). Therefore, there is a need to explore improvements, e.g. innovative building materials such as Phase Change Materials (PCMs) and Vacuum Insulations Panels (VIPs), to reduce energy use and the environmental footprint of the building sector. Using these novel isolation materials, the thermal inertia of a building is increasing while thermal comfort and energy savings is achieved ([Zhang et al., 2007](#)). The function of PCM is as follows; undergoing a

phase transition, during daytime, PCMs can absorb part of the ambient heat through a melting process while during the night this heat is released by a solidification process in these PCMs, resulting in a lower heat flow from outdoors to indoors and vice versa. The energy savings achieved in summer when using PCMs in selected Mediterranean regions, were experimentally found to be even about 10% ([de Gracia et al., 2010](#)).

These innovative building materials were originally developed in and for central and northern Europe ([Dutil et al., 2011](#)), where the main energy demand is during winter (heating); while their performance in southern European countries (e.g Spain, Portugal, Italy, Greece, Cyprus etc.), where the main energy demand is during summer (cooling), has not been thoroughly studied yet ([Dutil et al., 2011](#)). Therefore, PCMs can be part of the building materials matrix. For more than three decades they have been incorporated into gypsum, plaster board and concrete ([Tyagi & Buddhi, 2007](#)). Their incorporation into building materials results in an increased thermal mass control ([Mukhopadhyaya et al., 2014](#)). PCMs are applied either in the building's walls, either inside other building components, or in heat and cold storage units ([Tyagi & Buddhi, 2007](#)). If applied externally on the walls, can capture a large proportion of solar irradiation and reduce fluctuations in the internal ambient temperature. This can result in an effective shift of thermal loads to off-peak electricity periods ([Farid et al., 2004](#)).

On the other hand, VIPs have 10 times higher thermal resistance values than other conventional insulation materials. They are high performance, lightweight, and thin materials, making them highly effective and therefore attractive to the construction industry. VIPs offer high insulation value per unit of thickness, reduced shipping costs and low material volume ([Mukhopadhyaya et al., 2014](#)).

2.2 Photocatalytic nanomaterials

Some of the most common indoor pollutants are the Environmental Tobacco Smoke, resulting to cancer and severe irritations ([Franza et al., 2004](#)), formaldehyde which leads to irritation in the eyes, throat, nauseous and difficulty in breathing ([Salthammer et al., 2008](#)). This can be found in isolative materials, in synthetic fabrics, carpets, and paints

(Whisthaler et al., 2008). Ozone can be produced by photocopy machines, laser printers etc. (Jerrett et al., 2005), Volatile Organic Compounds (VOCs) responsible also for the creation of photochemical smog and ground level ozone (DOE, 1996) indoors, they can be found in building materials, paint products, carpets, adhesives, cosmetic products, cleaning products. Tobacco smoke also increases the levels of VOCs, which are also found to be 2 -10 times higher indoors than outdoors (Jerrett et al., 2005).

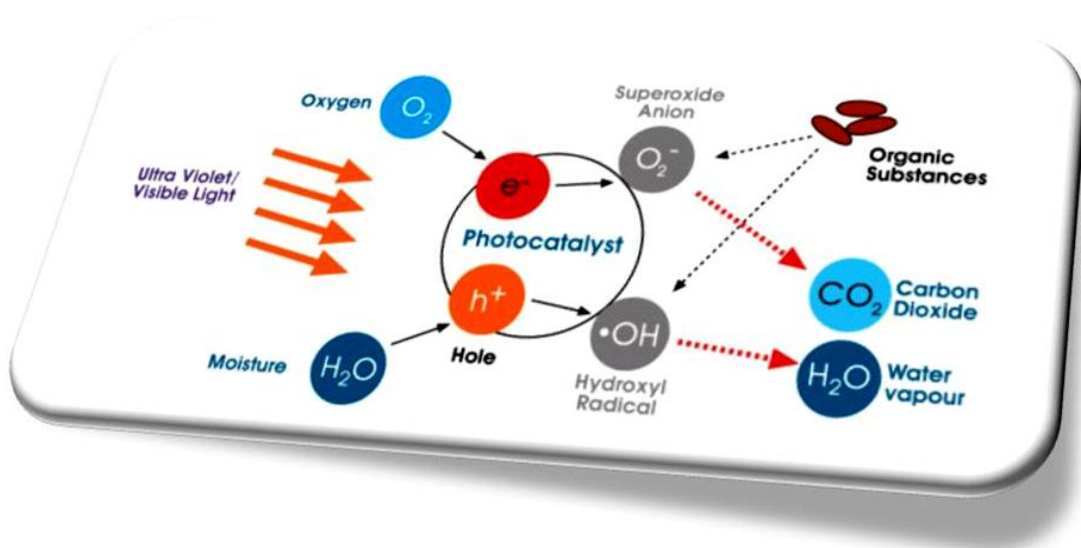


Figure 1. Photocatalytic reactions process.
(Acquired from: CAPAROL Farben Lacke Bautenschutz GmbH)

Photocatalysis is generally thought of as the catalysis of a photochemical reaction at a solid surface, usually a semiconductor. During this process, there must be at least two reactions occurring simultaneously, the first involving oxidation, from photogenerated holes, and the second involving reduction, from photogenerated electrons. Both processes must be balanced precisely in order for the photocatalyst itself not to undergo change (Pelizzetti et al., 1986; Serpone et al., 1989; Ollis et al., 1993; Kamat et al., 1993; Hoffmann et al., 1995; Fujishima et al., 2000; Mills et al., 1997; Peral et al., 2000; Ollis et al., 2000; Tryk et al., 2000; Fujishima et al., 2002).

In 1972, the pioneers of photocatalysis, Fujishima and Honda, achieved an electrochemical photolysis of water at a semiconductor electrode (Fujishima & Honda, 1972). Since 1977, when Frank and Bard first examined the possibilities of using TiO_2 to decompose cyanide in water (Frank & Bard, 1997), there has been increasing interest in environmental applications (Fujishima et al., 1999). TiO_2 is almost an ideal photocatalyst

in several respects. The increased availability of the materials, the relatively low cost, high chemical stability and with highly oxidizing photogenerated holes make it a perfect candidate in this sector (Fujishima et al., 2000). The holes, the $\cdot\text{OH}$ radicals, the O^{2-} , the H_2O_2 and the O_2 itself can all play important roles in the photocatalytic reaction mechanisms. A photocatalyst can achieve complete oxidation of the organic pollutants via hydroxyl radicals $\cdot\text{OH}$ and/or valence band holes h^+ generated when the semiconductor is exposed to UV irradiation (Fujishima et al., 2008; Hapeshi, 2009). Photocatalysis can be successfully used for real condition application in order to decompose air or liquid pollutants (Fujishima et al., 2000) and enhance the quality of atmospheric air (Chen et al., 2009). Another important parameter of the process is the size of the nanoparticles, the smaller the better photocatalytic activity this has (Zhao et al., 2003). Furthermore, the presence of dissolved oxygen in the liquid phase is expected to enhance photocatalytic oxidation since oxygen traps the photogenerated conduction band electrons to form superoxide radical anions (Xekoukoulakis et al., 2011).

Nanomaterials can be used, not only mixed with building envelope matrices, but also as coatings on building blocks, or pavements, for photocatalytic or antibacterial applications (Kapridaki & Maravelaki-Kalaitzaki, 2013). When investigating photocatalytic performances, the source of the irradiation provided to the catalyst must be further analyzed due to the fact that in real-time outdoor applications, the nanomaterials might appear to have a lower performance, due to uncontrollable environmental parameters. Nonetheless, there have been several nanomaterials synthesized and proven to be effective photocatalysts under visible light (Kiriakidis & Binas, 2014).

2.2.1 Applications of photocatalytic nanomaterials

Pavement coatings

There are many examples of photocatalysts applied on pavements, for urban depollution. The use of Titania in pavements has received lots of attention; however, the method of applying it is still unclear. In a study by Hassan et al., (2016) warm mix asphalt (WMA) is produced via two application methods. A water based TiO_2 solution as a thin coating and the use of TiO_2 as a modifier to asphalt binder in the preparation of warm mix asphalt. However, as a modifier to the binder, the TiO_2 was not effective in degrading NO_x in

the air. This might be due to the small amount on the photocatalyst on its surface. As a surface spray coating, Titania was effective in removing nitrogen oxide with efficiency from 31-55% and maximum removal was a rate was 0.05 L/m^2 . Nonetheless, the durability of the spray should be further studied. An increase in flow rate and relative humidity negatively impacted the effectiveness of the pollutant reduction. Contrary to this, as expected, the increase in UV light intensity improved the removal efficiency of the pollutant by the surface coating.

Antibacterial coatings

One of the important functions of nanomaterials that can be used in the building industry is also the destruction of fungi and bacteria. Especially in indoor environments, these are the main causes for the degradation of building materials and also for many health-related issues ([Pacheco-Torgal & Jalali, 2011](#)).

Antibacterial activity of zinc oxide nanoparticles has received significant interest worldwide ([Sirelkhatim et al., 2015](#)). Zinc Oxide is a metal oxide widely used in nanomaterial applications. It is a promising wide direct band gap semiconductor with energy band gap of $E_g=3.37 \text{ eV}$, an exciton binding energy of 60 meV, low cost and simple production with a variety of fabrication methods ([Cho, Jung, & Lee, 2008](#)). It may also be used as gas sensor ([Kiriakidis et al., 2012](#)), transparent conductor ([Mhlongo et al., 2014](#)), and catalyst ([Koutantou et al., 2013](#)). A hybrid nanostructure of Ag/ ZnO can be used also as a coating on wooden surfaces for hygienic requirements indoors ([Bazant et al., 2014](#)).

In a research conducted by [Pacheco-Torgal and Jalali \(2011\)](#) in the performance of TiO_2 as an antibacterial, it was shown that the addition of TiO_2 with a size of 21 nm to the bacterial colony was enough to destroy all bacteria in 60-120 min. The best results were obtained for a TiO_2 concentration of 0.01 and 10 mg/ml. Similarly, D. Venieri and co-workers have studied the degradation of pathogens and have shown the total degradations of E-coli, K- pneumonia and other bacterial colonies in the presence of Mn doped TiO_2 ([Venieri et al., 2014](#)). In these studies, it is widely accepted that hydroxyl radicals are the main species responsible for the bactericidal capacity of photocatalysis and they possess also a destruction capacity 1000–10,000 times more effective than chemical disinfection products ([Pacheco-Torgal & Jalali, 2011](#)).

In addition, Silver (Ag), incorporation into TiO_2 nanoparticles may increase their antibacterial effectiveness dramatically. Particularly silver doped Titania has 100% bacteria destruction after just 2 min. In the building sector, TiO_2 can be used as a thin film on wood (with an application of 1.5 mg/cm^2) in order to prevent fungi growth. Also, thin films of 20-50 nm thickness coated on adobe blocks by sol-gel increase their water absorption and bactericidal capacity. The main problem in this area is the wavelength that is needed for their activation, i.e. UV from 200-400 nm; however, this can be overcome by the fabrication of visible light activated photocatalysts ([Pacheco-Torgal & Jalali 2011; Binas et al., 2012](#)).

Cultural Heritage coatings

Recently, TiO_2 has been addressed also as a coating in stone surfaces for preventing deposition of organic particulates. This application is widely used in the area of cultural heritage. They are attractive for the conservation of buildings by preserving the integrity of stone against the deposition. Therefore this minimized the maintenance of the building facades from cleaning. However, although they do not catalyze CO_2 , which is the main reason of darkening the stones they are effective in degrading uncombusted hydrocarbons and photocatalytic stone coating can improve overall environmental conditions ([Colangiuli et al., 2015](#)).

The main issue that must be taken into account in this application on cultural heritage stones and buildings is the photo-induced super hydrophilicity which might affect negatively the stone; while it remains still unclear whether the penetration is caused by the coating ([Colangiuli et al., 2015](#)). Since water destroys the stone, the main target is to fabricate hydrophobic coatings against water penetration. Therefore, for stone protection, multifunctional products must be used. A way to do that is by mixing TiO_2 nanoparticles with polymeric materials. Some of these polymeric materials are well established as water repellents for stone, so having maximum photocatalytic effectiveness with minimum aspects of water penetration ([Colangiuli et al., 2015](#)).

Mixing of titanium and silicon alkoxides in the presence of oxalic acid and organic silica oligomers is a way of producing photocatalytic and hydrophobic SiO_2 -crystalline TiO_2

nanocomposites. However, photocatalytic TiO_2 decomposes and mineralizes a variety of inorganic and organic compounds; this is an aspect that must be taken into account when mixing these materials. Also, the polymer should not inhibit the photocatalytic properties of the photocatalyst ([Colangiuli et al., 2015](#)).

Acrylic polymers have various disadvantages. In a study ([Colangiuli et al., 2015](#)), in order not to destroy the polymeric partner, a commercial perfluorinated product was chosen. The C-F strong bond was found to preserve the polymer chain from mineralization and thus promoted photocatalysis. These fluorinated polymers, with high water repellent properties, are stable, durable and widely used organic materials for stone protection. The authors of this study evaluated the films produced, both for photocatalytic and hydrophobic effectiveness and found that they can improve the performance of the stones within buildings. The addition of a 3% Titania water solution to a commercial fluorinated polymer (10% in water solution) showed that photocatalytic TiO_2 and fluoropolymers can be an effective way to provide properties of self-cleaning and prevention of water penetration, improving the durability performances of the stone with 90% effectiveness in Rhodamine B, without decreasing the hydrophobicity of the polymer. Its chemical structure, which relies on both the strength of the C–F bond and the absence of C–H bond, is able to prevent polymer degradation by photocatalytic activities of the TiO_2 nanoparticles. This combination of materials does not also affect the color; it only changes it below the threshold of human color change perception. Outdoor long exposure should also be investigated for the scale up results of this combo Titania with the polymer in stone façades ([Colangiuli et.al, 2015](#)).

In another research conducted on the materials used for cultural heritage, it was shown that the synthesized hybrid SiOx consolidates the porous limestone by improving the stone performance characteristics, without significantly altering the stone microstructure; thus allowing the liquid and vapor circulation within the porous matrix. The SiOx, has the advantage to be a crack-free material which is an important feature for the successful application of consolidates. The low viscosity value of the SiOx facilitates its penetration in a depth of more than 2 cm under the treated surface ([Maravelaki et al., 2015](#)).

Another nanomaterial recently studied as a photocatalyst is graphene. Graphene, as individual sheets of carbon atoms bonded in a honeycomb lattice, has attracted much attention because of its unique properties and potential applications. It composites with other nanomaterials, but especially graphene–metal oxide gain attention because they

seem to boost catalytic procedures and storage reactions in energy conversion applications. Graphene induces new properties, such as high dye adsorption capacity extended light absorption range, and enhanced charge separation and transportation properties, which enhance the overall photocatalytic performance (Hu et al., 2013). Graphene is a flat monolayer of carbon atoms with perfect two-dimensional carbon structure. It has a tremendously high conductivity, superior electron mobility, high specific surface area and therefore, the composites of graphene with metal oxides may lead to a variety of environmental and energy-related applications. The large demand for graphene makes the synthesis of graphene one of the key steps to meet various research needs. Challenges on the use of graphene are the high cost and energy consuming synthesis, therefore making it a less competitive material for the massive needs required by the building industry. Moreover, a very careful design of composites must be done and also the mechanism of photocatalytic enhancement by graphene–metal oxide composites is still relatively uncertain (Hu et al., 2013).

2.3 Semiconductors $\text{TiO}_2 - \text{ZnO}$

Titanium dioxide (TiO_2 or Titania) is one of the most used nanoparticles, with a worldwide interest for its high photocatalytic effectiveness (Colangiuli et al., 2015). It exists in three phases, rutile, which is the most stable one, anatase and brookite (Fig. 2). As it is known from several studies, anatase has more photocatalytic activity than rutile, and the best one is met at anatase/ rutile mixtures. Titania is proposed for several environmental applications such as air purifier, waste water treatment cleaning, water disinfection and photo-induced hydrophilic coating with self-cleaning properties (Colangiuli et al., 2015). As expected, this highly used nanomaterial is also used often by the building industry. It can be embedded in bulk concrete, mortars, ceramic or as a coating on glass and stone (Colangiuli et al., 2015; Binas et al., 2016).

TiO_2 is an effective photocatalyst and it contributes to the fight against air pollution. The degradation of several pollutants may take place when incorporating Titania into concrete. For instance, degradation of gases such as NO_x , carbon monoxide, VOCs,

chlorophenols, and aldehydes from vehicle and industrial emissions take place on a surface enriched with Titania nanoparticles ([Sanchez & Sobolev, 2010](#)).

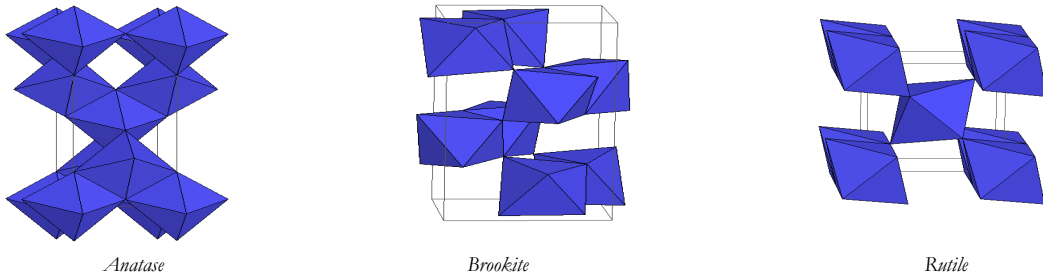


Figure 2. Anatase, Brookite and Rutile phases of TiO_2

Furthermore, partially replacing cement with nano TiO_2 particles in a cementitious matrix achieves high compressing and flexural strength ([Kurapati, 2014](#)). A scale-up application has already been achieved and in the market, one may find components for façades in buildings, pavements, and roads in European countries and Japan. Another application of Titania is that it accelerates the early age hydration of Portland cement improving its strength; however aging due to carbonation may result in photocatalytic effectiveness loss ([Sanchez & Sobolev, 2010](#)).

Self-cleaning/photocatalytic properties are known since the 1960s, but only recently they have been widely exploited. The first application was in the self-cleaning concrete placed on the church “Dives in Misericordia” in Rome. It is composed of 346 concrete blocks made of white cement and TiO_2 . It was observed that increasing the content of TiO_2 in cement by 1% leads to a proportional increase in photocatalytic activity ([Pacheco-Torgal & Jalali, 2011](#)).

Zinc Oxide

Zinc Oxide (ZnO) is a promising wide direct band gap semiconductor ($E_g=3.37\text{eV}$), with a large exciton binding energy of 60meV ([Cho et al., 2008](#)). It has low cost and simple fabrication process, and therefore finds a variety of applications, such as in chemical sensors ([Cho et al., 2008](#)), transparent conductors ([Kajbafvala et al., 2012; Mhlongo et al., 2014; Motaung et al., 2014](#)), catalysis ([Zacharakis et al., 2013; Koutantou et al., 2013](#)), and gas sensors ([Kiriakidis et al., 2012](#)). ZnO nanomaterials annual

production is accounted to be 550 tones worldwide and 55 tones in Europe (Piccinno & Gottschalk, 2012). Several techniques of ZnO synthesis, such as sol-gel organometallic hydrothermal and facile microwave-assisted synthesis (Singh & Nakate, 2013) have been exploited. The latter is a widely applied technique, since it is efficient, fast and has a low cost. Compared to conventional heating, the microwave technique has several advantages, including quick homogenous volumetric heating, enhanced reaction selectivity and energy efficiency (Kajbafvala et al., 2012).

A rich literature on the synthesis strategies of ZnO nanostructures, by means of hydrothermal processes, is available. Amin et al. (2011) controlled the pH, precursor concentration, temperature and growth time for the synthesis of ZnO and obtained a flower-like morphology at alkaline pH (8 to 12.5), whereas at lower pH rod-like nanostructures were obtained (Amin et al., 2011). Baruah and Dutta also examined the role of pH and found that the growth of nanorods was faster when the growth solution was kept at basic pH (Baruah & Dutta, 2009). Moreover, other studies have dealt with the ZnO nanostructures morphology, underlining the fact that NaOH concentration, temperature, and the reaction time cause important effects (Jiang et al., 2007; Wang et al., 2008). Additional studies have focused on the toxicity assessment of nanoparticles and possible damage to ecosystem and human health from nanomaterial releases to the environment (Hischier & Walser, 2012; Baalousha et al., 2016; Bystrzejewska-Piotrowska et al., 2009; Xiong et al., 2011). Many studies focused on the photocatalytic behavior of ZnO.

2.4 Critical Process Parameters

It is crucial to be able to predict the key process parameters for each function of nanomaterials. However, it is very difficult to make these predictions due to the interrelation between many parameters, and the fact that the one influences the other, especially when it comes to multifunctional materials.

During nanoparticles synthesis a critical process that must be paid attention is the control of particle growth, which is vital for the upscale commercialization of nanotechnology. This is, however, troublesome and a complex procedure due to the fact that when trying to control one particle characteristic this often leads to altering others. For the control of

average particle size, critical parameters are the concentration and the interaction between temperature and concentration. For the control of particle size distribution, critical parameters are flow rate and interaction between flow rate and concentration. For product yield control important factors are mainly temperature and concentration and for the control of relative crystallinity critical parameters are the temperature, the concentration and the interaction between flow rate and temperature ([Kriedemann & Fester, 2015](#)).

Incorporating nanoparticles in building materials is a procedure that also has critical parameters to be paid attention at. Firstly a major parameter is the big scale fabrication process and how nanotechnology can scale up the production from a lab scale to an industrial scale. A solution regarding cementitious nanomaterials would be to reduce the dimensions of cement, where a substantial improvement in strength can already be obtained through the large scale milling of cement to a finer form ([Rana et al., 2009](#)). Furthermore, the selection of matrix is of crucial importance since it can affect the effectiveness of nanomaterials, or even react in such a way that unwanted by-products may be produced. For a multifunctional material, the incorporation of two or more nanomaterials is essential, making this process even more complex.

Moreover, after the choice of the matrix, during mixing process, the crucial parameter that must be paid attention is the dispersion problem, since nanoparticles tend to agglomerate thus minimizing their effective surface area. Analytically, the most significant issue for all nanoparticles is that of effective dispersion. Nanoparticles tend to self-aggregate, which then reduces the benefits of their small size ([Sanchez & Sobolev, 2010](#)). In a study ([Mudimela et al., 2009](#)) the possibility of calcining at 700 °C was investigated, as a way of growing nanoparticles on the surface of the cement. This treatment was done in order to overcome dispersion problems, which are commonly faced when incorporating nanoparticles to building matrices. However, during this treatment, cement might undergo chemical alterations, interfering with its good properties as a building material and making it useless in this field. After an X-Ray Diffraction (XRD) analysis of cement no major changes were found, only new peaks corresponding to graphitized carbon appeared at the XRD spectra. Gypsum phase also vanished, maybe due to gypsum dehydration. Further heat treatment (900 °C) led to the formation of free lime phase, CaO, maybe due to the decomposition of Ca_3SiO_5 to Ca_2SiO_4 . So the introduced nanomaterials, in this study CNTs and CNFs, could be homogeneously dispersed in the concrete. Nevertheless, calcination over 750 °C degrees was shown to chemically and

physically effect the cement particles, therefore this temperature limitation must be taken into account when fabricating concrete with the above induced nanoparticles, via this method ([Mudimela et al., 2009](#)).

Therefore, as said for minimizing the dispersion problems, growth of nanoparticles on the matrices is suggested. Therefore calcination of building materials is required. However, this may alter the characteristics of matrices like calcareous or limestone materials. Lastly, the number of nanoparticles inside the material is a critical parameter since higher concentration might not always be more effective than lower; therefore, there must be an optimum concentration when using nanoparticles inside building materials. Lastly, another important parameter of the process is the size of the nanoparticles, the smaller the better photocatalytic activity this has ([Zhao et al., 2003](#)). Furthermore, the presence of dissolved oxygen in the liquid phase is expected to enhance photocatalytic oxidation since oxygen traps the photogenerated electrons to form superoxide radical anions ([Xekoukoulakis et al., 2011](#)).

2.5 Limitations, Challenges and Drawbacks in the construction industry

Except these critical process parameters, there are some limitations and disadvantages of nanomaterials and their use in the construction industry.

More specifically attention should be paid to the possibility of water penetration inside the building matrices with the use of nanomaterials. Clay particles are hydrophilic therefore attention should be given to the control of water requirements in clay-cement composites. A water reduction can be achieved by organic cation exchange modification, where organic cations replace sodium or calcium in the interlayer, reducing their hydrophilicity. Recently chemical binding of polyvinyl alcohol has been used in order to create linked clay particle chains which, when incorporated in cement, can improve its performance ([Sanchez & Sobolev, 2010](#)). Moreover when nano-coating is used in cultural heritage stones the main issue that must be taken into account is the photo-induced super hydrophilicity which might affect negatively the stone ([Colangiuli et al., 2015](#)).

As already mentioned a major challenge of nanomaterials in the construction sector is the lack of homogenous dispersion. In a cement matrix, the nanomaterials tend to agglomerate and therefore cannot be homogeneously dispersed by a simple mixing procedure (Mudimela et al., 2009). Particularly CNTs/ CNFs have high hydrophobicity and strong self-attraction. Their incorporation in the construction industry seems highly attractive, yet rather complex. Resolving, therefore, this issue related to dispersion and understanding the complex mechanisms in the paste and the interactions at interfaces is key to parameters of optimization of incorporation CNTs/ CNFs to concrete (Sanchez & Sobolev, 2010). Additional steps may further be required when mixing these materials such as purification, functionalization before mixing. However, these might still result in poor bonding between nanomaterials CNT/ CNF and cement. Some researchers have focused on overcoming this problem introducing a simple method for the creation of good dispersion of carbon nanomaterials. These nanomaterials are first grown on the surface of matrix particles, specifically silica fume and cement particles. For this growth, silica particles with the size from 100 nm to 2 μm were chosen. Silica is used as micro filler in concrete to increase its strength and is also used as a reactant in the pozzolanic reaction during the hydration of cement. Also, cement is chosen, as the most important construction material. Cement consists of around 1–20 μm sized particles with broad size distribution and contains iron oxide. It also contains SiO_2 , MgO , and Al_2O_3 , which are known to be good supporting materials for the CNT growth (Mudimela et al., 2009). This way the growth of the nanomaterials inside the building materials has improved previous dispersion problems.

Other limitations for the use of nanomaterials are the compatibility of nanomaterials with the building materials. Specifically, as regard to Titania nanoparticles, some studies claim that when Titania is mixed with cement, there are more complexities than when coated on other substrates like glass and ceramics. Cement has a low surface area and poor stability, which are adverse to the photocatalytic reaction so it causes a bad impact on the application of TiO_2 in building matrices. Also after time, their effectiveness drops. Particularly after 4 months, the photocatalytic effect seems to decrease regardless whether it was as a coating on the surface or mixed with the bulk. This might be caused due to iron species and constituents such as Ca^{2+} , Na^+ , OH^- , that cause surface carbonization of gas–solid interface, leading to the peeling of the photocatalyst layer. Surface carbonation can reduce photocatalytic efficiency due to lower power size distribution and total porosity reduction. On the influence of the pH on photocatalytic

cement, it was found that high pH values ($\text{pH} > 10$) could reduce the photocatalytic degradation rate i.e. of reactive yellow dye (Wang et al., 2015).

Nonetheless, since cementitious materials are the most commonly used building materials, some method to improve the photocatalytic effects of photocatalytic cement concrete much be found i.e. by introducing high porosity activated carbon in concrete, design macro air voids and control the micro pore structure of the concrete. In a recent work, Wang et al., 2015, have focused on TiO_2 induced cement; photocatalytic expanded shale and photocatalytic exposed aggregate concrete were prepared to improve the utilization ratio, photocatalytic effect and long-term catalytic performance of TiO_2 in cementitious materials. The pollutant was benzene and it decreased with the increase of the TiO_2 concentration and the porosity of the expanded shale. There was an observed inevitable decrease in the photocatalytic effect when photocatalytic expanded shale was mixed with concrete and therefore the photocatalytic exposed aggregate concrete had a higher photocatalytic activity than the concrete prepared by using photocatalytic limestone coarse aggregate. The effectiveness of the photocatalytic exposed aggregate concrete remained at 80%, even 10 months after the first synthesis. This way of enhancing the photocatalytic activity of TiO_2 instead of mixing with building materials proved to be effective and durable (Wang et al., 2015). Overall expanded shale, has a more stable composition, structure and a richer porous system. Therefore, using it as the substrate could increase the reaction areas of photocatalysis and improve the stability of TiO_2 (Wang et al., 2015).

Another limitation of the nanoparticles use in the construction industry is the fact that when nanomaterials are used for strength enhancement, materials with high strength are associated with high density and lead to increased weight of the structure (Kurapati, 2014).

Attention should be also paid on the light source when using photocatalytic nanomaterials. Photocatalytic materials can be activated by the UV-A source of the sun, so outdoors applications are highly popular lately. However the natural irradiation outdoors, for activation of the photocatalyst may vary according to the time of the day, the season, the geographical position and the weather locally. Therefore the fabrication of visible light activated photocatalysts would develop the application of photocatalysis in the building sector for indoor use and enhancement of the indoor air quality (Binns et al., 2012).

Additionally, very important limitation for the use of nanomaterials in the construction industry is their high cost. This is attributed due to the novelty of the technology and the complexity of the equipment used for preparation and characterization techniques. However, costs have been shown to decrease over time and as manufacturing technologies improve, these costs may further decrease. Moreover, it is expected that these nanomaterials will enable unique solutions to complicated problems leading to large scale applications, therefore, making the cost effective (Rana et al., 2009). For the use of specifically CNTs a serious drawback on the use of these nanomaterials in the building industry is the fact that carbon nanotubes are very costly, preventing the scale-up of their use in the nearest future (Pacheco-Torgal & Jalali, 2011). This is also observed in the use of graphene, which has high cost and energy consuming synthesis, therefore making it a less competitive material for the massive needs required by the building industry (Hu et al., 2013). Their high cost contributes to the difficulty of massive production of these materials in order to be incorporated in the building industry. Except all these, some basic drawbacks of the use of nanomaterials in the construction industry involve health and environmental issues. Nanotechnology based construction products could be harmful to health. Moreover, constructive infrastructure is provided in the natural environment, therefore all materials used in these facilities need to be compatible to the natural environment with as closer to zero environmental effect as possible. The most common potential problems include the release of materials via dust into airways, materials entering into groundwater, and exposure to potentially harmful materials during construction and maintenance procedures.

2.6 Nanotechnology and environmental assessment – Life Cycle Analysis

The Life Cycle Assessment (LCA) methodology has been scarcely applied in the nanotechnology research field (e.g. (Hischier & Walser, 2012; Slotte et al., 2015)) and therefore advantages and disadvantages, from a sustainability perspective, remain largely unknown. LCA is a comprehensive and robust tool to assess the environmental

sustainability of a product or a system and it introduces environmental considerations for decision and policy makers, researchers and communities (Foteinis et al., 2015).

Several studies underline the importance of characterization techniques for environmental studies (Baalousha et al., 2016; Stone et al., 2010). For instance, the toxicity of the nanoparticles is associated with their minuscule dimensions and large surface area, comparable to their size. Their toxicity increases due to the reactivity of their large surface area and the ability to penetrate into cells (Xiong et al., 2011; Papadaki et al., 2017). Other works highlight the cytotoxicity of nanomaterials and nanocomposites (Wang et al., 2008). The main mechanism of toxicity of nanomaterials is considered to be through oxidative stress, which damages lipids, DNA, carbohydrates, and proteins, and can lead to alterations in cell membrane properties disrupting vital cellular functions (Heinlaan et al., 2008). In vitro studies showed that the toxicity of ZnO was due to solubilized Zn ions as proved with recombinant Zn-sensor bacteria (Heinlaan et al., 2008). ZnO cytotoxic potential can be minimized by various ways, e.g. by using iron as a dopant for ZnO nanoparticle, since in vitro oxidative stress profiling of ZnO nanoparticles showed features connected to metal fume fever when exposed to aerosolized metal oxide nanoparticles (George et al., 2010). Nanoparticle in vitro toxicity testing requires a careful characterization of particle properties, since current test methods are likely to be influenced by nanoparticles' properties. The risk assessment of nanoparticles needs an adaptation of existing cytotoxicity methods or the development of new test systems. Therefore, nanoparticles cytotoxicity test are urgently needed (Kroll et al., 2009) while characterization techniques on the structure of nanomaterials can seem helpful when assessing their toxicity and oxidative damage to organisms, through an investigation of nanomaterials properties (Stone et al., 2010). Thus, environmental and ecotoxicology studies should incorporate characterization techniques for the estimation of their agglomeration, surface area, surface chemistry and composition (Stone et al., 2010) as well as other parameters obtained solely by several characterization techniques.

Although there are many research studies on the application on nanomaterials in the construction industry, there are several gaps that are successfully filled in this thesis. Life cycle analysis tool, according to the author's best knowledge, has not been used for the assessment of the synthesis of nanoparticles, taking into account important structural characteristics of the nanoparticle. Therefore understanding the environmental sensitive

parts of nanoparticle synthesis is a significant step towards sustainable production of high functioning nanomaterials. Furthermore there is a lack of researches where novel building materials are applied in actual buildings and demo constructions in order to assess their performance with real time data. In this thesis this is also achieved for the thermal behavior of novel building materials, as well as the photocatalytic behavior of nanomaterials inside demo houses. Little focus has been given also in the scientific community on the incorporation of photocatalytic nanomaterials in different building matrices. Most researches focus on cementitious based nanomaterials, whereas in this thesis cementitious, cementitious paint and calcareous fillers based photocatalytic materials are being studied. Moreover several parameters that can affect the behavior of the photocatalyst, before incorporated in the matrix (doping, oxygen vacancies enhancement, temperature treatment, power variation) but also after being mixed with the different building materials (temperature treatment, concentration variation of the photocatalytic nanomaterial) are being for the first time further studied in this PhD thesis.

Chapter III

Experimental Procedure

Methodology

In this chapter, the experimental analysis and methodology of the thesis will be presented. The most active and high functioning photocatalytic materials, namely TiO₂ and ZnO were selected for this thesis. Photocatalytic nanomaterials used for Air quality can be used as coatings on building blocks, or pavements, but also mixed inside building envelope matrices. Therefore both these scenarios were studied, firstly as bulk photocatalysts, and then mixed in building materials (BMs). Different characterization techniques were used to measure the specific characteristics of nanomaterials. These techniques were used because they enable the identification of crystal structure, size and surface composition, oxygen defects and provide insight on their properties, as nanomaterials and on their photocatalytic activity and potential environmental risks through further environmental testing ([Baalousha et al., 2016](#)). In this thesis the characterization techniques used were, XRD, UV-Vis, PL, XPS, SEM, TEM, BET. During characterization results the errors of the instrumentation are negligible, since only good signal spectra's were kept for this research and repetition of the results was done when necessary. BET instrumentation is calculated to have a smaller than 1% error and some cases even 0.1% error was calculated. Further errors were eliminated, since all characterization results were well compared with databases available. XPS errors were eliminated by using NIST database and calibration of carbon 1s peak. For insufficient noisy signals of XPS spectra 1% error could be applicable.

Parameters influencing their photocatalytic behavior were further investigated. It is known that interfering with the size, surface area and oxygen defects of a nanomaterial enhances their photocatalytic activity ([Zhang et al., 2014](#)). Therefore the change of temperature, power, introduction of dopants, and ammonia exposure, are the parameters detailed investigated in order achieve a medium size with high surface area and higher oxygen vacancies photocatalyst with enhanced performance. Analysis on their surface area, oxygen concentration and defects, the size of the particles, and orientation are being presented through several characterization techniques. These led to the correlation of several structural characteristics with the application of our interest, i.e photocatalysis, and a step towards more effective photocatalyst that can be used in the construction industry. Their photocatalytic performance of these bulk photocatalyst was then studied under different techniques due to the specific availability of the instrumentations.

After the detailed investigation of the structural parameters, which influenced the photocatalytic performance of bulk photocatalysts, the choice of building matrices as well as the appropriate photocatalyst was conducted. For building matrix three common used, cost effective and widely available construction materials were chosen, that is cement, cement paint and calcareous fillers. The photocatalyst chosen in this procedure were Titania based photocatalyst, since these are proved to be more effective than ZnO based nanomaterials. In this step the selection of these samples was based on several previous studies of the TCM group ([Binas et al., 2012; Venieri et al., 2014](#)) revealing the high efficiency of TiO₂ nanomaterials. The first sample is TiO₂ doped with Mn, and called TCM, while the second sample is TiO₂ undoped. In order to make a comparison of their effectiveness, these two materials have been compared with two well known industrial Degussa P-25 and Crystal Global.

Temperature treatment of nanoparticles incorporated inside building matrices is well known already from the literature to be a future step for novel photocatalytic building materials, therefore, the studied samples were also investigated under T treatment of 700 °C. Moreover, since the amount of the nanomaterial used inside the building material is also of significant importance, 0.2, 1 and 2% of Titania was selected to be incorporated inside these building matrices. In a further step, these nanomaterials were studied both in real time Demo house, but also in a handmade photocatalytic apparatus. For eliminating errors in all the photocatalytic experiments a reference -blank sample was constantly examined simultaneously for a good comparison between the tested samples. Repetition

of several experiments was also conducted. In the case of handmade apparatus, the formaldehyde sensor has a significant accuracy of 0,001 and the error claimed by the manufacturer to be $\pm 10\%$. Calculating the average percent difference of the repeated experiments, % Difference = $\frac{|E1-E2|}{\frac{1}{2}|E1+E2|} \cdot 100$, it was calculated that both photocatalytic

apparatus boxes have a 25% difference in their results, leading to a possible 75% accuracy of the set-up and the method used.

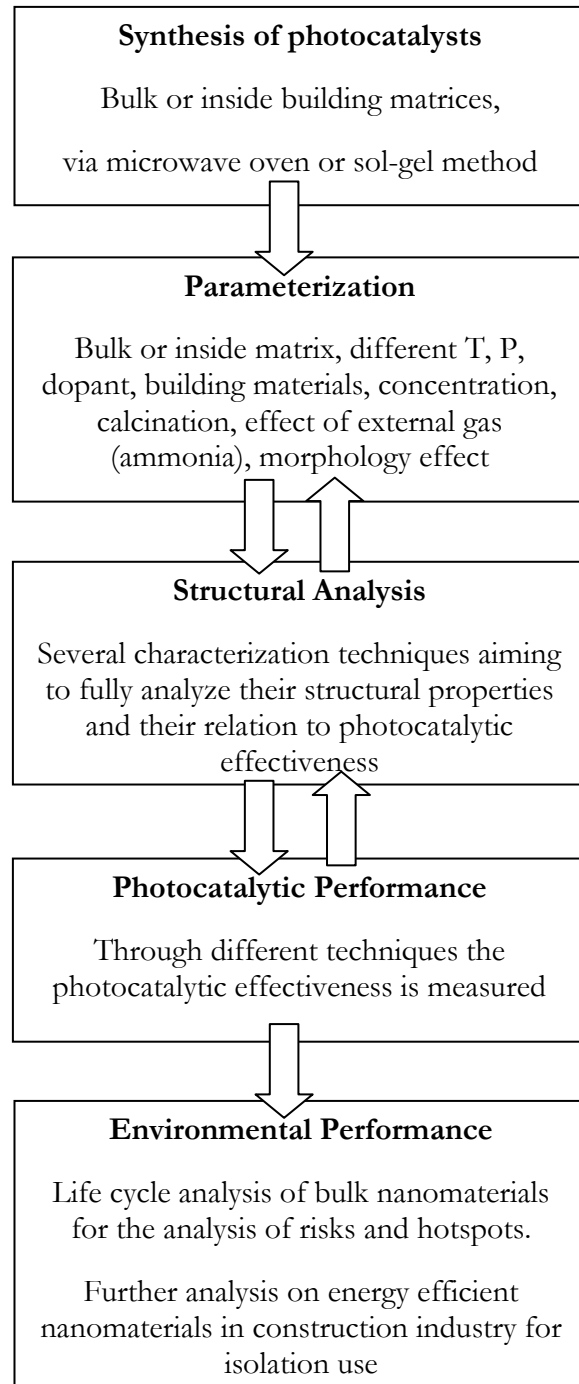
Based on our findings, life cycle assessment was chosen to be conducted on the most important and environmental costly procedure of the nanoparticles technology, that is their synthesis. This was done in order to identify environmental hotspots and possible replace them in the future synthesis of nanomaterials for energy save, keeping their photocatalytic effectiveness intact. Further analysis was decided to be conducted for Demo houses incorporating novel isolative materials, since this gives further insights on embodied energies and hidden risks of the use of new technologies in building constructions.

Table 1. Experimental Procedures, samples and techniques used.

	#	Nanomaterials	Parameterization	Synthesis method	Characterization Techniques	Photocatalytic Performance
Bulk Nanomaterials	1	ZnO	1.Temperature 2.Power	Microwave Oven	XRD, SEM, BET, PL, UV Vis	Acetaldehyde (Gas)
	2	ZnO	Stirring Time	Microwave Oven	SEM	
	3	ZnO	Doping	Microwave Oven	XRD, SEM, BET, PL, UV Vis, XPS	
	4	TiO ₂	Oxygen vacancies via Ammonia exposure	Sol -gel	XRD, SEM, UV Vis, XPS	Methylene Blue (Liquid)
Incorporated in building matrices	5	TiO ₂	1. Building matrix (calcareous, cement, cement paint) 2. Concentration of nanoparticles 3. Industrial vs. Lab 4. Temperature Treatments	Sol- gel Industrial	XRD, SEM, BET, TEM, FTIR, XPS	1. Demo house 2. Photocatalytic handmade Apparatus Under Formaldehyde
Isolative Materials	6	Phase Change Materials	1 year recorded data from Demo Houses	Industrial	Energy Performance & LCA	

In Table 1 all samples used in this research are presented, together with their names, parameters studied in each case, synthesis methods, characterization techniques used and finally the method their photocatalytic and environmental performance was conducted (see also Diagram 1).

Diagram 1. Experimental procedure



The above samples were selected after several experiments conducted in order to find the optimum characteristics. Therefore in this thesis we have selected the optimum samples for presentation, excluding all other samples that were fabricated and studied throughout this entire 4 year research program according to their characteristics, or performance. Further details for the set up and experimental procedure of every experiment are presented below.

3.1 Synthesis and Characterization Techniques

3.1.1. Microwave oven synthesized ZnO nanoparticles

In this section, the synthesis and characterization techniques used for the fabrication of series 1 and 2 and 3 (*Table 1*) are being presented.

Synthesis

For the synthesis procedure 0.1 M zinc nitrate hexahydrate ($\text{Zn}(\text{NO}_3)_2 \cdot 6\text{H}_2\text{O}$) (98%, Aldrich) was dissolved in 250 ml distilled water. Hexamethylenetetramine HMT, $((\text{CH}_2)_6\text{N}_4)$ was used as the hydroxide, HMT is expected to release hydroxyl ions and modify the nucleation process (Xiangdong et al., 2005). 0.2 M Sodium Hydroxide (NaOH) was used for pH control. The solution was stirred and transferred in autoclave vessels of 70 mL volume and irradiated in a microwave reactor (Anton Paar microwave reaction system- Multiwave 3000) for 15 min, at 90 °C and 110 W microwave power. Then, a set of experiments were performed by keeping the microwave power constant at 110 W and varying the annealing temperature (from 90 °C, to 150 °C and 220 °C, which was the upper limit of the microwave oven) and another, by keeping the annealing temperature constant at 90 °C and varying the microwave power (from 110 W to 310 W and 710 W). In all cases, the resulting precipitate was washed with distilled water and

ethanol several times and dried in ambient temperature overnight. The remaining ZnO powder was calcined for 2 h, in the oven, at 200 °C.

For the doped series, a similar procedure was followed, using a microwave oven for 15 min at 220 °C. 0.25 at% of copper nitrate hexahydrate ($\text{Cu}(\text{NO}_3)_2 \cdot 6\text{H}_2\text{O}$) or manganese nitrate hexahydrate ($\text{Mn}(\text{NO}_3)_2 \cdot 6\text{H}_2\text{O}$) or cobalt nitrate hexahydrate ($\text{Co}(\text{NO}_3)_2 \cdot 6\text{H}_2\text{O}$) were each added into the zinc precursor solution. The remaining products were kept at room temperature for overnight then dried in oven at 200 °C for 2 h. The selected concentration of the dopants was 0.25% atomic percent.

Characterization Techniques

All measurements were conducted at room temperature. Their crystallographic structure was examined using a Panalytical X' Pert PROPW 3040/60 diffractometer equipped with a Cu-K α ($\lambda = 0.15405$ nm) monochromated radiation source. The surface morphology of the samples was observed using an Auriga ZEISS scanning electron microscopy (SEM) operated at an accelerating voltage of 5keV. For optical characterization a Perkin Elmer Lambda 950 UV/VIS/NIR spectrophotometer and Perkin-Elmer LS-55 Fluorescence Spectrometer were used, also UV/Vis Spectroscopy (Perkin Elmer LAMBDA 750S). The specific surface area and the pore volume of the samples were examined by nitrogen (N_2) physisorption using a Micromeritics TRISTAR 3000. The samples were prior degassed at 90°C overnight under continuous N_2 gas flow in order to remove moisture. X-ray Photoelectron Spectrometer (XPS) analysis was done using a VG ESCALab 220i XL instrument, equipped with an Al K α source.

3.1.2 Sol gel synthesized TiO_2 nanoparticles

Ammonia exposed TiO_2 samples

Ammonia exposure of anatase Titania was studied in order to assess if the presence of external gas can influence the photocatalyst, and if ammonia contributes to oxygen defects, enhancing the photocatalytic activity of the samples. In this section, the synthesis and characterization techniques used for the fabrication of series 4 are being presented.

Synthesis

Titanium dioxide nanopowders of various dopants were prepared using the modified sol-gel method. TiO_2 was doped at a concentration rate of 1%, with transition metals (such as Mn, Co and Fe), and poor metals (such as Al and In). A comparative study of their photocatalytic activity (individually discussed in the next chapter) in relation with the structural characterization, with and without the presence of NH_3 gas, is presented in this section. A co-precipitation method was used to prepare metal- doped TiO_2 nanoparticles with a molar ratio of 1 mol%. Doped titanium dioxide was precipitated at $\text{pH} \sim 8$ from an aqueous solution of TiOSO_4 and doped (Mn-, Co-, Fe-, Al-, In-) by the addition of ammonia. After aging the suspension overnight, the precipitate was filtered and dried under air at 373 K. The residue was crushed to a fine powder and calcined in a furnace at 973 K for 3 h.

All chemicals which were used for the preparation of metal doped catalysts were purchased from Aldrich and were of analytical reagent grade with no further purification. The reagents applied in the study were titanium (IV) oxysulfate hydrate ($\text{TiOSO}_4 \times \text{H}_2\text{O}$), manganese (II) acetate tetrahydrate Mn ($\text{CH}_3\text{COO})_2$, cobalt (II) acetate tetrahydrate ($\text{Co}(\text{CH}_3\text{COO})_2$), iron nitrate, Aluminum nitrate, Indium nitrate and ammonium hydroxide (25% NH_4OH)

Characterization Techniques

The crystal structure, particle size, and morphology were examined with powder X-ray diffraction (XRD) and SEM respectfully. Powder X-ray diffraction patterns were collected on a Rigaku D/MAX -2000H rotating anode diffractometer (Cu Ka radiation) equipped with the secondary pyrolytic graphite monochromator operated at 40 kV and 80mA over the 2θ collection range of 10–80°. The scan rate was 0.05°s⁻¹. The UV-visible diffuse reflectance spectra of the final powders were measured on a Perkin Elmer LAMBDA 950 with BaSO_4 , as reference standard. The UV– visible diffuse reflectance spectra of the final powders were measured on a Perkin Elmer LAMBDA 950 with BaSO_4 , as reference standard. The diffuse reflectance spectra were plotted as the Kubelka– Munk function, $F(R)$, versus wavelength based on the Kubelka– Munk equation: $F(R) = (1-R)^2 / (2R)$, where the reflectance is $R = R_{\text{sample}} / R_{\text{reference}}$. Band gaps were then determined from the Kubelka– Munk function and the Tauc plots.

Surface morphology and elemental analysis of the samples were carried out using scanning electron microscopy (SEM) and an energy dispersive spectrometer (EDS) on a JSM-6390 LV instrument. A detailed analysis through X-ray Photoelectron Spectroscopy (XPS) is presented *and the introduction of NH₃ gas in situ was conducted for the first time inside the chamber of the XPS* (at Queensland University of Technology, Australia).

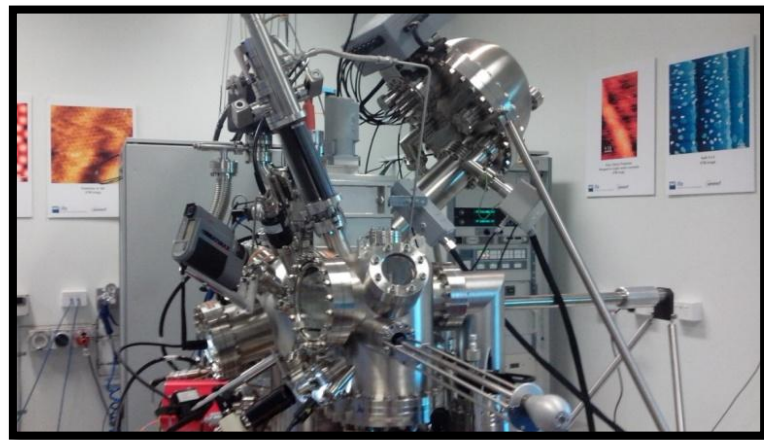


Image 3. Queensland University of Technology (QUT)- Australia – XPS instrument

3.1.3 Incorporation of TiO₂ in building matrices

As already mentioned photocatalytic materials can be used as coating (bulk form) or mixed inside building matrices. In this section, we have selected four nanomaterials, from previous studies, and further analyzed their photocatalytic effectiveness while

incorporated into three major building envelopes. Due to the high efficiency of TiO₂ nanomaterial as a photocatalyst, in comparison to ZnO, all materials studied in this section are based on Titania nanopowders (series number 5, *Table 1*)

The selection of two Titania produced in laboratories is based on several previous studies of the TCM group ([Binas et al., 2012](#); [Venieri et al., 2014](#)) revealing the high efficiency of TiO₂ nanomaterials. The first sample is TiO₂ doped with Mn, and called TCM, while the second sample is TiO₂ undoped, (called undoped). In order to make a comparison of their effectiveness, these two materials have been compared with two industrial photocatalytic materials, Degussa P-25 and Crystal Global. These four nanocatalysts have been mixed with calcareous filler, cement and cement paint, separately and in different concentrations (0.2%, 1% and 2%). The concentrations were kept low so that the overall cost of a future scale up project in the housing sector, could be affordable. All the combinations of nanomaterials mixed with building materials, as mentioned above, were studied and analyzed in Room Temperature (RT) and also some were analyzed further, calcined at 700 °C.

Synthesis

Chemicals for the preparation of TCM-1 nanoparticles were purchased from Aldrich and were of analytical reagent grade. Conventional commercially available calcareous filler, cement paint (from Italcementi CTG group) and cement (Lafarge, Heracles) were used as building materials (BMs).



Image 4. Cement paint material

For the preparation of undoped and Mn doped TiO_2 Titanium (IV) oxysulfate hydrate ($\text{TiOSO}_4 \cdot x\text{H}_2\text{O}$), manganese (II) acetate tetrahydrate, $\geq 99\%$ and titanium (IV) tetraisopropoxide purchased from Aldrich were applied. The samples were prepared by a sol–gel method. The photocatalyst was obtained by precipitating titanium dioxide on manganese dioxide (MnO_2), employing TiOSO_4 . The hydrated manganese dioxide sol was obtained by mixing the required volumes of manganese acetate, i.e. $\text{Mn}(\text{CH}_3\text{COO})_2$, 0.1 M and potassium permanganate KMnO_4 , 0.1 M solutions and stirring the mixture for 24 h at room temperature. The obtained sol was mixed with a solution of TiOSO_4 . The concentration of TiOSO_4 in the final solution was 0.1 M. The colloidal solution was stirred at room temperature for 48 h, in order to obtain the adsorption equilibrium. During this phase an exchange of Mn with Ti occurs and the final sol was a mixture of both dioxides. After this step, the remaining Ti^{4+} ions were forced to precipitate by adding NH_3 solution so that the final pH was 7. The gel formed was stirred continuously at room temperature for aging (48 h). After aging, the sol was separated using centrifuging or alternatively it was filtered under vacuum, to obtain a powder. The powder was then washed with distilled water until free of sulfate and ammonium ions. The powders, after drying at 100 °C, were calcined for 3 h at 700 °C (Binas et al., 2012).

Characterization

Their crystallographic structure was examined using a Panalytical X’Pert PROPW 3040/60 diffractometer equipped with a Cu-K α ($\lambda = 0.15405$ nm) monochromated radiation source. The surface morphology of the samples was observed using an Auriga ZEISS scanning electron microscopy (SEM) operated at an accelerating voltage of 5 keV. The specific surface area and the pore volume of the samples were examined by nitrogen (N_2) physisorption using a Micromeritics TRISTAR 3000. The samples were prior degassed at 90 °C overnight under continuous N_2 gas flow in order to remove moisture. X-ray Photoelectron Spectrometer (XPS) analysis was done using a VG ESCALab 220i XL instrument, equipped with an Al K α source. Transmission electron microscope (TEM), images and selected area electron diffraction (SAED) images were captured using JEOL TEM-2100 microscope.

3.2 Photocatalytic Performance experiments

3.2.1 Photochemical Static Reactor for Acetaldehyde degradation

In this experiment the ZnO series number 3 (*Table 1*) are being assessed as photocatalysts. The experimental setup used in this experiment is a Photochemical Static Reactor coupled with on-line Fourier Transform Infrared Spectroscopy (PSR/FTIR), intended for qualitative and quantitative reactants and volatile products analysis. Acetaldehyde, CH₃CHO, was the volatile organic compound used as a pollutant. This selection was based on its increased abundance in both indoor and outdoor environment (Papadimitriou et al., 2011; Papadimitriou et al., 2011b). The experimental setup consisted of four main units: the gas supply and preparation glass vacuum line with several storage bulbs, the optical cell/reactor assorted with two retractable NaCl windows transparent to IR region, a Fourier Transformed Infrared spectrometer (FTIR, Jasco 6300) to monitor reactant and products concentrations, and two light sources (UV and Visible) positioned at a distance of 80 cm from the photocatalysts. The first light source was a 300 W Osram lamp (Ultra Vitalux) with a maximum intensity of ~350 nm. The second light source was a 500 W Vito halogen projector lamp (VT 364) with broad emission spectra (350–1050 nm) and maximum intensity at ~720 nm. The emission spectra of the visible light source simulates satisfactorily the indoor light conditions (Papadimitriou et al., 2011).

3.2.2 Methylene Blue (MB) decolorization

Photocatalytic degradation of MB (C₁₆H₁₈C₁N₃S) in the aqueous solution (10 mg L⁻¹) was carried out under UV (310–400 nm wavelength) using a mercury Lamp (Spectrolite ultraviolet quartz pencil lamp/I = 4.5 mW cm⁻²) and visible-light (Philips TLD, 18 W-840) irradiation with emission spectra of 380 nm to 680 nm and max. intensity 460 nm. The photocatalysts used were TiO₂ based samples, before and after NH₃ exposure (series number 4, Table 1). 100 mg of photocatalyst was added into a 100 ml of aqueous MB (10

ppm) solution. Prior to irradiation, the suspensions were sonicated in the dark for 30 min to ensure establishment of an adsorption–desorption equilibrium among the photocatalyst, MB and atmospheric oxygen. After recovering the catalyst by centrifuging, subsequent variations in the MB concentration were analyzed by an Ultraviolet–visible spectrophotometer (VARIAN Cary 50) and the adsorption peak at 664 nm (max for MB) was recorded (Binas et al., 2011) .



Image 5. Photocatalysis in dyes at FORTH/IESL

3.2.3 Demo houses

Two demo houses have been constructed and are located on the combined premises of the Foundation for Research and Technology/ Institute of Electronic Structure and Laser -Hellas (FORTH/IESL) and the Science and Technology Park of Crete (STEP C) in the outskirts of Heraklion, Crete. Both demo houses have the same dimensions of 3 x 3 x 3 m. The Demo houses were designed for two purposes. First of all, they can be test bed houses for thermal behavior of innovative isolative materials (the procedure for which will be described in the last chapter, series number 6, *Table 1*). Secondly, they were

constructed for the real time application of photocatalytic materials (series number 5, *Table 1*). In that sense, the “red house” is the reference house and the “green house” is a host area for panels covered with photocatalytic nanomaterials combined with building materials. These panels are then placed throughout the house, and 6 UV lamps (300 W) are placed in front of them in a distance of 40-50 cm (see *Image 6*). The sensors placed in both houses record a value of the total VOCs every 40 seconds. The recorded value does not represent concentration in units, but they should only be treated as a comparative value. The interior temperature is recorded with EPO-Elements 8.1 software, in 40 seconds intervals. Cooling and thermal units (HVAC) are placed in both houses offering full thermal and humidity control and management. Rh%, Lighting, Temperature and air flow are managed by the BMS software (Building Management System). All recorded data are stored through EPO Elements 8.1 software and both BMS and EPO are managed from the control room, a small room in between the two Demo houses, but also remotely via computer.



Image 6. Demo houses, stages of construction and photocatalytic plasterboards for testing process.

3.2.4 Handmade Photocatalytic Apparatus

For the needs of a smaller scale photocatalytic chamber, a handmade apparatus was constructed. A properly sealed Pyrex glass chamber of 5.5 L was placed inside an aluminum box of 50 x 50 cm. This box was equipped with 10 UV lamps PHILIPS, T8, 15 W, and two fans, for good ventilation.



Image 7. Handmade Photocatalytic Apparatus: Aluminum box, Pyrex chamber, BM samples with different coating, HCHO sensor, HCHO solution.

The formaldehyde sensor used was the FP-30 RIKEN KEIKI sensing HCHO levels of 0.01 ppm to 1ppm. This sensor has a significant accuracy of 0,001 and the error claimed by the manufacturer to be $\pm 10\%$. The final solution was 10 μL of HCHO 37 w/v% dissolved in 120 mL H_2O . 10 μL of this solution was also used in every measurement, and the initial concentration in the chamber was measured to be 0.5 ppm. Common commercial plasterboard was cut into small panels of 8 x 10 x 1 cm each and on each one a different photocatalytic BM was applied as slurry, which was left to dry for several days.

The samples studied in this section are TiO_2 based samples, incorporated inside BMs (series number 5, *Table 1*). Several experiments were conducted in this section. In *Table 2* we present all the samples analyzed.

Table 2. Samples tested in photocatalytic Apparatus

Sample Name	Building Material	TiO ₂ % concentration	TiO ₂	Temperature Treatment (°C)
BM1	Calcareous Filler	0.2	TCM	-
BM2	Calcareous Filler	1	TCM	-
BM3	Calcareous Filler	2	TCM	-
BM6	Calcareous Filler	2	TCM	700
BM9	Calcareous Filler	2	P25	-
BM73	Calcareous Filler	0	-	-
BM51	Cement	2	TCM	-
BM57	Cement	2	P25	-
BM75	Cement	0	-	-
BM27	Cement paint	2	TCM	-
BM33	Cement paint	2	P25	-
BM74	Cement paint	0	-	-

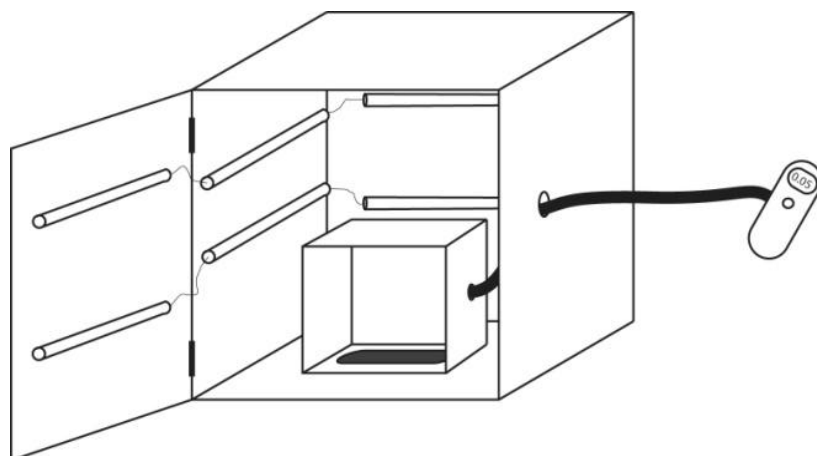


Image 8. Schematic representation of handmade photocatalytic apparatus. Photocatalytic Reactor connected to HCHO mobile sensor

Chapter IV

Characterization Results

4.1 ZnO characterization results

4.1.1 The effect of different Temperature and Power

X- Ray Diffraction

The X-Ray diffraction patterns of ZnO, synthesized with varied temperature and microwave power, are shown in *Fig 3a* and *b*, respectively. The obtained diffraction patterns were in good agreement with the Joint Committee on Powder Diffraction Standards (JCPDS card no. 36: 1451) and are indexed as hexagonal wurtzite zinc oxide, without any impurities. In all the spectra, the (101) reflection emerges with the highest intensity.

Fig.3a indicates that the sample annealed at 90 °C has much lower peak intensity, compared to its counterparts annealed at 150 and 220 °C. However, the sample annealed at 220 °C showing the highest peak intensity exhibited also a blue shift towards lower 2θ angles. This shift is indicative of a change in the material lattice parameters, particularly in the increase in the d-spacing and grain size, (see *Table below*). In addition, the increase in the plane reflections intensity indicates the high purity of ZnO, as a function of high temperature and impurities decrease.

Fig 3b indicates that the samples synthesized using higher microwave power have higher peak intensity, in comparison to those prepared at lower powers, indicating the increase of purity of ZnO as a function of high microwave power.

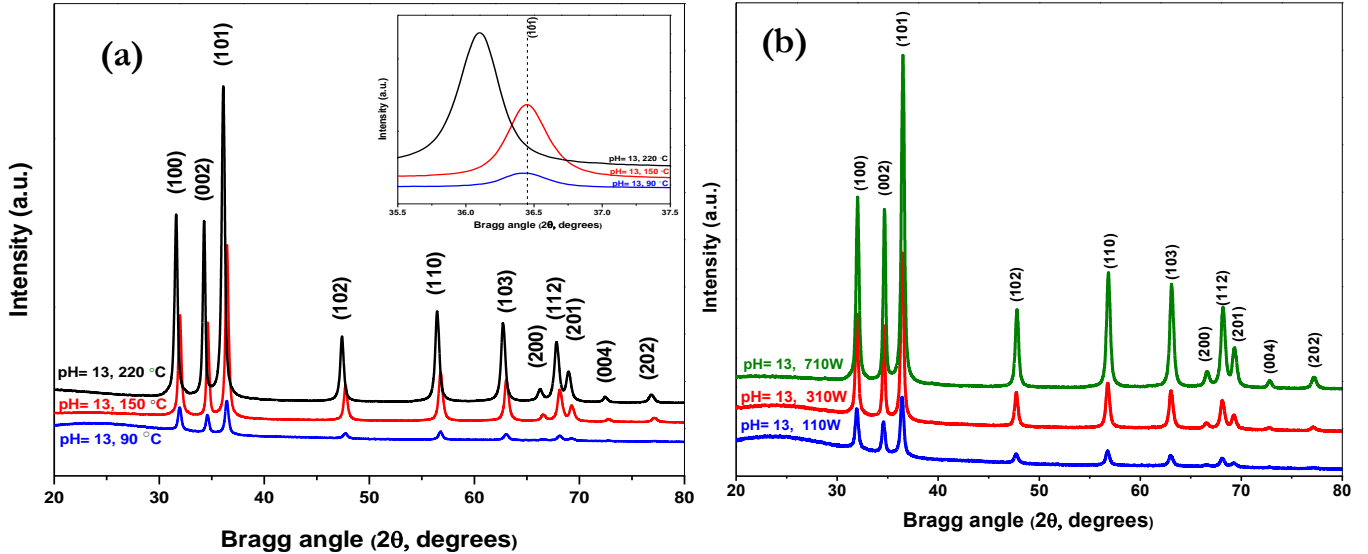


Figure 3. XRD patterns of zinc oxide at different (a) temperature and (b) microwave power.

The crystallite sizes were calculated using the Debye-Scherrer's formula, i.e.

$$D = \frac{0.9\lambda}{\beta \cos\theta} [1]$$

where D is the grain size, λ is the X-ray wavelength used, β is the peak FWHM and θ is diffraction angle at (hkl) Miller indices, in this case $\theta_{(101)}$ (Kaneva et al., 2011). The changes in the lattice parameters were calculated using Bragg's law,

$$n\lambda = 2ds\sin\theta [2]$$

(Kalantar-zadeh, Fry, 2008), corresponding to wurtzite structure (*Table 3*), (Kashif et al., 2012).

Scanning Electron Microscopy

The SEM images of the ZnO samples, at various microwave power and various annealing temperatures, are shown in *Fig. 4*. The sample prepared at 90 °C temperature and 110 W microwave power has ‘nano-platelet’ morphology and very tiny particles attached to the ‘platelets’ covered by thin “fabric” wall. The structures had a size of approximately 300- 400 nm. Increasing the power to 310 W, these platelets come out clear on one center forming spherical ball. The surface area of the materials was also increasing. The platelets become thinner and larger, of diameter around 400-600 nm.

At 710 W, these platelets grew in horizontal directions forming large clusters, equal to several microns. The platelets became even thinner, less than 50 nm thin, and more agglomeration was observed. Similar behavior was found when the synthesis temperature was increased; creating smaller clusters of nanoplatelets form and their surface area was increased significantly (*Table 3*). The increase of temperature created highly porous nanostructures (*Fig 4e*). At 150 °C the diameter was observed to be around 400 nm and a further increase in the T up to 220 °C made these structures to have even smaller diameters around 200 nm and highly porous.

BET surface area

The BET analysis technique was used for measuring the nanoparticles’ specific surface area. For pH 13, at 110 W power and 90 °C temperature, the surface area was 10.44 m²/g (*Table 3*). With an increase of power to 310 W and 710 W, the surface area increases to 12.88 and 14.60 m²/g, respectively. Temperature increase had a more profound effect on the surface area, since when increasing the temperature to 150 °C, keeping the microwave power constant at 110 W, the surface area mildly increased to 11.64 m²/g, whilst when the temperature increased to 220 °C the surface area is grossly increased to 18.09 m²/g.

As far as porosity is concerned, at 110 W power and 90 °C it was 0.054 cm³/g, increasing to 0.089 cm³/g when the power reaches 310 W, while it remained stable, i.e. 0.082 cm³/g, at 710 W. The increase of temperature on the other hand increased the porosity profoundly, making it from 0.065 cm³/g at 150 °C to 0.107 cm³/g at 220 °C.

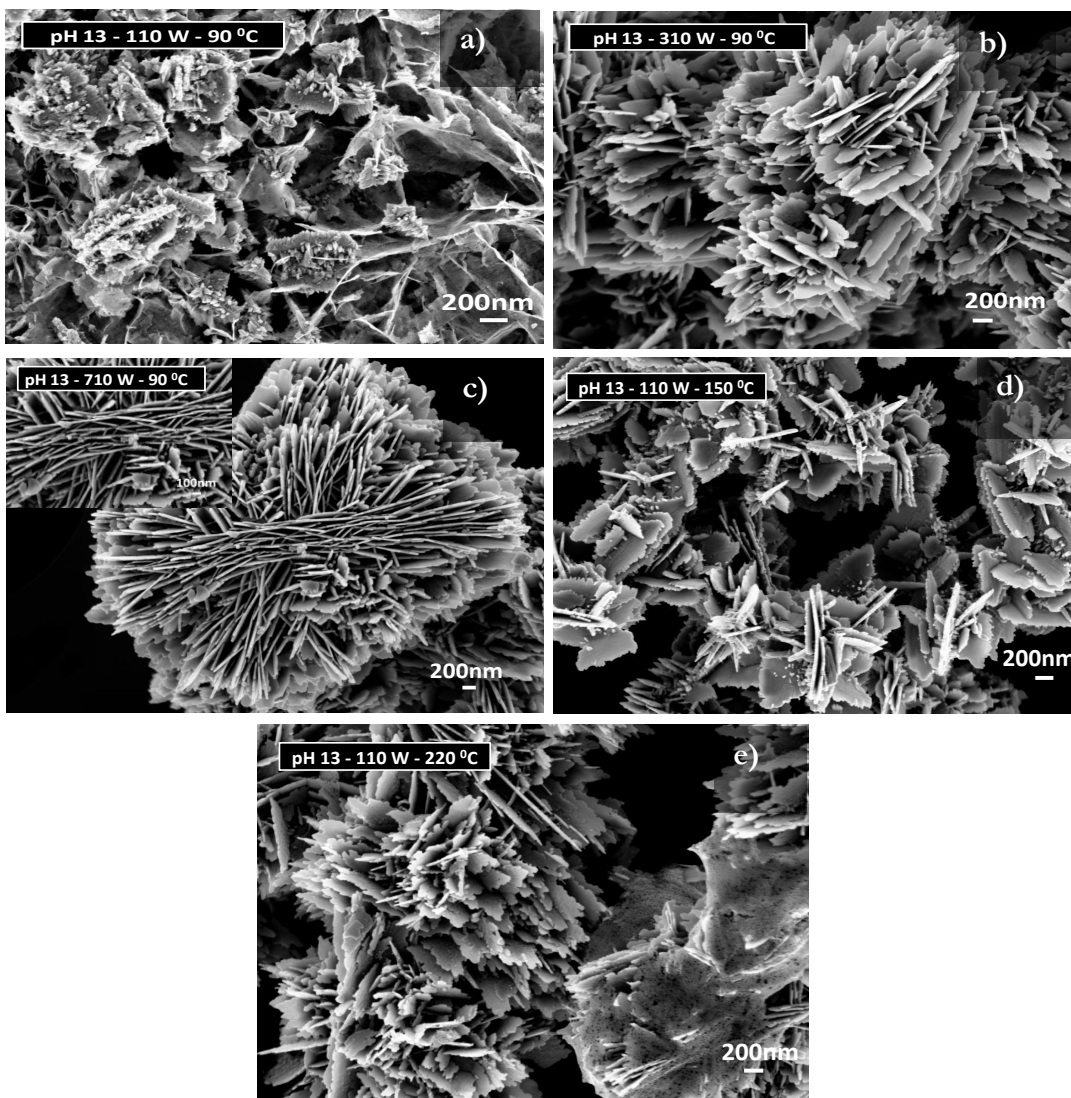


Figure 4: SEM images on different synthesis conditions: a. 110 W – 90 °C; b. 310 W – 90 °C; c. 710 W - 90 °C; d. 110 W – 150 °C; and e. 110 W – 220 °C

Optical Measurements

State of the art robust techniques for nanomaterials characterization were used, in order to investigate the nanostructures chemical composition and several other important characteristics, such as their Energy band Gap (E_g), the oxygen vacancies, interstitials and possible defects. Using UV-Vis spectroscopy the absorption spectra was measured and is presented in Fig. 5a and b. When keeping the annealing temperature constant at 90 °C, the absorption peak of lower power (110 W) was 374 nm, shifting to lower wavelengths of 366 nm when reaching the 310 W; however with further increase of power it shifts again to higher wavelengths of 377 nm.

Nonetheless, when keeping microwave power constant at 110 W and increasing the temperature from 90 °C to 150 °C the absorption peaks shift from 374 nm to 378 nm, while a further increase in temperature (220 °C) shifts the wavelengths to lower, particularly to 371 nm. The red shift in these spectra represents the reduction of oxygen defects and a blue shift represents the increase of oxygen defects (Zhang et al., 2010).

Fig.6a and *b* show the PL spectra of ZnO powders, in different powers and temperatures, excited at the wavelength of 350 nm. The PL intensity increased with increased power, while the opposite was observed with increased temperatures. The PL emission is the result of the recombination of excited electrons and holes. The larger the oxygen vacancy content, the stronger the PL signal. Broad PL signal is attributed to the oxygen vacancies and defects on the surface (Zhang et al., 2010).

The absorption wavelength shifted to lower wavelengths when increasing the power, particularly it shifts from 391 nm to 389 nm; whereas, when increasing the temperature it shifted to higher wavelength, from 391 nm to 392 nm. Also in these spectra, the red shift in these spectra represents the reduction of oxygen defects and a blue shift represents the increase of oxygen defects (Zhang et al., 2010).

In the photoluminescence spectra there are emission bands in UV and visible spectra. The UV peak is considered as the characteristic emission of ZnO and assigned to the exciton transition due to the recombination of generated electrons and holes (Zhang et al., 2008; Xu et al., 2013). The main peaks appear at around 390 nm, 419 nm and 478 nm with some small differences between the different samples prepared at varied power and temperature conditions. The highest intensity peak, at 390 nm, is due to excitation, corresponding to excitonic recombination (Mhlongo et al., 2014), while the other peaks are attributed to defects. Particularly, at around 420 nm we find a peak attributed to O interstitials, while at 478 nm the transition between O vacancies and interstitials is being observed. The near band edge UV emission is stronger for pH 13 at microwave power of 710 W and at 90 °C, whereas in visible emission it is almost the same.

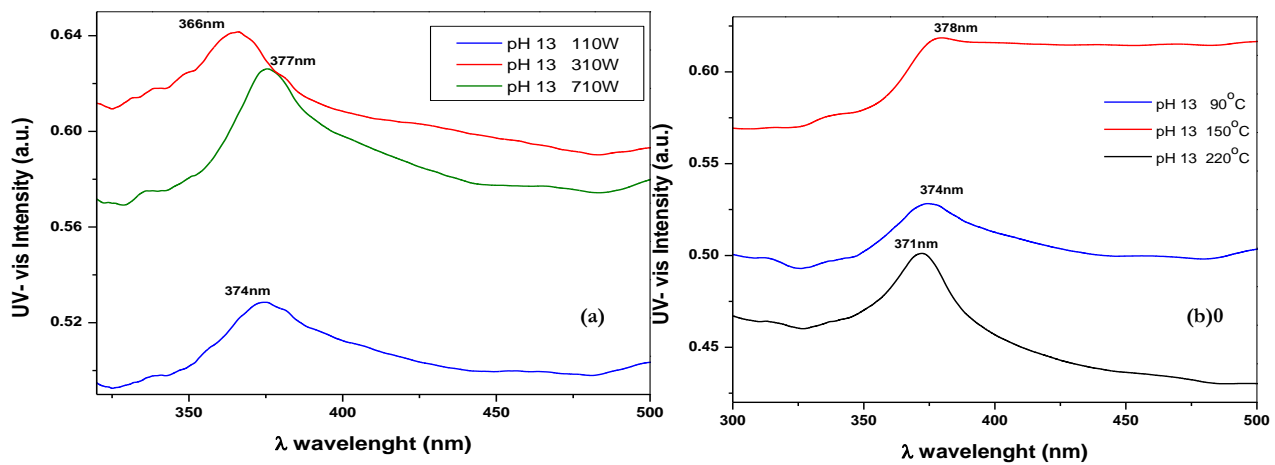


Figure 5. UV-visible spectroscopy on different (a) power and (b) temperature.

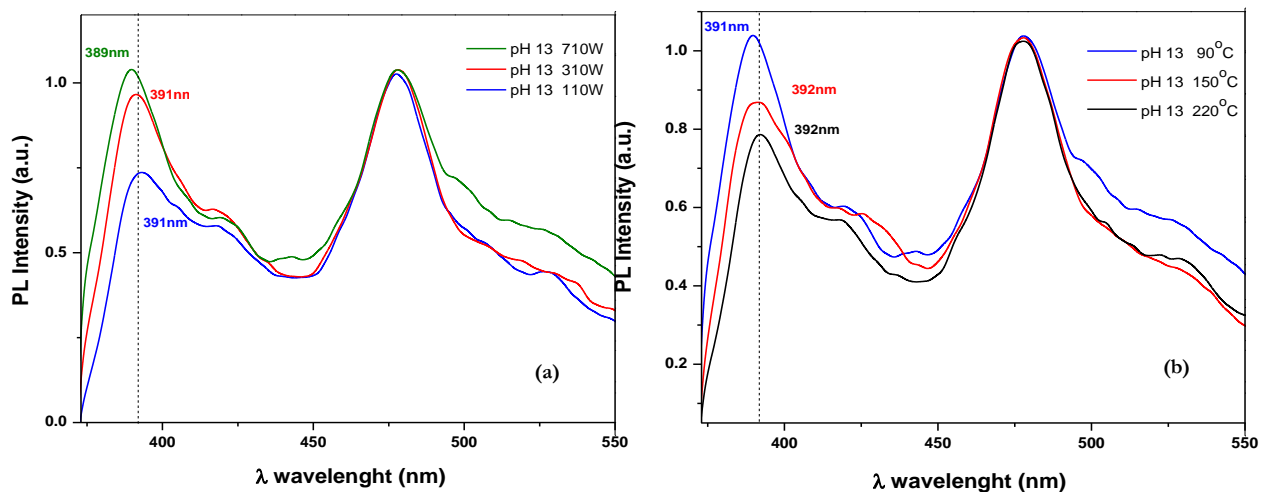


Figure 6. PL of zinc oxide with different (a) power and (b) temperature

Table 3: Lattice parameters, crystallite size & surface area, from XRD & BET

pH	Power (W)	Temp (°C)	Lattice parameters		Crystallite Size (nm)	d- spacing (nm)	Energy band Gap (eV)	Surface Area (m ² /g)	Porosity (cm ³ /g)
			a (nm)	c (nm)					
pH13	110	90	0.285	0.493	22.40 ± 0.40	0.2464 ± 0.0005	3.31 ± 0.01	10.44 ± 0.01	0.054 ± 0.004
pH13	310	90	0.284	0.493	24.83 ± 0.80	0.2463 ± 0.0005	3.38 ± 0.01	12.88 ± 0.14	0.089 ± 0.006
pH13	710	90	0.284	0.492	24.01 ± 0.30	0.2469 ± 0.0005	3.28 ± 0.01	14.60 ± 0.02	0.082 ± 0.003
pH13	110	90	0.285	0.493	22.40 ± 0.40	0.2464 ± 0.0005	3.31 ± 0.01	10.44 ± 0.01	0.054 ± 0.004
pH13	110	150	0.284	0.493	23.62 ± 0.30	0.2463 ± 0.0005	3.28 ± 0.01	11.64 ± 0.02	0.065 ± 0.005
pH13	110	220	0.287	0.497	24.47 ± 0.80	0.2486 ± 0.0005	3.34 ± 0.01	18.09 ± 0.04	0.107 ± 0.006

4.1.2 The morphological effect of different stirring time

Under the same synthesis procedure as thoroughly described above, the change of one parameter - the stirring time of the initial solution- resulted in significant structural changes for ZnO nanostructures. The formation remarks and patterns of the structural differences, according to the change of power (110-710 W), and pH (7 and 13) as provided only by Scanning Electron Microscope imaging (for resolution of 1 µm and 100 or 200 nm) are presented. Overall, the stirring time of these nanomaterials was one hour less than the ones in the previous section.

It is well known that controlling the morphology of nanoparticles is of key importance for their several uses in the construction industry, but also in other industries. For each applications there is a necessity for larger shapes, or smaller, 1D, 2D or 3D morphologies. Furthermore the dispersibility of nanomaterials, which is of great importance as already mentioned in the construction industry, can be achieved via specific nanoparticles morphologies. For instance spherical, non agglomerated nanoparticles in cement matrix proved to be effective in improving the mechanical properties of cement mortar ([Singh et al, 2015](#)).

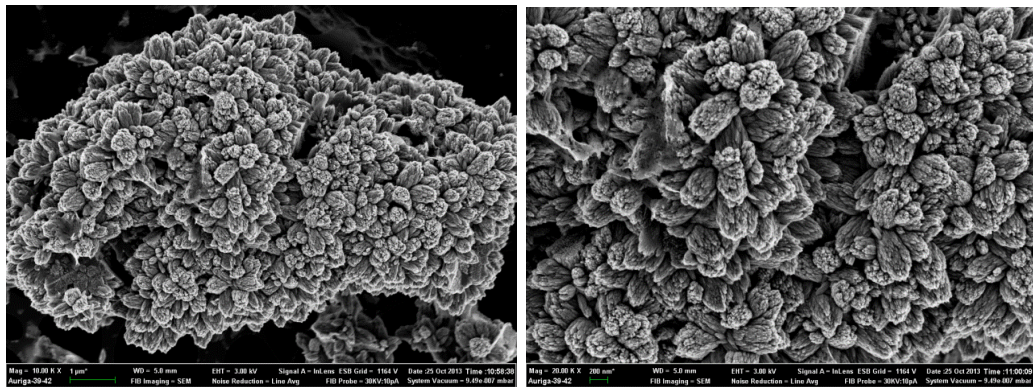


Figure 7. ZnO microwave synthesized nanopowders with pH 7 - power 310 W

When starting with a pH of 7 and power set at 310 W we do not observe the formation of any specific nanoshapes ([Fig.7](#)). Whereas in [Figure 8](#) we can observe the successful formation of hexagonal nanorods, even when set at lower powers (110 W), a process which can be attributed to the increase of their pH, from 7 to 13.

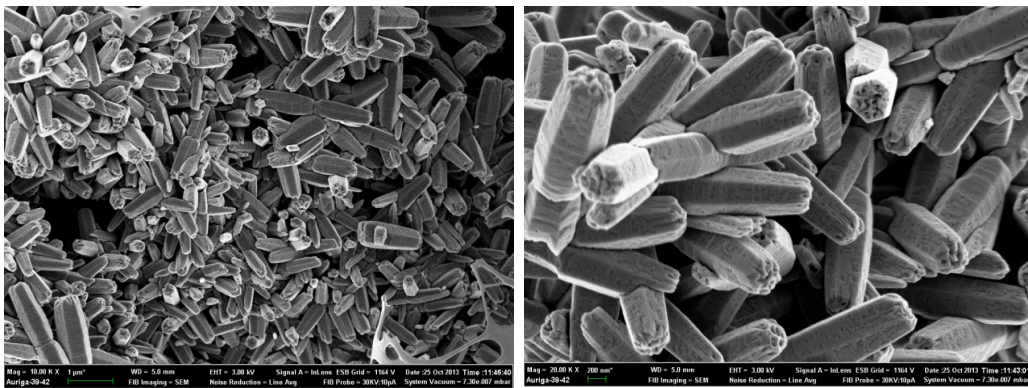


Figure 8. ZnO microwave synthesized nanopowders with pH 7 – power 510 W

The increase of power helps shape the nanostructures, observing hexagonal nanostructures for the first time when power is set at 510 W (Fig. 8). Their structures are longer and as power increases they become shorter and thicker (Fig. 9) (Zhang et al., 2014). Surface area and porosity seems to increase as well. Moreover they seem to form denser and bigger clusters.

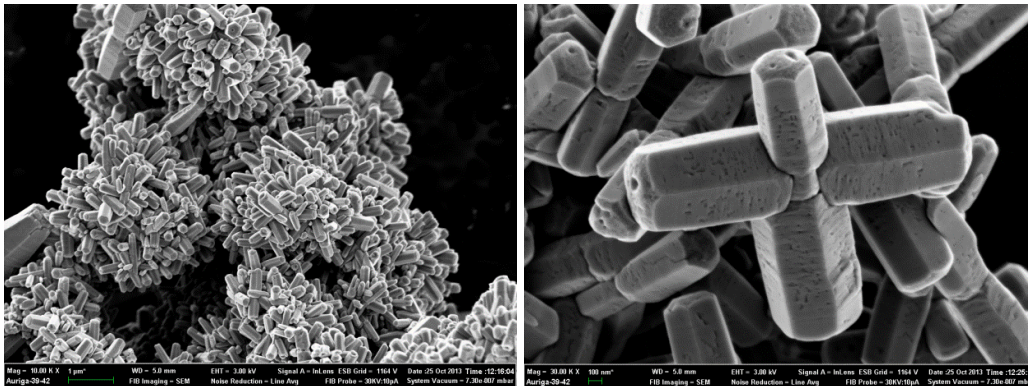


Figure 9. ZnO microwave synthesized nanopowders with pH 7 – power 710 W

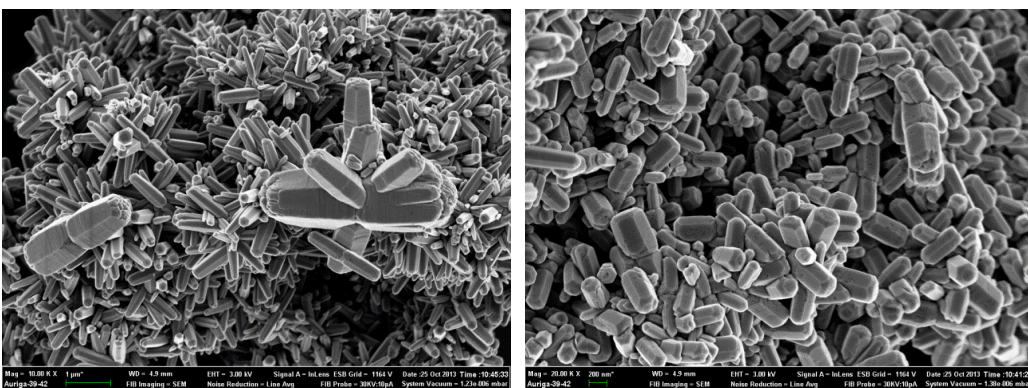


Figure 10. ZnO microwave synthesized nanopowders with pH 13 -power 110W

The increase of pH helps the nanostructures to format at an even lower power (Fig. 10). These new formed hexagonal nanorods are longer and thinner than in lower pH. The increase of power here is what makes them thinner and denser. They create many clusters and while having lost their hexagonal shape they are observable as very thin nanorods.

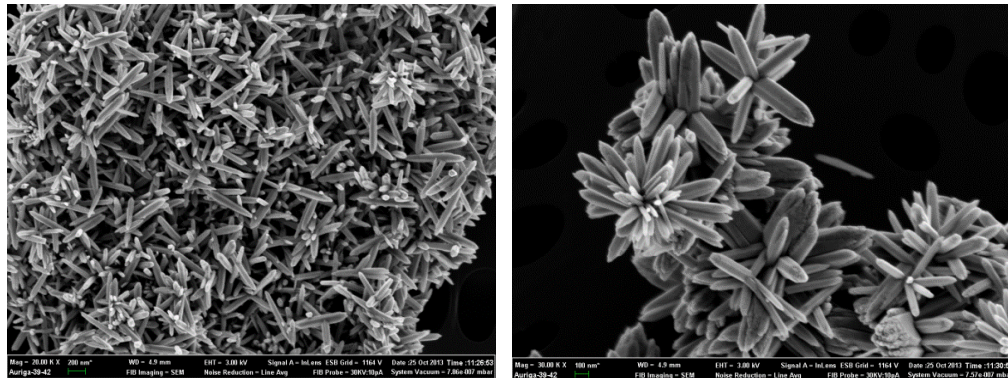


Figure 11. ZnO microwave synthesized nanopowders with pH 13 -power 310 W

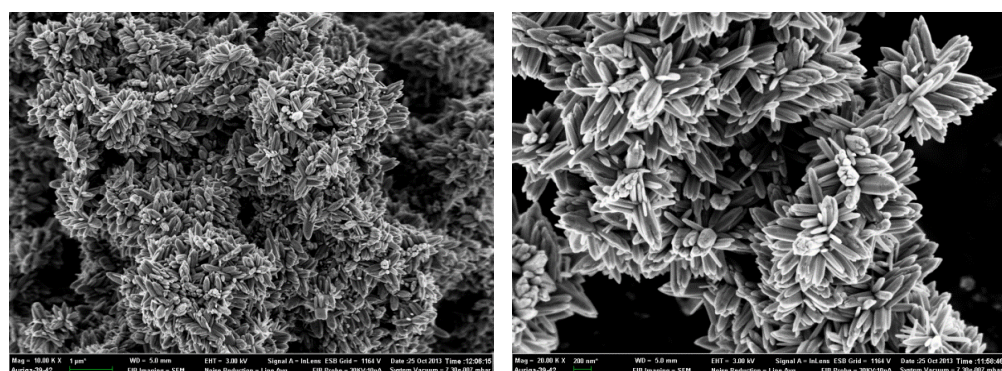


Figure 12. ZnO microwave synthesized nanopowders with pH 13 - power 510 W

A further increase of power up to 710 W results to the creation of platelets (Fig. 13). In the previous section, platelets were also formed, at a lower power of 310 W. This means that similar structural morphologies could have an effect on other characteristics of nanomaterials (like surface area, porosity, optical characteristics, etc) and can be achieved following several different synthesis paths. In this case, increasing the stirring time ([section 4.1.1](#)) results in similar morphologies (and possibly some common surface area characteristics) as observed when stirring time is decreased and power increased.

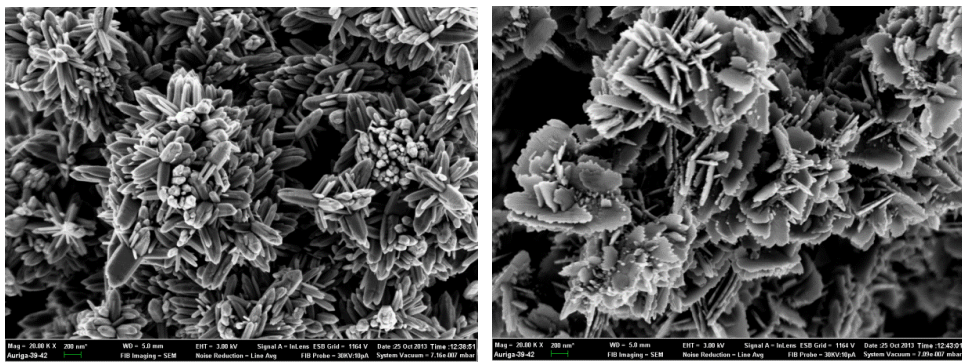


Figure 13. ZnO microwave synthesized nanopowders with pH 13 – power 710 W

Therefore different synthesis paths could possibly lead to similar or even same nanomaterials. Taking into account an environmental assessment of the synthesis procedure will help to identify the hotspots of these processes, and steps which lead to higher environmental impacts can subsequently be avoided. These classifications help us see nanomaterials from a different perspective. When taking also their environmental impact into account, we can achieve in creating the same nanostructures via different routes, with less hazards, risks and a lower environmental impact. Through these choices the optimization of the synthetic process can be achieved, while taking into account their environmental costs. This is a step forward sustainable synthesis of nanoparticles that can be used in the construction industry.

Overall the size of crystallites, the surface area, the porosity and the morphology are factors that affect highly the photocatalytic performance of a nanomaterial. During synthesis the increase of temperature and power, increases crystallite size, surface area and porosity. Especially for porosity, this is mainly affected positively by the increase of temperature rather than power increase. Temperature increase leads to higher agglomerations in the nanostructure. Furthermore, power increase makes the nanostructures thinner and denser, therefore even bigger agglomerations than in the case of T increase are observed. On the other hand pH increase helps the nanostructures morphology creation during lower T and P. Also similar nanoshapes are observed with the increase of stirring time to the nanoshapes observed while increasing P, therefore P increase could be substituted to higher stirring time, a procedure that could be also less environmentally intense.

All in all the effectiveness of nanoparticles increases with the increase of crystallite size (average size is preferable) surface area and porosity. In this case the increase of T and P could lead to more effective photocatalysts. However both P and T increase lead to higher agglomerations, making the dispersion problem (in the case of mixing them into building materials) even bigger. This could be solved by the manipulation of pH control, while increased pH leads to same morphologies in lower T and P therefore to lower agglomerations. Also increased stirring time could lead to substitution of the P and also agglomeration problems can be avoided. However for higher photocatalytic efficiency more oxygen vacancies are desired, therefore the increase of power could be beneficial.

	Crystallite Size	Surface Area	Porosity	Morphology	Oxygen vacancies
Temperature	Increased T increases cryst. size	Increased T increases surface area	Increased T increases porosity	Increased T : more agglomeration	Increased T, higher oxygen vacancies
Power	Increased P increases cryst. size	Increased P increases surface area	Increased P increases porosity	Increased P: thinner and denser & more agglomeration	Increased P, higher oxygen vacancies
pH				Increased pH helps them shape in lower T and P and less agglomerated	
Stirring time				increased stirring time could lead to same shapes with lower P	

Image 9 Critical process parameters that affect the photocatalytic behavior.

4.1.3 The effect of doping in ZnO nanostructures

Photocatalytic effectiveness is also achieved by the introduction of dopants in order to enhance response to visible-light and reduce recombination of photo-generated electrons

and holes (Zhang et al., 2010). Therefore Mn, Co and Cu were selected for doping the ZnO nanostructures.

X-Ray Diffraction

The X-Ray diffraction patterns of undoped and Mn, Co, Cu doped ZnO nanostructures displayed in *Fig. 14* exhibited sharp and intense diffraction peaks corresponding to the hexagonal wurzite structure of ZnO (JCPDS card no. 36: 1451). No diffraction peaks due to other secondary phases such as metallic Zn, Cu, Mn, and Co and oxides of these metals were detected. An obvious shift towards lower 2θ side in diffraction peaks position as well as an increase in diffraction peaks intensity with Mn, Cu, and Co doping was observed. This shift can be clearly observed on an inset in *Fig. 14* showing the enlarged diffraction peak corresponding to (101) plane where the peak positions of the (101) plane for Cu, Mn, and Co doped ZnO nanostructures were found to shift towards lower diffraction angles with Co doped ZnO exhibiting an unnoticeable shift.

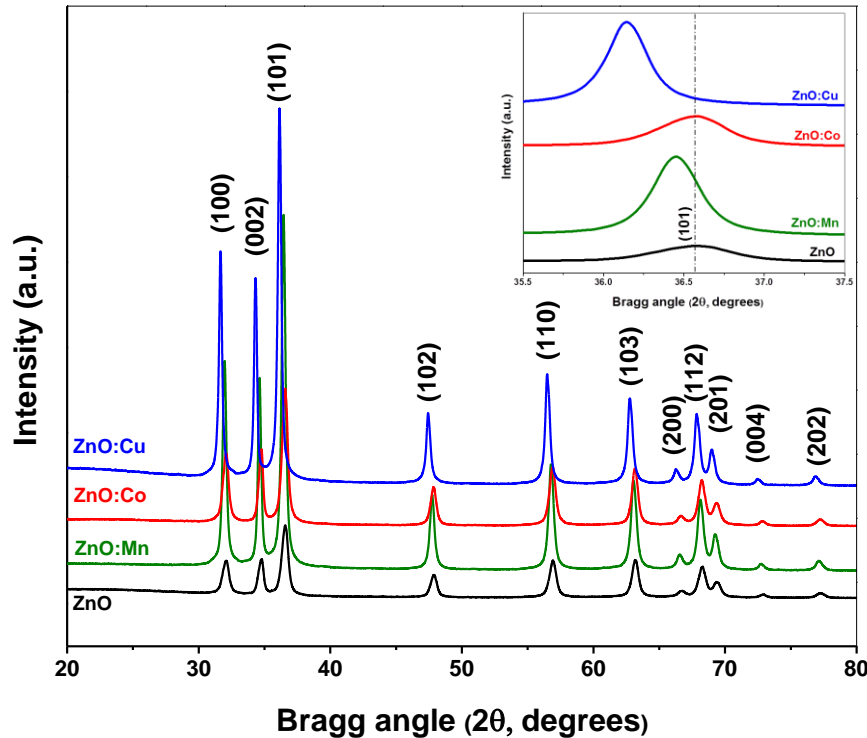


Figure 14 XRD patterns of zinc oxide undoped and Cu, Co, Mn-doped

The crystallite sizes are increasing in the order of Co, Mn and Cu. Moreover the atomic radius of Zn is 142 pm, while Cu has 145 pm, Co 152 pm and Mn 161 pm (Shakti & Gupta, 2010; Rajendar et al., 2012; Phan et al., 2010; Chen et al., 2014; Gercsi et al., 2010). The shift towards lower diffraction angles is evidence of substitution of larger ionic radii of Mn²⁺, Co²⁺, and Cu²⁺ into positions of smaller ionic radii Zn²⁺ which then leads to lattice expansion. In actual fact, replacement of Zn⁺ by Mn²⁺/Co²⁺/Cu²⁺ dopant ions may cause expansion/compression of the unit cell resulting to variation in various parameters including micro-strain due to lattice mismatch and distortion. The shifting trend towards lower diffraction angles in this case indicates that Mn²⁺/Co²⁺/ Cu²⁺ dopant ions entered into the ZnO crystal lattice to substitute for Zn²⁺ ions, which then led to lattice distortion of ZnO nanostructures and subsequent diffraction peak shift. Similar shift towards lower wavelengths has also been reported elsewhere (Mhlongo et al., 2014). The average crystallite sizes of both undoped and Mn²⁺/Co²⁺/ Cu²⁺ doped ZnO samples were calculated from the broadening of the intense (101) diffraction peak using the Debye- Scherrer's formula (Chand et al., 2012) shown in equation [1]. As observed from *Table 4*, the average crystallite size increased from 14.71 to 16.53, 21.59, and 24.61 with Co²⁺, Mn²⁺ and Cu²⁺ doping, respectively. Increase in the average crystallite size with doping arises from the fact that more distortions are being produced around the dopant ions and this leads to lattice expansion due to mismatch between ionic radii. Nonetheless this might also be the case for the increase in crystallite size observed in the Cu doped samples. This sample appears to have the highest increase in crystallite size, even though Cu has the smallest atomic radius and the closest to Zn than the other dopants. This could be attributed due to the strains cause by the substitution.

Table 4: Summary of lattice parameters, optical band gap and surface area

Sample	Lattice parameters		Crystallite Size (nm) XRD	d- spacing (nm) XRD	Optical band Gap(eV)	Surface Area (m ² /gr) BET
	a (nm)	c (nm)				
ZnO pure	0.3249	0.5206	14.71	0.2454	3.19	23.89
ZnO : Co	0.3261	0.4962	16.53	0.2455	3.16	24.84
ZnO : Mn	0.3263	0.5005	21.59	0.2461	3.11	9.62
ZnO : Cu	0.3262	0.5192	24.61	0.2482	3.13	2.99

Scanning Electron Microscopy

The SEM microscope of the ZnO samples is shown in *Fig. 15*. ‘‘Nano-platelets’’ morphology is observed with very tiny particles attached to the ‘platelets’ covered by thin fabric wall. Elemental analysis on the nanoplatelets was done by using energy dispersive spectrometer (EDS) (see *Appendix*). The peaks show the presence of zinc and oxygen.

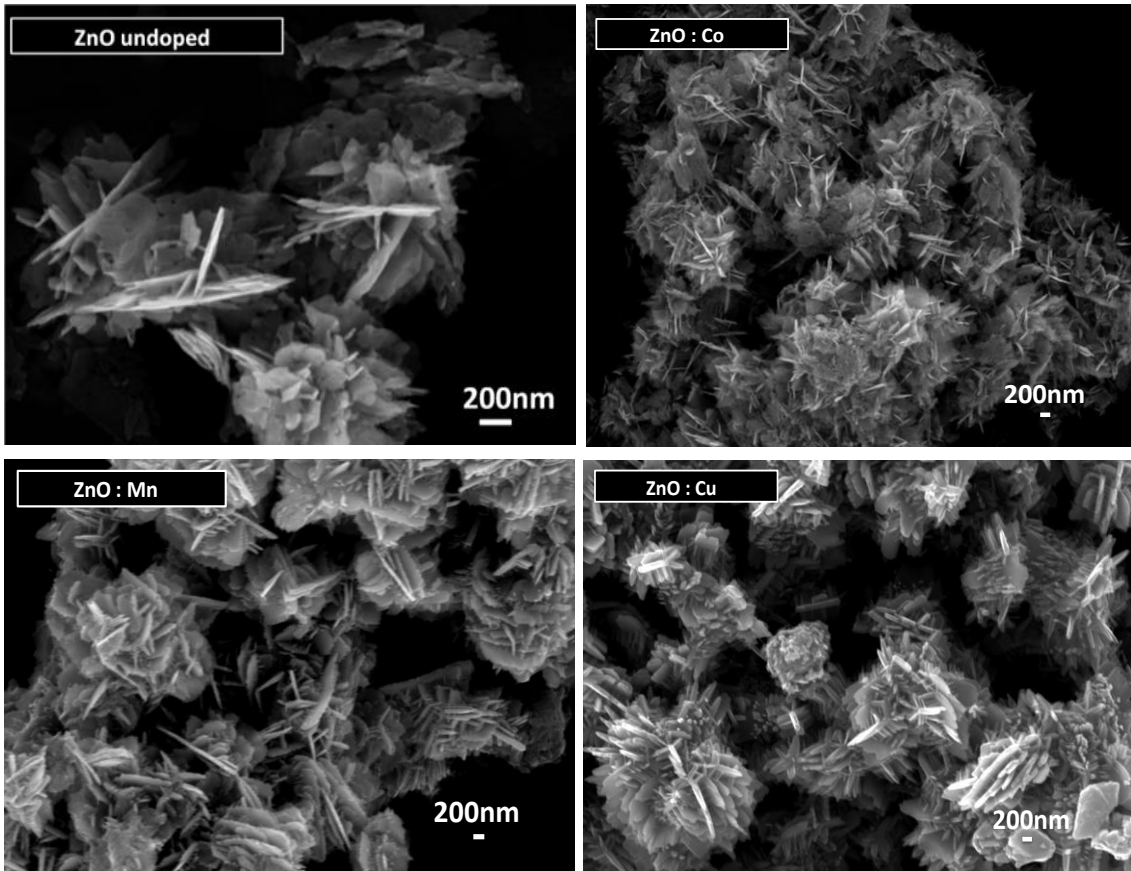


Figure 15 SEM images of ZnO samples doped with Co, Mn and Cu, at 200 nm.

More specifically we find 50.4% Zn and 46.7% O at zinc doped with copper, 44.5% Zn and 25.2% O at zinc doped with manganese and finally 45% Zn and 48.3% O at zinc doped with cobalt. The introduction of dopants increases the platelets size; however, the porosity of the particles becomes less and only in the case of Co, the nanoparticles are more porous than that of pure ZnO nanoparticles.

BET surface area

As we already discussed there is a linear relationship between the photocatalytic activity and surface area of photocatalysts. Also the selection of dopants plays a significant role on the surface area and porosity of the powder. More specifically, ZnO doped with Co revealed higher surface area of $24.84 \text{ m}^2/\text{g}$ and porosity $0.176 \text{ cm}^3/\text{g}$, the undoped ZnO showed the surface area of $23.89 \text{ m}^2/\text{g}$ surface area and $0.115 \text{ cm}^3/\text{g}$ porosity, while Mn and Cu displayed the lowest surface areas accounting to 9.62 and $2.99 \text{ m}^2/\text{g}$, respectively and similarly the porosity accounts for 0.055 and $0.027 \text{ cm}^3/\text{g}$ respectively. Such a lower surface area may be justified by aggregation of nanoplatelets. This is a crucial part of photocatalytic BMs since agglomerated nanoparticles enhance the dispersion problems of the nanomaterials inside the building matrices, making them inefficient photocatalysts.

Optical measurements

The reflectance spectra of all doped and undoped samples of ZnO nanostructures are presented in *Fig.16a*. It is obvious that Mn appears to have the lowest reflectance, less than 60% whereas the undoped sample appears to have a reflectance percentage of around 90%.

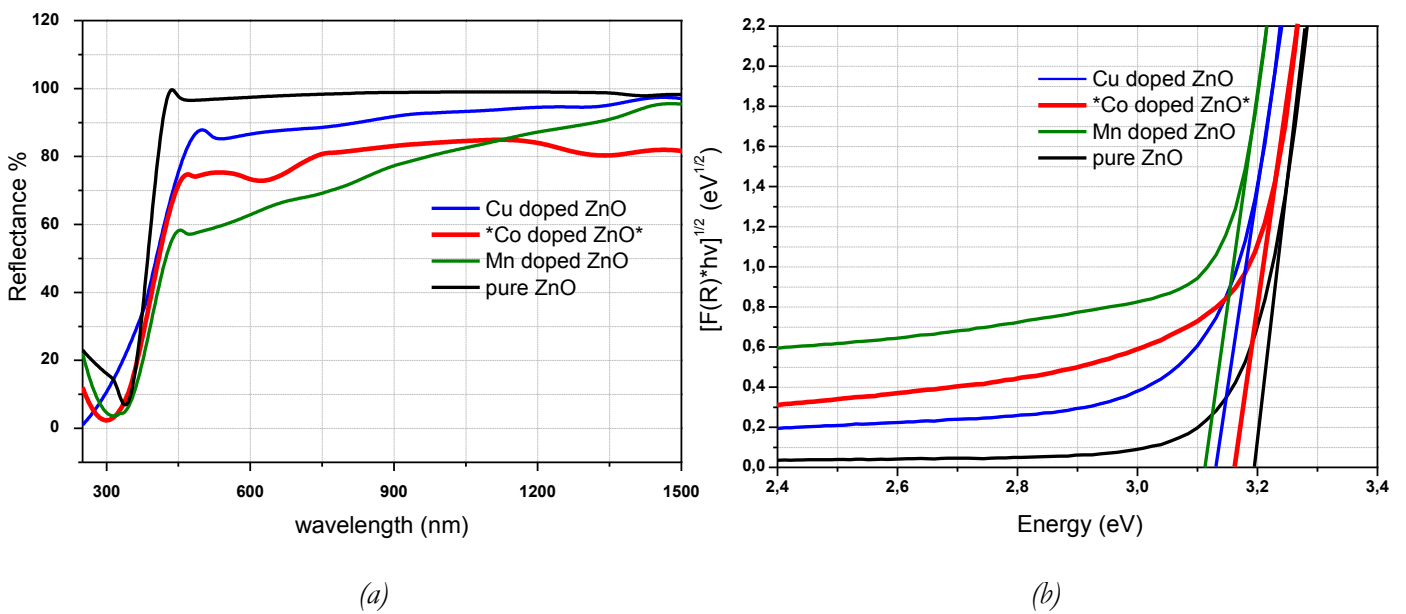


Figure 16(a) Reflectance spectra and (b) representation of Kubelka- Munk functions for ZnO samples

The energy band gap (E_g) was calculated by the extrapolation of the linear part of the graphs in *Fig.16b*, using the Kubelka- Munk formula and the optical band gaps are show in *Table 4*. It clear that upon doping the band of the ZnO reduces slightly compared to that of undoped ZnO, denoting that Cu²⁺, Mn²⁺ and Co²⁺ are incorporated within the ZnO lattice.

Photoluminescence measurement

Fig.17 shows PL spectra of ZnO powders with different dopants, excited at wavelength of 350 nm. The PL intensity increases once we introduce the doping, with Co having the highest intensity. The absorption wavelength switched from 383 nm in the undoped ZnO to 391 nm with Co and Cu doping, whereas Mn shifted the wavelength to 394 nm. In the photoluminescence spectra of zinc oxides, there are emission bands in the regions of UV and visible; UV peak is considered as the characteristic emission of ZnO and assigned as the band edge emission or the exciton transition (Kundu et al., 2011, Vanheusden et al., 1996; Zhang et al., 2008). The highest intensity peak is due to excitation, while the other peaks at higher wavelengths (450-550 nm) are due to the defects. The main peaks are observed at 390 nm and 478 nm. The PL emission peak located at around 390 nm corresponds to the excitonic recombination (Dai et al., 2003; Ridhuan et al., 2012) while the violet emission at 402 nm is due to electron transition from the conduction band to the VZn level (Mhlongo et al., 2014). UV and visible emission is much stronger for Co-doped ZnO, therefore Co- ZnO has higher oxygen vacancies (see also XPS section), resulting to possible higher photocatalytic behavior, followed by Mn- ZnO and Cu- ZnO. More oxygen vacancies produce more recombination centers. Therefore more oxygen vacancies also yield more photocatalytic reactive centers and improve the photocatalytic activity for the sample (Zhang et al., 2010).

According to other reports, the peaks at 420 nm and 485 nm are related to interstitial oxygen levels in zinc oxide and the transition between vacancy of oxygen and interstitial oxygen, respectively (Chand et al., 2012).

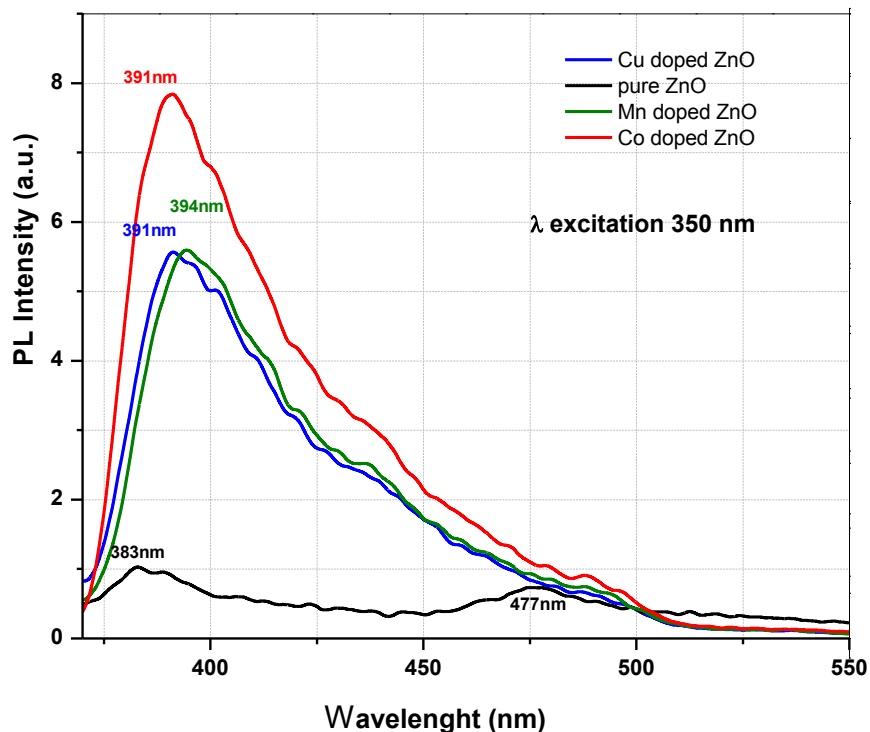


Figure 17. PL of zinc oxide doped with Cu, Mn and Co.

XPS analysis

For the detailed information of the surface chemical composition of the ZnO nanostructures X-ray photoelectron spectroscopy (XPS) analysis is presented in this section. The typical XPS wide survey spectra of various dopants of ZnO (a) pure ZnO, (b) ZnO doped with Co (c) ZnO doped with Mn and (d) ZnO doped with Cu are depicted in the *Appendix*. The peaks of Zn, O, C and the dopants, Co, Mn and Cu respectively were detected as shown in the wide survey spectra. Binding energies are corrected using the C 1s peak with a binding energy of 284.6 eV as a reference (Wagner et al., 1979). The presence of carbon is due to the absorbed carbon on the surface after the exposure of the samples to the atmosphere (Al-Gaashani et al., 2012).

Table 5. XPS details for binding energy and atomic concentration

Sample	Element Peaks	Binding Energy	Concentration %
ZnO pure	C 1s	283.91	7.28
	C 1s	285.66	0.30
	O 1s (O _l)	528.98	17.07
	O 1s(O _v)	530.54	11.92
	O 1s	532.47	0.20
	Zn 2p 3/2	1020.17	31.66
	Zn 2p 1/2	1043.25	17.05
ZnO: Co	Zn 2s	1194.30	14.51
	C 1s	283.66	14.08
	C 1s	285.15	13.90
	O 1s	530.85	11.72
	O 1s	532.98	2.59
	O 1s	528.93	12.92
	Zn 2p 3/2	1020.22	22.05
ZnO: Mn	Zn 2p 1/2	1043.30	12.03
	Zn 2s	1194.19	10.61
	Co 2p	780.59	0.05
	Co 2p	785.19	0.04
	C 1s	283.73	17.50
	C 1s	285.11	9.95
	O 1s	530.96	3
ZnO: Cu	O 1s	529.28	12.21
	O 1s	531.10	15.76
	Zn 2p 3/2	1020.59	17.60
	Zn 2p 1/2	1043.67	9.49
	Zn 2s	1194.72	8.09
	Mn 2p	655.06	2.78
	Mn 2p	625.65	0.00
	Mn 2p	662.29	2.51
	C 1s	284.05	21.09
	C 1s	286.09	5.95
	O 1s	530.69	14.92
	O 1s	528.97	9.27
	O 1s	530.20	1.95
	Zn 2p 3/2	1020.27	23.92
	Zn 2p 1/2	1043.35	13.20
	Zn 2s	1194.19	8.66
	Cu 2p	951.20	0.20
	Cu 2p	948.60	0.27

From these results it is obvious that only photoelectron peaks of the elements of Zn, O, C, and the dopants (Cu, Mn, Co) are observed and also the Auger peaks of Zn LMM. The high resolution XPS spectra are presented in [Appendix](#). The 0 1s peak is found in [Fig.19](#), the Zn 2p in [Fig.18](#) and also Co 2p, Mn 2p and Cu 2p are found in [Appendix](#).

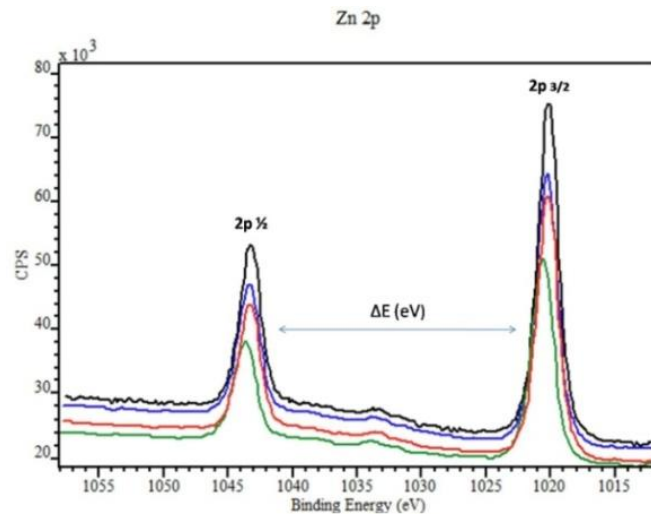
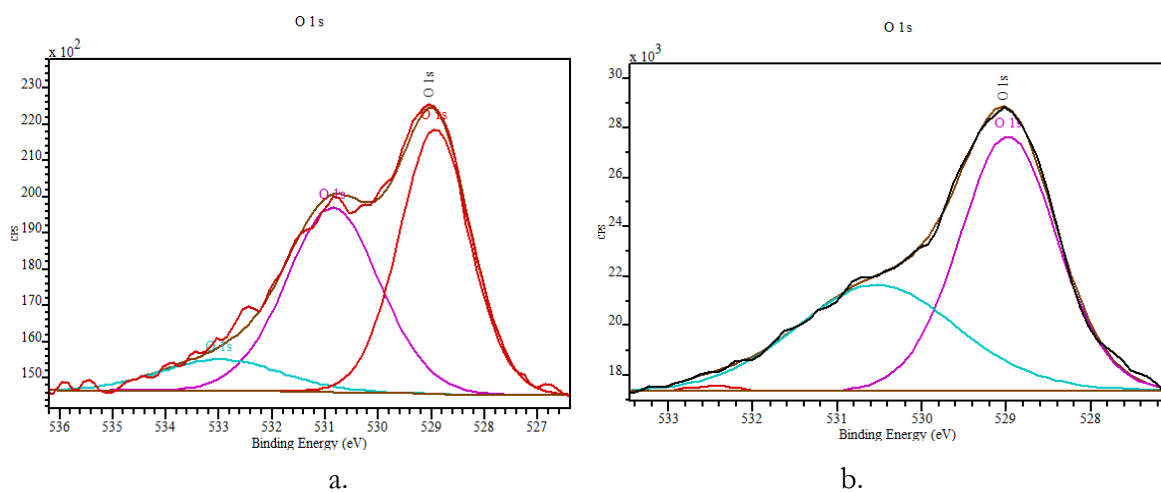


Figure 18. XPS spectra for Zn 2p peaks

From [Fig 18](#) and [Table 5](#), the Zn 2p for Cu doped ZnO has two fitting peaks at 1043.35 eV and 1020.27 eV, the Mn doped at 1043.67 eV and 1020.59 eV, the Co doped at 1043.30 eV and 1020.22 eV and lastly the undoped 1043.25 eV and 1020.17 eV. Those peaks are ascribed to Zn 2p $\frac{1}{2}$ and Zn 2p $\frac{3}{2}$. Therefore it can be observed that the binding energy of the differences between Zn 2p $\frac{1}{2}$ and Zn 2p $\frac{3}{2}$ (ΔE) is, for all samples 23.08 eV. These results indicate that the chemical valence of Zn at the surface of all our samples is +2 oxidation states ([Al-Gaashani et al 2012](#)).



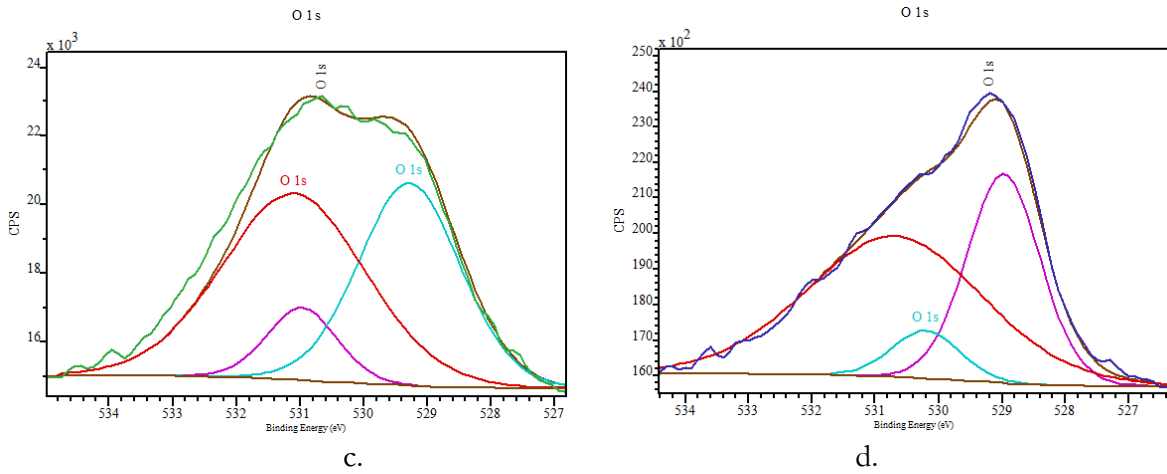


Figure 19: XPS spectra for O 1s Gaussian fitted peaks (a) pure (b) Co doped ZnO (c) Mn doped (d) Cu doped.

In Fig. 19 the XPS core-level spectra of O 1s is shown. Three different peaks are found to be fitting by Gaussian fit. Particularly, in Cu doped ZnO O1s peaks are met at 528.97 eV which accounts for the Zn- O bonding, the other in 530.20 which corresponds to the adsorption of oxygen species, and the intensity of that correlates with the photocatalytic behavior and the last one in 530.69 eV corresponds to the defects, shown also at PL. At the pure sample the lower energy binding peaks and at the same time the highest intensity peak (O_L), corresponds to the bonding of zinc with oxygen, at 528.98 eV, the second peak (O_V) at 530.54 eV corresponds to the oxygen species on surface; and the last at 532.47 eV to defects or contamination. Same peaks are found in Co and Mn also samples, and are in good agreement with the literature (Wagner et al., 1979). Interestingly we observe that the ratio (lattice/surface) of the Co doped samples is, O_L at 528.93 eV to O_V at 530.85 eV is 12.92 eV /11.72 eV is 1.1 whereas this ratio in all the other doped samples is higher, or even much higher (Cu and Mn) than 1. Meaning that in the Co doped sample the oxygen found in the lattice of ZnO is almost equal to the amount which was found on the surface of the material and attributed to the hydroxyl radicals or the oxygen vacancies or defects on the surface. This is something that will possibly enhance the photocatalytic activity of the material, as the oxygen vacancies/ defect and the hydroxyl radicals are crucial factors in this procedure. Also in Co doped sample the peak that corresponds to the adsorption of oxygen species on the surface is very high in comparison to other doped samples. Additionally the details of XPS analysis are given in Table 5. The atomic concentrations are also listed in there. The results show that the

O/Zn is lower than 1 (or slightly similar to 1 for Mn doped samples) confirming that the powders are pure ZnO ([Al- Gaashani et al 2012](#)).

The effect of lattice/surface oxygen in photocatalytic nanomaterials

It is known that there is a direct correlation between the surface photocatalytic activity and the lattice/ surface ratio found on the surface of a material. The surface defects (like oxygen vacancies) can promote the separation of electron–hole pairs under irradiation, and therefore, enhance the activity during photocatalytic reaction ([Yan et al., 2013](#)). It is well understood therefore, that the lower the lattice/surface ratio the higher photocatalytic efficiency is expected.

More specifically the physically absorbed hydroxyl groups are removed when a sample is measured under the ultrahigh vacuum of the XPS. Therefore the hydroxyl groups observed are due to ·OH and H₂O, strongly bound to surface defects on the nanomaterial. Hydroxyl groups are linked to surface defects. Moreover higher value for O 1s means higher amount of surface defects and hydroxyl groups. Many studies have shown that the photocatalytic performance is strongly related to the oxygen defect concentration and type of defect. The presence of surface hydroxyl groups facilitates the trapping of photo induced electrons and holes, therefore, enhances the photocatalytic efficiency ([Zhang et al., 2014](#)).

4.2 TiO₂ characterization results

4.2.1 The effect of Ammonia exposure

Anatase TiO₂ is a high performing photocatalyst. In this section we will investigate the ammonia exposure on the structural effect of TiO₂ bulk nano-photocatalyst. All the ammonia exposed samples are presented with red, and before being exposed, with black. In all the XRD we observe no difference before and after ammonia exposure. Except in Indium doped sample, where the intensity of the main peak decreases. The grain size remains the same (*Table 4*) except in the case of Co, Al and In where the crystallite size decreases after NH₃ exposure. Regarding the E_g only in the case of Mn we observe a small decrease.

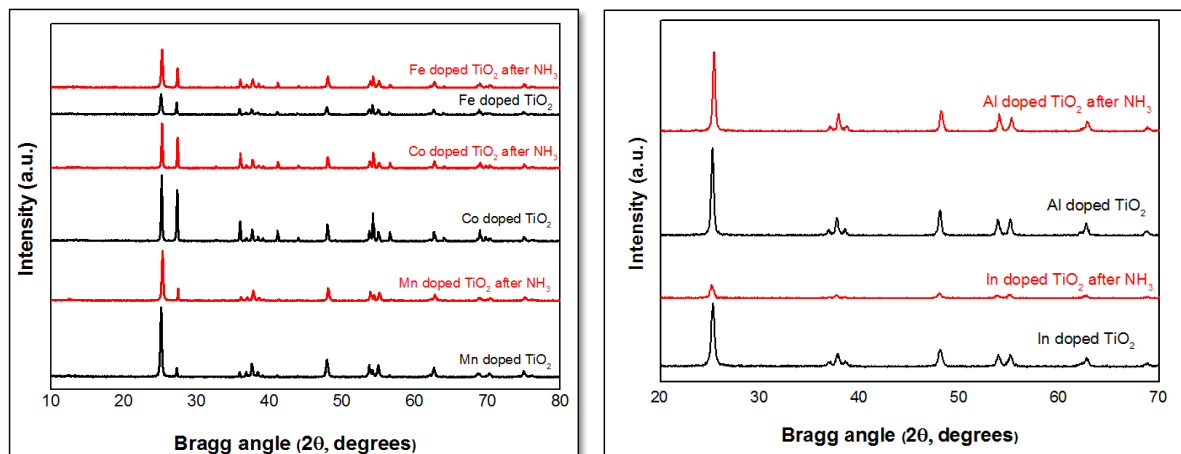


Figure 20. XRD patterns of TiO₂ doped with In, Al, Mn, Co and Fe; red: after Ammonia exposure, black: before Ammonia exposure.

From XRD patterns, we observe that Al and In doped samples have 100% anatase whereas Fe, Co, and Mn have a combination of anatase and rutile phase. Taking into account the optical measurement (*Fig. 20*), we observe a peak in the visible region in Co doped sample, expecting some photocatalytic behavior in this region. Moreover in poor metals, In and Al doped samples, the ammonia seems to influence their optical results.

Table 6. Crystallite sizes and Energy band gap of TiO_2 doped samples

Doped TiO_2	Crystallite size (nm) Anatase	Energy Band gap (eV)
Mn	35.4	2.6
Mn after NH_3	35.4	2.3
Co	32	2.3
Co after NH_3	28.3	2.1
Fe	32.7	2.6
Fe after NH_3	32.5	2.6
Al	28.3	3.0
Al after NH_3	25.8	3.1
In	23	3.1
In after NH_3	19.3	3.0

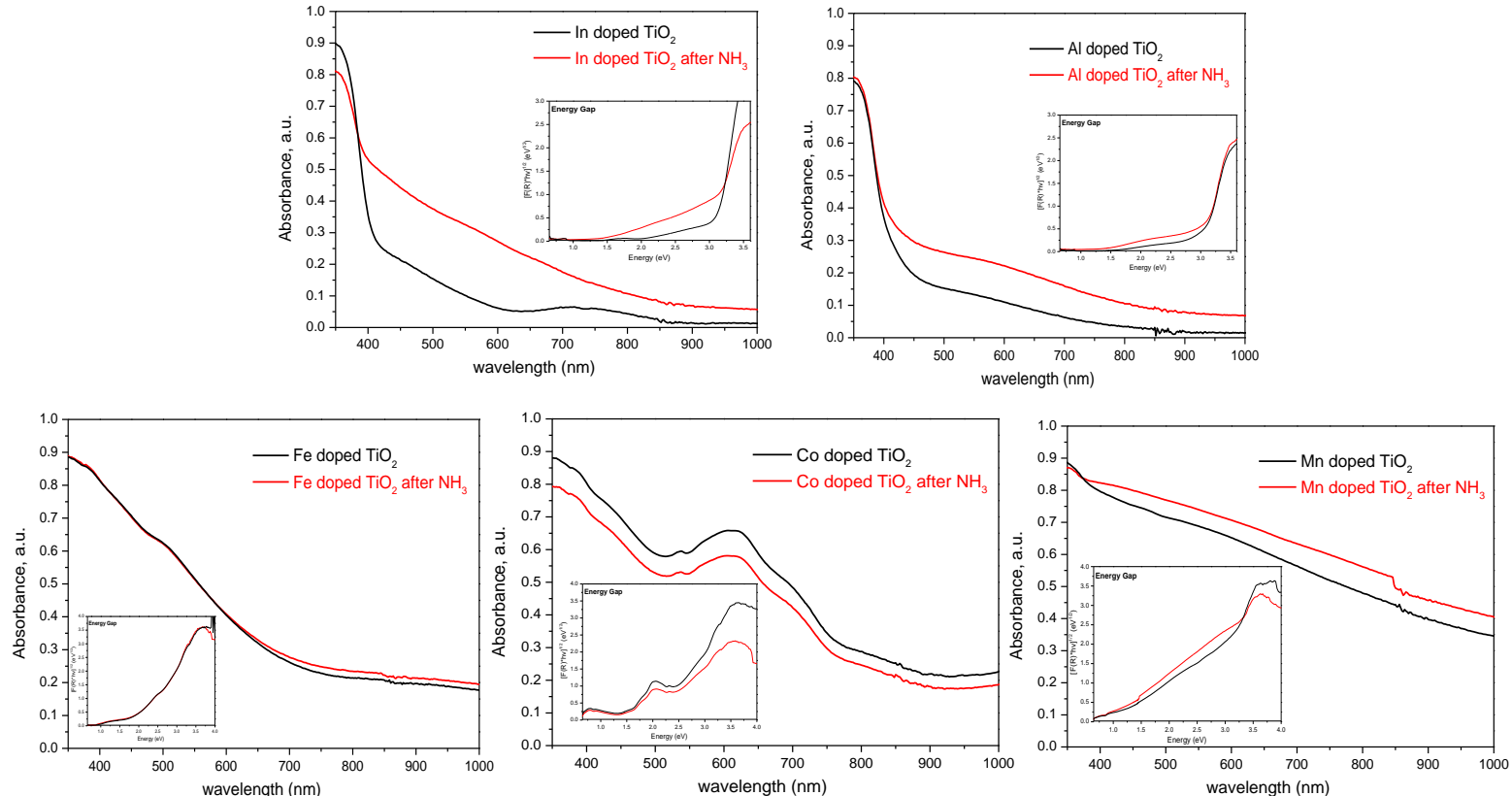


Figure 21. UV Vis spectra of TiO_2 doped with In, Al, Mn, Co and Fe samples

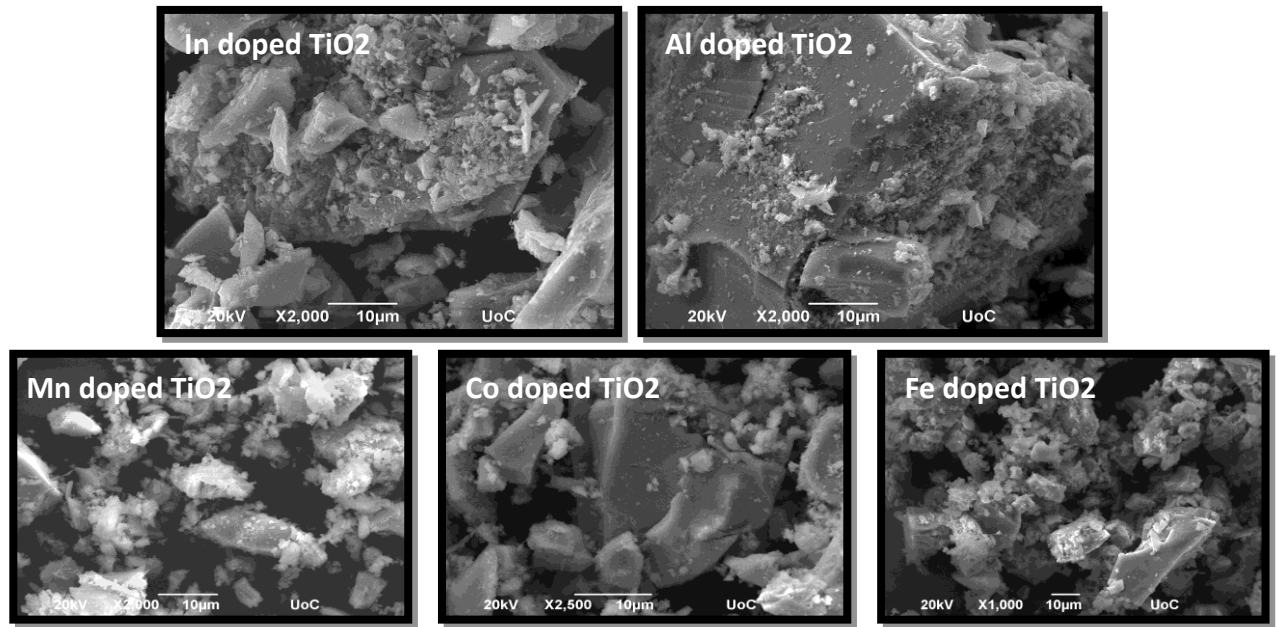


Figure 22. SEM images of TiO_2 doped with In, Al, Mn, Co and Fe.

X-Ray Photoelectron Spectroscopy

For details surface analysis, the introduction of NH_3 gas *in situ* was conducted for the first time inside the chamber of the XPS, providing us with knowledge on the possible influence of ammonia exposure on the surface of our photocatalytic nanomaterials.

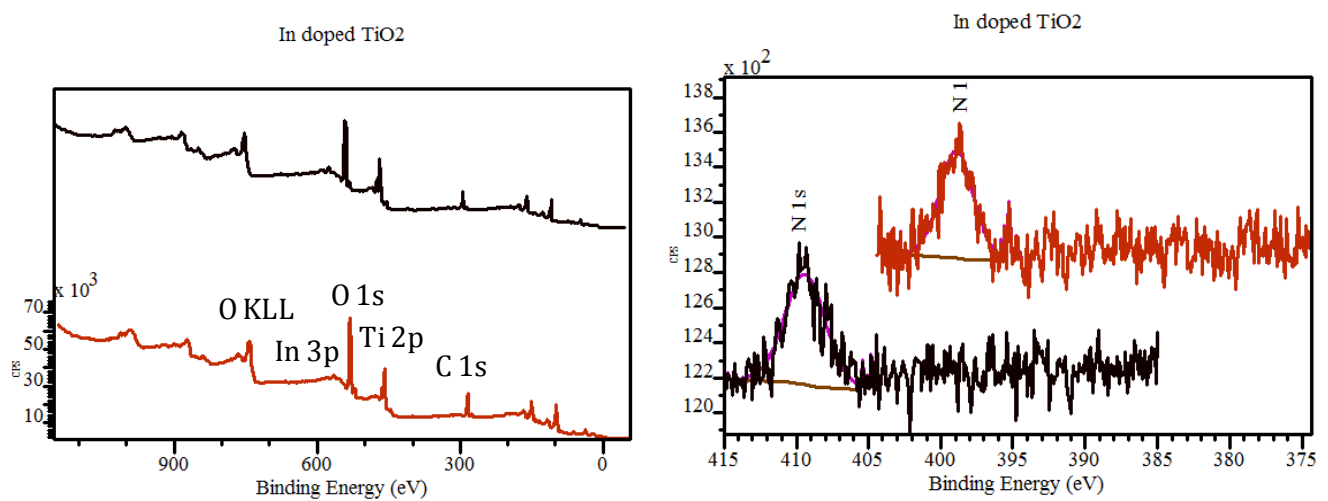


Figure 23. XPS spectra of In doped TiO_2

Binding energies are corrected using the C 1s peak with a binding energy of 284 eV as a reference ([NIST database version 4.1](#)). In the Indium sample we observe higher concentration of oxygen than all the other samples accounting to 58%, the N 1s peak ([Fig. 23](#)), Ti 2p and C1s ([Supplementary](#)) remain unchanged. In this section also the ratio between O_L and O_V peaks is presented. As stated earlier O_L is the peak of oxygen found in smaller binding energies (around 529 eV) and corresponds to the Ti-O bonding, or else the bulk oxygen in the TiO₂ lattice ([Yan et al., 2013](#)). The second peak, O_V, corresponds to the surface oxygen and presents the adsorption of oxygen or hydroxyl radicals ·OH and is associated closely to the photocatalytic behavior of the sample.

From all figures below, and [Table 7](#), it is clear that in all our samples, the ammonia exposure affected the oxygen of our samples. Specifically in the In doped sample, the ratio O_L/O_V is 0.7 meaning that ·OH or surface oxygen is higher in concentration to bulk oxygen, before and after ammonia exposure. This results to higher photocatalytic performance expectations from this sample.

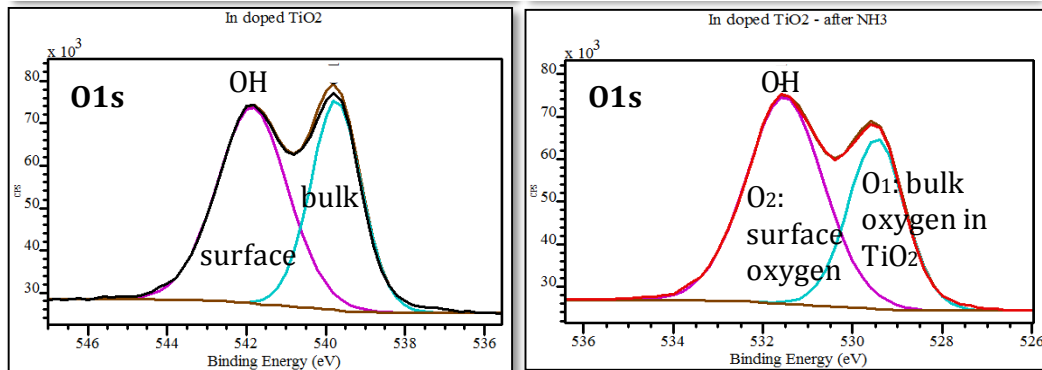


Figure 24. XPS high resolution O1s spectra of In doped TiO₂

In the rest of the samples same results are found, In Al doped samples the total concentration of oxygen remains very low, 17% and in the Ti spectra Ti³⁺ is observed, in the Mn 2p Al₂O₃ is also found. The O_L/O_V ratio is also smaller than 1. In Co doped samples O_V remains very high, before and after ammonia exposure. However the oxygen found in the lattice (O_L) before ammonia is 14% and after it decreases to 5%. In Fe doped samples we observe F³⁺ and a small amount of Fe²⁺ we also observe a very low concentration of OH- groups. Lastly in Mn doped sample the O_L decreased radically from 28% to 12%.

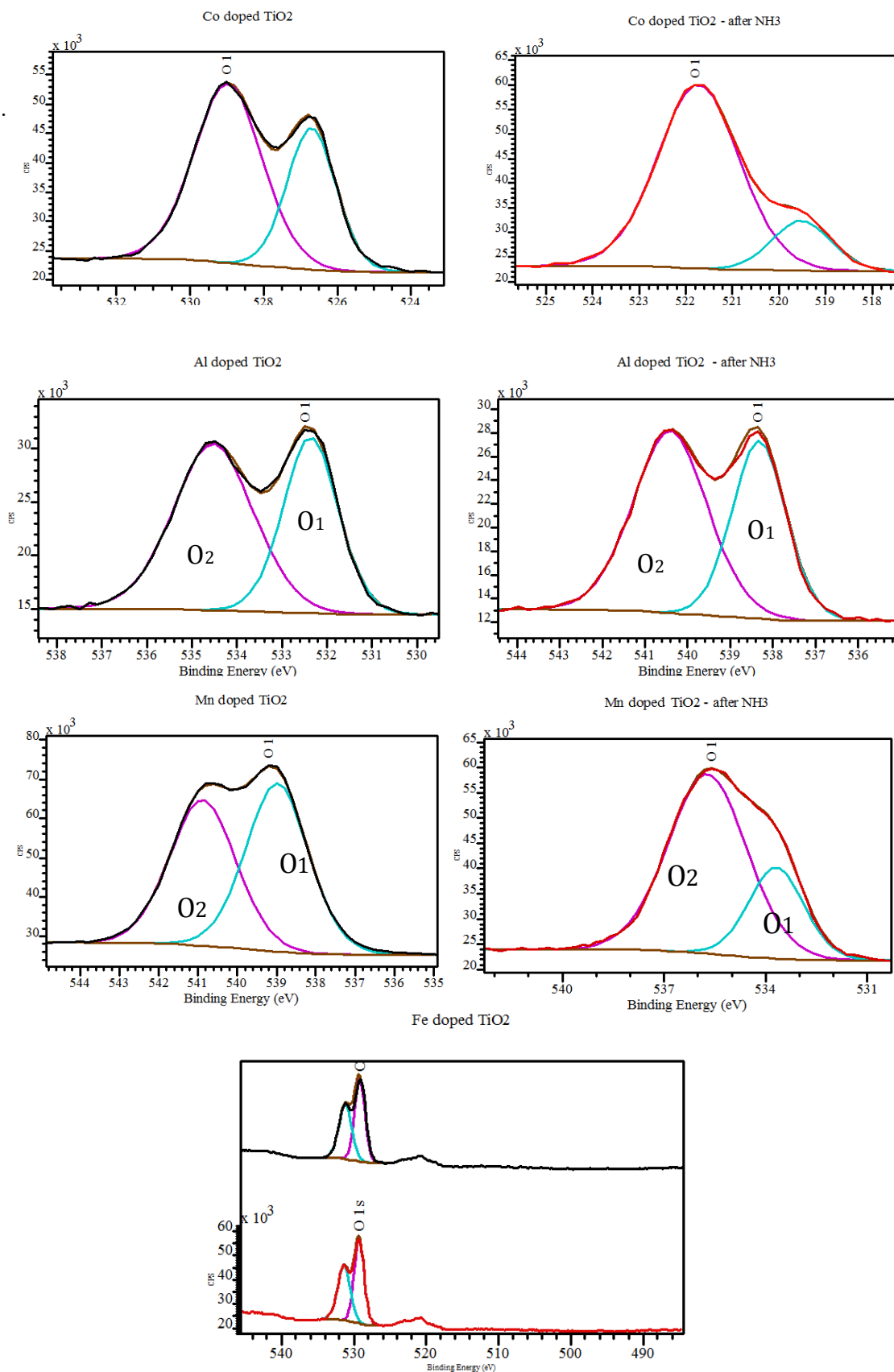


Figure 25. XPS high resolution O1s spectra

O1: O lattice and O2: O vacancies

Table 7: XPS results for In, Al, Fe, Co and Mn doped TiO₂. Binding energy, oxygen concentration, O_L/O_V concentration, and nitrogen concentration.

Before						After NH ₃					
TiO ₂ doped with	Binding energy (eV)	Oxygen concentr. %	O _L +O _V %	O _L /O _V	Nitrogen concentr. %	TiO ₂ doped with	Binding energy (eV)	Oxygen concentr. %	O _L +O _V %	O _L /O _V	Nitrogen concentr. %
In	O _V	33				In	O _V	33			
	O _L	25	58	0.7	1		O _L	20	53	0.6	1
Al	O _V	14				Al	O _V	14			
	O _L	10	24	0.7	0.7		O _L	10	24	0.7	1
Fe	O _V	26				Fe	O _V	24			
	O _L	30	56	>1	0.7		O _L	30	54	>1	1.3
Co	O _V	24				Co	O _V	24			
	O _L	14	38	0.6	5.2		O _L	5	29	0.2	5.5
Mn	O _V	25				Mn	O _V	35			
	O _L	28	53	>1	3		O _L	12	47	0.3	3

From this chapter we conclude that an area with gaseous ammonia seems to affect the structural characteristics of the photocatalyst, and possibly the photocatalytic performance of it. This will be further studied in the next section. Overall the ammonia lowered the amount of oxygen concentration (O_L+O_V) in all the samples; meaning that the oxygen vacancies possibly decreased. All spectra shifted due to oxygen decrease, in all samples we observed Ti⁴⁺ with a small contribution of Ti³⁺ due to an oxygen deficiency in the TiO₂ lattice.

In some of the samples (In, Al, Co) O_V is higher than O_L meaning that there are high amounts of oxygen vacancies and hydroxyl groups and is expected to affect the photocatalytic results. Also the photocatalytic effectiveness is expected to be higher for In doped samples since the total O % is higher from all the other samples, Nitrogen concentration is higher in Cobalt doped samples, something that will possibly affect the photocatalytic performance also. Overall non transition metals are highly affected by NH₃.

4.2.2 The incorporation of TiO_2 in Building Materials

X- Ray Diffraction

From the XRD patterns TiO_2 has been well identified. Only P-25 sample appears to have a small peak in rutile phase whereas all the rest samples have 100% anatase phase. TCM (anatase TiO_2) appears to have high sharp peaks narrower than the rest of the samples, indicating higher crystallinity with lower surface deficits and better oriented crystals. The broader peaks of Crystal Global (anatase TiO_2) and P-25 (~3:1 anatase: rutile TiO_2) could be caused by strain and defects. Also, as noticed from the *Table 8* below, the broader the peaks the smaller the crystalline size is. Therefore TCM has the higher crystalline size.

We have examined also the three building materials via their XRD patterns and the results are presented here. It appears that the peaks of calcareous fillers are similar to the peaks of cement paint and are well defined as Calcium Carbonate, CaCO_3 or else calcite. However for cement the XRD peaks are different and match to elements like Tricalcium silicate 3CaOSiO_2 (in the highest amount, marked with *) but also Quartz (an element used in cement because it is inert and provides strength) (SiO_2) as well as several other compounds such as calcium, iron aluminum oxides, and Mg oxides, and also Brownmillerit, or else $2\text{CaOFe}_2\text{O}_3$.

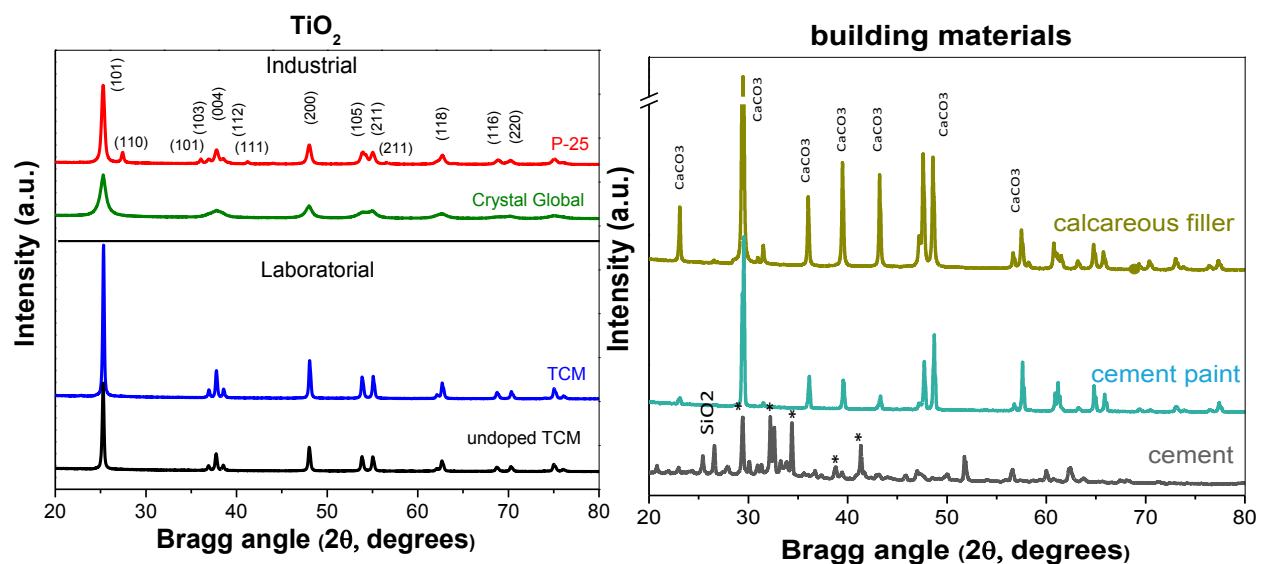
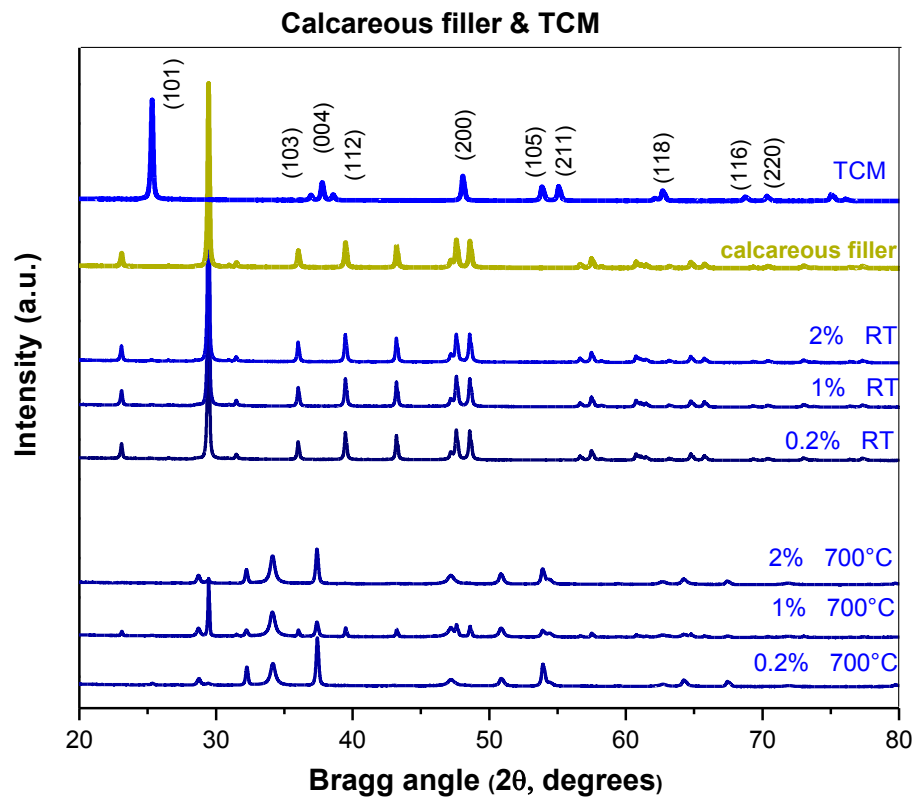


Figure 26. XRD patterns of Titania samples and building materials

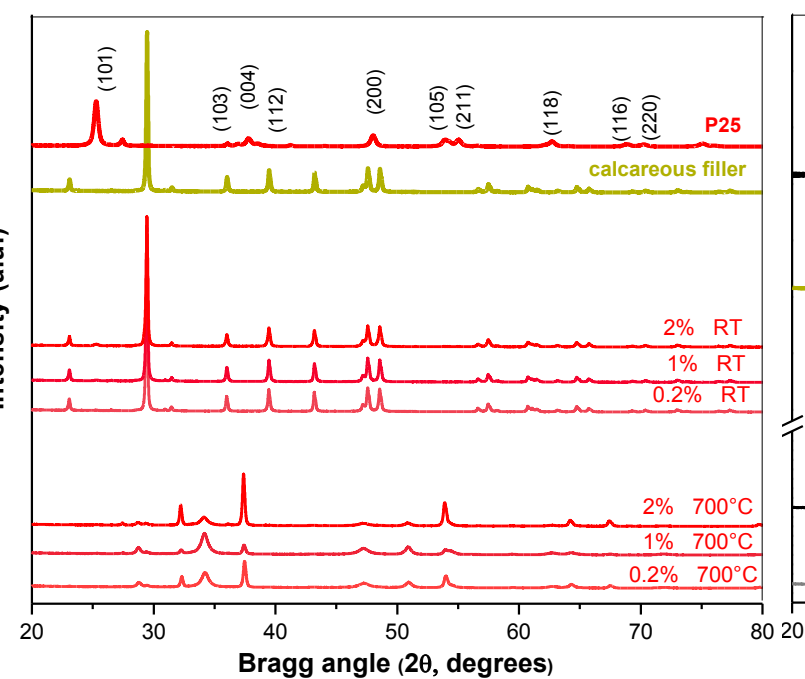
After mixing nanopowders with building materials, in different concentration and before and after annealing we come up to the following graphs. For both TCM and P-25 we conducted XRD measurements in all their concentration and also calcined and not calcined for the mix with calcareous filler. For the rest we present the XRD patterns of the highest concentration of Titania (2%). For RT what we conclude is that TiO_2 is not visible at any concentration and the pattern remains unchanged through the 3 different concentrations ([Appendix](#)). This is in good agreement with the next section of XPS analysis. In RT the patterns with all different concentrations and different Titania are identical, and match the pure calcareous filler pattern, with calcite peaks being prominent.

Interestingly in TCM, P25, and Crystal Global samples inside calcareous filler, after calcinations there is a peak of TiO_2 appearing in 2% concentration, whereas there was not before calcinations process. In the undoped sample, we do not identify any Titania peaks before or after T treatment.



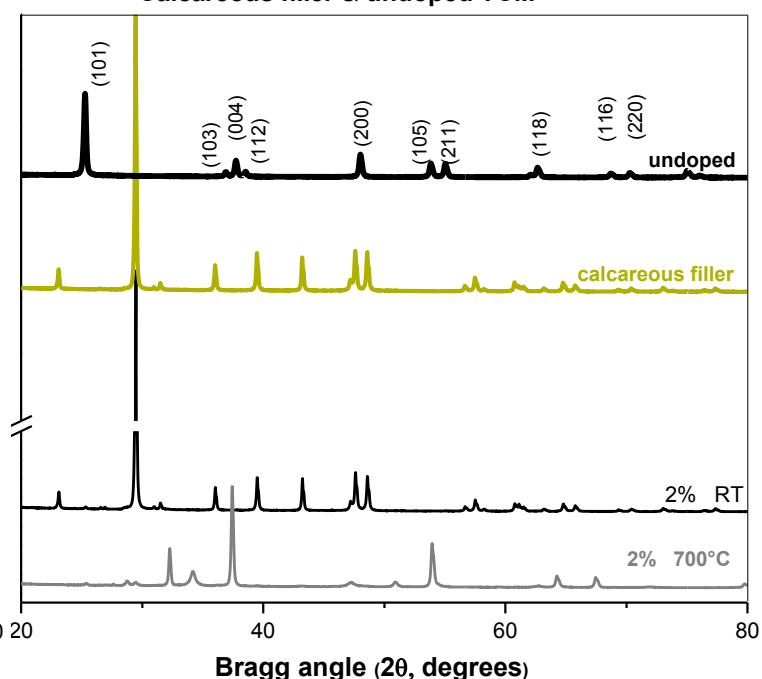
a.

Calcareous filler & P25



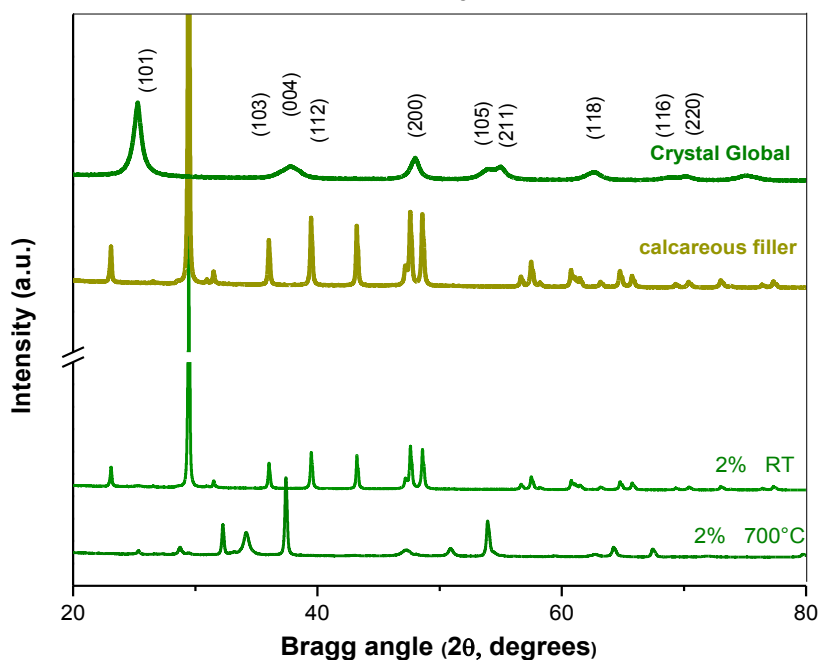
b.

Calcareous filler & undoped TCM



c.

Calcareous filler & Crystal Global



d.

Figure 27. All TiO₂ samples in different concentrations and T, inside calcareous filler, a. TCM, b. P25, c. Undoped, d. Crystal Global.

The calcined samples of calcareous filler mixed with photocatalytic materials show new peaks that correspond to calcium hydroxide or else Portlandite, $\text{Ca}(\text{OH})_2$, then Calcium oxide or else Lime, CaO and some remaining calcite. Also as already mentioned TiO_2 peaks appear in these samples. Only in case of 1% TCM in calcareous filler calcined at 700 °C there is a peak that appears to be a very strong remaining calcite peak, maybe due to something that occurred during calcinations process of this specific sample. After the calcination of calcareous filler it is expected that calcite turns into lime and CO_2 . Therefore the TiO_2 are now able to be identified in the samples after calcination. Further on, lime together with water produces Portlandite which together with CO_2 produces again calcite.

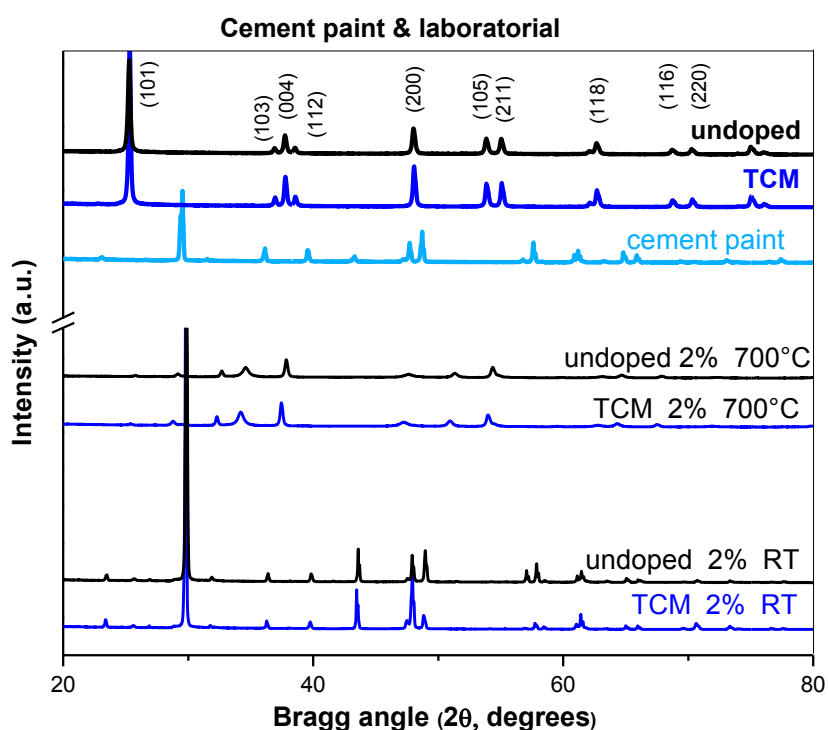
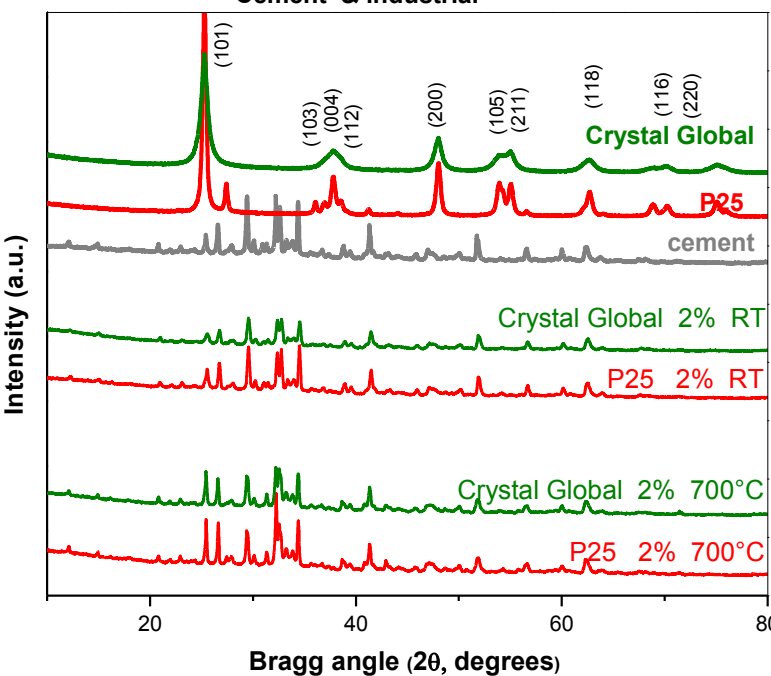


Figure 28. XRD patterns of TCM, undoped, and cement paint. Also 2% TCM, and 2% undoped, inside cement paint, before and after calcination.

In the matrix of cement paint, all RT samples are identical with the bulk cement paint. On the other hand the calcined have a different pattern which corresponds also here (like in calcareous fillers), to calcium oxide, or else lime CaO , calcium hydroxide, or else Portlandite. Also in cement paint all Titania is identified only in the calcined samples.

P25 and Crystal Global
Cement & industrial



TCM and undoped
Cement & laboratorial

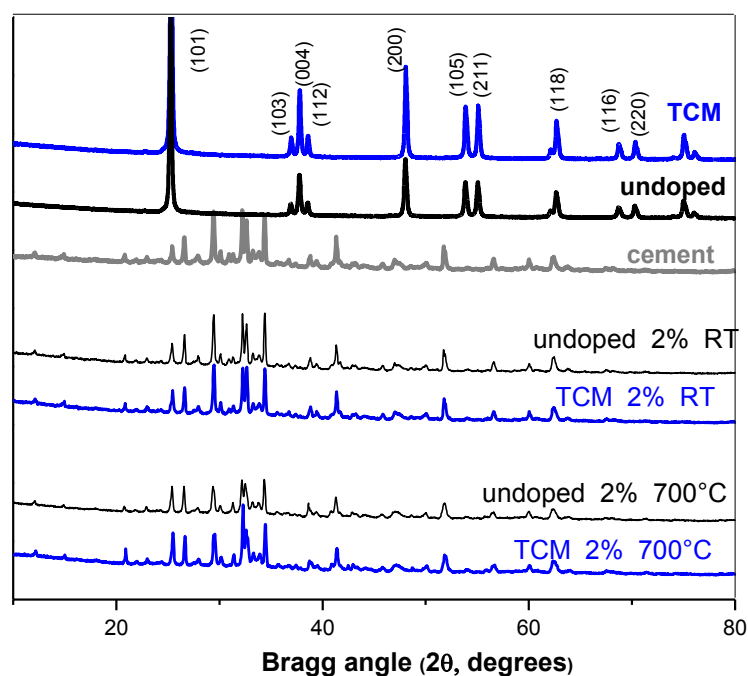


Figure 29 XRD patterns of Crystal Global, P25, TCM, undoped, and cement. Also 2% Crystal Global, 2% P25, 2% TCM, and 2% undoped, inside cement, before and after calcination.

In cementitious matrix, the Titania peak is found in both calcined and non calcined samples for all the tested TiO_2 samples. The peaks do not appear to have any change, in regard to the temperature treatment. Coming back to our introduction, this proves that cement can be a good match for synthesis of nanomaterials inside their matrix minimizing dispersion problems, while the growth will be inside the matrix.

Particularly from *Fig 29 and 30* it is clear that after 700 °C calcination, cementitious materials do not change, whereas calcareous and cement paint appear to have big differences. Structural cementitious resistance to T has been reported to some recent studies (Mudimela et al., 2009); however, their mechanical properties and possible changes after T treatment must be well studied.

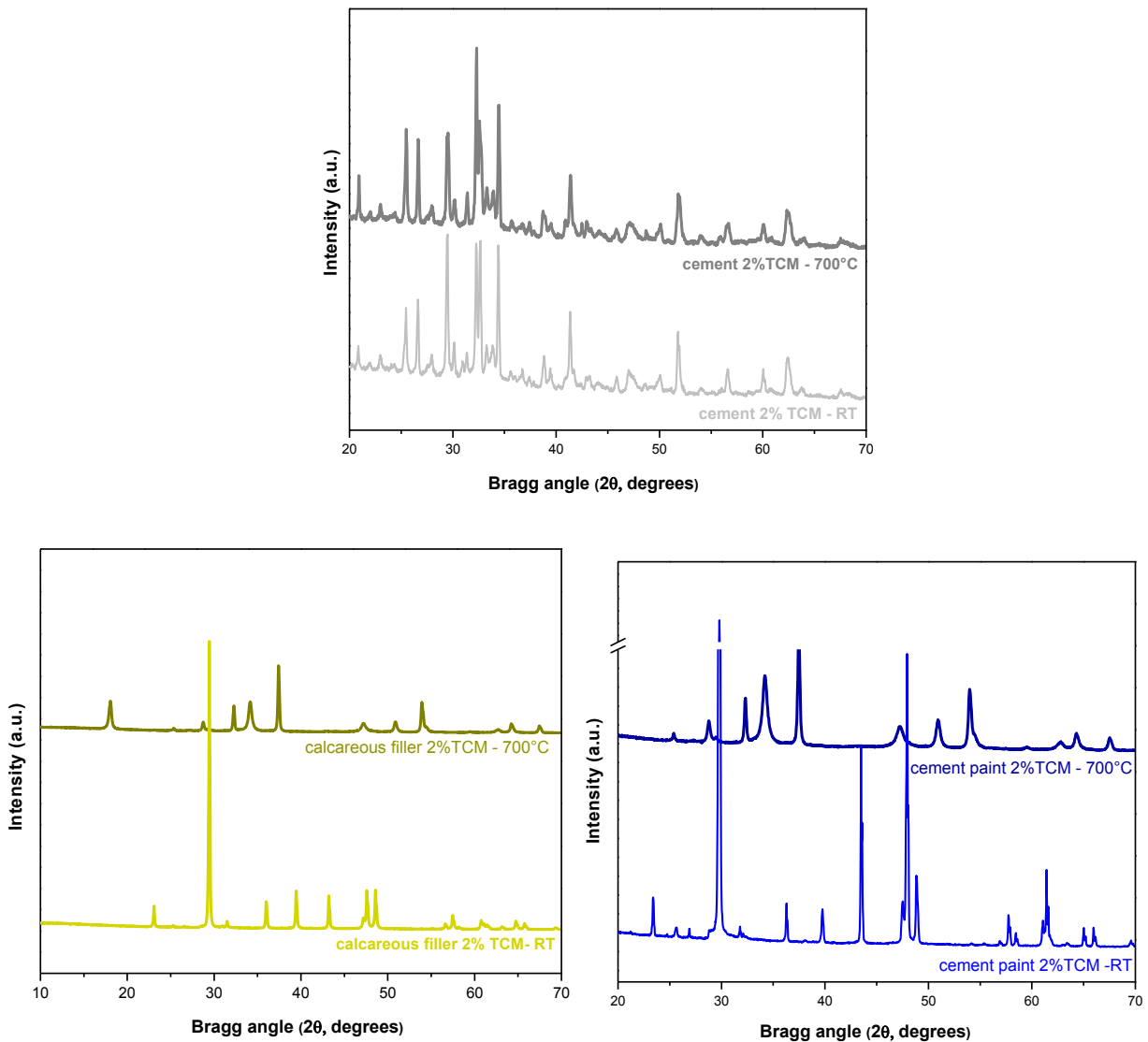


Figure 30. XRD patterns of cement, calcareous filler and cement paint with 2% TCM before and after calcination.

Overall from this structural analysis we observe that in order to mix nanomaterials inside building matrices several aspects should be paid attention to. A low concentration of 2% TiO_2 could not be identified in XRD measurements in calcite based samples (calcareous filler and cement paint) but it could be identified in cement based materials. Therefore in real scale applications the amount of photocatalyst used should be decided according to the matrix used. Furthermore the calcination helps the photocatalyst to be found in higher concentrations; however, not all matrices can undergo temperature treatment since this can alter their mechanical properties. Particularly T treatment of 700 °C alters calcite into lime, Portlandite and CO_2 , and then with the water of the atmosphere, calcite is being recreated. On the other hand cement materials do not appear any alteration for

T treatment of 700 °C, making this matrix very promising for solving the dispersion problems analyzed previously and a possible promising photocatalytic building material.

BET surface area

From the BET measurements TCM nanoparticles appeared to have surface area of 10.77 m²/g and pore volume of 0.06 cm³/g; whereas cement paint appears to be highly non porous and with a very small surface area, maybe due to the aggregation of the material. Particularly, it appeared to have a surface area of 0.07 and almost no porosity was measured. It was also observed that when the mixture of TCM with cement paint was analyzed, the surface area increased to 0.29 m²/g and the porosity increased from almost zero to 0.002 cm³/g.

Table 8: Structural characteristics of all Titania samples and all building materials.

Sample	Crystallite Size (nm)	d- spacing (nm)	Surface Area (m ² /gr)	Pore volume (cm ³ /g)
TCM	38.689	0.351	10.77	0.06
undoped	34.347	0.352	32.42	-
P25	21.591	0.352	66.17	0.20
Crystal global	12.865	0.352	78.02	0.24
<i>Calcareous fillers</i>			1.38	0.008
<i>Cement paint</i>			0.07	0.0001
<i>Cement</i>			2.21	0.007

Table 9: Surface Area, pore volume, and pore sizes as obtained from BET surface area analysis

	Sample Name	description	Surface Area	Pore volume	Pore Size
			m ² /gr	cm ³ /g	(nm)
BULK	BM76	TCM	10.77	0.06	21.76
	BM78	undoped	31.27	0.16	20.42
	BM77	P25	66.17	0.20	13.30
	BM79	Crystal Global	78.02	0.23	12.06
	BM73	calcareous filler	1.38	0.008	47.58
	BM74	cement paint	0.070	0.0001	8.36
	BM75	cement	2.21	0.007	13.15
Calcareous	BM3	2% TCM	1.55	0.01	25.85
	BM6	2% TCM 700°C	12.48	0.12	40.23
	BM8	1% P25	1.80	0.01	22.34
	BM9	2% P25	2.34	0.01	23.20
	BM10	0.2% P25 700°C	12.92	0.07	22.28
	BM11	1% P25 700°C	14.61	0.12	33.04
	BM12	2% P25 700°C	13.45	0.06	19.56
	BM15	2% undoped	2.35	0.008	15
	BM18	2% undoped- 700°C	14.45	0.08	24.16
	BM21	2% Crystal Global	5.75	0.01	9.03
	BM24	2% Crystal Global- 700°C	13.70	0.08	25.43
	BM27	2% TCM- RT	0.29	0.02	33.40
	BM30	2% TCM 700°C	14.45	0.13	36.30
Cement Paint	BM33	2% P25 RT	0.96	0.006	26.42
	BM36	2% P25 700°C	15.53	0.13	33.13
	BM39	2% undoped- RT	0.28	0.001	29.43
	BM42	2% undoped- 700°C	13.71	0.11	33.82
	BM45	2% Crystal Global- RT	3.96	0.008	8.04
	BM48	2% Crystal Global- 700°C	12.14	0.12	38.06
	BM 51	2% TCM - RT	2.27	0.01	19.44
	BM 57	2% P-25 - RT	2.94	0.01	16.50
Cement	BM63	2%undoped- RT	2.75	0.01	15.35
	BM66	2% undoped- 700°C	2.28	0.01	24.73
	BM72	2%Crystal Global- 700°C	1.92	0.009	19.62

Increasing the concentration of Titania, does not have a direct effect on either the surface area or the porosity, and interestingly when calcined the samples of cement paint and calcareous filler have a much higher surface area, porosity and pore volumes. P25 and Crystal Global Titania have high surface area, particularly $66.17 \text{ m}^2/\text{g}$ and $78.02 \text{ m}^2/\text{g}$ respectively. Undoped appears to have a surface area of $31.27 \text{ m}^2/\text{g}$. TCM has very big porosity, in the size of 21.76 nm and from the BMs, the more porous one, with also bigger porous sizes, is calcareous filler and the highest surface area is found in cement.

Transmission electron microscope (TEM)

A higher crystallite size after calcination is observed. Comparing the different building materials calcined (with 2% TiO_2), the highest crystallite size is found in calcareous filler (51.07 nm), followed by cement paint (46.74 nm) and lastly cement with 29.46 nm . From TEM we have calculated also the d-spacing, which is slightly different to XRD calculations. In TCM we observe an increase in crystallite size and d-spacing. High crystallinity, from SAED image plus higher surface area, porosity and porous size (*see Table 9*) is observed. From literature, P25 is measured to have crystallite size of 21 nm ([Ohno et al., 2001](#)).

Table 10: TEM results for crystallite size and d-spacing of Titania before and after incorporation in building matrices.

Sample	Average Crystallite size by TEM (nm)	d-spacing by TEM (nm)
Calcareous 2% TCM	43.07	0.290
Calcareous 2% TCM- 700C	45.46	0.400
Calcareous 2% P25	23.15	0.366
Calcareous 2% P25 -700C	51.07	0.336
Calcareous 2% Cryst. G.	7.10	0.378
Calcareous 2% Cryst. G.-700C	41.00	0.360
Cement Paint P25 -700C	46.74	0.419
Cement P25- 700C	29.46	0.338
TCM	37.86	0.415
P25	20.91	0.413
Undoped	37.51	0.426
Crystal Global	23.66	0.317

In the following pictures (*Fig. 31 and 32*) we observe the morphological differences of calcined and not calcined samples in TCM inside calcareous filler. We observe that calcined samples tend to agglomerate more; therefore the surface area is increasing and this agglomeration makes the TEM images harder to interpret ([Kapridaki et al., 2014](#)).

The size of their crystallites is also increasing with T increase. However agglomeration of the BMs leads to low dispersion of the nanoparticles inside the matrix and therefore low photocatalytic performance.

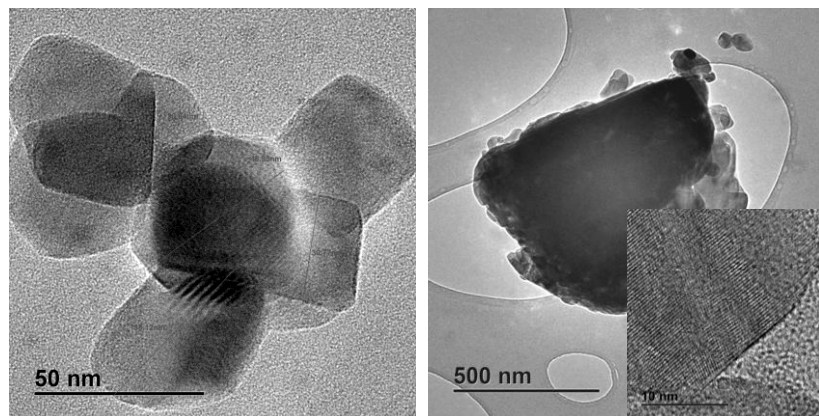


Figure 31 Calcareous filler with 2% TCM not calcined

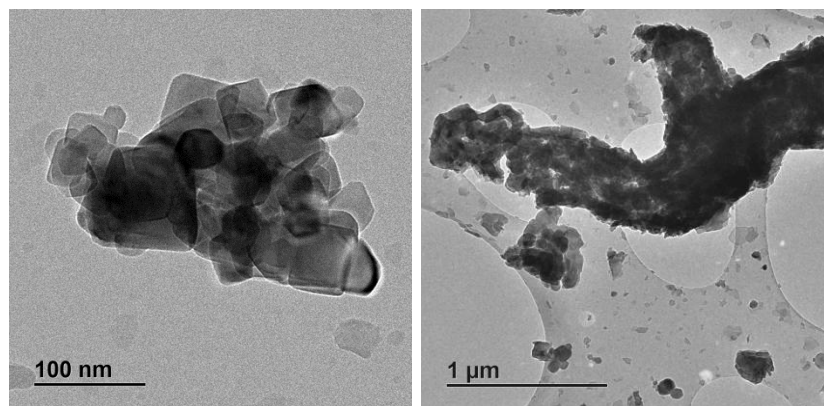


Figure 32 Calcareous filler with 2% TCM calcined at 700 °C

In the following picture we observe the differences in structures in the two P25, with calcareous filler. We observe the big increase in crystallite size and the SAED image shows high crystallinity.

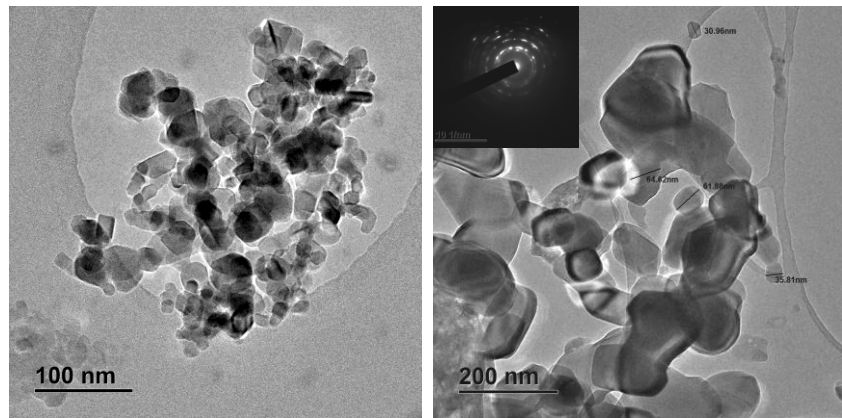


Figure 33. Calcareous filler with 2% P25, left: not calcined and right: calcined at 700 °C

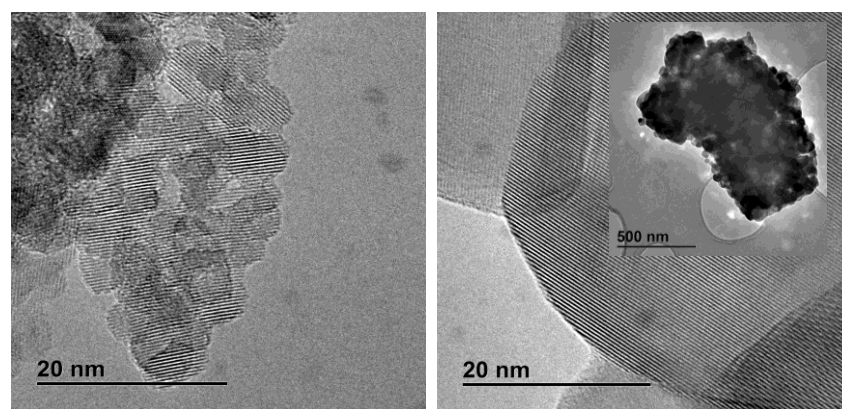
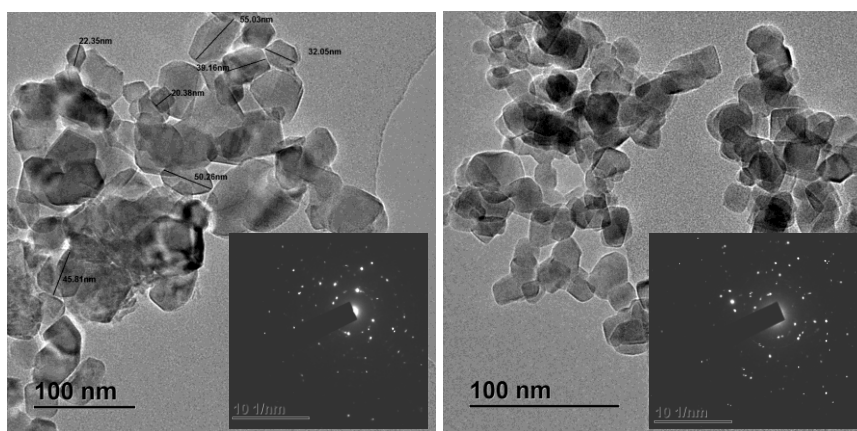


Figure 34. Calcareous filler with 2% Crystal Global, left: not calcined, right: calcined -700 °C

The big increase in crystallite size is also observed in Crystal Global sample, where the crystallites increased from 7.10 nm to 41 nm. Lastly in Fig. 35 different Titania samples are presented. It is therefore clear that the high surface area of crystal global sample is attributed to the high agglomerations observed. Also the biggest crystallite sizes are found in the TCM sample, something similar to the findings of the XRD measurements.



TCM

P25

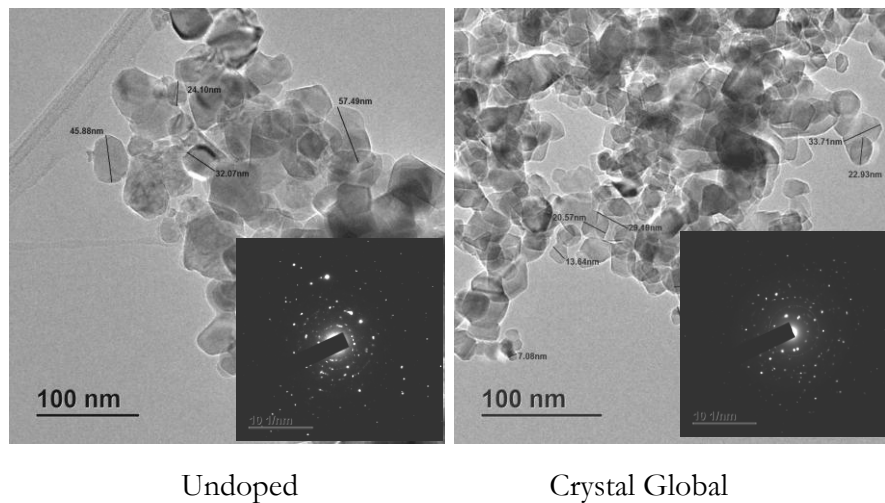


Figure 35 TEM for TiO_2 samples, TCM, P25, undoped, Crystal Global.

Scanning Electron Microscopy

The instrument used is described in the section on ZnO synthesis. Morphologically different Titania concentrations are of course not expected to have differences in SEM images, neither different TiO_2 samples (TCM, P25, undoped or Crystal Global) inside the building matrices, since the highest concentration of 2% is still very low. More details are provided in [Appendix](#). The main goal of this section is to identify the differences in morphology comparing calcined and not calcined BMs, but also differences between the three BMs.

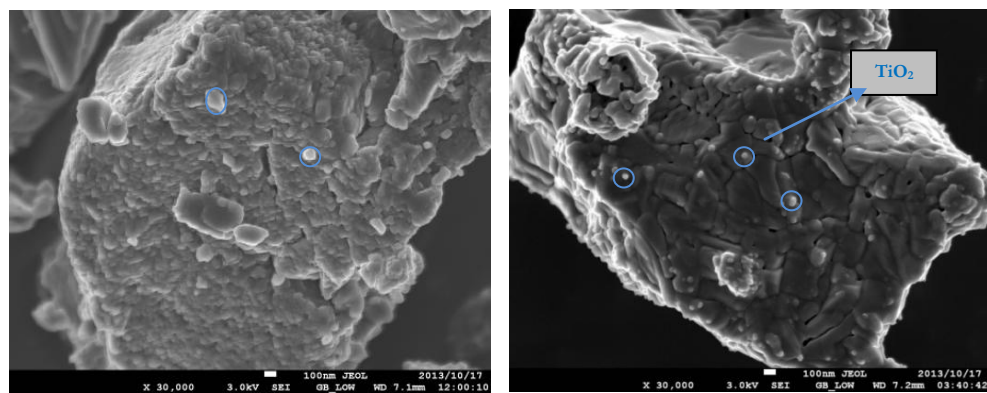


Figure 36 a. Calcareous filler 2% TCM not calcined and **b.** Calcareous filler 2% TCM 700 °C

In Fig. 36 we observe that after calcination calcareous seems to become condensed and more agglomerated with higher surface area. As already observed from BET, this BM is highly porous in comparison to the non-calcined one. Moreover, after XRD measurements, we concluded that TiO_2 nanoparticles are

Table 11: EDX analysis of all TiO_2 samples

	TCM	P25	undoped	Crystal Global
Carbon	5.28	17.06	15.96	43.67
Nitrogen	17.15	17.09	13.15	17.60
Oxygen	58.94	38.50	22.08	30.31
Aluminum	0.08	0.18	0.20	0.09
Titanium	18.32	27.17	48.10	8.29
Silicon	-	-	-	0.03
Sulphur	-	-	-	0.02
Aurum	0.23		0.51	
Total			100%	

more profound in the samples only after calcination. This could be the reason why in Fig. 36b more nanoparticles of TiO_2 are visible than in Fig. 36a (some of them marked with blue circles).

This result is in good agreement with the EDX analysis (*Appendix*) where Ti is found only in calcined samples of 2% concentration. Interestingly, the EDX on the P25 sample inside calcareous showed a small concentration of Titania in the RT sample, specifically $0.47 \pm 0.02\%$ but also here, after calcination Ti was found to be $6.88 \pm 0.05\%$. As expected also high amounts of C, Ca Si, Al, Mg are found.

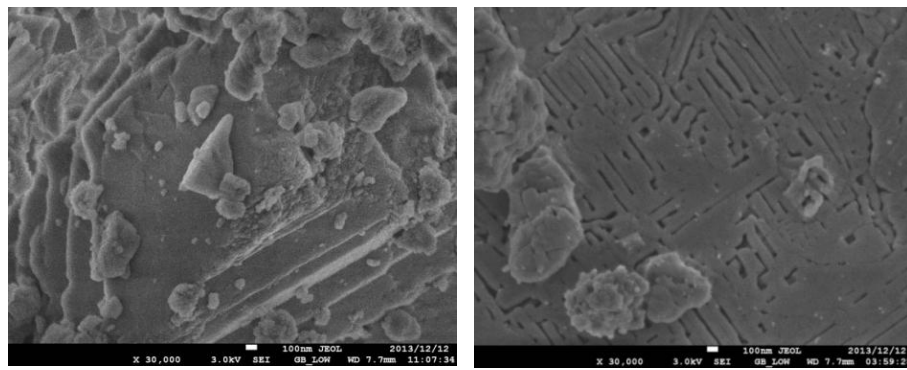


Figure 37 a. Calcareous filler not calcined and b. Calcareous filler calcined at $700\text{ }^{\circ}\text{C}$ mixed with 2% Crystal Global

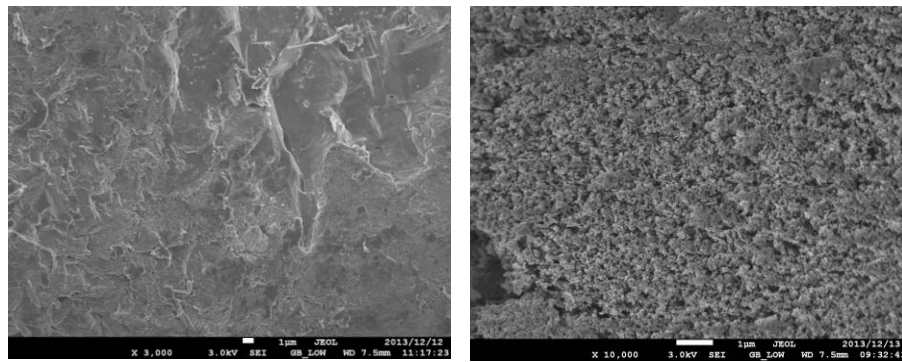


Figure 38 a. Cement paint not calcined and **b.** Cement paint calcined at 700 °C mixed with 2% P25

Fig 37, 38, 39, 40 present the calcareous filler, cement paint, and cement in RT and after 700°C treatment. Calcareous seems to be influenced highly by T increase, and its morphology, despite the fact that it is more porous, seems highly dense with some new formation starting building up (*Fig. 37b*). One the other hand in *Fig 39, 40* it is clear that cement after T treatment becomes highly porous.

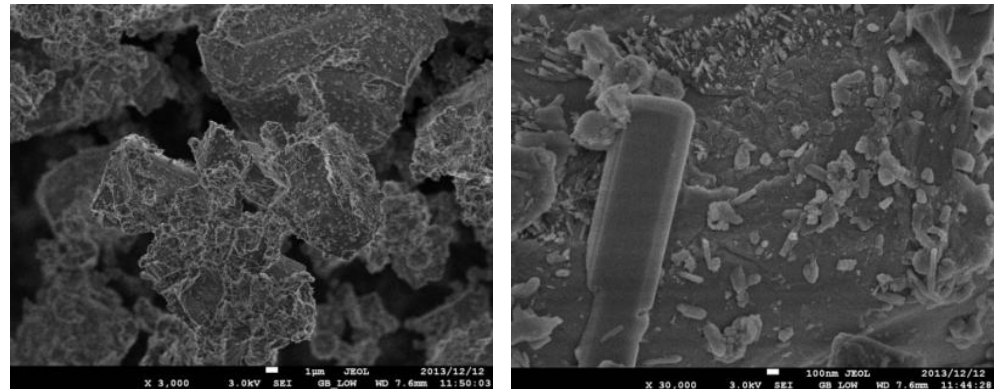


Figure 39 Cement not calcined

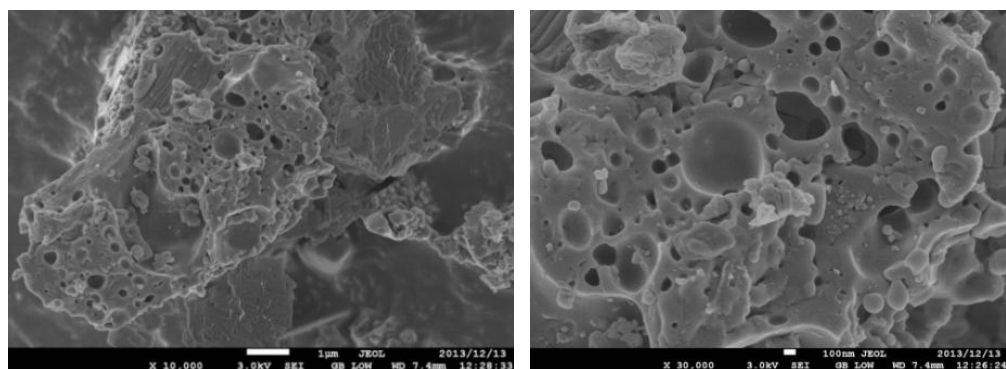
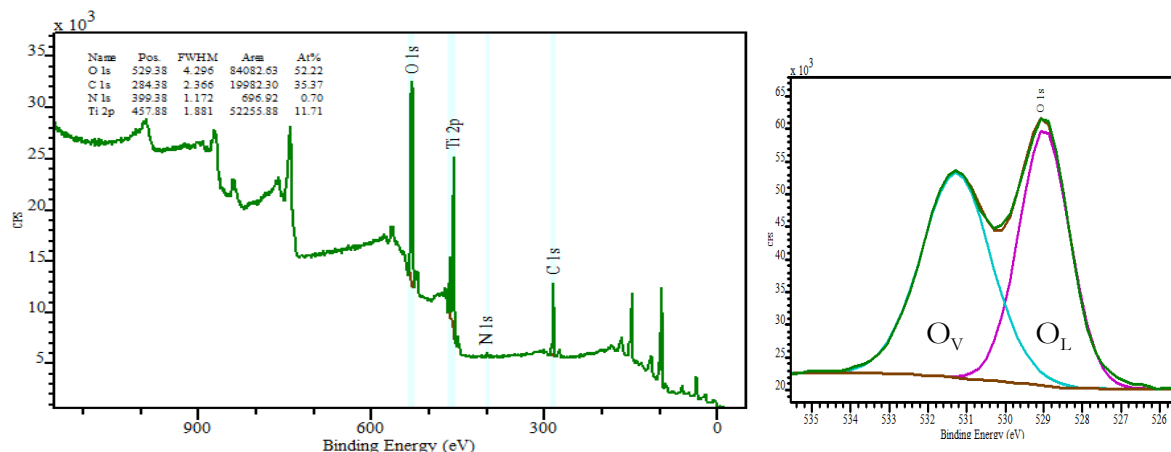


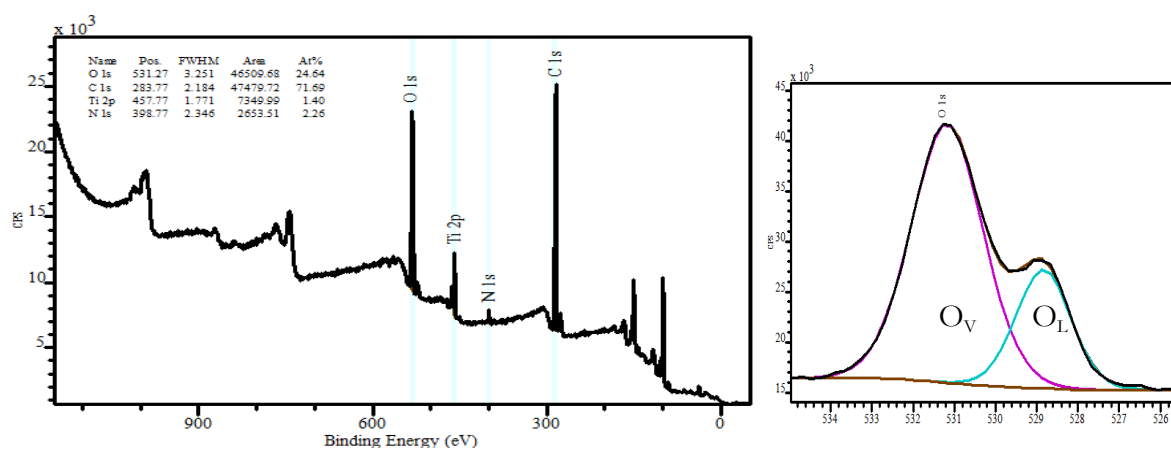
Figure 40 Cement calcined at 700 °C mixed with 2% TCM

X-ray Photoelectron Spectrometer (XPS)

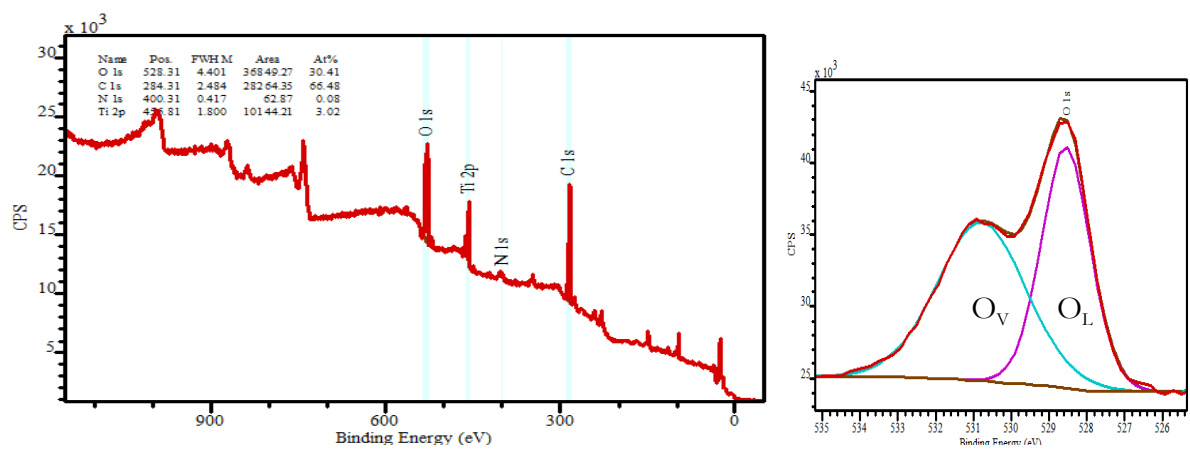
Binding energies are corrected using the C 1s peak with a binding energy of 284.6eV as a reference (Wagner et al., 1979).



Crystal Global



Undoped



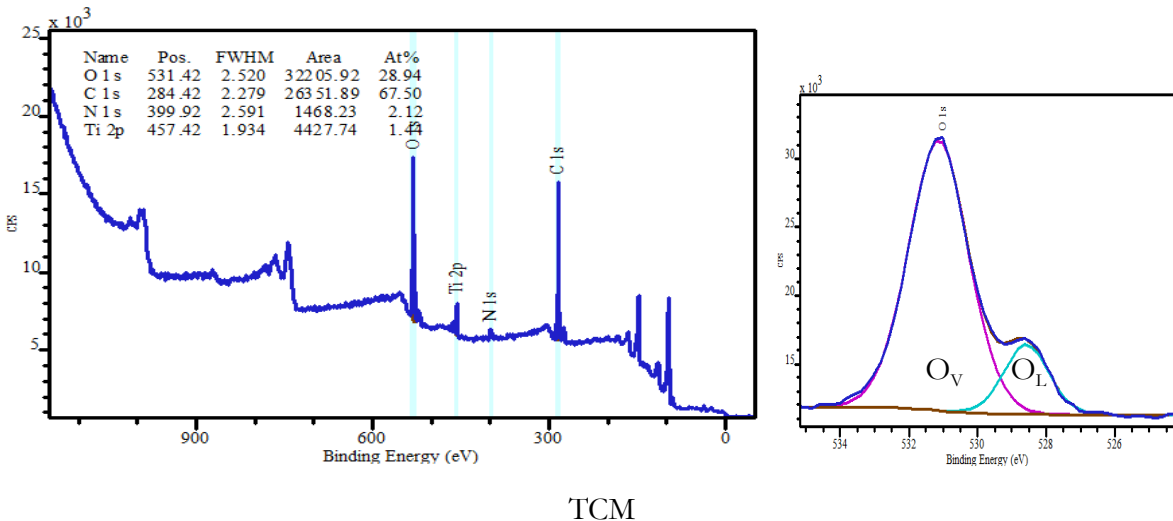


Figure 41 XPS spectra of TiO_2 , Crystal Global, undoped, P25 and TCM.

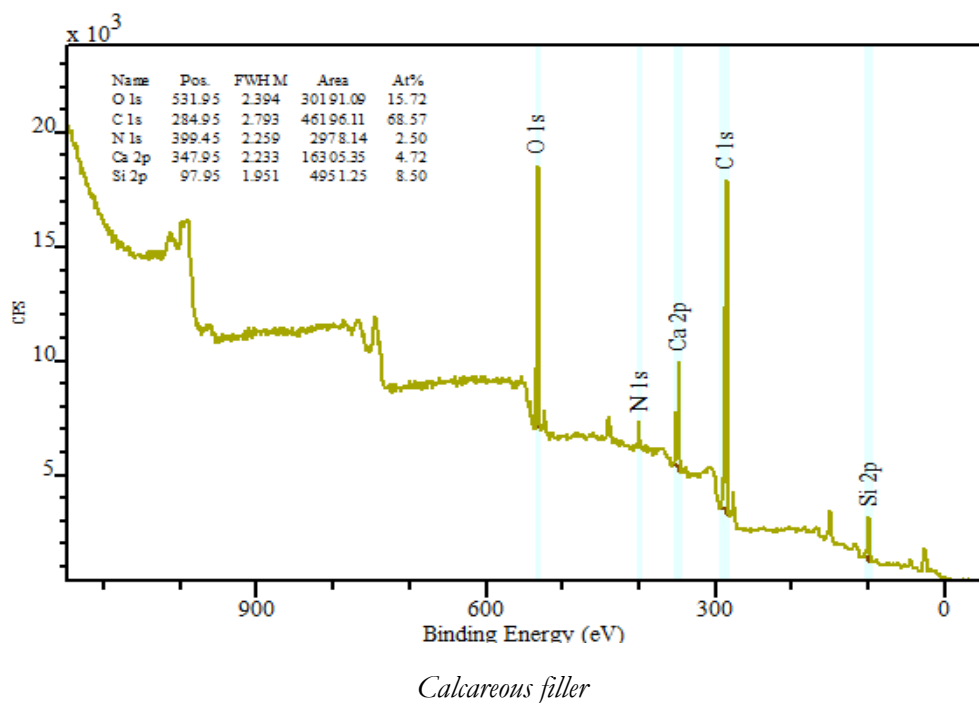
In Fig. 41 the XPS spectra of TiO_2 bulk materials are presented, with the concentration of all elements found on their surface. Ti, O, C, N peaks were identified. Laboratorial samples appear to have very high concentration of N, something that could help their photocatalytic efficiency under visible light. In the right side of the figures above, the high resolution spectra of O1s peak for each Titania sample is presented. In all samples 2 peaks are fitted. The low binding energy peak O_L corresponds with the Ti-O bonding, or else the bulk oxygen in the TiO_2 lattice (Yan et al., 2013). The second peak, O_V corresponds with the surface oxygen and presents the adsorption of oxygen or hydroxyl radicals $\cdot\text{OH}$ and is associated closely to the photocatalytic behavior of the sample (Yan et al., 2013; NIST database).

The laboratorial samples have a ratio of O_L/O_V smaller than the laboratorial, meaning that $\cdot\text{OH}$ or surface oxygen is higher in concentration than bulk oxygen. Also higher concentration of oxygen than all the other samples accounting to almost 52% is found in Crystal Global sample.

As we already mentioned there is a direct correlation between the surface photocatalytic activity and the lattice/surface ratio found on the surface of a material. The surface defects (like oxygen vacancies) can promote the separation of electron–hole pairs under irradiation, and therefore, enhance the activity during photocatalytic reaction (Yan et al., 2013). Defects play important roles in photocatalysis. Changing their concentration ratio of lattice/surface defects improves the electron-hole separation efficiency, enhancing the photocatalytic efficiency significantly. A smaller ratio of lattice/surface is observed to

have better photocatalytic performance (Yan et al., 2013) and this is something we have also observed (see also photocatalytic section).

Following, the XPS spectra of BMs are presented, and are in good match with the XRD results in the previous section. O, C, Ca, Si were detected. It is observed that the concentration of oxygen in calcareous is 15%, the calcium almost 5% carbon around 68% and silicon around 8%; in cement paint oxygen is 31%, of calcium 10%, carbon 52% and silicon 6%. In cement, the oxygen concentration is more than 30%, calcium concentration is at 3% silicon concentrations are at 41% and carbon concentration is almost at 24%.



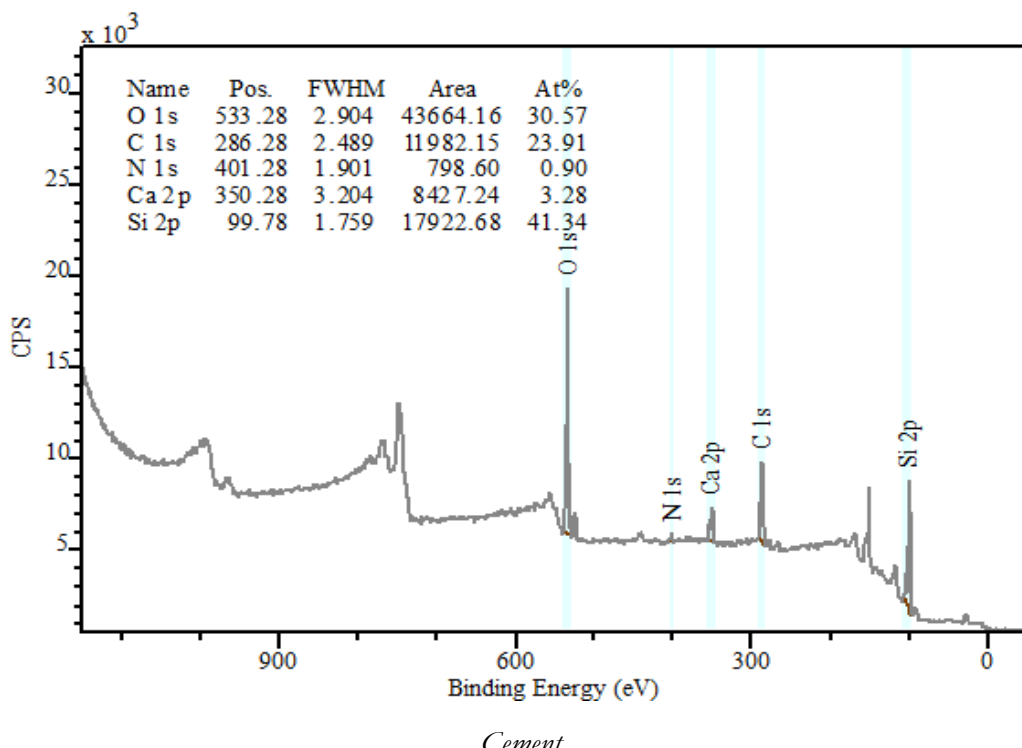
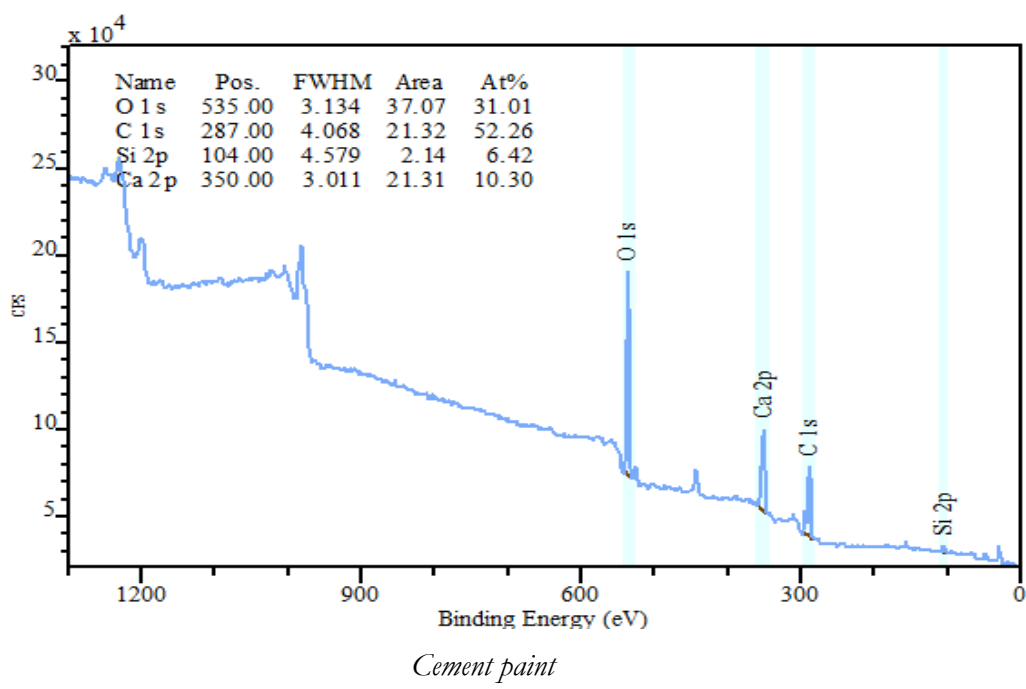


Figure 42. XPS spectra of calcareous filler, cement paint and cement.

Chapter V

Photocatalytic Performance Results

In this chapter the photocatalytic performance of the nanomaterials already characterized, will be studied. Photocatalysis was performed in several different ways. Initially the bulk nanomaterials were tested; therefore ZnO doped was measured at the Laboratory of Photochemistry and Kinetics, Department of Chemistry, University of Crete, under acetaldehyde gas exposure. Next, anatase TiO₂ before and after NH₃ exposure was examined under liquid solutions of Methylene blue for the effects of ammonia in the photocatalytic process at FORTH/IESL at TCM lab. After this, the TCM sample was placed inside Demo houses for the real time photocatalytic test and ultimately all previously analyzed building materials were placed on a small size plaster panel and tested in a handmade photocatalytic apparatus, under UV irradiation.

5.1 Indoor photocatalytic behavior of ZnO-Acetaldehyde degradation

The degradation is calculated from $\frac{(C_0 - C)}{C_0} \times 100\%$ versus time. C_0 represents the initial concentration, C the concentration after t period of time. In the following graphs the degradation of acetaldehyde is presented. From $t=0$ until the dotted line crosses x-axis, the sample was under the exposure of acetaldehyde, without any light source, therefore the adsorption is depicted there. The right part of the graphs, after the dotted line, presents the degradation under a light source for which the adsorption of the previous

stage must be excluded though. Therefore, in Co doped ZnO sample under UV the adsorption is very high, but after turning on the lights we do not observe any photocatalytic activity since the slope of the line remains unchanged. This was observed for all samples (Co, Mn, Cu) except Co doped ZnO under visible light. For Co doped ZnO around a 10% increase of the degradation of acetaldehyde is observed on top of the high rate of adsorption, which reduces the pollutant up to more than 65% in 90 min exposure. Adsorption is observed in *Fig. 43 a, b, c*, on the right part of the graph, before the lights were turned on. Heterogeneous photocatalysis, as a chemical reaction, follows some reaction kinetics. In this case it follows pseudo first order reaction kinetics, $-\ln(C/C_0) = kt$, where Co is initial concentration and C, concentration during time. The rate constant values were calculated from the slope of the plot of $-\ln(C/C_0)$ vs. time (Sarkar et al., 2015). It is calculated to be $k = (16.6 \pm 0.1) \cdot 10^{-3} \text{ min}^{-1}$.

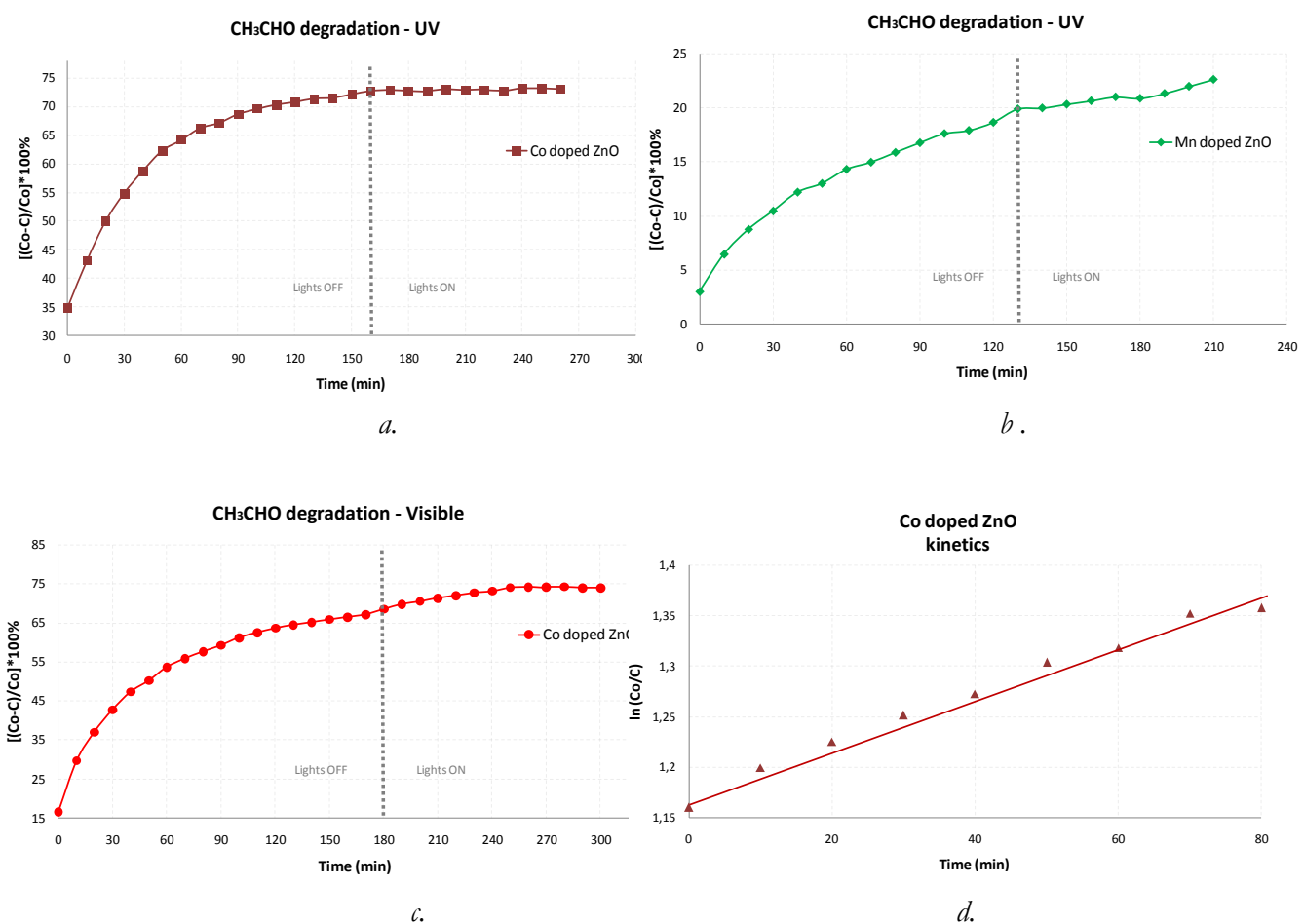


Figure 43 a. Acetaldehyde degradation of Co doped ZnO under UV **b.** Acetaldehyde degradation of Mn doped under UV **c.** Acetaldehyde degradation of Co doped ZnO under Visible light **d.** Kinetics of Co doped ZnO under visible

5.2 The effect of Ammonia exposure for Methylene Blue (MB) degradation

The decolorization of MB in relation to time is presented in *Fig. 44* Co represents the initial concentration, C the concentration after t period of time. A high degradation rate of poor metals is observed, whereas Fe, Mn and Co do not show any activity. Adsorption is measured and excluded from the degradation results in the following graphs.

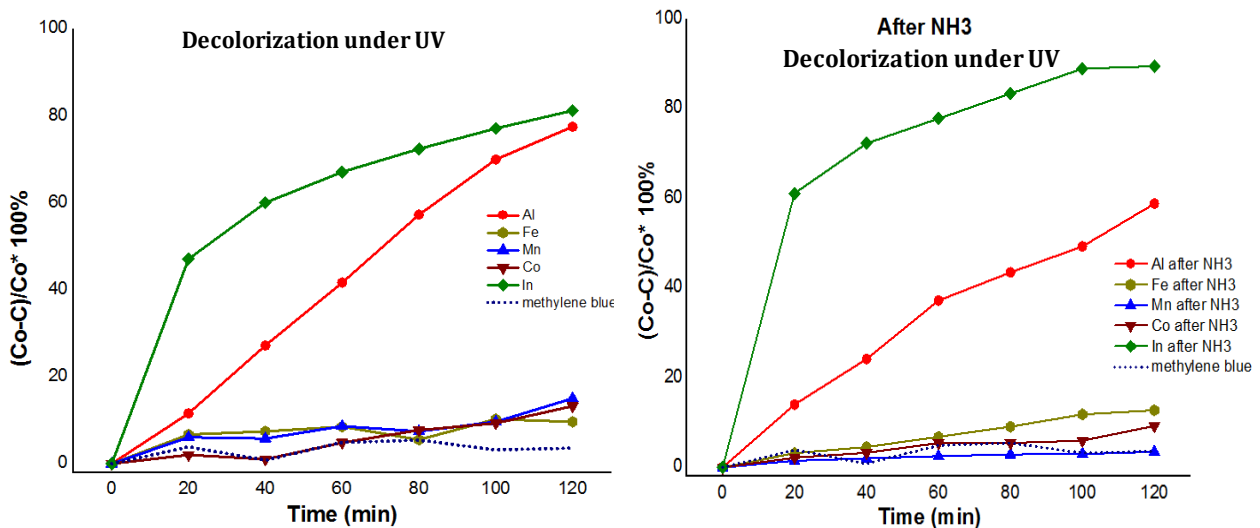


Figure 44. Decolorization under UV light **a.** before ammonia and **b.** after ammonia

It is also noticeable that in the In doped sample there is a 10% increase of the decolorization rate after NH₃ exposure. In the Al doped sample the decolorization reaches ~ 60% and in In almost 90%.

The decolorization and kinetics of the In doped samples is presented in *Fig. 45*

$$k = (12.5 \pm 1.5) \cdot 10^{-3} \text{ min}^{-1}$$

$$\text{and after NH}_3: k = (17.4 \pm 2.3) \cdot 10^{-3} \text{ min}^{-1}$$

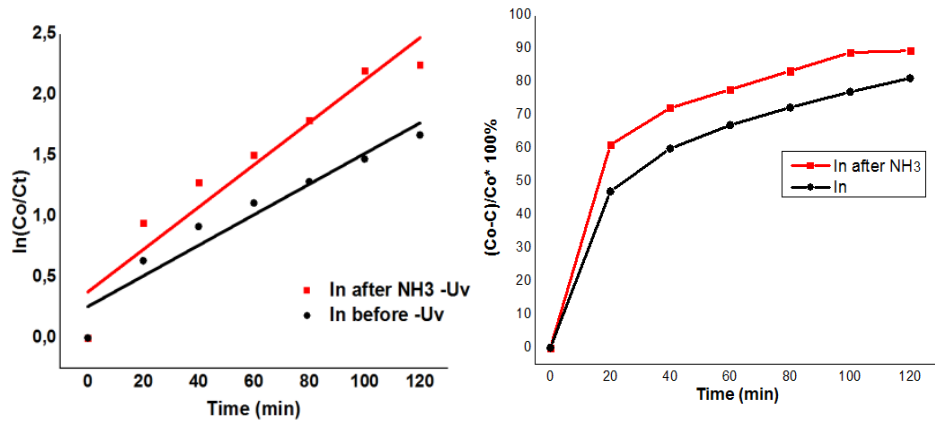


Figure 45. Decolorization and Kinetics of In doped sample

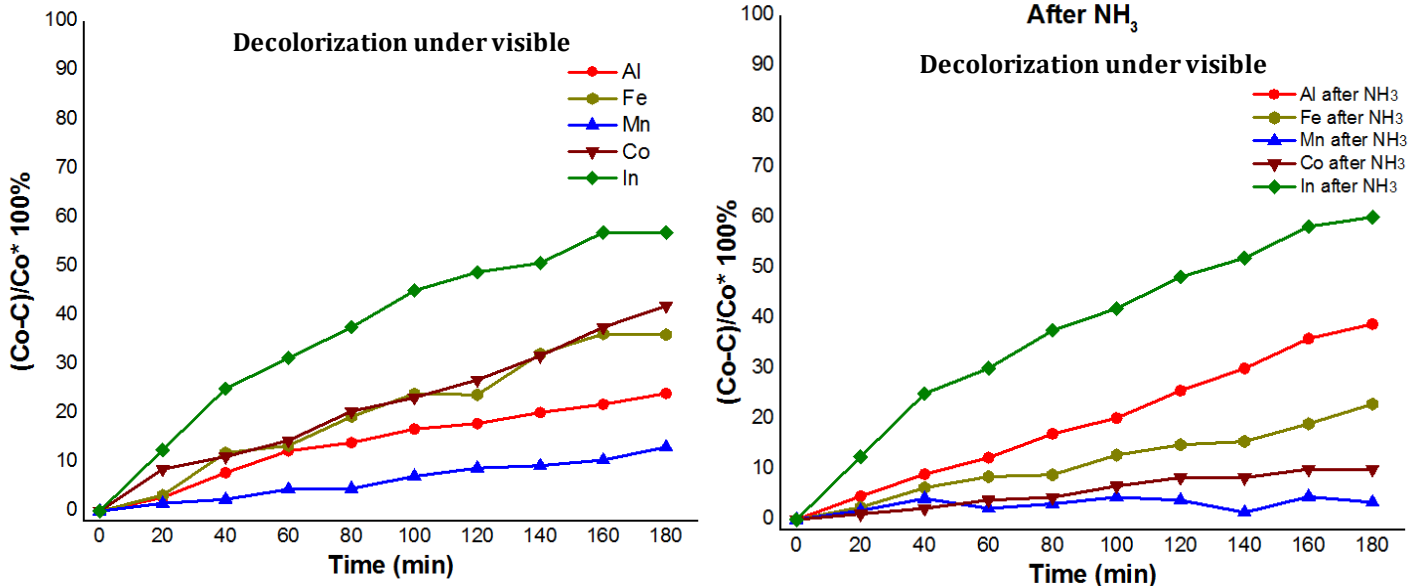


Figure 46 Decolorization under visible light **a.** before ammonia and **b.** after ammonia

The In doped sample is also under visible light the most prominent possible photocatalyst as it decolorizes MB at a percentage of 60%. Co doped anatase TiO₂ increases ~30% its decolorization rate under visible light in comparison to UV, this is something expected after the peak observed at the UV-Vis measurement. Here we observe no effect from NH₃ under visible light.

Overall we observe that In doped anatase TiO₂ has the highest decolorization rate, especially under UV irradiation. Ammonia exposure seems to positively influence the

decolorization process. Indium was also found to have a higher oxygen concentration, while O_L/O_V was lower than 1, indicating a higher concentration of $\cdot HO^-$ compared to oxygen in the lattice.

Taking into account the structural results from [section 4.2.1](#) it is also observed that the higher photocatalytic performances were observed surprisingly to 100% anatase TiO_2 and 0% rutile. Also crystallite size is known to have an impact on photocatalysis and it is observed that lower sized have higher decolorization rates. The optical Co peak in visible region obtained from UV-Vis matches the higher decolorization under visible for Co doped sample. Moreover an environment with gaseous ammonia results to lowering the amount of total O 1s in all doped TiO_2 samples. However ammonia increased the concentrations of hydroxyl group and oxygen vacancies (O_V) which enhanced photocatalytic performance. Indium doped sample appeared to have the highest photocatalytic activity. This could be attributed to the low lattice/surface rate and also to the high total amount of oxygen in the surface of the sample. Similar results are met in Al doped sample. Samples with hydroxyl and oxygen vacancies smaller than the amount of oxygen in their lattice ($O_L/O_V > 1$) appear to have almost zero decolorization rate. Cobalt doped sample shows some decolorization under visible, and this could be attributed to the nitrogen found on its surface.

This analytical investigation of ammonia exposure on photocatalysts provided further considerations to a topic which is highly complex. Several parameters can influence the effectiveness of a photocatalyst and cannot be estimated prior to actual photocatalytic measurements. In the lab scale a photocatalyst can be measured in accordance to the degradation of each gas or dye selected at the point of the experiment. However, the presence of other gases in the atmosphere (ex. Ammonia etc.) can influence its performance either positively or negatively. Moreover, the issue of by-products of this procedure is a topic that also must be analyzed carefully, prior to application the public sphere. In the next section, a photocatalytic experiment is conducted in a real time test bed facility, the Demo house.

5.3 Real time application Photocatalysis- Demo houses

TCM material has been selected for application in the Demo houses. This sample was mixed inside calcareous filler and water and subsequently placed as a coating on common plasterboards. The total surface covered with photocatalytic materials was 8 m². Temperature was kept stable at 23 °C and humidity at 60%, following human comfort zones. The change of Rh from 60% to 45% was also tested, since it is a factor highly influencing the level of pollution inside a house as well as the oxidation and reduction reactions in photocatalytic processes (Guo et al., 2008). The pollutant used is a common indoor pollutant and considered to be highly dangerous (Shiraishi et al., 2007; Wan et al., 2009). The pollutant formaldehyde HCHO 37% (w/v) can be found in regularly available furniture, carpets, paints and building materials (Kim et al., 2011). An amount of 10 µL of this pollutant was placed in each house. In the first stage, the VOCs level was examined compared to levels of humidity. A small increase in the levels of recorded VOCs was observed when humidity increased. The panels were placed inside the Demo houses, before the application of any nanomaterial on them, for the observation of any change on VOCs levels inside the house, due to the addition of extra building materials. BMs have an impact on iAQ, and it has been observed that an increase of VOC levels has occurred.

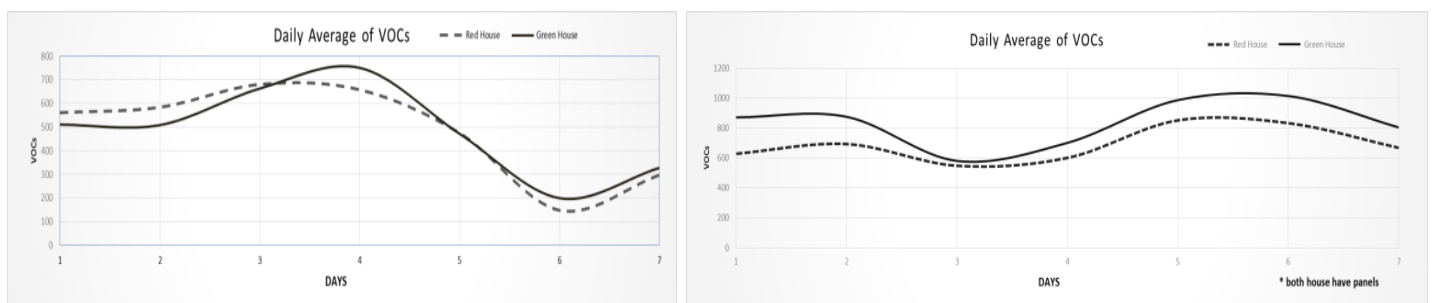


Figure 47. VOCs levels at 60% Rh without plaster boards, and with plasterboards.

After the plasterboards were placed in both houses (Fig. 47 right graph) (without any photocatalytic material on) the value of the total VOCs has increased due to the embodied pollutants found on such building envelopes surfaces. Since this experiment

lasted for several months, a seasonal dependence of the pollutants inside the house was observed.

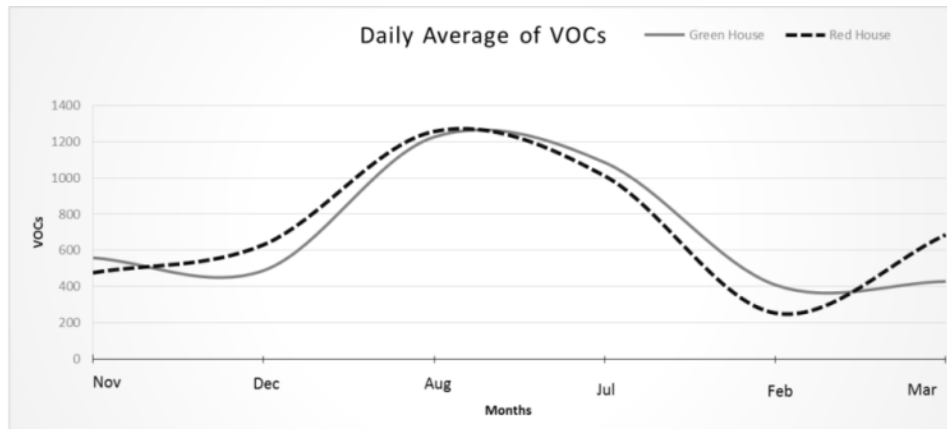
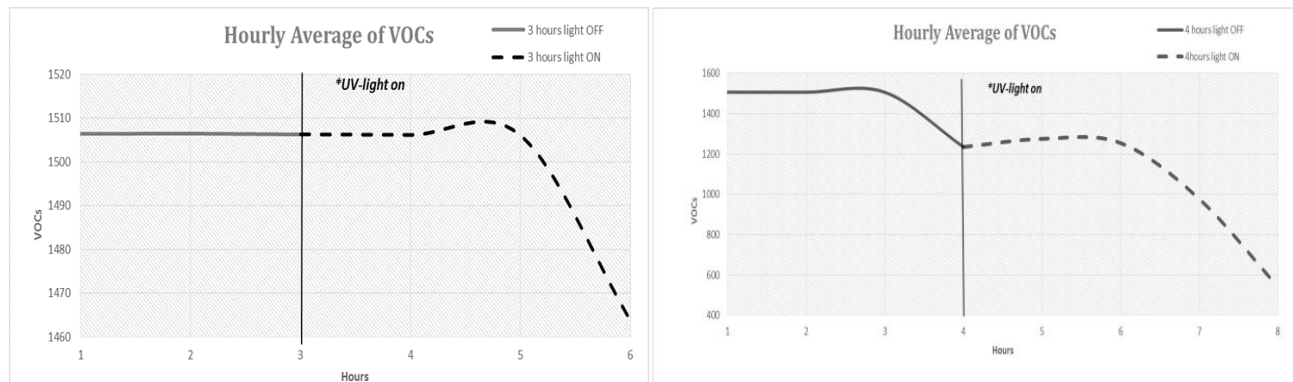


Figure 48. Seasonal dependency of VOCs level per month.

In *Figure 48* we see the monthly rate of pollutants inside the two houses, providing us with the conclusion that even indoor air pollution is highly seasonal dependant and exterior temperature, sunlight and also positioning of the system (house) plays a role in the level of the pollutants.

In this stage, the main problems of scaling up a photocatalytic performance of nanomaterials were recognized. The pollutants have a natural rate of degradation in a test bed of this large scale. The season the experiment was conducted also played an important role. High sensitivity of the sensing system inside the houses caused the results to fluctuate strongly.

For the photocatalytic experiment, all UV lamps were turned on for different durations, 3 h 4 h and 10 h. The levels of VOCs per h, before and after lighting are presented in the following graphs.



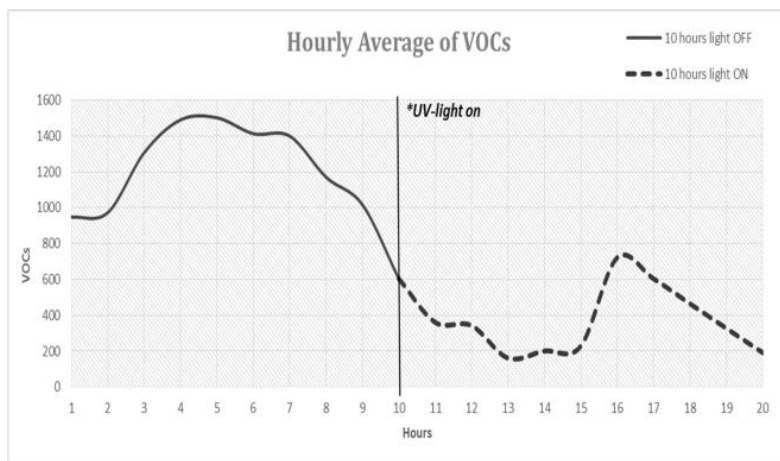


Figure 49. VOCs levels before and after light exposure for 3h, 4h and 10h.

From these graphs, a decrease in pollutant level was observed under UV radiation. Nonetheless, the photocatalytic procedure is multi parametric and the degradation of the pollutants after some hours under UV radiation cannot be attributed with the utmost certainty to the photocatalytic behavior of the materials synthesized. Therefore further photocatalytic experiments, a smaller scale, must be carried in order to test BMs.

On the other hand, this section provided us with several conclusions on the behavior of pollutants inside a house, which is also in good agreement with previous studies on the issue. Particularly temperature and humidity increase positively influences the indoor VOC levels. Humidity is a factor that has been reported to influence the levels of indoor air pollution ([Reinikainen et al., 2003](#)). Moreover, building materials are major sources of pollution, decreasing the iAQ. The use of low emission BMs contributes to reducing the ventilation needs and therefore lowering the energy consumption ([WHO, 2014](#)). Lastly T is a basic requirement for indoor air quality, since high values of T have consequences on the levels of humidity, having direct or indirect contribution to higher pollutant levels ([Kosatsky, 2005](#)).

5.4 Formaldehyde degradation in Photocatalytic Apparatus

Several factors contributed to the results of this experiment. As stated from the previous section, the levels of HCHO increased with the introduction of BMs in the chamber. Initial T was measured to be 25 °C and reached 35 °C after 2h of UV irradiation. The humidity started at a concentration of 30% and dropped to 22% after 2 h. T and Rh% played also a role in the HCHO levels as described in the previous section. All samples started with the initial concentration of 0.5 ppm and in the most cases, under UV light, a decrease of this concentration over time was observed. In dark conditions, without any UV light, the value is named as t=-30 min and on t=0 min the lights were turned on. Therefore factors such as adsorption of the BM could be excluded. As becomes clear from the graph below, when pure BMs were studied during UV light, the concentration of HCHO increased. This can possibly be explained by the initial increasing T and the following decrease after the lights were turned off. We observe a full degradation of the HCHO when the cement sample was tested after 190 min. This can be explained through the adsorption of the material, or other elements in the chamber, due to a lower Rh%, possible losses of the system, or the small but considerable flow rate of sampling by the sensor.

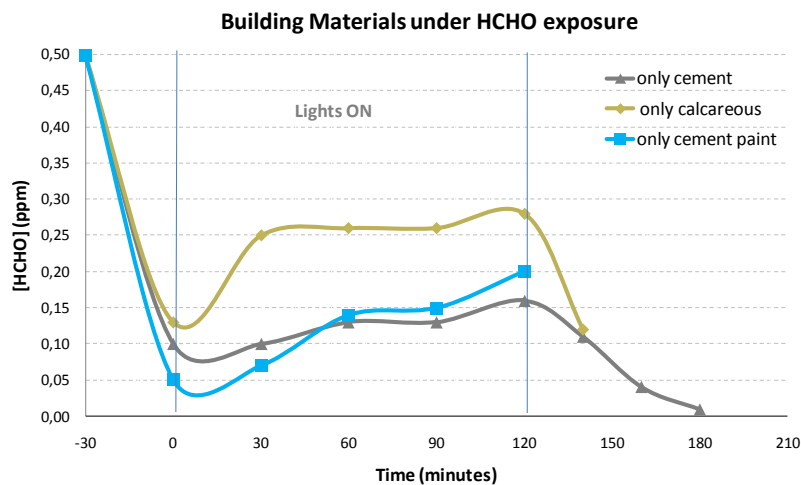


Figure 50. BMs photocatalytic behavior. The section between the two lines crossing x-axis is the period when the lights were on, outside of that the lights were off.

Due to all these the duration of the experiment was kept at 120 min. The three BMs incorporating 2% of TCM and 2% of P25 are presented.

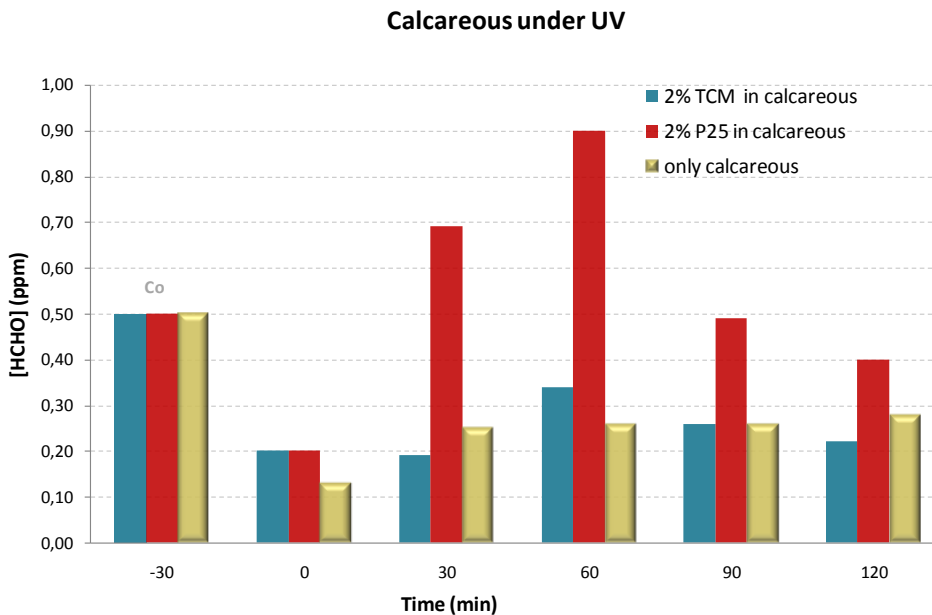


Figure 51. Formaldehyde degradation with 2% TCM in calcareous filler, 2% P25 in calcareous filler and pure calcareous filler.

Calcareous filler mixed with TCM or P25 are presented in Fig 51. The results show that a high pollutant degradation in all three samples is observed at $t=0$. This initial degradation of HCHO from these three samples is as follows; for bulk calcareous it is 74%, TCM in calcareous degrades at 60% and P25 in calcareous likewise at 60%. This could be attributed to the adsorption of the materials, which decreases after the incorporation of nanomaterials. After the initial degradation of the pollutant, the levels are increasing in all three samples, this could be explained due to desorption, or the increase of T due to the presence of BM in the chamber. The overall degradation of HCHO is observed to be 44% in bulk calcareous, 56% in TCM with calcareous and 20% in P25 with calcareous. We observe that in this case that the addition of TCM possibly enhanced the degradation rates of the sample with a 12% extra degradation rate, and may be attributed to the photocatalytic process that took place.

Analyzing the cementitious materials, specifically pure cement, we observe the following. Bulk cement appears to have an initial degradation rate of 80%, TCM in cement 80% and P25 in cement 82%. This proves that cement is absorbing pollutants highly, with or

without the presence of Titania. This is something expected from literature available, where the high porous nature of cementitious materials enables the deposition of organic and inorganic pollutants and particulate matter (Bertrand et al., 2009). The overall degradation of formaldehyde from pure cement is 68%, for TCM in cement 64% and for P25 in cement matrix is 60%. This means that cement has an intense behavior as a BM in relation to pollutants, specifically to formaldehyde and most likely the results are not dependable on whether there is nanoparticles of Titania incorporated in it or not. It appears to have a high adsorption rate, and interestingly during a 120min period there is not any noticeable desorption or a high pollutant increase, making this materials an interesting BM for future studies. Both Titania samples did not contribute to the increase of the formaldehyde level. The high adsorption rate of cement is due to its high surface area which is 2.21 m²/gr, in calcareous it is 1.38 m²/grand in cement paint 0.070 m²/gr.

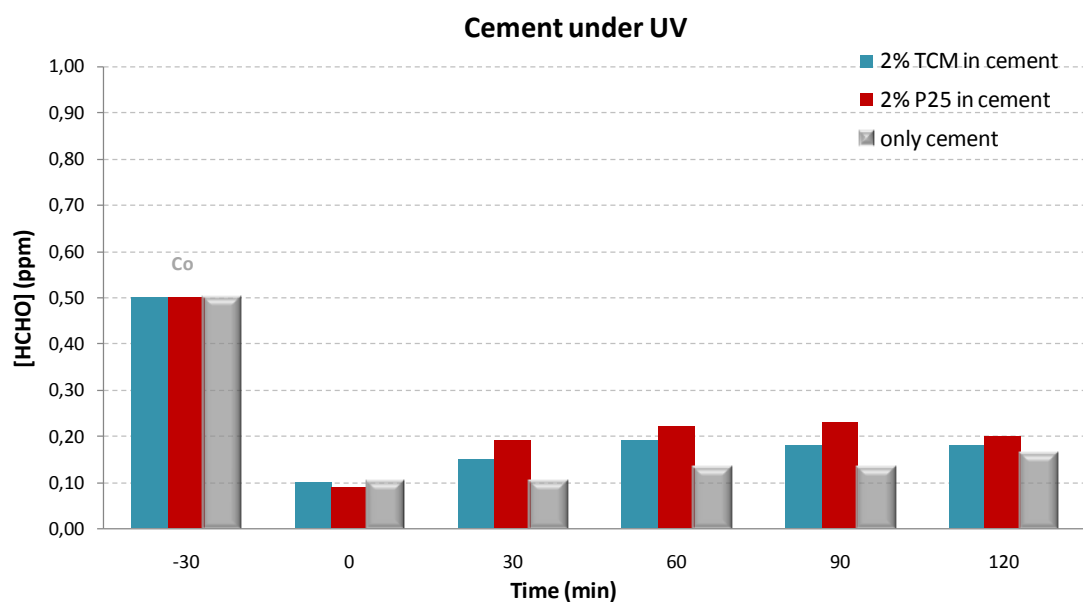


Figure 52. Formaldehyde degradation with 2% TCM in cement, 2% P25 in cement and pure cement.

In cement paint samples, similar behavior is observed. The initial degradation is very high, and accounts for bulk cement paint 90%, TCM in cement paint 78% and P25 in cement paint 90%. This is a very high degradation, taking into account also that cement paint has the smallest size pores of the three BM. The overall degradation is calculated to be 60% for bulk cement paint, cement paint with TCM at 70% and cement paint with P25 at 46%. A 10% increase of HCHO degradation is observed after TCM incorporation in the matrix.

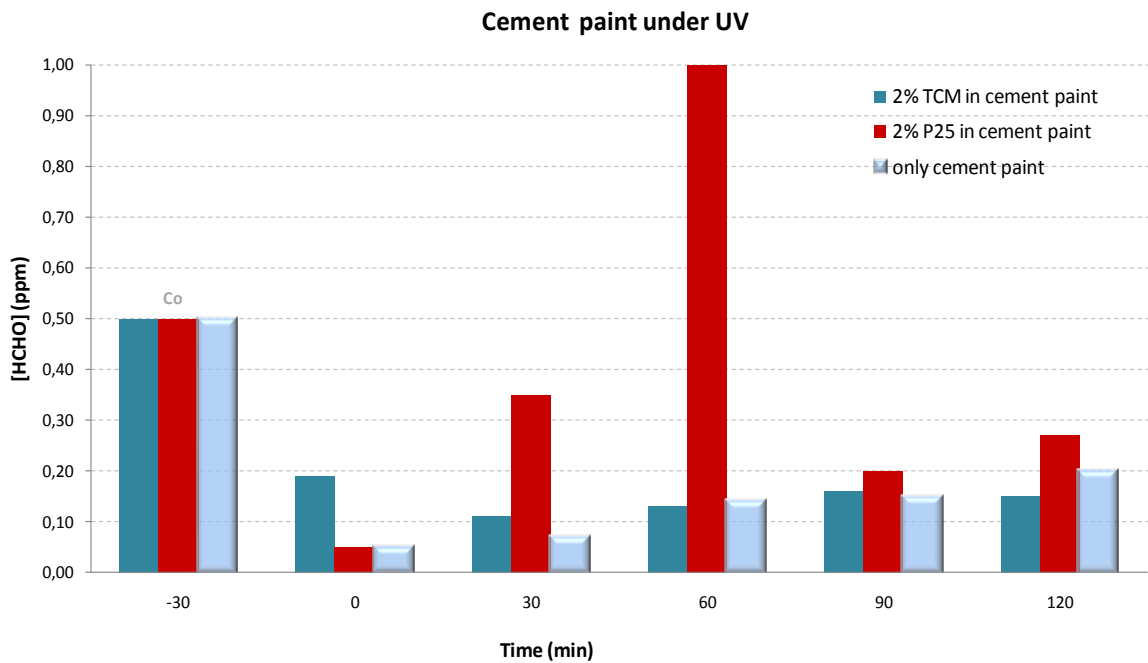


Figure 53. Formaldehyde degradation with 2% TCM in cement paint, 2% P25 in cement paint and pure cement paint.

In the case of calcareous and cement paint matrices, P25 contributed highly to an enormous increase on pollution levels, making this nanomaterial under this pollutant a very weak candidate.

This observation also was made by the TCM lab in collaboration with ISPRA, JRC Italy in the past, when tested P25 on BMs (calcareous filler) had again an enormous increase of formaldehyde levels, at levels of more than 30 mg/m³. This shows that P25 is observed to have HCHO as a possibly by- product of its photocatalytic procedure, or that this Titania could be affected under calcareous (and cement paint in our case) mix and result to higher formaldehyde levels.

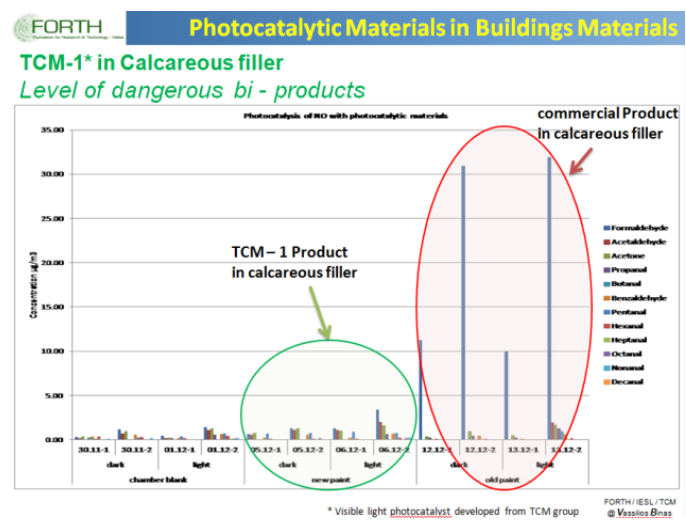


Image 10 FORTH/ ISPRA JRC results on TCM and P25 in calcareous filler

For further investigation in this particular phenomenon Fourier Transform infrared spectroscopy (FTIR spectroscopy) measurements were conducted for all three BMs and sample 2% TCM in calcareous and 2% P25 in calcareous in order to detect possible organic compounds that might undergo oxidation.

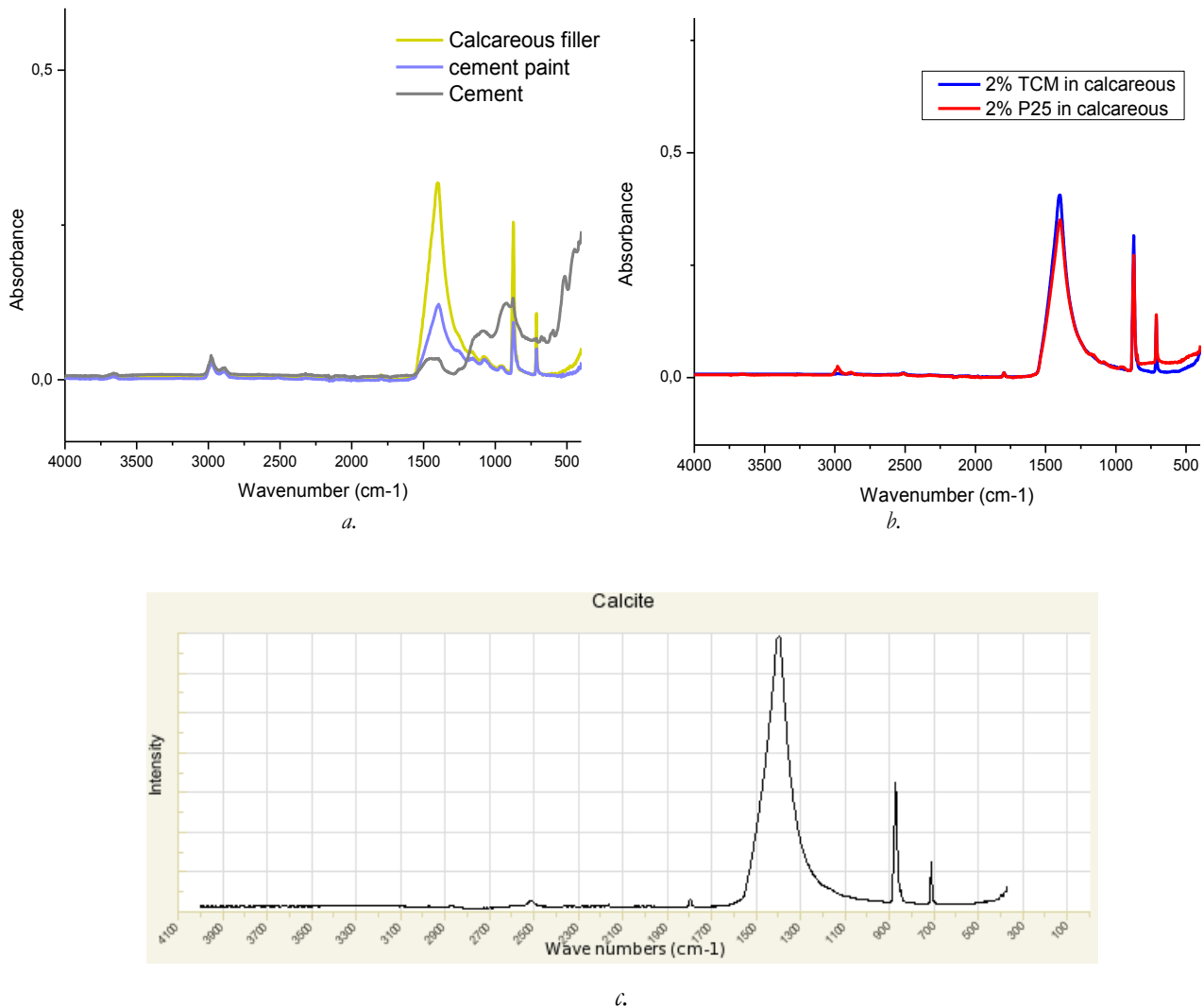


Image 11 a. FTIR of calcareous filler, cement paint and cement **b.** FTIR of calcareous filler incorporating 2% TCM and 2% P25, **c.** Reference calcite FTIR acquired from RRUF database.

From these measurement we can clearly see that cement paint and calcareous materials have the same spectra and very different to cement. Their absorbance in the region of 900-1200 wavenumbers corresponds to organic compounds where carbon bonds with C-

O, C-N, C-C and also from Image 13 *a* and *b* we also observe peaks at 2511 and 1794 corresponding organic compounds, C=O, C=C, C=N.

Table 12: Overall degradation of formaldehyde in three different building matrices for two Titania samples, TCM and P25

Calcareous filler	Overall Degradation of HCHO %	Cement	Overall Degradation of HCHO %	Cement paint	Overall Degradation of HCHO %
Bulk	44	Bulk	68	Bulk	60
TCM	56	TCM	64	TCM	70
P25	20	P25	60	P25	46
TCM 700 °C	72				

Comparing TCM and P25 behavior, we can summarize them in the next two graphs.

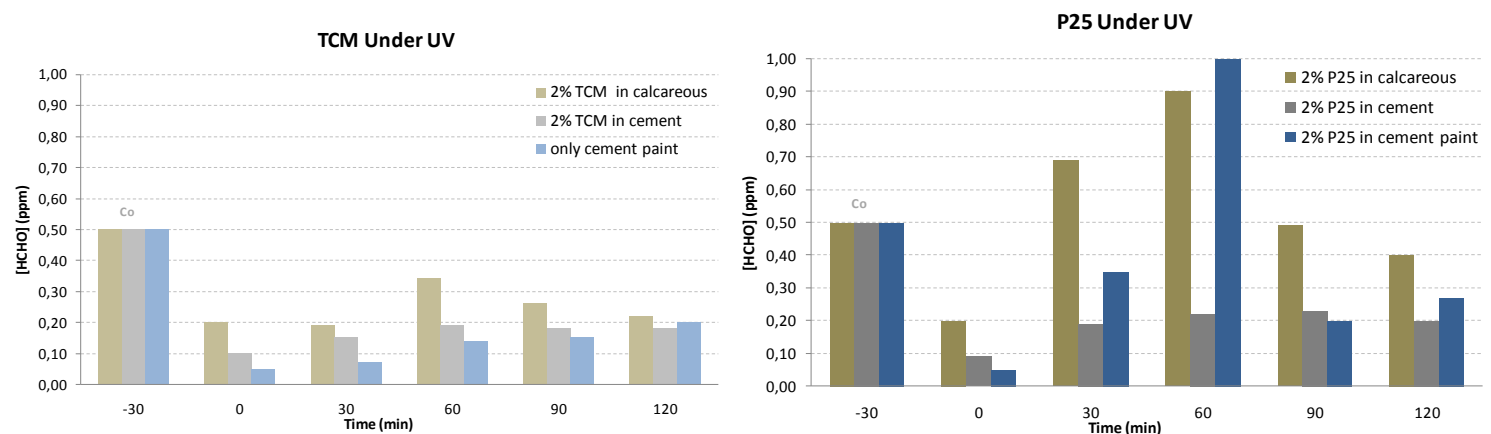


Figure 54. TCM and P25 incorporated in different building materials

It is clear again that P25 inside a building matrix increases the pollution level dramatically, with TCM having a high degradation rate, without any rise of HCHO levels at any point during 120 min. excluding the behavior of the substrate under HCHO, TCM appears to degrade even more in the case of calcareous and cement paint (12% and 10% respectively). Nonetheless, cement as a substrate appeared to have the lowest HCHO levels through the experiment for all Titania samples. In [Fig.51](#) it is clear that calcareous indeed seems to have a higher possible photocatalytic rate of 12% however, during the whole experiment the pollution increases inside the chamber much more than cement, and in the case of cement paint, it increases even more.

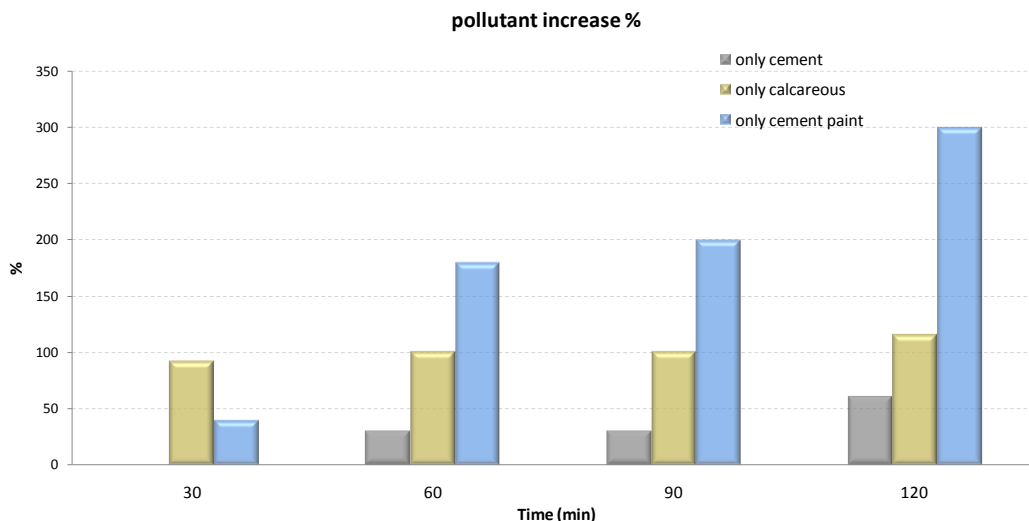


Figure 55. Pollution increase after the use of different building material, cement, cement paint, calcareous filler.

Taking into account different concentration levels of TCM inside the BM, specifically calcareous, we tested 0.2%, 1% and 2% concentration. Taking into account that an increase in the HCHO levels inside the chamber could be also attributed to desorption, then we can observe that 0.2 and 1% Titania appears to have no degradation effect after desorption, whereas 2% seems an appropriate concentration. Also, it is known that the increase of TiO_2 concentration can affect the light penetration therefore minimizing the photocatalytic effectiveness ([Xekoukoulotakis et al., 2010](#)).

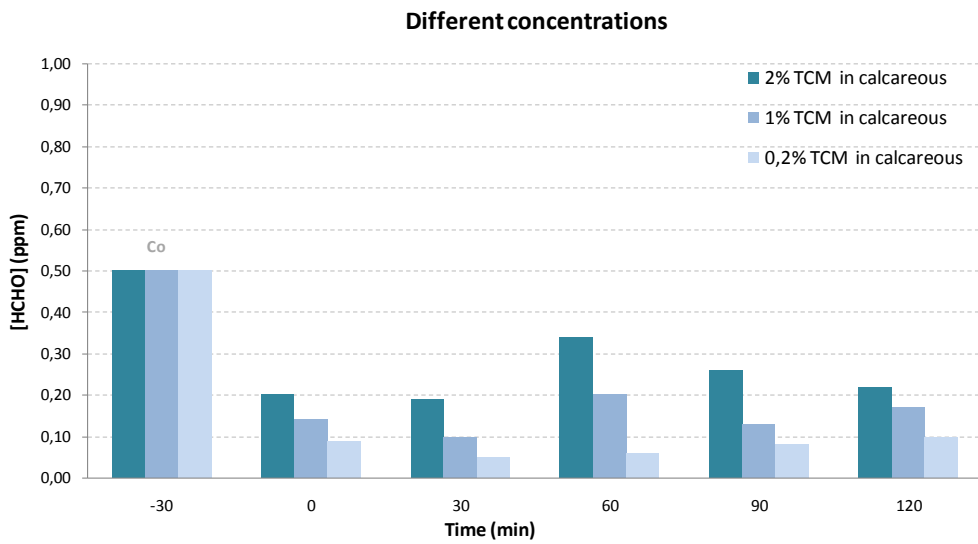


Figure 56. Formaldehyde degradation with 2%, 1% and 0,2% TCM in calcareous filler

Later we studied the photocatalytic behavior of calcined and non-calcined materials, in order to identify whether calcination influences the process. It is visible that the process is enhanced by calcination samples, while the initial degradation is 94% being the highest amount noticed. Overall the degradation rate is 72%, whereas in the non-calcined sample it is 56% and the pure calcareous had a degradation rate of 44%. Therefore calcined sample increased degradation above the substrate, by 28%.

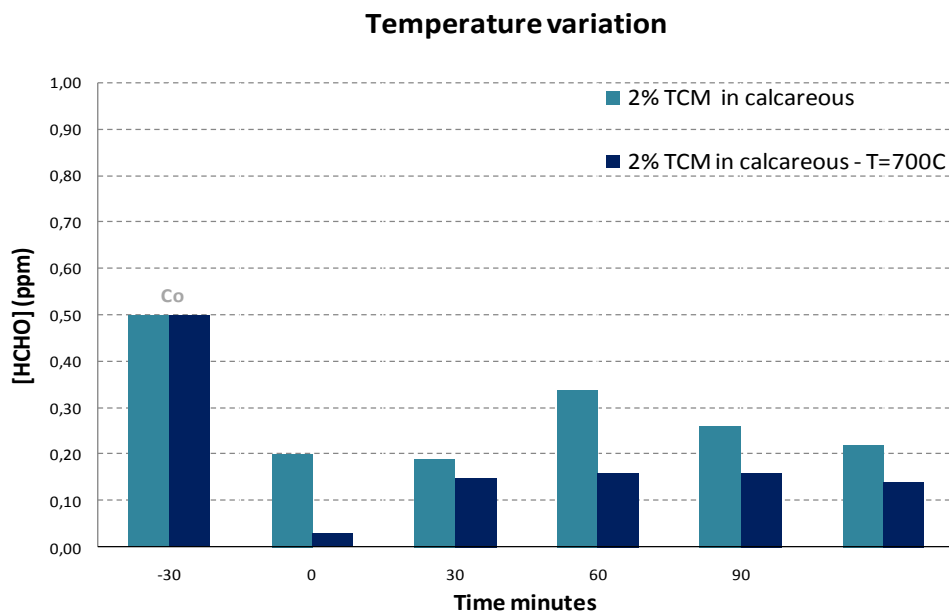


Figure 57. Formaldehyde degradation with 2% TCM in calcareous filler before calcination, and after, under 700 °C.

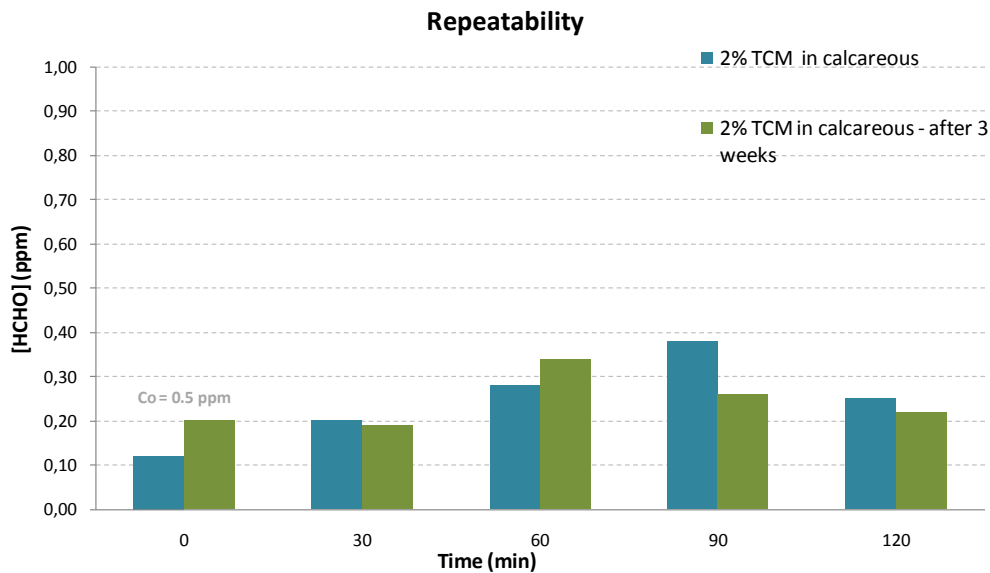


Figure 58. Repeatability of 2% TCM in calcareous filler after three weeks

Finally, after 3 weeks the panels remained unchanged and the repeatability of the experiment was successful.

Overall, the study of BM with PC has shown that:

- There is an increase in pollution after BMs entering the chamber
- P25 generates dangerously high amounts of formaldehyde in calcareous and cement paint based matrices possibly due to organic compounds found in the matrix
- Cement has the lowest pollution rates, and highest adsorption of pollutants
- Calcined materials have higher degradation and adsorption rates
- Higher T increases pollutant levels, despite the small decrease of Rh%

Overall the increase of temperature increases pollutant level, which is also increased by the addition of any building material inside an area. The high surface area of cement makes all photocatalytic cement based materials to absorb a huge amount of pollutants, therefore decreasing dramatically the pollution inside a house. Moreover P25 or any other photocatalyst examined did not seem to show increase on the overall formaldehyde level when incorporated inside cement based materials. In order to minimize dispersion

problems when mixing BM with photocatalytic nanoparticles, a method for this would be to grow the nanoparticles on the BM matrix, therefore T treatment would be necessary. In cement based materials calcination has already proved to not alter the characteristics of the cement (see XRD results), therefore cement seems appropriate materials for this procedure. Photocatalytic results have also proven that calcined samples have higher degradation and adsorption rates than not calcined. Thus cement based nanomaterials would be a possible high effective photocatalyst BMs.

As calcareous samples and cement paint materials are concerned they are both calcite based BMs. Both materials (especially cement paint) have a very high adsorption rate of pollutants and interestingly P25 reacts with the possible organic compounds found in these two BMs and not in cement. Nonetheless the highest photocatalytic results are achieved under calcareous fillers incorporating TCM.

Chapter VI

Environmental Performance

In Europe, the building sector currently is the main contributor towards its total energy consumption and CO₂ emissions, as it accounts for 40% of the energy consumed (Bernardo et al., 2016; Stephan & Stephan 2016) and is responsible for around 36% of CO₂ emissions (Nolte & Strong, 2011). To this end, the European Council, via the Directive on Energy Performance of Buildings (EU, 2010) has taken the initiative to improve energy efficiency in the building sector, by reducing energy consumption, minimizing related wastage (EU, 2010) and improve indoor Air quality. Currently, there is a lack of sufficient thermal envelope insulation in building stocks in southern European countries, while cooling (mainly air conditioning) is an important contributor to the overall energy consumption (Nolte & Strong, 2011). Therefore, there is a need to explore improvements, (innovative building materials), to reduce energy use and the environmental footprint of the building sector. Moreover, the use of photocatalytic nanomaterials should be applied also in the building sector in order to reduce emissions but also to contribute more to the energy savings through the smaller energy loss necessary for air ventilation.

In that sense whereas there are plenty of researches focusing on the structural characterization of nanoparticles and their performances in several sectors, and also there is a focus on environmental risks that these nanomaterials can have; little attention has been given to combine environmental assessment methods closely together with structural analysis and photocatalytic performances in order to assess, rethink, and optimize several steps in the field of materials sciences. In this sense, this is the first time a connection of material sciences with environmental studies is being made. This may be

used as the base for advancing photocatalytic nanomaterials and introduce environmental considerations that will allow a sustainable process scale-up.

This chapter presents two cases of a life cycle analysis conducted for innovative nanomaterials that can be used in the area of the building sector. In this analysis *a.* the hotspots of synthesis procedure of photocatalytic nanomaterials is being made in order to make a step towards photocatalysts' optimization regarding their efficiency but also their environmental behavior. The second case includes, *b.* the case study of two innovative isolative materials with data acquired for real time use of these is being made investigating on their construction environmental weakness and embodied energies, but also on the overall energy savings these provide to the building sector.

6.1 Life Cycle Analysis of ZnO Nanopowders

This section focuses on the facile microwave-assisted synthesis technique with an aim to examine the parameterization impact on ZnO nanostructure structural characteristics and its effect on their environmental footprint. This study may be used as the base for advancing the synthesis of nanoparticles and introduce environmental considerations for optimized sustainable nanomaterials.

Nanomaterials have a greater surface area to volume ratio than this of their conventional forms, leading to greater chemical reactivity and affecting their strength. This high surface area leads to enhanced surface activity that can be exploited for several applications([Alagarasi, 2011](#)). Therefore the nanomaterials' surface area is very important and can affect the material's efficiency. For example, when nanomaterials, are used for photocatalytic applications, the surface area of the aggregate particles formed in aqueous solution determines their photocatalytic activity ([Zacharakis et al., 2013](#)).

However, although, the structural characterization of ZnO nanoparticles and the effect of their synthesis conditions have been well studied, a comprehensive study dealing with the effect of the different synthesis parameters on their structure and most importantly on the way this affects their environmental sustainability is still pending. This section contributes toward this end by utilizing characterization results from laboratory scale

experiments and uses them to assess the environmental sustainability of facile microwave-assisted ZnO nanostructures.

Environmental Analysis

In order to assess the environmental sustainability of the produced facile microwave-assisted ZnO nanostructures, presented in [Section 4.1.1](#) the life cycle assessment (LCA) methodology, as set by ISO 14044 and 14040 ([ISO 14044:2006, 2006; ISO 14040:2006, 2006](#)), was employed. A cradle-to-gate LCA was performed using laboratory experimental data; the geographical coverage of this work is South Africa. Finally, through a sensitivity analysis the geographical coverage was expanded to include Europe and North America (US). The software package SimaPro 8.0.3 was used.

The functional unit quantifies the performance of a product system and provides a reference to which the input and output data are normalized ([ISO 14040:2006, 2006; ISO 14044:2006, 2006](#)). The physicochemical properties of the fabricated ZnO nanostructures, such as size, shape, surface area and crystallinity, are important parameters for environmental studies ([Stone et al., 2010](#)). Amongst them, the surface area is also an important parameter for several ZnO nanostructures applications, such as photocatalysis and photolysis ([Zacharakis et al., 2013; Koutantou et al., 2013](#)). Therefore, 1 m²/g, i.e. the surface area, of ZnO nanostructure was set as the functional unit. Moreover, the system boundaries of the LCA determine which processes, materials, energy flows and activities are included in the analysis. In this work, all main flows (e.g. electricity, materials etc.) are inside the boundaries. Moreover, this work presents a cradle-to-gate LCA, i.e. from raw material to ZnO nanostructures fabrication, and as such the distribution, use and disposal of the ZnO nanostructures are external to system boundaries. Electricity consumption was assumed to originate from South Africa's electrical grid, where ZnO nanostructures fabrication took place. South Africa's electricity mix is dominated by fossil fuels, mainly coal ([U.S. Energy Information Administration, 2015](#)), which is expected to have a negative effect on the results.

In order to model the environmental footprint of the system under study, the ReCiPe impact assessment method was used. ReCiPe comprises of two sets of impact categories (i.e. midpoint and endpoint), with associated sets of characterization factors, taking into account a broad set (18 impact categories) of environmental issues. In order to make

interpretation easier, this large number of midpoint indicators can be grouped in the next step into the three areas of protection, namely “Human Health”, “Resources” and “Ecosystems”, weighted and aggregated into a single score (Ioannou-Ttofa et al., 2016).

Environmental Results

As a base scenario (S0) the fabrication of ZnO nanostructures at 110 W microwave power and 90 °C annealing temperature was used. This is the initial scenario and it will be used for all comparisons, i.e. varied microwave power and varied synthesis temperature. As a functional unit 1 m²/g of the fabricated ZnO nanostructures, i.e. the surface area, was used. As shown in *Fig 59* ethanol usage is the main environmental weakness, since is the main contributor to most impact categories, i.e. “climate change”, “Ozone depletion”, “freshwater eutrophication”, “photochemical oxidant formation”, “terrestrial ecotoxicity”, “agricultural land occupation”, “urban land occupation”, “natural land transformation”, “water depletion”, “metal depletion” and “fossil depletion”. Specifically, for purifying ZnO nanoparticles large quantities of de-ionized water and ethanol are required. De-ionized water has a small environmental footprint, compared to ethanol. The reason is that the production of high purity ethanol requires natural and is also an energy intensive process. The second environmental weakness that was identified is the oven drying process. The prolong time, i.e. 2 h, required for the calcination of the ZnO powder at high temperature, i.e. 200 °C, is responsible for this. Oven drying has a high relative contribution to most impact categories. The underlying reason for the oven drying relative high contribution is not the oven itself as a material, which has a very low relative contribution (<1%), but electricity consumption from South Africa’s fossil fuel depended energy source. This is the reason (i.e. fossil fuel extraction and combustion) why the oven drying is the relative main contributor to the impact categories “terrestrial acidification” and “marine eutrophication” and “human toxicity”. The remaining processes exhibit a low to negligible relative contribution to most impact categories. Specifically, the autoclave is closely followed by the stirring process and they both have a relatively high impact on “terrestrial ecotoxicity” and “natural land transformation” impact categories. Similarly, these contributions are attributed to the electricity required to drive the process and not to their construction materials, as will be discussed below. Finally, all inorganic chemicals required for the ZnO fabrication have low contributions. Specifically, zinc nitrate has a small relative contribution on “human toxicity” and

“metal” and “water depletion” impact categories, whilst the use HMT, and NaOH have a very small to minimal relative contribution as shown in [Fig. 59](#).

South Africa’s fossil fuel depended energy mix contribute to the overall environmental impacts since, fossil fuel extraction, refining and combustion, apart from affecting the impact categories ‘fossil depletion’ (owing to extraction) and to a lesser degree ‘metal depletion’ (owing to equipment construction), also releases toxic compounds, such as nitrogen oxides, heavy metals, sulphurous compounds and polycyclic aromatic hydrocarbons (PAHs) ([Ioannou-Ttofa et al., 2016](#)). These releases are affecting the impact categories “ecotoxicity” (i.e. marine and freshwater ecotoxicity) and “toxicity”(human toxicity). Finally, phosphate emissions from coal extraction affect the “freshwater eutrophication” impact category ([Ioannou-Ttofa et al., 2016](#)).

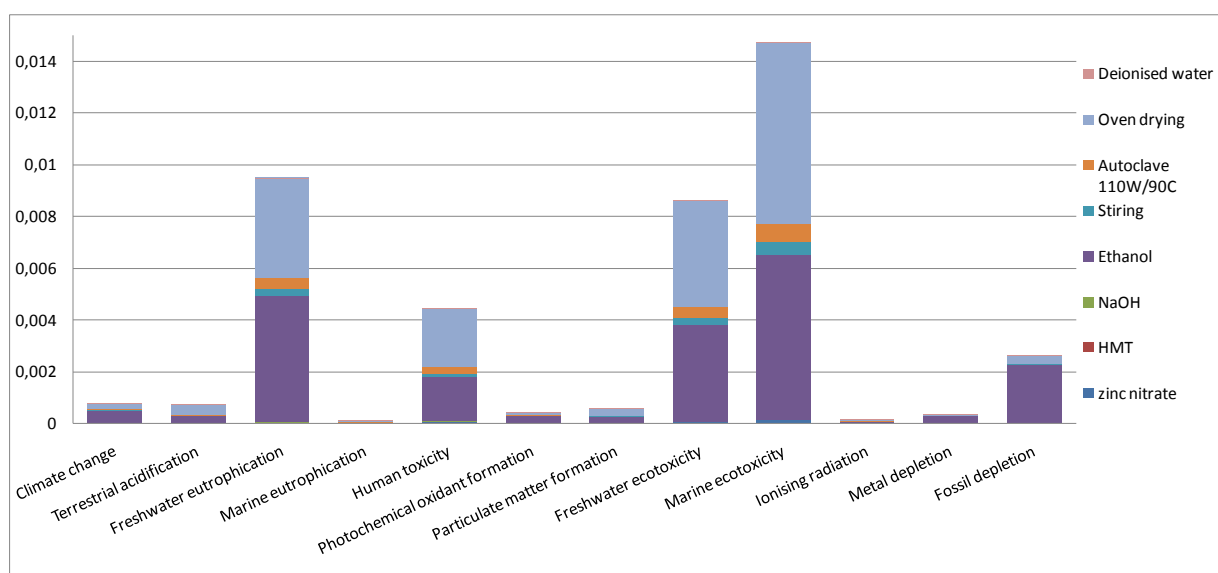


Figure 59 Impact categories for the fabrication of ZnO nanostructures (microwave power 110 W, temperature 90 °C).

Effect of microwave power on sustainability

First the effect of the microwave power is examined by using two different scenarios, apart from S0, Scenario 1 (S1) and scenario 2 (S2) entail the use of higher microwave power, 310 W and 710 W, respectively, using a constant temperature of 90 °C. [Fig 60](#) shows the comparative analysis of the three different scenarios, S0, S1, S2, using

ReCiPe's three endpoint damage categories, namely "Human Health", "Resources" and "Ecosystems". As shown, the first two damage categories are mainly affected by the facile microwave-assisted technique, while the latter ("Ecosystems") exhibits an overall low score. As noted above, the main contributor to these impact categories is ethanol, followed by electricity consumption from the oven process and to a lesser degree from the autoclave and the stirring processes. The damage category "Human health" is mainly affected from emission originating from ethanol production process and from emission emanating from the processing and burning of fossil fuels for electricity generation. Moreover, the comparative analysis revealed that S2 (710 W/90 °C) has the lower total environmental footprint, followed by S1 (310 W/90 °C), while S0 (110 W/90 °C) exhibited the highest environmental footprint. Specifically, the total environmental footprint of S1 and S2 is ~18% and ~27% lower than S0. Therefore, when you want to synthesize a higher surface area nanomaterial, high microwave power results to decreased environmental footprint.

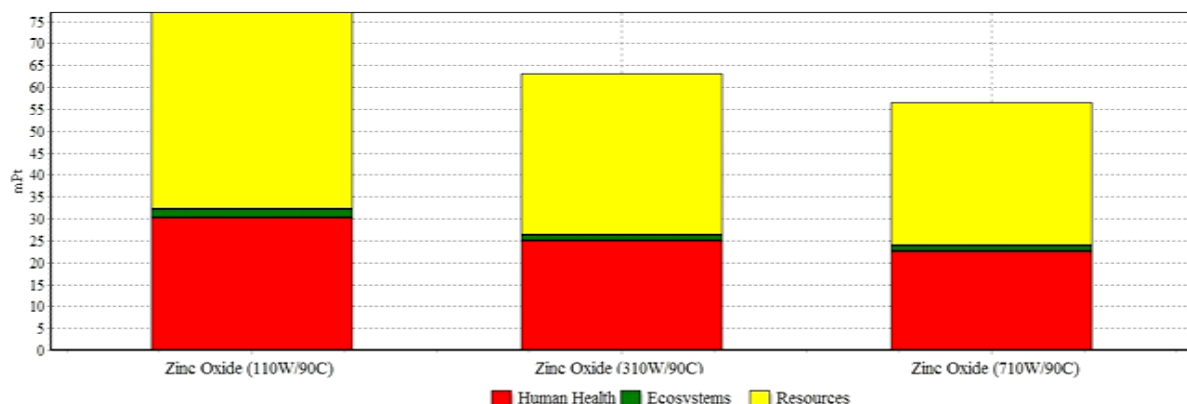


Figure 60. Comparative analysis of varying the microwave power (110 W, 310 W, 710 W at 90 °C temperature) on the environmental sustainability of ZnO nanostructures.

Effect of annealing temperature

The second key synthesis parameter examined here in was the effect of annealing temperature on the environmental sustainability of the ZnO nanostructures. For this reason the base scenario, S0, was compared to scenario 3 (S3) and 4 (S4), where microwave power was set at 110 W and annealing temperature was increased to 150 °C and 220 °C, respectively. *Fig 61* shows the contribution of each process on the three

damage categories, and a similar pattern with the one identified when varying the microwave power, is observed. Increasing the autoclave's temperature has a positive effect on the ZnO nanostructures environmental sustainability, with S3 (150 °C) and S4 (220 °C) having a ~10% and ~41% lower total environmental footprint, compared to S0. Therefore, high temperatures could sustainability improve ZnO nanostructures environmental sustainability, since they largely improve the surface areas, which can be useful for several applications in nanotechnology.

The results obtained both from varying the microwave power and annealing temperature imply that increasing both variables in the study ranges, result to reduced environmental footprints. This reduction of the environmental footprint is attributed to the improved ZnO specific surface area, as this was our functional unit.

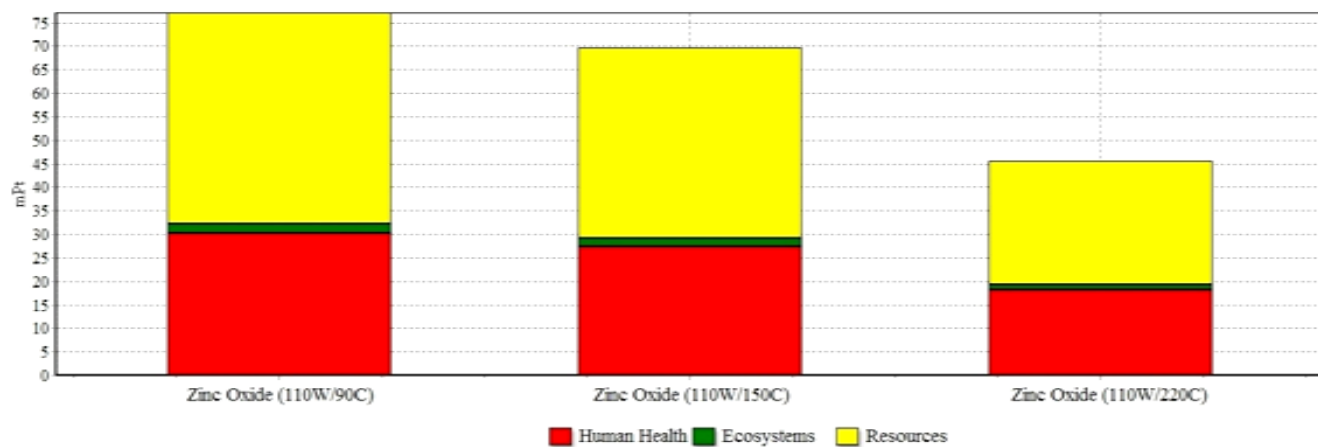


Figure 61. Comparative analysis of varying synthesis temperatures (90 °C, 180 °C and 220 °C, at 110 W microwave power) on the environmental sustainability of ZnO nanostructures,.

Sensitivity Analysis-Effect on diversifying the electricity mix

The main environmental weakness identified in this work are a) the use of ethanol, required for ZnO nanostructures purification, followed by b) electricity consumption, required for the calcination of the ZnO powder. In order to minimize the ethanol use, prolonged calcination times, much higher than 2 hrs, would be required; thus bringing forward electricity consumption. How electricity is generated varies, as different mixes of generation technologies are used in different countries (Slotte et al., 2015). Therefore, the environmental footprint of different electricity mixes could vary significantly. For this reason, a sensitivity analysis was carried out dealing with the introduction of different

electricity sources, as well as with the introduction of renewable energy systems to solely provide for the electricity needs. Apart from South Africa's electricity mix, which was used during the experimental procedure, the effect of Europe's (EU 27) and USA's average electricity mixes, on the total environmental sustainability was examined. Also, the effect of substituting fossil fuels with renewable energy was examined, as a best case scenario. The use of hydro, wind and solar energy was examined.

Fig. 62 shows sensitivity analysis results. Both EU-27 and USA electricity mix can reduce the total environmental footprint of ZnO nanostructures by ~14 % and ~9 %, respectively. This is attributed to the highest share of renewable energy in those mixes, with EU-27 having a highest share of renewable energy compared to the average USA mix and thus exhibiting an overall better environmental performance. The use of renewable energy can further reduce the total environmental footprint of the process, with hydro and wind both claiming a reduction of ~25% and solar claiming a reduction of ~22%.

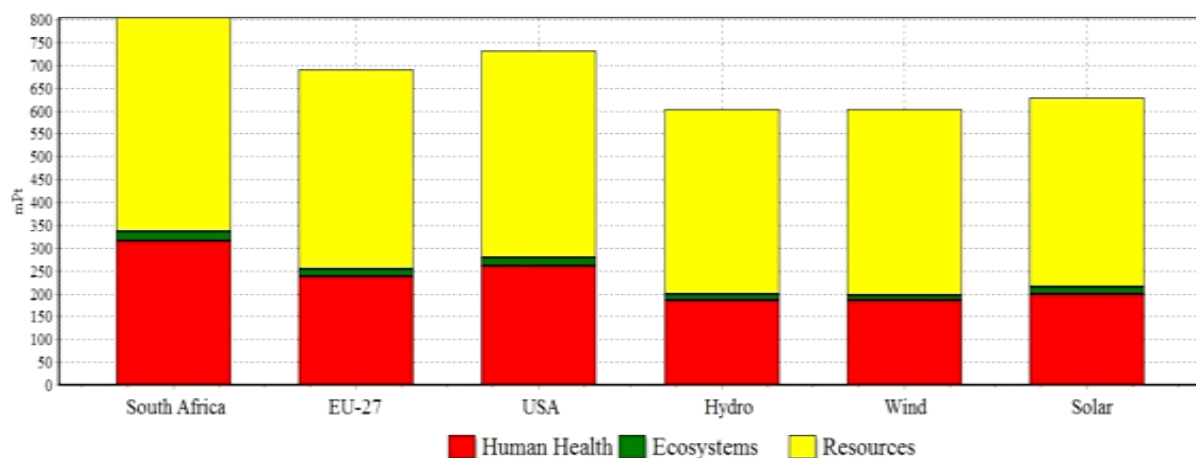


Figure 62. Comparative analysis of ZnO nanostructures by using different energy mixes.

Therefore, the use of renewable energy is a feasible alternative that can considerably improve the environmental sustainability of ZnO nanostructures, produced by the facile microwave-assisted. It can also allow the reduction of the large volumes of ethanol required for the purification process, by providing prolonged calcination times with low environmental impact. Another possible scenario to reduce the environmental footprint

of ZnO nanostructures could be the use of ethanol produced from sugars fermentation, instead of fossil fuels.

Overall, from this LCA it was found that synthesis temperature and microwave power are inversely proportional to environmental sustainability, i.e. high temperature and microwave power lead to reduced environmental footprint. The reason is that with a small increase in the total electricity consumption the ZnO nanostructures surface area, (which is the parameter of our interest) is substantially improved. Furthermore, the main environmental weaknesses identified were; a) the use of ethanol, required for ZnO nanostructures purification, followed by b) electricity consumption, required for the calcination of the ZnO powder. A sensitivity analysis using different electricity mixes revealed that an energy mix based on renewable sources can considerably improve the environmental sustainability of ZnO nanostructures

6.2 Novel isolative building materials in Demo houses- Environmental assessment and Energy Performance

In this section we will investigate a different category of novel building materials; the one that belongs to the thermal efficiency of the building sector. In that perspective, two isolative materials placed inside the Demo houses will be analyzed. The Phase Change Materials (PCMs) and the Vacuum Insulation Panels (VIPs).

Although there have been several previous works on the use of insulation materials, and specifically PCMs in buildings, most of them focus on the analysis of the components of the materials and their properties (Tyagi & Buddhi, 2007; Farid et al., 2004; Zalba B et al., 2003; Su et al., 2016), e.g. whereas little focus is given to the environmental assessment of these materials throughout their life span, via the LCA methodology. Therefore, in this chapter is a complete cradle-to-grave LCA, including the manufacturing, operation, and disposal of PCMs was carried out.

The actual thermal behavior of both demo houses was identified using measured data acquired over a reference period spanning for more than one year and their daily energy consumption was estimated using this data. Then, a cradle-to-gate analysis was carried out to a) assess the impact of energy savings on the building's total environmental footprint and b) determine if energy savings balance out the higher initial environmental impact of these materials.

PCMs and VIPs were found to reduce indoor daily temperature fluctuations, achieving thus better indoor thermal comfort and energy savings. Nonetheless, taking into account the embodied energy, PCMs and VIPs, as construction materials, lead to about 34% higher total environmental impact compared to the application of solely conventional materials for building insulation. However, when energy savings from the operation phase are taken into account VIPs and PCMs are found to be more environmentally friendly under the mild Mediterranean climatic conditions, compare to conventional envelope insulation materials.

One demo house (red house) was covered internally with PCMs containing plaster (namely PCMs-23 from Maxit/ SGW) and externally with VIPs from Porextherm, while the other (green house) was constructed using only conventional building materials, i.e. without PCMs and VIPs, in order to be used as the reference house. The VIPs used had a silvery to white color, a density between 150-300 kg/m³, thermal conductivity at ambient pressure and at 22.5 °C < 0.019 W/(mK), heat resistance between -50 °C to 120 °C and interior pressure < 5 mbar. The PCMs had a compressive strength > 2 N/mm², thermal conductivity > 0.3 W/mK and a water vapor diffusion resistance μ equal to 10. The product system is the complete demo house; therefore the functional unit that best describe it is one cubic meter (1 m³). The system boundaries, starting from the construction, operational, within a timeframe of 25 years, and ending with the disposal or recycle phase, were determined. Moreover, energy is the most important resource used in a building over its lifetime (Huang et al., 2015; EU 2010). Therefore, the energy consumption for maintaining indoor thermal comfort, under the local climate conditions (23 °C in winter and 24 °C in summer), was considered in the analysis. Energy consumption was estimated on a year-round base.

Table 13: Life Cycle Inventory for the two demo-houses

Demo Houses		Red House		Green House	
Material	Description	Quantity	Unit	Material	Description
Fine plaster		100 kg	100 kg	100 kg	100 kg
Plaster		230 kg	230 kg	230 kg	230 kg
Wall Primer		90 kg	90 kg	90 kg	90 kg
Cement board		477 kg	477 kg	477 kg	477 kg
Rockwool		115 kg	115 kg	115 kg	115 kg
Plasterboard		414 kg	414 kg	414 kg	414 kg
Paint		34 kg	34 kg	34 kg	34 kg
Oil for wood		4 L	4 L	4 L	4 L
Wood paint		2 L	2 L	2 L	2 L
Adhesive for VIP		-	90 kg	-	90 kg
Anti-fire coating		-	3.6 kg	-	3.6 kg
PCM-23		-	850 kg	-	850 kg
VIPs		-	294 kg	-	294 kg
Wood		545 kg	545 kg	545 kg	545 kg
Water		970 kg	970 kg	970 kg	970 kg
Inert PCMs (plaster)		-	-	-	680 kg
Wall window		1	1	1	1
Roof window		1	1	1	1
Aluminum door		1	1	1	1

Insulating performance

In the graphs below the temperature behavior inside the house is presented. The first graph represents the values of the use of solely PCM, whereas in the second graph the addition of VIPs took place. As expected in the first graph the T variations were noticeably perceptible in temperatures around 23 °C, which was expected since the melting T of selected PCMs is at 23 °C. The use of solely PCMs enhanced the thermal behavior of the house, for most of the period that this was studied. However, in warmer months (from June – September) when the house's temperature reaches around the 25 °C mark a threshold is observed. This means that red house does not have a better thermal behavior than the reference green house in warmer months. This could mean that there is a possible higher thermal release during the night and eventual storage of this heat inside the house. This is expected from PCMs since they perform well within a small temperature range, while outside this range they simply behave like any conventional building envelope material. The thermal behavior enhances when using PCM-23 together with VIPs. After that, the house was found to have higher T stability than before, making the not isolative house deeply dependable on the outdoor temperature ([Fig.63, 64](#)). Comparing the contemporaneous results solely with PCMs to those of combined PCMs with VIPs the enhancement of insulation that VIPs offer is clear.

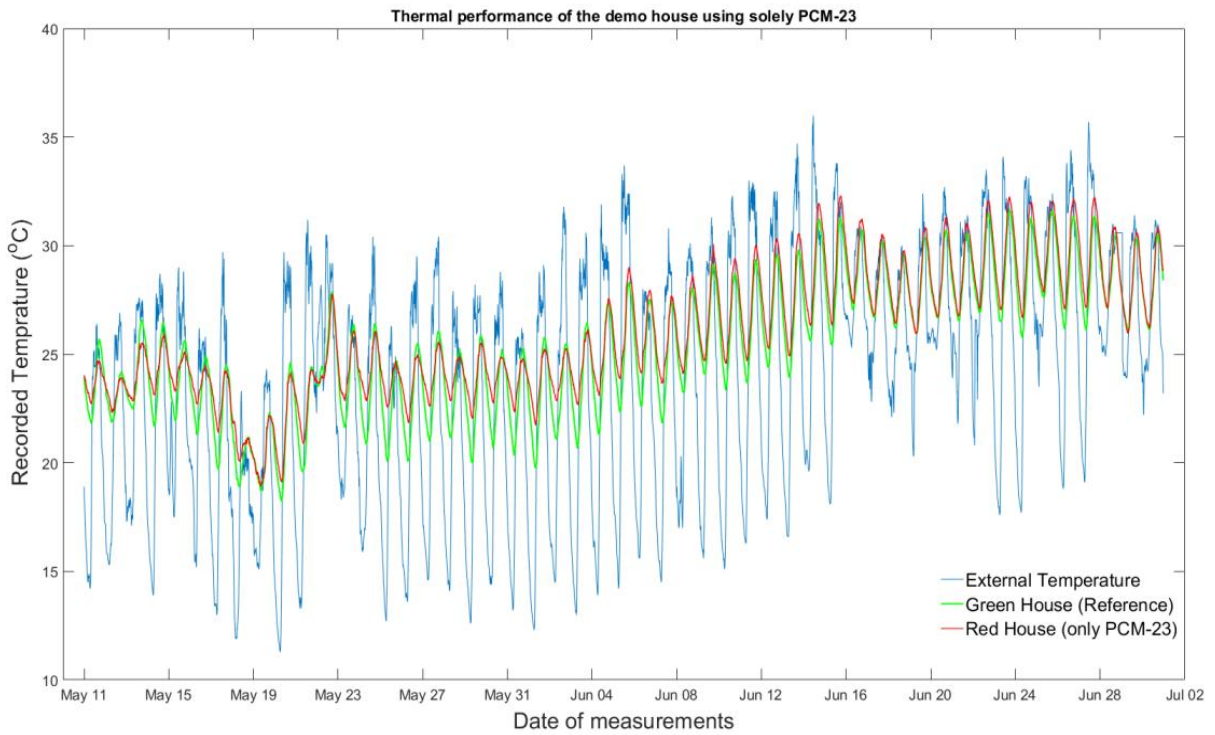


Figure 63. Temperature profile of the demo houses using only PCMs-23

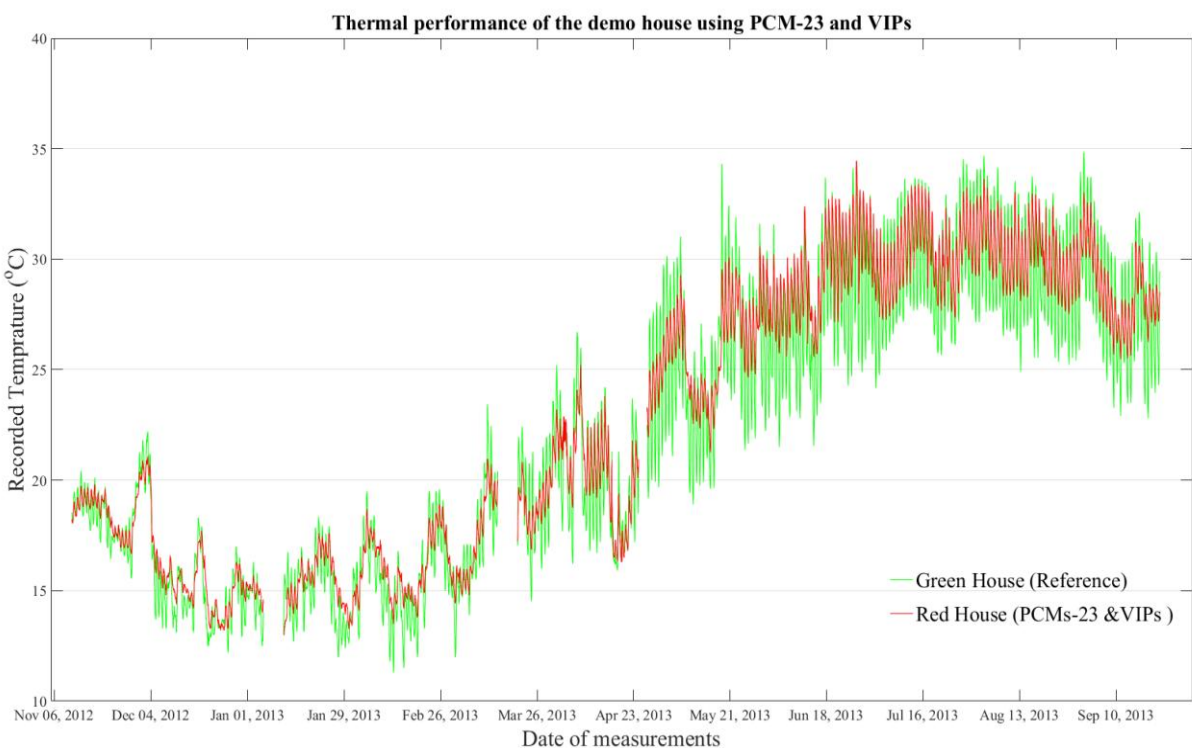


Figure 64. Demo houses temperatures using PCMs-23 & VIPs

As expected, better thermal behavior is achieved with the use of isolative materials; however, we will investigate on these materials' embodied energy in order to assess them environmentally. Therefore the life cycle assessment of the two houses is presented now. Results are shown per functional unit, 1 m^3 .

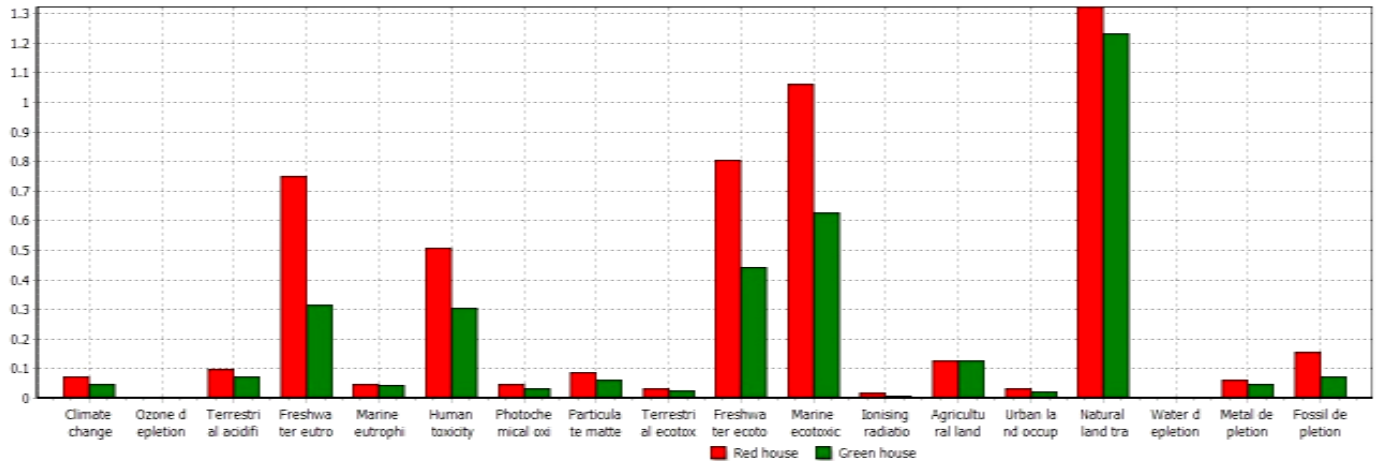


Figure 65. Normalized impact scores of the “red” (PCMs and VIPs) and “green” demo house.

In terms of ReCiPe's 18 impact categories, the red house exhibited higher scores and especially on the categories of freshwater eutrophication, human toxicity, freshwater ecotoxicity and marine ecotoxicity. These higher normalized scores are mainly attributed to the construction of VIPs, and to a smaller degree of PCMs, which is an energy intensive procedure. Also, some of their main materials are associated with high environmental impacts, (expandable polystyrene for the case of VIPs and paraffin for the case of PCMs). Lastly, the transportation of these materials from their country of origin, namely Germany, to Crete contributes to the above mentioned impact categories. The aggregated environmental impacts of both demo houses, using ReCiPe endpoint method are presented in Fig 66. Due to the application of PCMs and VIPs the total environmental footprint of the red demo house is found to be $\sim 34\%$ higher than the reference demo house. Specifically, it is found that the red house exhibits a significantly higher score in the damage categories human health and resources, whilst both houses have a similar environmental performance in the damage category concerning ecosystems.

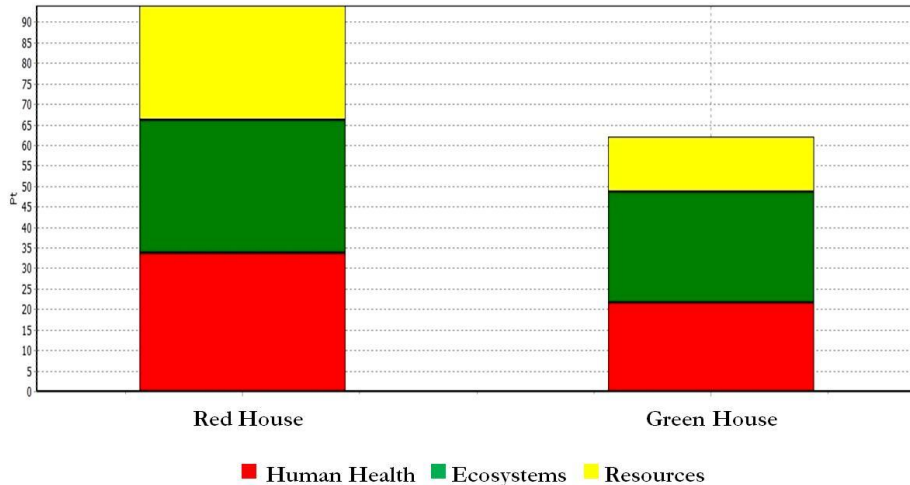


Figure 66. LCA Severity of damage categories for the (a) “red” and (b) “green” house expressed in a single score

In the reference demo house the windows, door and cement boards are the materials which contribute most to the environmental footprint. Apart from insulation, both houses utilize the same construction materials. Therefore, the higher scores of the red house are attributed to VIPs and PCMs installation, and especially the first, which exhibit a fourfold higher environmental footprint, compared to PCMs. The analysis revealed that PCMs contribute $\sim 7.5\%$ to the total environmental footprint of the red demo house, while VIPs exhibit a much higher contribution that reaches $\sim 31\%$ (Papadaki et al., 2013). Their sum is the reason for the higher aggregated environmental impact of the red house, when compared to the green house. Previous research in northern European climates shows that the biggest environmental impact of a house comes from the shell embedded materials (Blendini & Di Carlo, 2010).

As a result, the choice of the materials can minimize the environmental impact of a house, while recycling waste has a positive impact on the environmental effectiveness. Therefore, as expected, the use of PCMs and VIPs leads to a higher total environmental footprint during the construction phase of a building.

Nonetheless, the building sector has a long lasting operation stage, in which when it comes to isolative materials, the energy savings with the use of these materials is expected to be high. Nonetheless, improvements are achieved in thermal comfort, which can be translated to energy, and thus environmental, savings. As we already proved the red house is significantly more thermally stable, so it would require less energy to reach thermal comfort. In order to evaluate the energy savings from the application of PCMs

and VIPs, the energy consumption required to maintain indoor thermal comfort was estimated in both and compared. The daily energy consumption required to reach 23 °C during winter and 24 °C during summer, was estimated using equation: $Q = FU\Delta T$. Where Q is the thermal energy of the system in kcal, F is the interior surface area, U the thermal conductivity of the building materials used in the system and ΔT the temperature difference between the desirable interior T and the actual interior recorded T (Jamthe & Agrawal, 2013). Using the above equation the energy consumption of both demo houses was estimated. The highest differences between energy consumptions are observed during winter months, where PCM-23 show to have an optimal performance. In April and May outdoor temperatures are close to human comfort, thus the use of PCMs and VIPs lead to minimal energy consumption (<2 kWh) compared to the reference demo house which required up to three times the energy input to maintain comfort (4.3 kWh instead of 1.3 kWh). During warm summer months the PCMs are not as effective as during winter, but still the red demo house exhibits an overall excellent performance requiring only close to a third of the energy compared to the conventional green demo house. The estimated energy consumption was used as input in the LCA modeling.

Then when the energy savings derived from the use of VIPs and PCMs are taken into account the LCA results differ significantly. Results are presented in Fig. 67.

The Greek fossil fuel-depended energy mix (54% lignite, 11% crude oil, 17% natural gas, and 18% renewable energy) is a large factor which contributes to the elevated environmental impacts (Chatzisymeon et al., 2013). The reason is that the electricity provided by the Greek energy mix is associated with elevated impacts due to a) the extraction procedure of lignite, which is associated with airborne and waterborne emissions, posing stresses to the ecotoxicity and eutrophication impact categories, and b) fossil fuel burning for energy production, which, among others, results also to airborne emissions (Ioannou-Ttofa et al., 2016). The red demo house exhibits an overall better environmental performance, since during its lifespan it requires lower electricity inputs to maintain indoor thermal comfort, compared to the reference demo house. During their whole projected life span of 25 years, the green house would be responsible for 10.65 Pt/m³, whereas the red house would have a much lower environmental impact, amounting to 4.54 Pt/m³ (57% lower). The construction phase of the reference demo house has a minimal environmental impact (~6%), compared to the operational phase (~94%); whilst in the case of the red demo house the construction phase amounts to ~21% and the operational phase to the remaining ~79% of the total environmental

footprint. This is mainly attributed to the minimized energy use for maintain thermal comfort during the operational phase of the red house. As a result, it is estimated that the initial higher environmental footprint (construction phase) of the “red” demo house would be compensated for within a short amount of time, ~14 months.

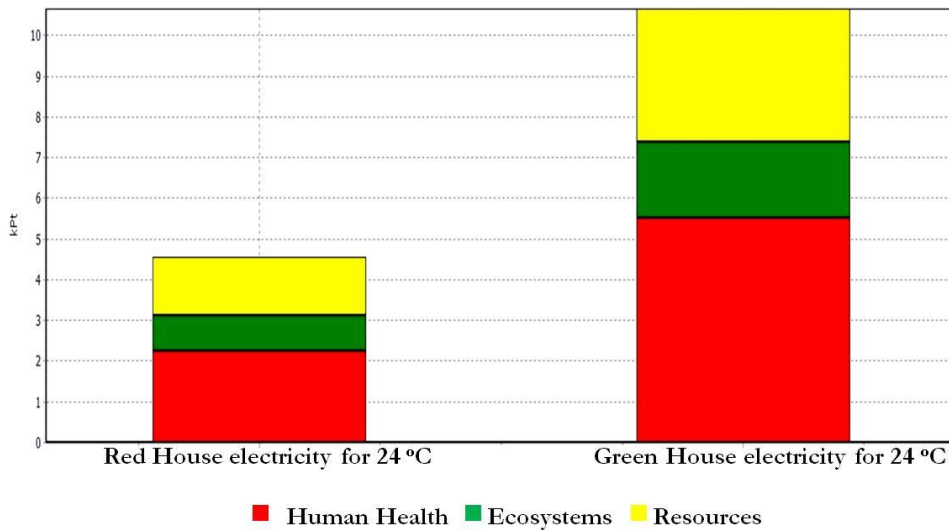


Figure 67. LCA Severity of damage categories for the construction and operation (i.e. energy required to maintain comfort) phase of the (a) “red” and (b) “green” house.

Other studies, focused solely on the LCA of PCMs, showed that their application leads to decreased energy consumption during the operation phase; however, it was shown also lead to a higher global impact, environmentally throughout the building's lifetime. Moreover, under summer conditions, PCMs have shown a higher reduction in energy consumption, resulting in a decrease in the global impact by 10% or even 12-14% (Castell et al., 2013). This technology can, therefore, be regarded as very efficient in regions with higher temperatures throughout the year, like Greece.

Taking into account the environmental aspects of the use of nanomaterials in the construction industry we conclude to the following considerations. Photocatalytic nanomaterials contribute to energy savings by lower ventilation losses. Studies show that ventilation accounts for 20% of the energy losses for UK buildings (Liddament & Orme, 1998). Nonetheless, ventilation is essential for indoor air quality but the energy loss is

excessive, and possibilities of minimizing this phenomenon must be investigated ([Orme, 2001](#)). From data acquired from Center of Renewable Energy in Greece, it is estimated that an average household uses 14.000 kWh /year. Highly energy intense buildings are hospitals, ([Santamouris et al., 1994](#)) with an annual average energy consumption of 407 kWh/year / m². Hospitals are responsible for a heavy amount of energy demand due to 24/7 operation, using larger energy amount than a residence building ([Kolokotsa et al., 2012](#)). Moreover, reduction of the consumed thermal energy in buildings can be achieved by reducing the overall heat transfer coefficient of the building's cell (insulation, double windows), thus increasing the heat recovery from the air ventilation system. However, during summer, excessive natural ventilation cannot be considered, due to the high ambient temperatures. Natural ventilation of buildings during the daytime results in overheating problems, and should be avoided. Nonetheless, natural ventilation of health care buildings located in urban areas may pose additional problems in relation to indoor air quality and the strict health standards that should be maintained in such buildings ([Santamouris et al., 1994](#)). Therefore, several restrictions of ventilation plus energy savings from ventilation could raise the need for future use of photocatalytic building materials.

Discussion

Nanoengineering is the technique of manipulating the nanostructures to develop a new generation of multifunctional materials with extra high mechanical performances and durability. The application of nanomaterials in the building industry seems promising. Isolative materials have big environmental impact for construction purposes, which after the consideration of their energy saving (1/3 less energy use) enhances the functionality of conventional building materials, contributing to high energy savings. Photocatalytic nanomaterials can also contribute highly to the environmental and financial gains in the construction industry.

At a nanoscale, when synthesizing a photocatalyst several parameters should be paid attention to, in order to enhance its properties. The size of crystallites, the surface area, the porosity and the morphology are factors that affect highly the photocatalytic performance of a nanomaterial. From this research we concluded that crystallite size, surface area and porosity can increase with the increase of temperature and power. Especially for porosity, this is mainly affected positively by the increase of temperature rather than power increase. Temperature increase however, leads to higher agglomerations in the nanostructure. This aspect of agglomeration will be of our focus for photocatalytic BMs since it is a problem causing lower photocatalytic effect. Furthermore, power increase makes the nanostructures thinner and denser, therefore even bigger agglomerations than in the case of T increase are observed. On the other hand pH increase helps the nanostructures shape without the need of very high T and P (and without many agglomerations) and also similar nanoshapes are observed with the increase of stirring time. Therefore power increase could be substituted with higher stirring time, a procedure that is also more environmental friendly. From previous studies we expect that the effectiveness of nanoparticles increases with the increase of crystallite size (average size is preferable) surface area and porosity. In this case the increase of T and P could lead to more effective photocatalysts. On the other hand both P and T increase lead to higher agglomerations. From our research while conducting PL measurements we also concluded that higher oxygen vacancies are observed when P is increased and are lower as T increases. It is known that for higher photocatalytic efficiency more oxygen vacancies are desired, therefore the increase of power could be beneficial (see [Image 9](#)). Conducting a LCA on the different synthesis parameters in order

to have the highest surface area for a nanomaterials, we have concluded that high temperatures could sustainability improve ZnO nanostructures since they largely improve the surface areas, which can be useful for several applications in nanotechnology. Nonetheless ethanol use must be minimized and also the location of synthesis of nanomaterials plays a very important role, since renewable energy dependent countries would have a minimum environmental cost.

For a better photocatalyst the introduction of dopants is almost necessary. We have observed that doping increases average crystallite size due the fact that more distortions are being produced around the dopant ions and this leads to lattice expansion due to mismatch between ionic radii. The introduction of dopants affects the porosity and surface area and preferably leading to a smaller E band gap that could lead to the fabrication of visible light photocatalysts. Higher O vacancies lead to higher photocatalysis. More oxygen vacancies produce more recombination centers. Therefore more oxygen vacancies also yield more photocatalytic reactive centers and improve the photocatalytic activity for the sample ([Zhang et al., 2010](#)). Doping has appeared to increase the oxygen vacancies of our tested samples.

As already discussed several times, many factors contribute to the enhancement of the photocatalytic activity, among these lattice/surface defects are of great importance. Under light irradiation and absorption of photo energy, electrons are transferred from valance band to the conduction band therefore electron holes are being created. In the case of no defects in the crystalline, these photogenerated electro-holes have a very fast recombination rate in the bulk and also on the surface. On the surface the photogenerated electrons and holes initiate photo-redox reactions, with the electrons reducing electron acceptors and the holes oxidizing electron donors. In the case of high defects in the crystalline, the holes can be trapped by defects and may act as new centers for recombination. These trapped holes can react with electron donors enhancing the photocatalytic activity. It is clear that surface defect play an important role in the photocatalytic activity and creating more defects in a sample is a way to promote their effectiveness as photocatalysts ([Yan et al., 2013](#)). Nonetheless there is a correlation between the photocatalytic effectiveness of a sample and its lattice/surface ratio as shown in all XPS results. The higher photocatalytic results are met in the lower lattice/surface ratio; meaning that the amount of surface oxygen (oxygen vacancies, defect of hydroxyl radical) is recommended to be higher than oxygen found in the lattice.

Photocatalysts with higher overall O concentration have higher photocatalytic efficiency. Even in liquid solutions, the presence of dissolved oxygen is expected to enhance photocatalytic oxidation since oxygen traps the photogenerated conduction band electrons to form superoxide radical anions (Xekoukoulakis et al., 2011). It was observed, throughout all the samples tested that when hydroxyl radicals or surface oxygen (attributes to surface oxygen) is much higher in concentration than lattice oxygen, this contributes to enhance photocatalysis. When lower than lattice oxygen, the nanomaterials appear no photocatalytic activity. This was observed for both ZnO and TiO₂ samples (*Table 13*).

Table 13. Lattice /surface ratio calculated for most of the photocatalytic samples

	Lattice/ Surface (O _L /O _V)
ZnO pure	1.43
ZnO: Co	1.1
ZnO: Mn	4
ZnO: Cu	4.7
Anatase TiO ₂ : In	0.7
Anatase TiO ₂ : Al	0.7
Anatase TiO ₂ : Mn	1.12
Anatase TiO ₂ : Fe	1.1
Anatase TiO ₂ : Co	0.6
TCM	0.19
Undoped	0.35
P25	0.83
Crystal Global	0.90

The smaller the ratio the higher photocatalytic activity is expected, due to enhanced surface defects. Nonetheless, there is an observed optimum amount of surface defects; beyond this the photocatalytic activity seemed to decrease. This was due to the fact that photocatalytic performance is not only attributed to the high amount of hydroxyl radicals and oxygen defects but to other factors also, like total O amount, the amount of O in the lattice or the nitrogen concentration, which appears to enhance visible light photocatalysis.

Furthermore, the ammonia exposure provided information regarding the oxygen defects, which highly affect the photocatalytic activity. The ammonia lowered the amount of oxygen concentration (O_L+O_V) in all the samples. Due to oxygen decrease and in all samples we observed Ti^{4+} with a small contribution of Ti^{3+} due to an oxygen deficiency in the TiO_2 lattice. Ammonia increased the concentrations of hydroxyl group and oxygen vacancies (O_V) which enhanced photocatalytic performance. Nonetheless, samples with hydroxyl and oxygen vacancies smaller than the amount of oxygen in their lattice ($O_L/O_V > 1$) appear to have almost zero decolorization rate.

When incorporating nanomaterials inside BMs careful considerations must be taken into account for better dispersion but also for minimizing by-products development. Calcination offers a solution to common dispersion problems, since nanoparticles can grow on a BM. Treatment also increases surface area, crystallite size and porosity and also surface area and porosity of the BM too. However, high calcination of nanoparticles can lead to agglomeration of these nanoparticles. Therefore, there must be paid attention to the choice of the temperature. When heating a BM there is a possibility of alteration of their mechanical properties. Our results showed us that calcareous fillers and cement paint have changed under 700 °C treatment. Cement, on the other side, has remained unchanged. Calcined photocatalytic BM offer also higher adsorption rate and maybe higher photocatalytic rate, but this must be further studied. Lastly very important step is the choice of the matrix, not only for the good dispersion but it has been observed that industrial common calcareous filler and cementitious paint have some organic compounds which seem to interfere with the P25 photocatalyst and produce even higher amount of formaldehyde than it was before.

Parameters that affect the photocatalytic procedure are also humidity, the type of BMs, temperature and seasoning. Anatase TiO_2 is a better photocatalyst than ZnO , with In and Mn doped TiO_2 samples having higher degradation rate against pollutants (such as NO and Formaldehyde). An amount of 2 or 5-10% photocatalyst in BM, for bigger constructions is optimum. However the amount of photocatalyst should depend on the matrix used as it could be less for cement than for calcite based materials. In addition, calcination processes must be considered only after investigating possible gases production that can affect the environmental impacts of BMs.

From an environmental perspective, calcareous filler has the smallest footprint if compared to cement or cement paint. It was also observed that calcareous filler had the highest degradation rate therefore a Life Cycle Analysis was not considered necessary since the energy savings from calcareous photocatalytic materials would be of course higher than the other two BMs. On a larger scale of nanomaterials application in housing, it was calculated that innovative nanomaterials used in building industry are environmental intense materials, however, taking into account their energy gains makes them compensate environmentally within 1 year.

Conclusion & Recommendations

During this PhD Thesis the structural photocatalytic and environmental behavior of photocatalytic materials has been studied. The most common photocatalysts analyzed were the ZnO and TiO₂, and they were studied under different synthesis methods and parameterization of several conditions in order to enhance their photocatalytic activity.

Higher purity ZnO was achieved by high microwave power, or higher Temperature, and taking into account the higher surface area achieved, the increase of these parameters leads to lower environmental impacts since a high functioning nanomaterial can be synthesized. For the first time, the synthesis of the nanoparticles was assessed under a life cycle analysis tool. This critical procedure of nanotechnology, was identified to have several environmental weakness, like ethanol use which its excessive use should be avoided, and electricity source contributes highly since several processes of the synthesis use this source (for example oven use). Renewable energy technologies can minimize these environmental impacts with hydro and wind both claiming a reduction of ~25% and solar claiming a reduction of ~22%. Interestingly, it was found that increasing the autoclave's temperature has a positive effect on the ZnO nanostructures environmental sustainability, with 150 °C and 220 °C having a ~10% and ~41% lower total environmental footprint, compared to 90 °C. Also increased power has lower environmental footprint. Particularly the total environmental footprint of 310 W and 710 W is ~18% and ~27% lower than using 110 W. Therefore, when you want to synthesize a higher surface area nanomaterial, high microwave power results to decreased environmental footprint.

Moreover, energy saving with the use of isolative materials in scale of Demo houses, leads to ~57% lower environmental footprint during a 25 years life span. Therefore, even though the application of high energy materials (like PCMs and VIPs) leads to an upfront higher environmental cost, this can be compensated within just over a year, when energy consumption is taken into account, leading to improved environmental performance.

According to the BM incorporating photocatalytic nanomaterials it has been proven that the temperature increases pollutant level, which is also increased by the addition of any building material inside an area. The high surface area of cement makes all photocatalytic

cement based materials to absorb a huge amount of pollutants, therefore decreasing dramatically the pollution inside a house. In cement based materials calcination has already proved to not alter the characteristics of the cement therefore cement seems appropriate materials for this procedure. Photocatalytic results have also proven that calcined samples have higher degradation and adsorption rates than not calcined. However, not all matrices can undergo temperature treatment since this can alter their mechanical properties. Particularly T treatment alters calcite into lime, Portlandite and CO₂, and then with the water of the atmosphere, calcite is being recreated. On the other hand cement materials do not appear any alteration for T treatment of 700 °C, making this matrix very promising for solving the dispersion problems analyzed previously and a possible promising photocatalytic building material. The calcination has several benefits, it increases crystallinity of nanoparticles, it increases porosity and surface area both of the BM and the nanoparticle, and it appears to have better dispersion while causes also higher degradation of pollutants. These accounts mainly for cement, which remained unchanged under T treatment, therefore its mechanical properties did not show any difference, whereas in the case of calcareous filler and cement paint several changes are observed after calcination. Thus cement based nanomaterials would be a possible high effective photocatalyst BMs. Both calcareous filler and cement paint materials (especially cement paint) have a very high adsorption rate of pollutants and interestingly P25 reacts with the possible organic compounds found in these two BMs which are not present in cement. This is a crucial step since instead of a decrease of formaldehyde levels, a huge value (more than 1 ppm) was observed. Nonetheless the highest photocatalytic results (12%) are achieved under calcareous fillers incorporating TCM. Therefore in construction industry, the choice of the matrix that will incorporate the photocatalytic nanomaterial is a crucial step. Further studies should be made on the photocatalytic performance of calcined cement enhanced with photocatalytic nanomaterials.

Photocatalytic performance is enhanced by doping. We have observed that doping increases average crystallite size due the fact that more distortions are being produced around the dopant ions; it affects the porosity and surface area. Doping has appeared to increase the oxygen vacancies of our tested samples, increasing therefore their photocatalytic behavior. Co doped ZnO showed some photocatalytic behavior (~ 10%) under visible light. Indium and Aluminum doped TiO₂ samples had a good photocatalytic response (90% and 60%) under UV and Co doped TiO₂ under visible (30%). Also Mn doped TiO₂ incorporated in BM (12% in calcareous filler) under UV.

Another important parameter that was investigated was the ratio between lattice oxygen (corresponding to the oxygen bonded with the metal) to surface oxygen which corresponds to hydroxyl groups and oxygen vacancies in the crystalline, found by XPS measurements. Samples with hydroxyl and oxygen vacancies smaller than the amount of oxygen in their lattice ($O_L/O_V > 1$) appear to have almost zero photocatalytic activity. Therefore a smaller ratio could lead to higher photocatalytic effectiveness. This was observed during all our samples. Moreover in order to enhance oxygen vacancies, we exposed our samples to gaseous ammonia. This led to increased concentrations of hydroxyl group and oxygen vacancies (O_V) which enhanced photocatalytic performance. Indium doped sample appeared to have the highest photocatalytic activity. This could be attributed to the low lattice/surface rate and also to the high total amount of oxygen in the surface of the sample. Similar results are met in Al doped sample. In the In doped sample there is a 10% increase of the decolorization rate after NH_3 exposure. The In doped sample is also under visible light the most prominent possible photocatalyst as it decolorizes MB at a percentage of 60%.

The photocatalytic activity of the BMs was tested inside Demo houses, with some observations on pollutant decrease; however conclusion in that part were made from the big relation between humidity-temperature and indoor pollution and also the seasonal dependency of pollution, even in indoor environments. Particularly, temperature and humidity increase positively the indoor VOC levels. In smaller scale experiments, Calcareous was found to have a possible photocatalytic activity that increased after calcination. Nonetheless, cement paint and cement appeared to almost vanish the pollutant, maybe due to their high adsorption. However, further studies must be made in different parameters as regard to the photocatalytic activity of BMs and a further LCA should be conducted taking into account cement based materials mixed with Titania calcined at different temperatures.

Overall, one important characteristic of a photocatalyst in order to enhance its performance is the ratio O_L/O_V . It has been proved in this thesis that samples with hydroxyl and oxygen vacancies higher or slightly equal to the amount of oxygen in their lattice, appear to have higher photocatalytic performance.

Moreover, taking into account the synthesis of photocatalytic nanomaterials, ethanol use and electricity source should be paid attention to. Both lead to higher environmental impacts and can be replaced with other ways, without interfering with the nanomaterial's performance as a photocatalyst, contributing sustainably to the total energy savings of a construction. On the other hand temperature increase does not affect negatively the environmental performance of the nanomaterials, since this is a parameter which results to a higher performing photocatalyst, thus decreasing further the energy losses via ventilation.

In this research further building matrices than cement have been studied and proved to have higher photocatalytic response than cement. Calcareous filler is an environmental friendlier construction material which showed higher photocatalytic performance than cement. Nonetheless attention must be paid to the fact that some industrial photocatalysts can react with possible organic compounds found in the calcareous filler, leading to forbidden increase of pollution levels. Moreover cement has been proved to have significant high absorption rate of pollutants and in case of calcination of construction materials for better dispersion of nanomaterials only cement would make the most appropriate candidate, since it does not alter its characteristics under temperature treatments of 700 °C.

The real-time use of innovative technologies in the construction industry is proved with several years' data, to increase the energy gains of a Demo house through isolation, despite the high energy demand for their fabrication. However, a larger scale photocatalytic performance test bed is proved to be influenced by several parameters like humidity-temperature and indoor pollution and also the seasonal dependency of pollution, even in indoor environments.

References

- Alagarasi, A. (2011). Introduction to Nanomaterials.
- Al-Gaashani, R et al., XPS and optical studies of different morphologies of ZnO nanostructures prepared by microwave methods, Ceramics International (2012), <http://dx.doi.org/10.1016/j.ceramint.2012.08.075>
- Amin, G., Asif, M. H., Zainelabdin, A., Zaman, S., Nur, O., & Willander, M. (2011). Influence of pH, Precursor Concentration, Growth Time, and Temperature on the Morphology of ZnO Nanostructures Grown by the Hydrothermal Method. *Journal of Nanomaterials*, 2011, 1–9. <https://doi.org/10.1155/2011/269692>
- Baalousha, M., Yang, Y., Vance, M. E., Colman, B. P., McNeal, S., Xu, J., Hochella, M. F. (2016). Outdoor urban nanomaterials: The emergence of a new, integrated, and critical field of study. *Science of the Total Environment*, 557–558, 740–753. <https://doi.org/10.1016/j.scitotenv.2016.03.132>
- Baruah, S., & Dutta, J. (2009). pH-dependent growth of zinc oxide nanorods. *Journal of Crystal Growth*, 311(8), 2549–2554. <https://doi.org/10.1016/j.jcrysgr.2009.01.135>
- Bazant, P., Munster, L., Machovsky, M., Sedlak, J., Pastorek, M., Kozakova, Z., & Kuritka, I. (2014). Wood flour modified by hierarchical Ag/ZnO as potential filler for wood-plastic composites with enhanced surface antibacterial performance. *Industrial Crops and Products*, 62, 179–187. <https://doi.org/10.1016/j.indcrop.2014.08.028>
- Bernardo, H., Antunes, C. H., Gaspar, A., Pereira, L. D., & da Silva, M. G. (2016). An approach for energy performance and indoor climate assessment in a Portuguese school building. *Sustainable Cities and Society*, 30, 184–194. <https://doi.org/10.1016/j.scs.2016.12.014>
- Bertrand R., Arnaud P., Francois O., Laurent G., Laurent B., 2009 , TiO₂– containing cement pasted and mortars: Measurements of the photocatalytic efficiency using a rhodamine B-based colourimetric test”, Solar Energy, 83, 1794 – 1801, Elsevier Inc
- Binas, V. D., Sambani, K., Maggos, T., Katsanaki, A., & Kiriakidis, G. (2012). Synthesis and photocatalytic activity of Mn-doped TiO₂ nanostructured powders under UV and visible light. *Applied Catalysis B: Environmental*, 113–114, 79–86. <https://doi.org/10.1016/j.apcatb.2011.11.021>
- Binas, V., Kortidis, I., Gagaoudakis, E., Moschovis, K., & Kiriakidis, G. (2016). Ageing Resistant Indium Oxide Ozone Sensing Films. *Sensor Letters*, 14(6), 563–566. <https://doi.org/10.1166/sl.2016.3665>
- Binas, Sambani K., Maggos T., Katsanaki A., & Kiriakidis G. (2011). Synthesis and photocatalytic activity of Mn- doped TiO₂ nanostructured powders under UV and visible light. “*Applied Catalysis B, Environmental*,” 113–114(March 2015), 79–86. <https://doi.org/10.1016/j.apcatb.2011.11.021>
- Bystrzejewska-Piotrowska, G., Golimowski, J., & Urban, P. L. (2009). Nanoparticles: Their potential toxicity, waste and environmental management. *Waste Management*, 29(9), 2587–2595. <https://doi.org/10.1016/j.wasman.2009.04.001>
- Castell, A., Menoufi, K., de Gracia, A., Rincón, L., Boer, D., & Cabeza, L. F. (2013). Life Cycle Assessment of alveolar brick construction system incorporating phase change materials (PCMs). *Applied Energy*, 101, 600–608. <https://doi.org/10.1016/j.apenergy.2012.06.066>
- Chand, P., A. Gaur, A. Kumar“Structural and optical properties of ZnO nanoparticles synthesized at different pH values” Journal of Alloys and Compounds 539 (2012) 174–178.Chatzisymeon, E. et al., 2013. Life cycle assessment of advanced oxidation processes for olive mill wastewater treatment. *Journal of Cleaner Production*, 54(April 2017), pp.229–234. Available at: <http://dx.doi.org/10.1016/j.jclepro.2013.05.013>.
- Chatzisymeon, E., Foteinis, S., Mantzavinos, D., & Tsoutsos, T. (2013). Life cycle assessment of advanced oxidation processes for olive mill wastewater treatment. *Journal of Cleaner Production*, 54(April 2017),

229–234. <https://doi.org/10.1016/j.jclepro.2013.05.013>

Chen, J., Poon, C., 2009. Photocatalytic construction and building materials: From fundamentals to applications. *Building and Environment* 44: 1899–1906

Chen,W., Liang, H., Ren,W., Shao, L., Shu, J., Wang, Z., (2014). “Complex spinel titanate as an advanced anode material for rechargeable lithium-ion batteries”, *Journal of Alloys and Compounds* 611 65–73

Cho, S., Jung, S.-H., & Lee, K.-H. (2008). Morphology-controlled growth of ZnO nanostructures using microwave irradiation: from basic to complex structures, (3), 12769–12776. <https://doi.org/10.1021/jp803783s>

Colanguli, D., Calia, A., & Bianco, N. (2015). Novel multifunctional coatings with photocatalytic and hydrophobic properties for the preservation of the stone building heritage. *Construction and Building Materials*, 93, 189–196. <https://doi.org/10.1016/j.conbuildmat.2015.05.100>

de Gracia, A., Rincón, L., Castell, A., Jiménez, M., Boer, D., Medrano, M., & Cabeza, L. F. (2010). Life Cycle Assessment of the inclusion of phase change materials (PCM) in experimental buildings. *Energy and Buildings*, 42(9), 1517–1523. <https://doi.org/10.1016/j.enbuild.2010.03.022>

di Franza, R., Aligne, A., Weitzman, M., 2004. Prenatal and postnatal environmental tobacco smoke exposure and children's health. *Pediatrics* 113:1007-1015. Dai, L., X.L. Chen, W.J. Wang, T. Zhou, B.Q. Hu, J. Phys.: Condens. Matter 15 (2003)2221.

DOE, Department of the Environment, London, UK, 1993. Third Report of the United Kingdom Photochemical Oxidants Review Group, Published by: Institute of Terrestrial Ecology (Edinburgh Research Station)

Dutil, Y., Rousse, D., & Quesada, G. (2011). Sustainable buildings: An ever evolving target. *Sustainability*, 3(2), 443–464. <https://doi.org/10.3390/su3020443>

EU. (2010). Directive 2010/31/EU of the European Parliament and of the Council of 19 May 2010 on the energy performance of buildings (recast). *Official Journal of the European Union*, 13–35. https://doi.org/doi:10.3000/17252555.L_2010.153.eng

Farid, M. M., Khudhair, A. M., Razack, S. A. K., & Al-Hallaj, S. (2004). A review on phase change energy storage: Materials and applications. *Energy Conversion and Management*, 45(9–10), 1597–1615. <https://doi.org/10.1016/j.enconman.2003.09.015>

Frank, S. N., & Bard, A. J. (1977). *Journal of the American Chemical Society*, 99(1), 303-304.

Foteinis S., C. E. (2015). Life cycle assessment of organic versus conventional agriculture . A case study of lettuce cultivation in Greece. *Journal of Cleaner Production*, (September). <https://doi.org/10.1016/j.jclepro.2015.09.075>

Fujishima, A., Zhang, X., & Tryk, D. (2008). TiO₂ photocatalysis and related surface phenomena. *Journal of Photochemistry and Photobiology C: Photochemistry Reviews*, 63(12), 515–582. <https://doi.org/http://doi.org/10.1016/j.surfrep.2008.10.001>

Fujishima, A., D.A. Tryk, in: A.J. Bard, M. Stratmann, S. Licht (Eds.),2002 Encyclopedia of Electrochemistry, Vol. 6: Semiconductor Electrodes and Photoelectrochemistry, Weinheim.

Fujishima, A., Rao, T., & Tryk, D. (2000). Titanium dioxide photocatalysis. *Journal of Photochemistry and Photobiology C: Photochemistry Reviews*, 1(1), 1–21. [https://doi.org/http://doi.org/10.1016/S1389-5567\(00\)00002-2](https://doi.org/http://doi.org/10.1016/S1389-5567(00)00002-2)

Fujishima, A. K. Hashimoto, T. Watanabe, TiO₂ Photocatalysis: Fundamentals and Applications, BKC, Tokyo, 1999

Fujishima, A., Honda, K., 1972. Electrochemical Photolysis of Water at a Semiconductor Electrode. *Nature* 238: 37-38

Gagaoudakis, E., Kortidis, I., Michail, G., Tsagaraki, K., Binias, V., Kiriakidis, G., & Aperathitis, E. (2016). Study of low temperature rf-sputtered Mg-doped vanadium dioxide thermochromic films deposited

- on low-emissivity substrates. *Thin Solid Films*, 601, 99–105. <https://doi.org/10.1016/j.tsf.2015.11.007>
- George, S., Pokhrel, O.E. S., Xia, O.E. T., Gilbert, O.E. B., Ji, K. Z., Schowalter, M., ... Ma, L. (2010). Use of a Rapid Cytotoxicity Screening Approach To Engineer a Safer Zinc Oxide Nanoparticle through Iron Doping, (January). <https://doi.org/10.1021/nn901503q>
- Gercsi, Z., Sandeman, K. G., (2010). “Structurally driven metamagnetism in MnP and related Pnma compounds”, Physical Review, The American Physical Society, DOI:10.1103/PhysRevB.81.224426
- Gobakis, K., Kolokotsa, D., Maravelaki-Kalaitzaki, P., Lionakis, S., Perdikatis, V., & Santamouris, M. (2013). Development and analysis of inorganic coating for energy saving for buildings, in. *Proc of Joint Conference 34th AIVC- 3rd TightVent- 2nd Cool Roofs' - 1st Venticool*.
- Granqvist, C. G., Azens, A., Heszler, P., Kish, L. B., & Österlund, L. (2007). Nanomaterials for benign indoor environments: Electrochromics for “smart windows”, sensors for air quality, and photocatalysts for air cleaning. *Solar Energy Materials and Solar Cells*, 91(4), 355–365. <https://doi.org/10.1016/j.solmat.2006.10.011>
- Guo, T., Bai, Z., Wu, C., & Zhu, T. (2008). Influence of relative humidity on the photocatalytic oxidation (PCO) of toluene by TiO₂ loaded on activated carbon fibers: PCO rate and intermediates accumulation. *Applied Catalysis B: Environmental*, 79(2), 171–178. <https://doi.org/10.1016/j.apcatb.2007.09.033>
- Hapeshi, A. Achilleos, M.I. Vasquez, C. Michael, N.P. Xekoukoulakis, D. Mantzavinos, D. Kassinos, 2009. Drugs degrading photocatalytically: Kinetics and mechanisms of of loxacin and atenolol removal on Titania suspensions. <http://doi.org/10.1016/j.watres.2009.11.044>
- Hassan, M. M., Asce, M., Dylla, H., & Asadi, S. (2016). Laboratory Evaluation of Environmental Performance of Photocatalytic Titanium Dioxide Warm-Mix Asphalt Pavements Laboratory Evaluation of Environmental Performance of Photocatalytic Titanium Dioxide Warm-Mix Asphalt Pavements, (March). [https://doi.org/10.1061/\(ASCE\)MT.1943-5533.0000408](https://doi.org/10.1061/(ASCE)MT.1943-5533.0000408)
- Heinlaan, M., Ivask, A., Blinova, I., Dubourguier, H., & Kahru, A. (2008). Toxicity of nanosized and bulk ZnO , CuO and TiO₂ to bacteria Vibrio fischeri and crustaceans Daphnia magna and Thamnocephalus platyurus, 71, 1308–1316. <https://doi.org/10.1016/j.chemosphere.2007.11.047>
- Hischier, R., & Walser, T. (2012). Life cycle assessment of engineered nanomaterials: State of the art and strategies to overcome existing gaps. *Science of the Total Environment*, 425, 271–282. <https://doi.org/10.1016/j.scitotenv.2012.03.001>
- Hu, C., Lu, T., Chen, F., & Zhang, R. (2013). A brief review of graphene–metal oxide composites synthesis and applications in photocatalysis. *Journal of the Chinese Advanced Materials Society*, 1(1), 21–39. <https://doi.org/10.1080/22243682.2013.771917>
- Huang, B., Xing, K., & Pullen, S. (2015). Energy and carbon performance evaluation for buildings and urban precincts : review and a new modelling concept. *Journal of Cleaner Production*, 1–12. <https://doi.org/10.1016/j.jclepro.2015.12.008>
- Ioannou-ttofa, L., Fotinis, S., Chatzisymeon, E., & Fatta-kassinos, D. (2016). Science of the Total Environment The environmental footprint of a membrane bioreactor treatment process through Life Cycle Analysis. *Science of the Total Environment*, The, 568, 306–318. <https://doi.org/10.1016/j.scitotenv.2016.06.032>
- IPCC, 2014. Climate Change 2014: Synthesis Report. Contribution of Working Groups I, II and III to the Fifth Assessment Report of the Intergovernmental Panel on Climate Change, Core Writing Team, R.K. Pachauri and L.A. Meyer. <http://dx.doi.org/10.1017/CBO9781107415324.004>.
- ISO 14040:2006. (2016). ISO 14040_2006(en), Environmental management — Life cycle assessment — Principles and framework.
- ISO 14044:2006. (2006). ISO 14044_2006 - Environmental management -- Life cycle assessment -- Requirements and guidelines.

- Jamthe, A. DP Agrawal, 2013, Approaches for energy harvesting and power management in wireless healthcare sensor networks. *International Journal of Computer and Communication Engineering* 2 (5), 596
- Jerrett, M., et al., 2005. Spatial analysis of air pollution and mortality in Los Angeles. *Epidemiology*, 16: 727–736.
- Jiang, L., Li, G., Ji, Q., & Peng, H. (2007). Morphological control of flower-like ZnO nanostructures. *Materials Letters*, 61(10), 1964–1967. <https://doi.org/10.1016/j.matlet.2006.07.167>
- Kajbafvala, A., Samberg, J. P., Ghorbani, H., Kajbafvala, E., & Sadrnezhaad, S. K. (2012). Effects of initial precursor and microwave irradiation on step-by-step synthesis of zinc oxide nano-architectures. *Materials Letters*, 67(1), 342–345. <https://doi.org/10.1016/j.matlet.2011.09.106>
- Kalantar-zadeh, F. (2008). Chapter 5 : Characterization Techniques for Nanomaterials. In *Nanotechnology-Enabled Sensors* (pp. 211–281).
- Kamat, P.V Chem. Rev. 93 (1993) 267. 5] A. Heller, Acc. Chem. Res. 28 (1995) 503–508.
- Kaneva, N. V., Dimitrov, D. T., & Dushkin, C. D. (2011). Effect of nickel doping on the photocatalytic activity of ZnO thin films under UV and visible light. *Applied Surface Science*, 257(18), 8113–8120. <https://doi.org/10.1016/j.apsusc.2011.04.119>
- Kashif, M., Hashim, U., Ali, M. E., Usman Ali, S. M., Rusop, M., Ibupoto, Z. H., & Willander, M. (2012). Effect of different seed solutions on the morphology and electrooptical properties of ZnO Nanorods. *Journal of Nanomaterials*, 2012. <https://doi.org/10.1155/2012/452407>
- Kim K., Shamin A.J., Lee J.T., 2011, “Exposure to Formaldehyde and Its Potentials Human Health Hazards”, Jornal of Environmental Science and Health, Part C, 29, 277-299, Published by Taylor and Francis Group.
- Kiriakidis, G. & Binas, V. Journal of the Korean Physical Society (2014) 65: 297. doi:10.3938/jkps.65.297
- Kiriakidis, G., Moschovis, K., Kortidis, I., & Binas, V. (2012). Ultra-low gas sensing utilizing metal oxide thin films. *Vacuum*, 86(5), 495–506. <https://doi.org/10.1016/j.vacuum.2011.10.013>
- Kolokotsa, D. (2017). Smart cooling systems for the urban environment. Using renewable technologies to face the urban climate change. *Solar Energy*. <https://doi.org/10.1016/j.solener.2016.12.004>
- Kolokotsa, D. Tsoutsos, T and Papantoniou, S.. 2012 Energy conservation techniques for hospital buildings. *Advances In Building Energy Research* Vol. 6 , Iss. 1
- Kolokotsa, D., Rovas, D., Kosmatopoulos, E., Kalaitzakis, K., 2011. A roadmap towards intelligent net zero- and positive-energy buildings. *Sol. Energy* 85, 3067–3084.
- Koutantou, V., Kostadima, M., Chatzisymeon, E., Frontistis, Z., Binas, V., Venieri, D., & Mantzavinos, D. (2013). Solar photocatalytic decomposition of estrogens over immobilized zinc oxide. *Catalysis Today*, 209, 66–73. <https://doi.org/10.1016/j.cattod.2012.11.004>
- Kriedemann, B., & Fester, V. (2015). Critical process parameters and their interactions on the continuous hydrothermal synthesis of ironoxide nanoparticles. *Chemical Engineering Journal*, 281, 312–321. <https://doi.org/10.1016/j.cej.2015.05.115>
- Kroll, A., Pillukat, M. H., Hahn, D., & Schnekenburger, J. (2009). Current in vitro methods in nanoparticle risk assessment : Limitations and challenges. *European Journal of Pharmaceutics and Biopharmaceutics*, 72(2), 370–377. <https://doi.org/10.1016/j.ejpb.2008.08.009>
- Kurapati S. (2014). Nanomaterials for Concrete Technology. *International Journal of Civil, Structural, Environmental and Infrastructure Engineering Research and Development (IJCSEIERD)*, 4(3), 79–90. Retrieved from <http://www.tjprc.org/view-archives.php?year=2014&jtype=2&id=26&details=archives>
- Kundu T.K., NantuKarak , PuspenderBarik , SatyajitSaha, NCRAMT|June 24-26, 2011 |Haldia, India International Journal of Soft Computing and Engineering (IJSCE) ISSN: 2231-2307, Volume-1,

- Liddament, M., & Orme, M. (1998). Energy and ventilation. *Applied Thermal Engineering*, 18(11), 1101–1109. [https://doi.org/10.1016/S1359-4311\(98\)00040-4](https://doi.org/10.1016/S1359-4311(98)00040-4)
- Maravelaki, N., Verganelaki, A., Kilikoglou, V., & Karatasios, I. (2015). Synthesis and Characterization of a Calcium Oxalate-Silica Nanocomposite for Stone Conservation. In G. Lollino et al. (Ed.), *Engineering Geology for Society and Territory - Volume 8: Preservation of Cultural Heritage* (Vol. 8, pp. 1–584). Springer International Publishing Switzerland 2015. <https://doi.org/10.1007/978-3-319-09408-3>
- Maravelaki-Kalaitzaki, P., Bakolas, A., Karatasios, I., & Kilikoglou, V. (2005). Hydraulic lime mortars for the restoration of historic masonry in Crete. *Cement and Concrete Research*, 35(8), 1577–1586. <https://doi.org/10.1016/j.cemconres.2004.09.001>
- Mills, A., S. LeHunte, J. Photochem. Photobiol. A: Chem. 108 (1997) 1–35.
- Mhlongo, G. H., Motaung, D. E., Nkosi, S. S., Swart, H. C., Malgas, G. F., Hillie, K. T., & Mwakikunga, B. W. (2014). Temperature-dependence on the structural, optical, and paramagnetic properties of ZnO nanostructures. *Applied Surface Science*, 293, 62–70. <https://doi.org/10.1016/j.apsusc.2013.12.076>
- Mudimela, P. R., Nasibulina, L. I., Nasibulin, A. G., Cwirzen, A., Valkeapää, M., Habermehl-Cwirzen, K., Kauppinen, E. I. (2009). Synthesis of carbon nanotubes and nanofibers on silica and cement matrix materials. *Journal of Nanomaterials*, 2009. <https://doi.org/10.1155/2009/526128>
- Mukhopadhyaya, P., Maclean, D., Korn, J., Reenen, D. Van, & Molleti, S. (2014). Building application and thermal performance of vacuum insulation panels (VIPs) in Canadian subarctic climate. *Energy & Buildings*, 85, 672–680. <https://doi.org/10.1016/j.enbuild.2014.08.038>
- National Institute of Standards and Technology (NIST) X-ray Photoelectron Spectroscopy Database, Version 4.1 ,Alexander V. Naumkin, Anna Kraut-Vass, Stephen W. Gaarenstroom, and Cedric J. Powell Nolte, I. & Strong, D., 2011. *Europe 's buildings under the microscope* B. P. I. E. (BPIE), ed.
- Nolte, I., & Strong, D. (2011). *Europe 's buildings under the microscope*. (B. P. I. E. (BPIE), Ed.).
- Nozik, A. J., Beard, M. C., Luther, J. M., Law, M., Ellingson, R. J., & Johnson, J. C. (2010). Semiconductor quantum dots and quantum dot arrays and applications of multiple exciton generation to third-generation photovoltaic solar cells. *Chemical Reviews*, 110(11), 6873–6890. <https://doi.org/10.1021/cr900289f>
- Ohno, T., Sarukawa, K., Tokieda, K., Matsumura, M., 2001. Morphology of a TiO₂ Photocatalyst (Degussa, P-25) Consisting of Anatase and Rutile Crystalline Phases. Research Center for Solar Energy Chemistry 203: 560–8531.
- Ollis, D.F., C. R. Acad. Sci. Paris, Serie IIC, Chim. 3 (2000) 405–411.
- Ollis, D.F. H. Al-Ekabi (Eds.), Photocatalytic Purification and Treatment of Water and Air, Elsevier, Amsterdam, 1993.
- Orme, M. (2001). Estimates of the energy impact of ventilation and associated financial expenditures. *Energy and Buildings*, 33(3), 199–205. [https://doi.org/10.1016/S0378-7788\(00\)00082-7](https://doi.org/10.1016/S0378-7788(00)00082-7)
- Pacheco-Torgal, F., & Jalali, S. (2011). Nanotechnology: Advantages and drawbacks in the field of construction and building materials. *Construction and Building Materials*, 582–590.
- Panagopoulou, M., Gagaoudakis, E., Boukos, N., Aperathitis, E., Kiriakidis, G., Tsoukalas, D., & Raptis, Y. S. (2016). Thermochromic performance of Mg-doped VO₂ thin films on functional substrates for glazing applications. *Solar Energy Materials and Solar Cells*, 157, 1004–1010. <https://doi.org/10.1016/j.solmat.2016.08.021>
- Papadaki, D., Fotinis, S., G.H. Mhlongo, S.S. Nkosi, D.E. Motaung, S.S. Ray, T. Tsoutsos, and G. Kiriakidis. 2017. “Life Cycle Assessment of Facile Microwave-Assisted Zinc Oxide (ZnO) Nanostructures.” *Science of The Total Environment*. Elsevier. doi:10.1016/j.scitotenv.2017.02.019.
- Papadaki, D., Binas, V., S. Fotinis, T. Tsoutsos, G. Kiriakidis. “Life cycle assessment for demo-houses

utilizing phase change materials and vacuum insulation panels” 3rd International Exergy, Life Cycle Assessment, and Sustainability Workshop & Symposium, 2013, (ELCAS-3), Oral presentation

- Papadimitriou, V. C., Stefanopoulos, V. G., Romanias, M. N., Papagiannopoulos, P., Sambani, K., Tudose, V., & Kiriakidis, G. (2011). Determination of photo-catalytic activity of un-doped and Mn-doped TiO₂ anatase powders on acetaldehyde under UV and visible light. *Thin Solid Films*, 520(4), 1195–1201. <https://doi.org/10.1016/j.tsf.2011.07.073>
- Phan, T.L., Yu, S.C., Vincent, R., Bui, H.M., Thanh, T.D., Lam, V.D., Lee, Y.P., (2010). “Influence of Mn doping on structural, optical, and magnetic properties of Zn_{1-x}Mn_xO nanorods”, *J. Appl. Phys.* 108, 044910 (2010); <http://dx.doi.org/10.1063/1.3478709>
- Pelizzetti, E., N. Serpone Homogeneous and Heterogeneous Photocatalysis, D. Reidel Publishing Company, Dordrecht, 1986.
- Peral, J X. Domènech, D.F. Ollis, *J. Chem. Tech. Biotech.* 70 (1997) 117–140.
- Piccinno, F., & Gottschalk, F. (2012). Industrial production quantities and uses of ten engineered nanomaterials in Europe and the world. <https://doi.org/10.1007/s11051-012-1109-9>
- Rana, A. K., Rana, S. B., Kumari, A., & Kiran, V. (2009). Significance of Nanotechnology in Construction Engineering. *International Journal of Recent Trends in Engineering*, 1(4), 6–8. Retrieved from <http://ijrte.academypublisher.com/vol01/no04/ijrte0104046048.pdf>
- Ray, S. S., & Bousmina, M. (2005). Biodegradable polymers and their layered silicate nanocomposites: In greening the 21st century materials world. *Progress in Materials Science*, 50(8), 962–1079. <https://doi.org/10.1016/j.pmatsci.2005.05.002>
- Rajendar, V., Venkateswara, K.R., Shobhan, K., Shilpa Chakra, C.H., (2012). “Effect of Co Doping on Structural and Magnetic Properties of ZnO Nanoparticles Synthesized by Novel Combustion Synthesis”, *Journal of Nano and electronic physics*, Vol.5 No1, 01022.
- Reinikainen, J., 2003. Significance of humidity and temperature on skin and upper airway symptoms. *Indoor Air* 13:344–352
- Ridhuan, N.S., K.A. Razak, Z. Lockman, A.A. Aziz, *PLoS ONE* 7 (2012) e50405.
- Sanchez, F., & Sobolev, K. (2010). Nanotechnology in concrete - A review. *Construction and Building Materials*, 24(11), 2060–2071. <https://doi.org/10.1016/j.conbuildmat.2010.03.014>
- Santamouris, M., Dascalaki, E., Balaras, C., Argiriou, A., & Gaglia, A. (1994). Energy performance and energy conservation in health care buildings in hellas. *Energy Conversion and Management*, 35(4), 293–305. [https://doi.org/10.1016/0196-8904\(94\)90062-0](https://doi.org/10.1016/0196-8904(94)90062-0)
- Salthammer, T., Mentese, S., Marutzky, R., 2010. Formaldehyde in the indoor environment. *Chemical Reviews* 110:2536–2572.
- Sarkar, S., Bhattacharjee, C., & Curcio, S. (2015). Studies on adsorption, reaction mechanisms and kinetics for photocatalytic degradation of CHD, a pharmaceutical waste. *Ecotoxicology and Environmental Safety*, 121, 154–163. <https://doi.org/10.1016/j.ecoenv.2015.04.036>
- Serpone, N E. Pelizzetti (Eds.), *Photocatalysis — Fundamentals and Applications*, John Wiley & Sons, New York, 1989.
- Singh, A. K., & Nakate, U. T. (2013). Photocatalytic Properties of Microwave-Synthesized TiO₂ and ZnO Nanoparticles Using Malachite Green Dye, 2013.
- Shakti, N., Gupta, P., (2010). “Structural and optical properties of sol-gel prepared ZnO thin film”. *Appl. Phys. Res.* 2(1), 19
- Shiraishi F., Nomura T., Yamaguchi S., Ohbuchi Y., 2007, “Rapid removal of trave HCHO from indoor air by an air purifier consisting of a continuous concentrator and photocatalytic reactor and its computer simulation”, *Chemical Engineering Journal*, 127. 157-165, Elsevier Inc

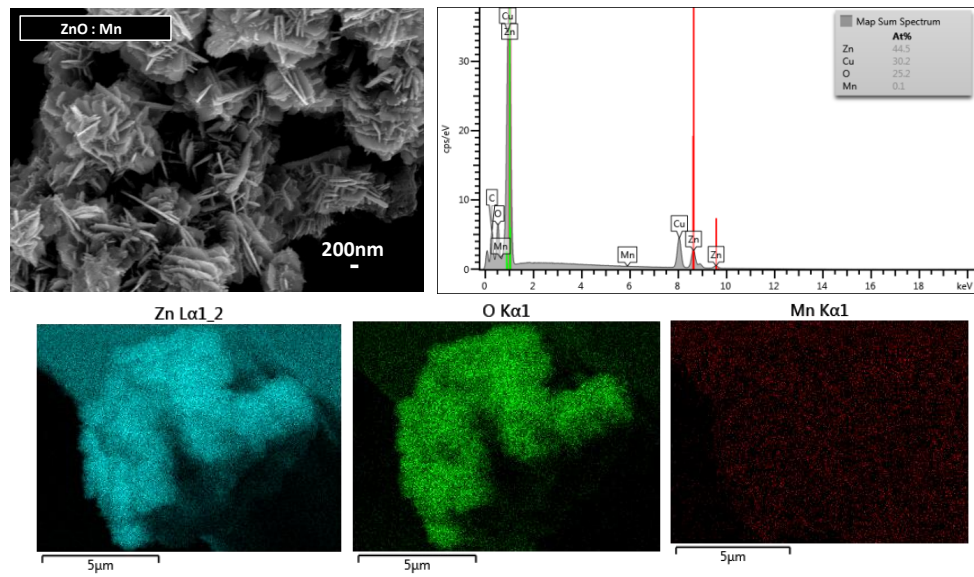
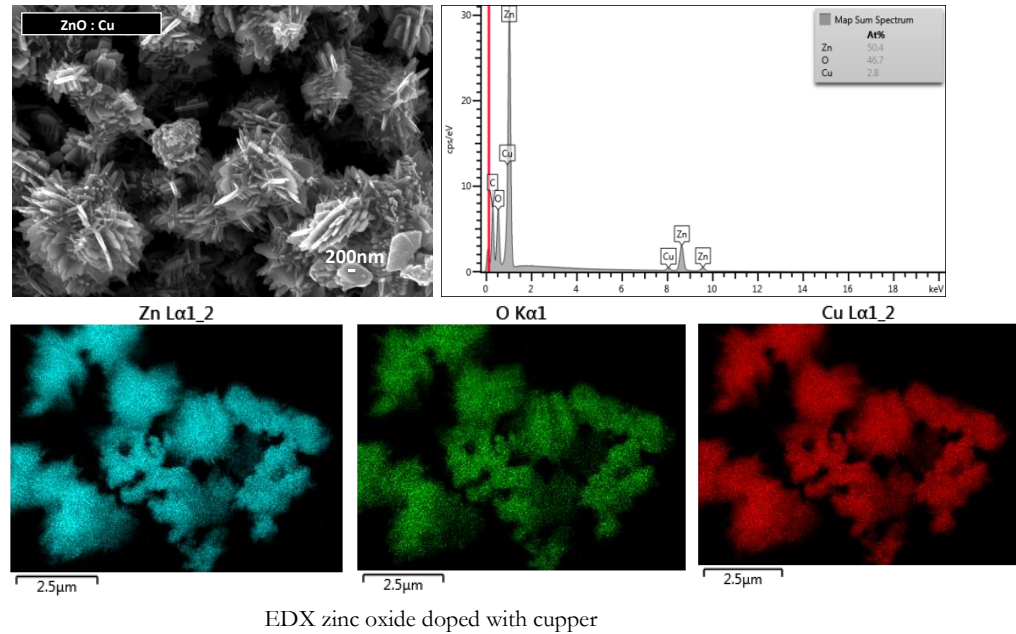
- Sirelkhatim, A., Mahmud, S., Seen, A., Kaus, N. H. M., Ann, L. C., Bakhori, S. K. M., Mohamad, D. (2015). Review on zinc oxide nanoparticles: Antibacterial activity and toxicity mechanism. *Nano-Micro Letters*, 7(3), 219–242. <https://doi.org/10.1007/s40820-015-0040-x>
- Slotte, M., Metha, G., & Zevenhoven, R. (2015). Life cycle indicator comparison of copper , silver , zinc and aluminum nanoparticle production through electric arc evaporation or chemical reduction. *International Journal of Energy and Environmental Engineering*, 233–243. <https://doi.org/10.1007/s40095-015-0171-3>
- Smith, G. B., Granqvist, C. G., & Press, C. R. C. (2011). Green Nanotechnology : Solutions for Sustainability and Energy in the Built Environment. *Review Literature And Arts Of The Americas*. <https://doi.org/10.1117/1.3562980>
- Stephan, A., & Stephan, L. (2016). Life cycle energy and cost analysis of embodied, operational and user-transport energy reduction measures for residential buildings. *Applied Energy*, 161(February), 445–464. <https://doi.org/10.1016/j.apenergy.2015.10.023>
- Stone, V., Nowack, B., Baun, A., van den Brink, N., von der Kammer, F., Dusinska, M., ... Fernandes, T. F. (2010). Nanomaterials for environmental studies: Classification, reference material issues, and strategies for physico-chemical characterisation. *Science of the Total Environment*, 408(7), 1745–1754. <https://doi.org/10.1016/j.scitotenv.2009.10.035>
- Su, X., Luo, Z., Li, Y., & Huang, C. (2016). Life cycle inventory comparison of different building insulation materials and uncertainty analysis. *Journal of Cleaner Production*, 112, 275–281. <https://doi.org/10.1016/j.jclepro.2015.08.113>
- Tsoutsos, T., Tournaki, S., Santos, C. A. de, & Vercellotti, R. (2013). Nearly Zero Energy Buildings Application in Mediterranean Hotels. *Energy Procedia*, 42, 230–238. <https://doi.org/10.1016/j.egypro.2013.11.023>
- Tryk, D.A., A. Fujishima, K. Honda, *Electrochim. Acta* 45 (2000) 2363–2376
- Tyagi, V. V., & Buddhi, D. (2007). PCM thermal storage in buildings: A state of art. *Renewable and Sustainable Energy Reviews*, 11(6), 1146–1166. <https://doi.org/10.1016/j.rser.2005.10.002>
- U.S. Energy Information Administration. (2015). U.S. Energy Information Administration, 2015(October 2014), 1–11.
- Venieri, D., Fragedaki, A., Kostadima, M., Chatzisymeon, E., Binas, V., Zachopoulos, A., ... Mantzavinos, D. (2014). Solar light and metal-doped TiO₂ to eliminate water-transmitted bacterial pathogens: Photocatalyst characterization and disinfection performance. *Applied Catalysis B: Environmental*, 154–155, 93–101. <https://doi.org/10.1016/j.apcatb.2014.02.007>
- Vanheusden, K., W.L. Warren, C.H. Seager, D.R. Tallant, J.A. Voigt, and B.E. Gnade Mechanisms behind green photoluminescence in ZnO phosphor powders, *J. Appl. Phys.* 79, 1996, pp. 7983-7990.
- Zhang, W.C., X.L. Wu, H.T. Chen, J. Zhu, and G.S. Huang, Excitation wavelength dependence of the visible photoluminescence from amorphous ZnO granular films, *J. Appl. Phys.* 103, 2008, pp. 093718-093722. Wagner, C.D., L.H. Gale, R.H. Raymond, Two-dimensional chemical state plots: a standardized data set for use in identifying chemical states by X-ray photoelectron spectroscopy, *Analytical Chemistry* 51 (1979) 466–482.
- Wan J.J., Jang Y.S., 2009, “The effect of environmental and structural factors on indoor air quality of apartments in Korea”, *Building and Environment*, 44, 1794-1802, Elsevier Inc.
- Wang, F., Yang, L., Wang, H., & Yu, H. (2015). Facile preparation of photocatalytic exposed aggregate concrete with highly efficient and stable catalytic performance. *CHEMICAL ENGINEERING JOURNAL*, 264, 577–586. <https://doi.org/10.1016/j.cej.2014.11.129>
- Wang, X., Du, Y., & Luo, J. (2008). activity Biopolymer / montmorillonite nanocomposite : preparation , drug-controlled release property and cytotoxicity, 7pp. <https://doi.org/10.1088/0957-4484/19/6/065707>

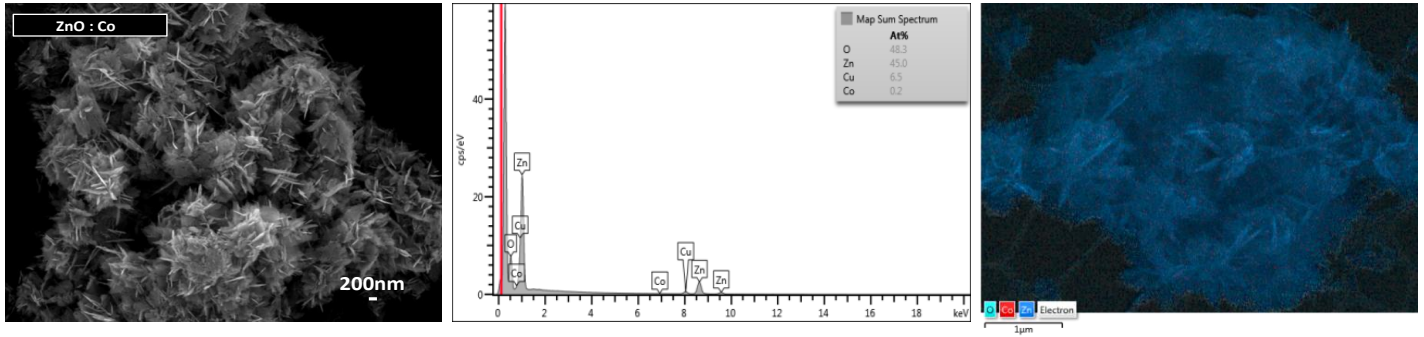
- Wang, Y., Li, X., Wang, N., Quan, X., & Chen, Y. (2008). Controllable synthesis of ZnO nanoflowers and their morphology-dependent photocatalytic activities. *Separation and Purification Technology*, 62(3), 727–732. <https://doi.org/10.1016/j.seppur.2008.03.035>
- Wisthaler, A., et al., 2008. Intercomparison of formaldehyde measurements at the atmosphere simulation chamber SAPHIR. *Atmospheric Chemistry and Physics*, 8:2189–2200.
- World Health organization, WHO, 2014. Retrieved from: http://www.euro.who.int/__data/assets/pdf_file/0006/298482/Health-risk-assessment-air-pollution-General-principles-en.pdf?ua=1 «Health risk assessment of air pollution».
- Xekoukoulakis, N. P., Drosou, C., Brebou, C., Chatzisymeon, E., Hapeshi, E., Fatta-Kassinos, D., & Mantzavinos, D. (2011). Kinetics of UV-A/TiO₂ photocatalytic degradation and mineralization of the antibiotic sulfamethoxazole in aqueous matrices. *Catalysis Today*, 161(1), 163–168. <https://doi.org/10.1016/j.cattod.2010.09.027>
- Xekoukoulakis, N. P., Xinidis, N., Chroni, M., Mantzavinos, D., Venieri, D., Hapeshi, E., & Fatta-Kassinos, D. (2010). UV-A/TiO₂ photocatalytic decomposition of erythromycin in water: Factors affecting mineralization and antibiotic activity. *Catalysis Today*, 151(1–2), 29–33. <https://doi.org/10.1016/j.cattod.2010.01.040>
- Xiangdong Gao, Xiaomin Li, A., & Yu, W. (2005). Flowerlike ZnO Nanostructures via Hexamethylenetetramine-Assisted Thermolysis of Zinc–Ethylenediamine Complex. *The Journal of Physical Chemistry B*. Retrieved from <http://pubs.acs.org/doi/abs/10.1021/jp046267s#.WIC-mTepFc8.mendeley>
- Xiong, D., Fang, T., Yu, L., Sima, X., & Zhu, W. (2011). Effects of nano-scale TiO₂, ZnO and their bulk counterparts on zebra fish: Acute toxicity, oxidative stress and oxidative damage. *Science of the Total Environment*, 409(8), 1444–1452. <https://doi.org/10.1016/j.scitotenv.2011.01.015>
- Xu, J., Shi, S., Li, L., Zhang, X., Wang, Y., Shi, Q., Wang, H. (2013). Luminescence Properties of Cobalt-Doped ZnO Films Prepared by Sol-Gel Method. *Journal of Electronic Materials*, 42(12), 3438–3444. <https://doi.org/10.1007/s11664-013-2719-4>
- Yan, J., Wu, G., Guan, N., Li, L., Li, Z., & Cao, X. (2013). Understanding the effect of surface/bulk defects on the photocatalytic activity of TiO₂: anatase versus rutile. *Physical Chemistry Chemical Physics : PCCP*, 15(26), 10978–88. <https://doi.org/10.1039/c3cp50927c>
- Zacharakis, A., Chatzisymeon, E., Binas, V., Frontistis, Z., Venieri, D., & Mantzavinos, D. (2013). Solar Photocatalytic Degradation of Bisphenol A on Immobilized ZnO or TiO₂, 2013, 1–10.
- Zalba B, Marin JM, Cabeza LF, & Mehling H. (2003). Review on thermal energy storage with phase change: materials, heat transfer analysis and applications. *Applied Thermal Engineering*, 23, 251–83.
- Zhao Y., Jung H.S., Jonathan R.W., 2003, “Auto regulation in the Biosynthesis of Ribosome’s”, Molecular and Cellular Biology, 23, 699-707, American Society For microbiology.
- Zhang, W. C., Wu, X. L., Chen, H. T., Zhu, J., & Huang, G. S. (2008). Excitation wavelength dependence of the visible photoluminescence from amorphous ZnO granular films. *Journal of Applied Physics*, 103(9), 0–5. <https://doi.org/10.1063/1.2924421>
- Zhang, X., Qin, J., Xue, Y., Yu, P., Zhang, B., Wang, L., & Liu, R. (2014). Effect of aspect ratio and surface defects on the photocatalytic activity of ZnO nanorods. *Scientific Reports*, 4, 4596. <https://doi.org/10.1038/srep04596>
- Zhang, Y., Zhou, G., Lin, K., Zhang, Q., & Di, H. (2007). Application of latent heat thermal energy storage in buildings: State-of-the-art and outlook. *Building and Environment*, 42(6), 2197–2209. <https://doi.org/10.1016/j.buildenv.2006.07.023>

Appendix

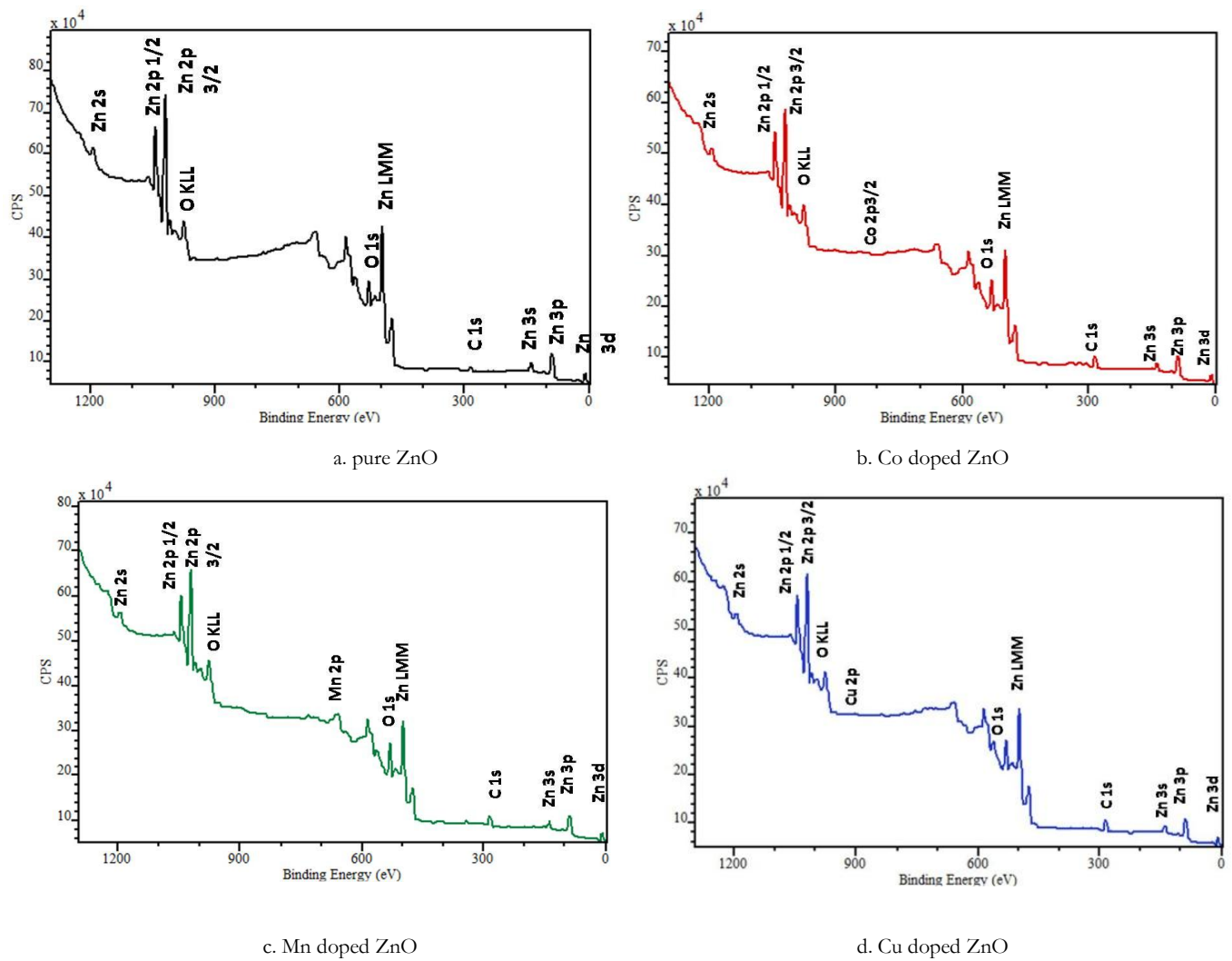
Supplementary for ZnO Doped series

SEM- EDX

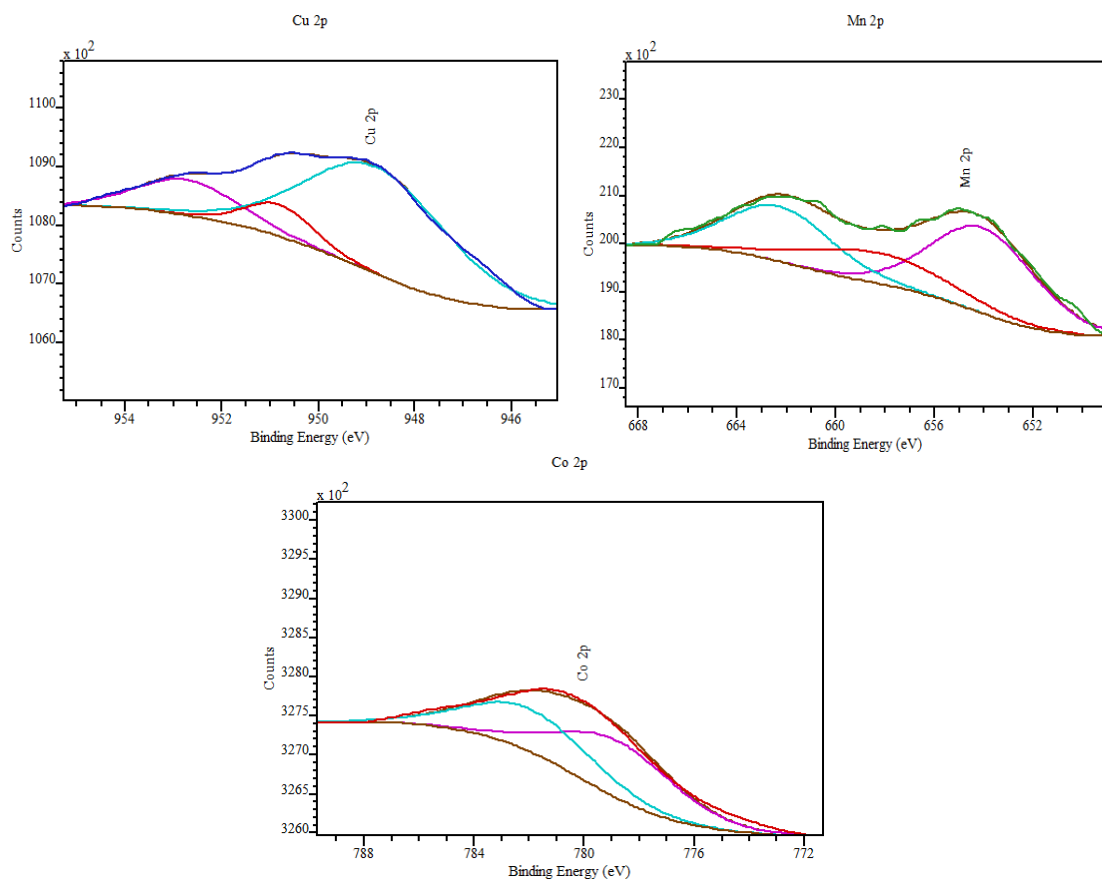




EDX zinc oxide doped with cobalt.

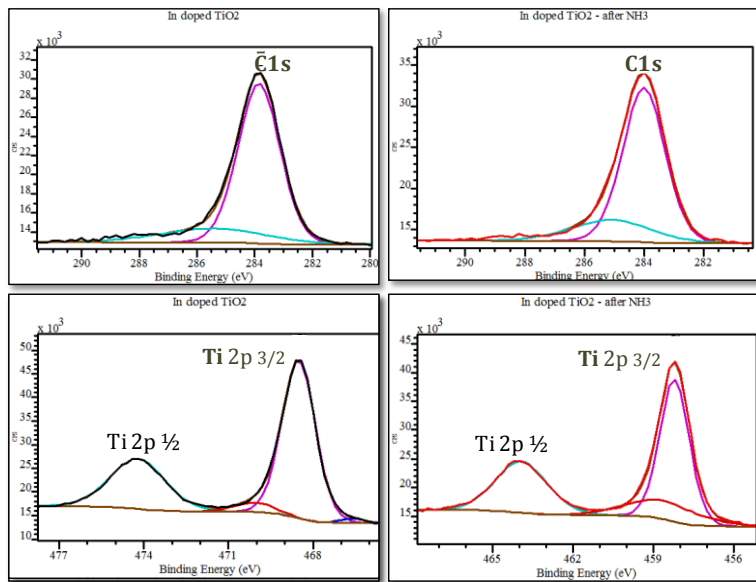


XPS spectra **a)** pure ZnO, **b)** Co doped ZnO, **c)** Mn doped ZnO, **d)** Cu doped ZnO.

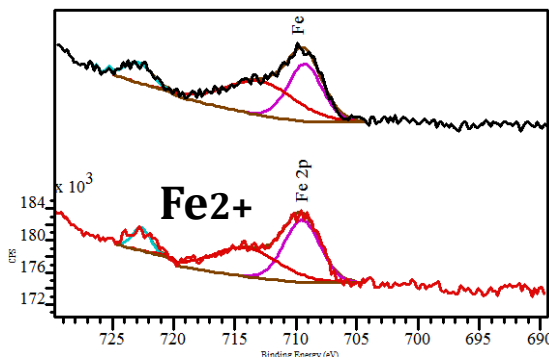


XPS high resolution spectra of (a) Cu 2p, (b) Mn 2p and (c) Co 2p.

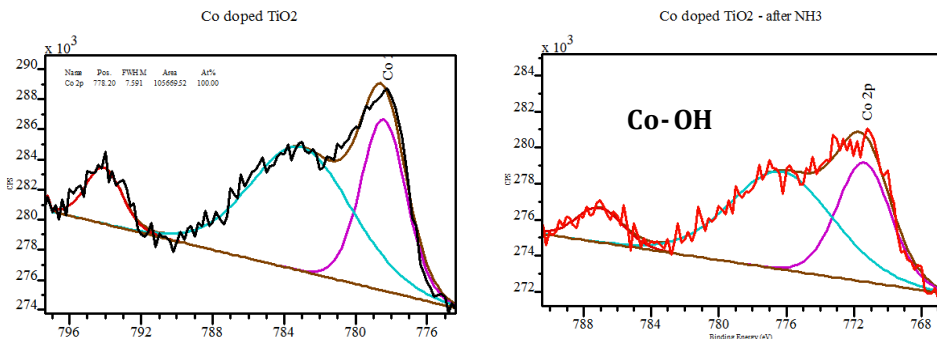
Ammonia exposed Samples



Fe doped TiO2



after NH₃

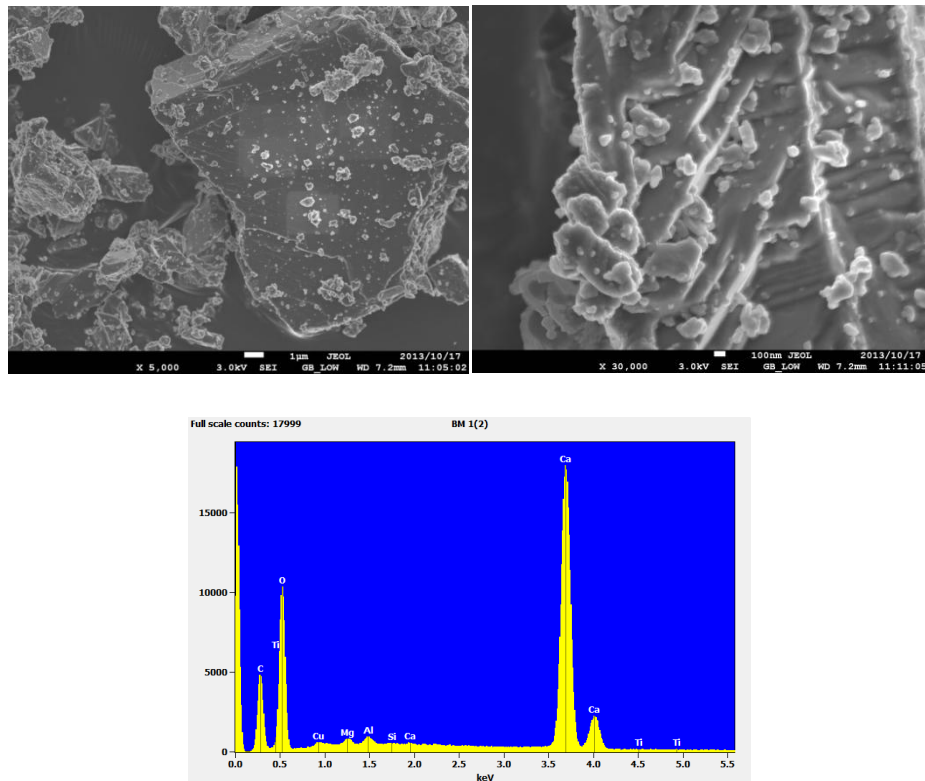


Building Materials

BULK	BM76	TCM
	BM78	undoped
	BM77	P25
	BM79	Crystal Global
	BM73	calcareous filler
	BM74	cement paint
	BM75	cement
CALCAREOUS FILLERS	BM1	calcareous filler & 0.2% TCM- RT
	BM2	calcareous filler & 1% TCM- RT
	BM3	calcareous filler & 2% TCM- RT
	BM4	calcareous filler & 0.2% TCM 700°C
	BM5	calcareous filler & 1% TCM 700°C
	BM6	calcareous filler & 2% TCM 700°C
	BM7	calcareous filler + P25 0.2% RT
	BM8	calcareous filler + P25 1% RT
	BM9	calcareous filler + P25 2% RT
	BM10	calcareous filler & 0.2% P25 700°C
	BM11	calcareous filler & 1% P25 700°C
	BM12	calcareous filler & 2% P25 700°C
	BM13	calcareous filler & 0.2% undoped- RT
	BM14	calcareous filler & 1% undoped- RT
	BM15	calcareous filler & 2% undoped- RT
	BM16	calcareous filler & 0.2% undoped- 700°C
	BM17	calcareous filler & 1% undoped- 700°C
	BM18	calcareous filler & 2% undoped- 700°C
CEMENT PAINT	BM19	calcareous filler & 0.2% Crystal Global- RT
	BM20	calcareous filler & 1% Crystal Global- RT
	BM21	calcareous filler & 2% Crystal Global- RT
	BM22	calcareous filler & 0.2% Crystal Global- 700°C
	BM23	calcareous filler & 1% Crystal Global- 700°C
	BM24	calcareous filler & 2% Crystal Global- 700°C
	BM25	cement paint & 0.2% TCM- RT
	BM26	cement paint & 1% TCM- RT
	BM27	cement paint & 2% TCM- RT
	BM28	cement paint & 0.2% TCM 700°C
	BM29	cement paint & 1% TCM 700°C
	BM30	cement paint & 2% TCM 700°C
	BM31	cement paint + P25 0.2% RT
	BM32	cement paint + P25 1% RT
	BM33	cement paint + P25 2% RT

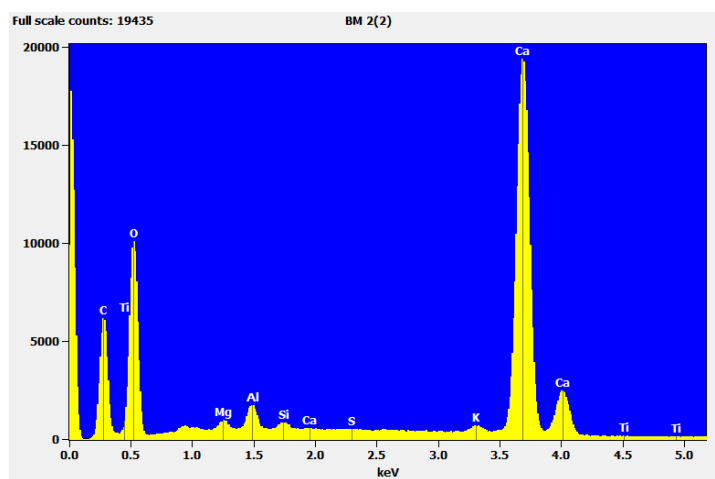
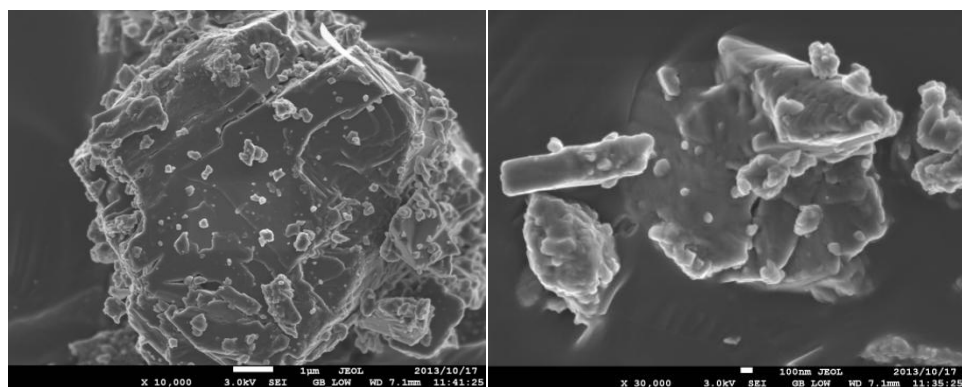
CEMENT	BM34	cement paint & 0.2% P25 700°C
	BM35	cement paint & 1% P25 700°C
	BM36	cement paint & 2% P25 700°C
	BM37	cement paint & 0.2% undoped- RT
	BM38	cement paint & 1%undoped- RT
	BM39	cement paint & 2%undoped- RT
	BM40	cement paint & 0.2%undoped- 700°C
	BM41	cement paint & 1%undoped- 700°C
	BM42	cement paint & 2%undoped- 700°C
	BM43	cement paint & 0.2% Crystal Global- RT
	BM44	cement paint & 1% Crystal Global- RT
	BM45	cement paint & 2% Crystal Global- RT
	BM46	cement paint & 0.2%Crystal Global- 700°C
	BM47	cement paint & 1%Crystal Global- 700°C
	BM48	cement paint & 2%Crystal Global- 700°C
	BM49	cement & 0.2% TCM- RT
	BM50	cement & 1% TCM- RT
	BM51	cement & 2% TCM- RT
	BM52	cement & 0.2% TCM 700°C
	BM53	cement & 1% TCM 700°C
	BM54	cement & 2% TCM 700°C
	BM55	cement + P25 0.2% RT
	BM56	cement + P25 1% RT
	BM57	cement + P25 2% RT
	BM58	cement & 0.2% P25 700°C
	BM59	cement & 1% P25 700°C
	BM60	cement & 2% P25 700°C
	BM61	cement & 0.2% undoped- RT
	BM62	cement & 1%undoped- RT
	BM63	cement & 2%undoped- RT
	BM64	cement & 0.2%undoped- 700°C
	BM65	cement & 1%undoped- 700°C
	BM66	cement & 2% undoped- 700°C
	BM67	cement & 0.2% Crystal Global- RT
	BM68	cement & 1% Crystal Global- RT
	BM69	cement & 2% Crystal Global- RT
	BM70	cement & 0.2%Crystal Global- 700°C
	BM71	cement & 1%Crystal Global- 700°C
	BM72	cement & 2%Crystal Global- 700°C

BM1



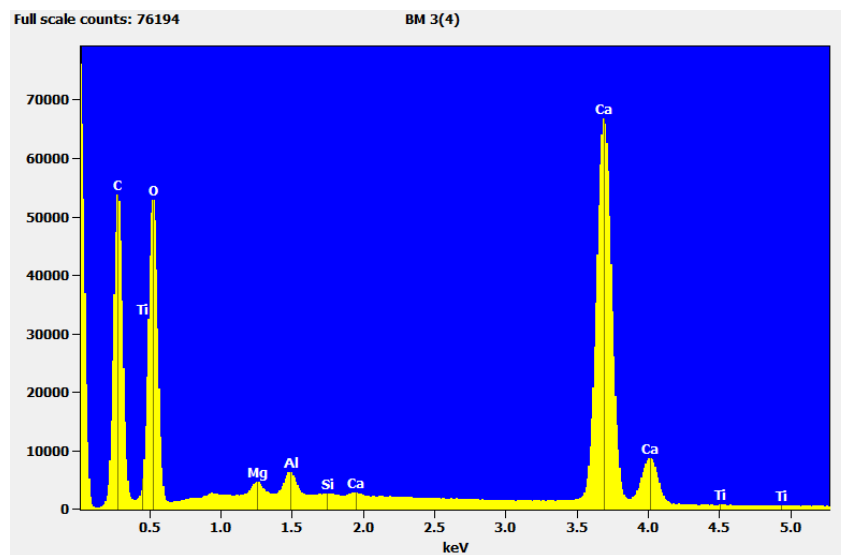
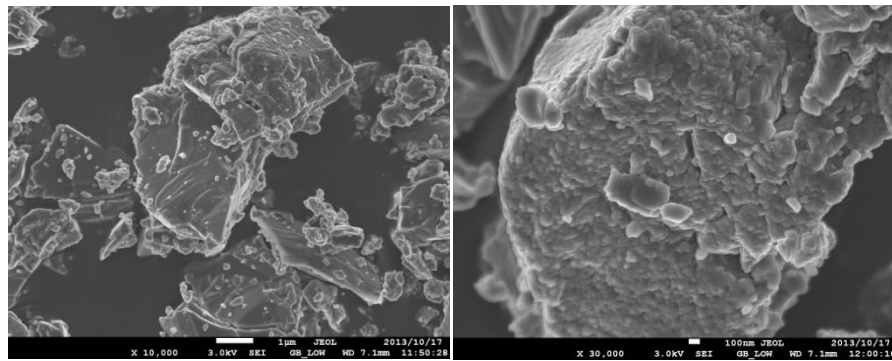
<i>Element Line</i>	<i>Weight %</i>	<i>Weight % Error</i>	<i>Atom %</i>	<i>Atom % Error</i>
<i>C K</i>	15.21	± 0.13	24.81	± 0.22
<i>O K</i>	45.70	± 0.25	55.94	± 0.31
<i>Mg K</i>	0.29	± 0.03	0.23	± 0.02
<i>Al K</i>	0.49	± 0.03	0.35	± 0.02
<i>Si K</i>	0.06	± 0.01	0.04	± 0.01
<i>Si L</i>	---	---	---	---
<i>Ca K</i>	37.85	± 0.14	18.50	± 0.07
<i>Ca L</i>	---	---	---	---
<i>Ti K</i>	0.00	---	0.00	± 0.00
<i>Ti L</i>	---	---	---	---
<i>Cu K</i>	0.41	± 0.09	0.13	± 0.03
<i>Cu L</i>	---	---	---	---
Total	100.00		100.00	

BM2



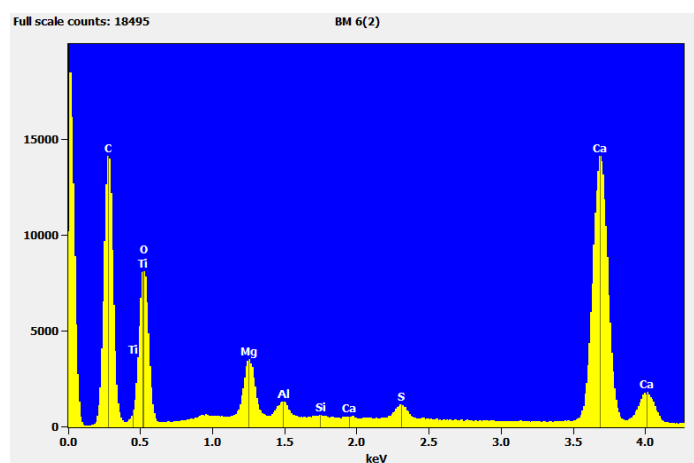
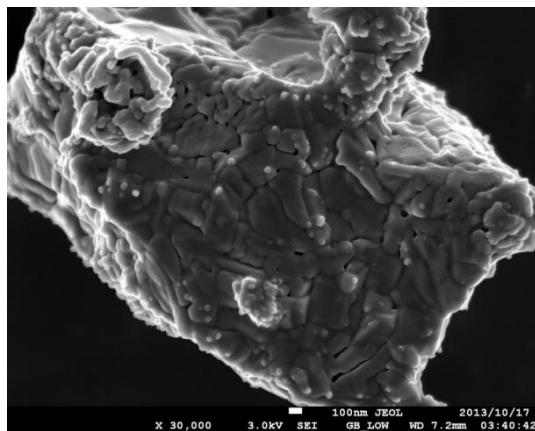
Element Line	Weight %	Weight % Error	Atom %	Atom % Error
<i>CK</i>	18.04	± 0.13	29.12	± 0.22
<i>OK</i>	42.27	± 0.24	51.21	± 0.29
<i>Mg K</i>	0.51	± 0.03	0.40	± 0.02
<i>Al K</i>	1.11	± 0.03	0.79	± 0.02
<i>Si K</i>	0.27	± 0.03	0.19	± 0.02
<i>Si L</i>	---	---	---	---
<i>S K</i>	0.06	± 0.01	0.04	± 0.01
<i>S L</i>	---	---	---	---
<i>KK</i>	0.59	± 0.04	0.29	± 0.02
<i>KL</i>	---	---	---	---
<i>Ca K</i>	37.15	± 0.14	17.96	± 0.07
<i>Ca L</i>	---	---	---	---
<i>Ti K</i>	0.00	---	0.00	± 0.00
<i>Ti L</i>	---	---	---	---
<i>Total</i>	100.00		100.00	

BM3



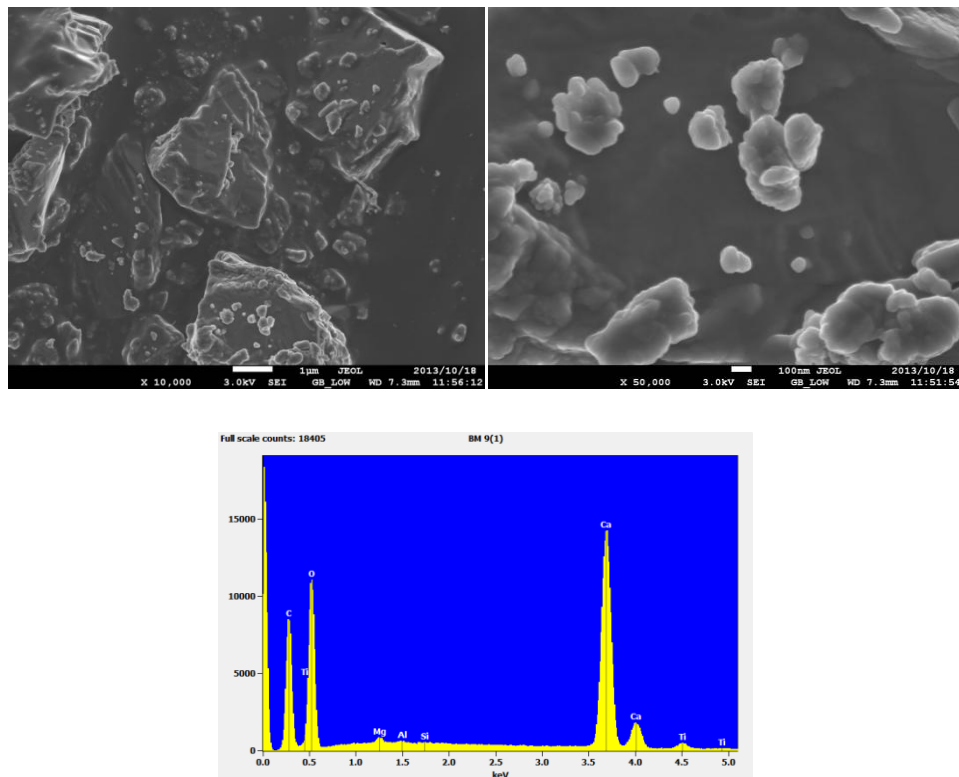
<i>Element Line</i>	<i>Weight %</i>	<i>Weight % Error</i>	<i>Atom %</i>	<i>Atom % Error</i>
<i>C K</i>	29.93	± 0.09	42.67	± 0.13
<i>O K</i>	42.22	± 0.15	45.18	± 0.16
<i>Mg K</i>	0.41	± 0.01	0.29	± 0.00
<i>Al K</i>	0.68	± 0.01	0.43	± 0.01
<i>Si K</i>	0.04	± 0.01	0.02	± 0.00
<i>Si L</i>	---	---	---	---
<i>Ca K</i>	26.72	± 0.07	11.41	± 0.03
<i>Ca L</i>	---	---	---	---
<i>Ti K</i>	0.00	---	0.00	± 0.00
<i>Ti L</i>	---	---	---	---
<i>Total</i>	100.00		100.00	

BM6



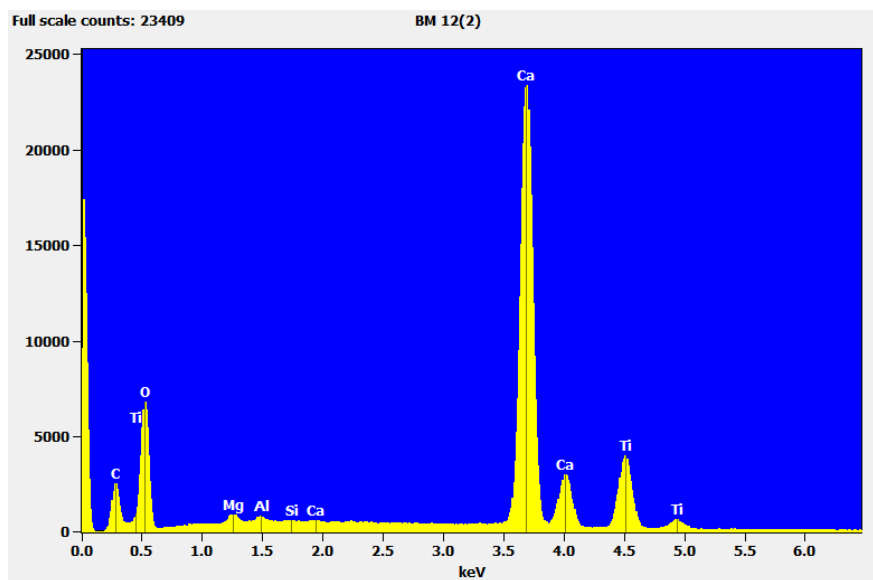
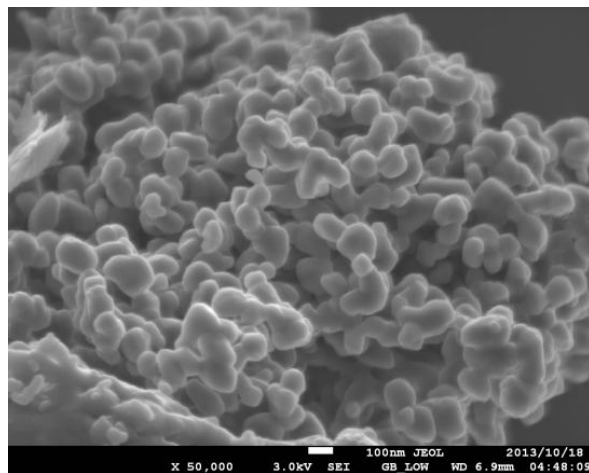
<i>Element Line</i>	<i>Weight %</i>	<i>Weight % Error</i>	<i>Atom %</i>	<i>Atom % Error</i>
<i>C K</i>	38.53	± 0.17	53.42	± 0.24
<i>O K</i>	32.32	± 0.22	33.64	± 0.23
<i>Mg K</i>	2.32	± 0.03	1.59	± 0.02
<i>Al K</i>	0.59	± 0.03	0.36	± 0.02
<i>Si K</i>	0.08	± 0.01	0.05	± 0.01
<i>Si L</i>	---	---	---	---
<i>S K</i>	0.71	± 0.03	0.37	± 0.01
<i>S L</i>	---	---	---	---
<i>Ca K</i>	25.37	± 0.11	10.54	± 0.04
<i>Ca L</i>	---	---	---	---
<i>Ti K</i>	0.08	± 0.02	0.03	± 0.01
<i>Ti L</i>	---	---	---	---
<i>Total</i>	100.00		100.00	

BM9



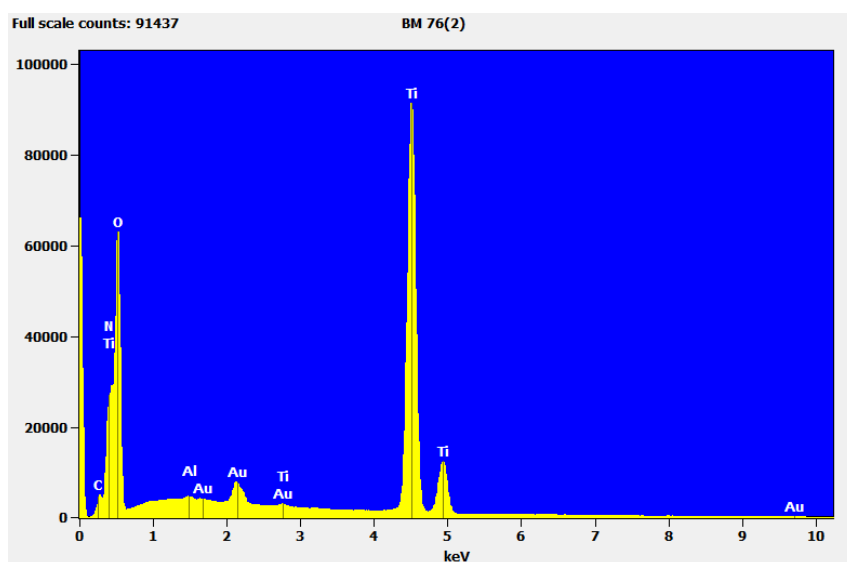
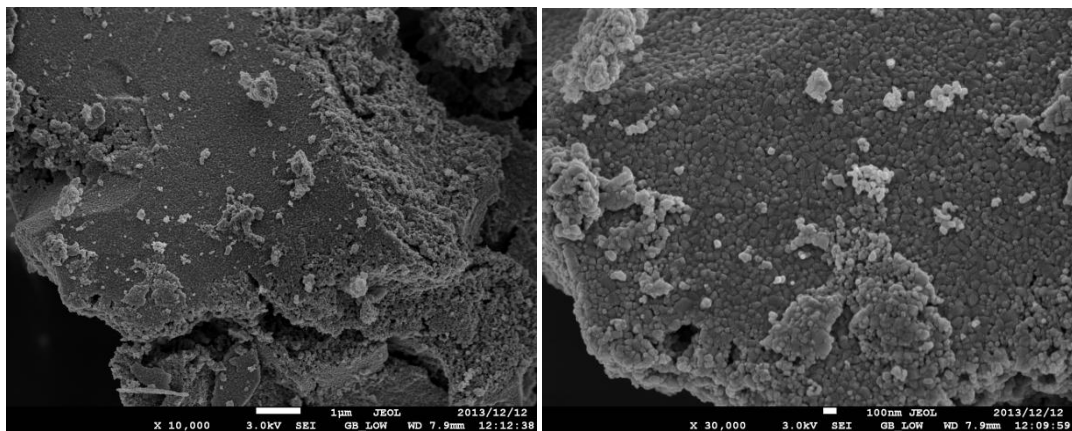
<i>Element Line</i>	<i>Weight % Error</i>	<i>Weight % Error</i>	<i>Atom % Error</i>	<i>Atom % Error</i>
<i>C K</i>	24.10	± 0.15	35.86	± 0.22
<i>O K</i>	45.10	± 0.24	50.36	± 0.27
<i>Mg K</i>	0.34	± 0.01	0.25	± 0.01
<i>Al K</i>	0.16	± 0.01	0.11	± 0.01
<i>Si K</i>	0.06	± 0.01	0.04	± 0.01
<i>Si L</i>	---	---	---	---
<i>Ca K</i>	28.99	± 0.12	12.92	± 0.05
<i>Ca L</i>	---	---	---	---
<i>Ti K</i>	1.26	± 0.05	0.47	± 0.02
<i>Ti L</i>	---	---	---	---
<i>Total</i>	100.00		100.00	

BM12



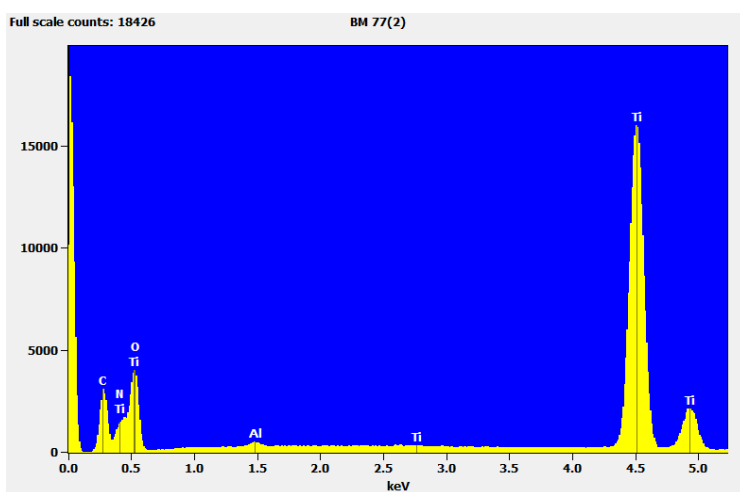
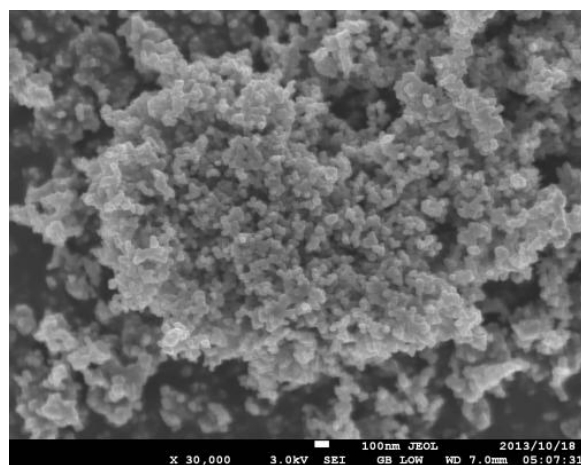
Element Line	Weight % Error	Weight % Error	Atom % Error	Atom % Error
<i>CK</i>	7.36	± 0.13	14.84	± 0.27
<i>OK</i>	33.34	± 0.65	50.45	± 0.99
<i>Mg K</i>	0.38	± 0.02	0.38	± 0.02
<i>Al K</i>	0.23	± 0.01	0.21	± 0.01
<i>Si K</i>	0.03	± 0.01	0.03	± 0.01
<i>Si L</i>	---	---	---	---
<i>Ca K</i>	45.04	± 0.15	27.21	± 0.09
<i>Ca L</i>	---	---	---	---
<i>Ti K</i>	13.62	± 0.10	6.88	± 0.05
<i>Ti L</i>	---	---	---	---
Total	100.00		100.00	

BM76



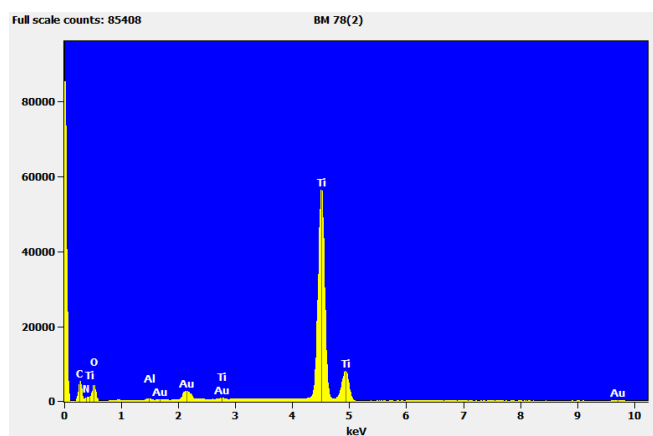
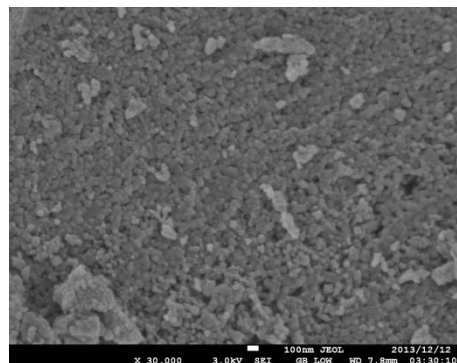
<i>Element Line</i>	<i>Weight %</i>	<i>Weight % Error</i>	<i>Atom %</i>	<i>Atom % Error</i>
<i>CK</i>	2.92	± 0.03	5.28	± 0.05
<i>NK</i>	11.06	± 0.05	17.15	± 0.08
<i>OK</i>	43.42	± 0.15	58.94	± 0.20
<i>AlK</i>	0.10	± 0.01	0.08	± 0.01
<i>TiK</i>	40.41	± 0.08	18.32	± 0.04
<i>TiL</i>	---	---	---	---
<i>AuL</i>	---	---	---	---
<i>AuM</i>	2.09	± 0.02	0.23	± 0.00
<i>Total</i>	100.00		100.00	

BM 77



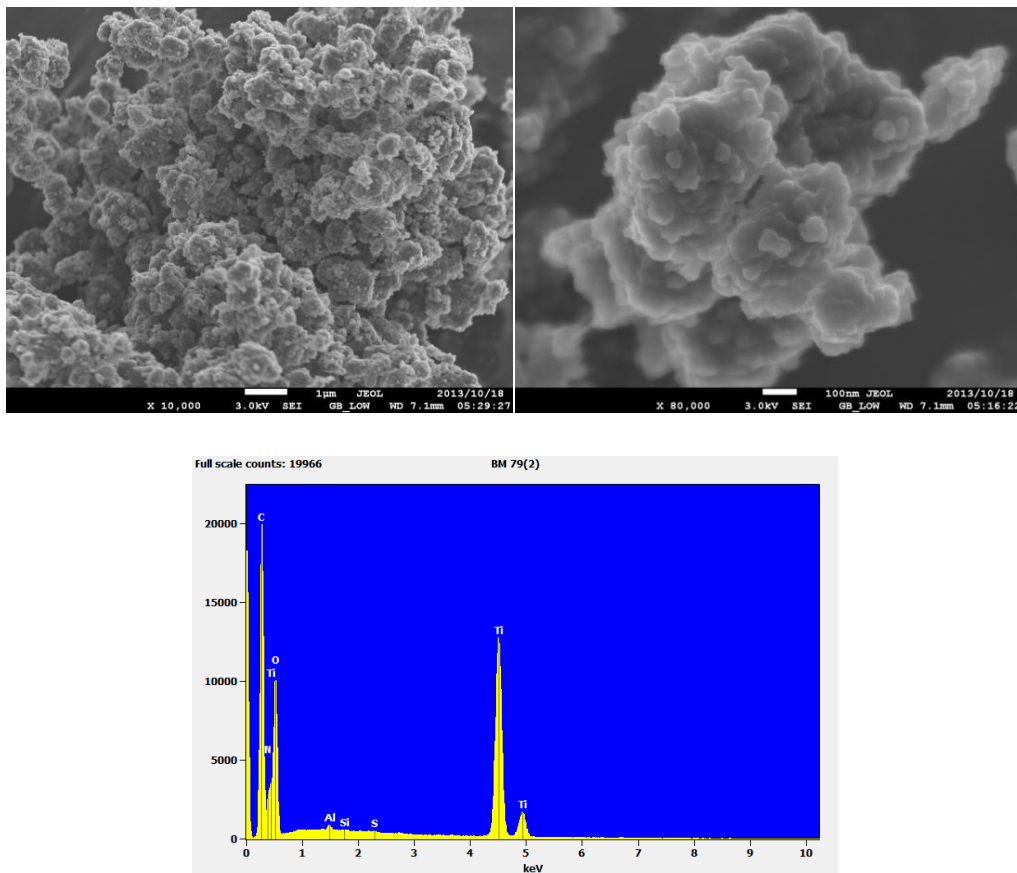
<i>Element Line</i>	<i>Weight %</i>	<i>Weight % Error</i>	<i>Atom %</i>	<i>Atom % Error</i>
<i>C K</i>	8.66	± 0.19	17.06	± 0.37
<i>N K</i>	10.12	± 0.22	17.09	± 0.37
<i>O K</i>	26.03	± 0.27	38.50	± 0.40
<i>Al K</i>	0.20	± 0.01	0.18	± 0.01
<i>Ti K</i>	54.99	± 0.18	27.17	± 0.09
<i>Ti L</i>	---	---	---	---
<i>Total</i>	100.00		100.00	

BM78



<i>Element Line</i>	<i>Weight %</i>	<i>Weight % Error</i>	<i>Atom %</i>	<i>Atom % Error</i>
<i>CK</i>	6.11	± 0.09	15.96	± 0.25
<i>NK</i>	5.87	± 0.10	13.15	± 0.22
<i>OK</i>	11.25	± 0.13	22.08	± 0.26
<i>AlK</i>	0.17	± 0.01	0.20	± 0.01
<i>TiK</i>	73.40	± 0.16	48.10	± 0.11
<i>TiL</i>	---	---	---	---
<i>AuL</i>	---	---	---	---
<i>AuM</i>	3.20	± 0.04	0.51	± 0.01
<i>Total</i>	100.00		100.00	

BM79



<i>Element Line</i>	<i>Weight %</i>	<i>Weight % Error</i>	<i>Atom %</i>	<i>Atom % Error</i>
<i>C K</i>	31.66	± 0.16	43.67	± 0.22
<i>N K</i>	14.88	± 0.49	17.60	± 0.58
<i>O K</i>	29.27	± 0.21	30.31	± 0.22
<i>Al K</i>	0.14	± 0.01	0.09	± 0.00
<i>Si K</i>	0.05	± 0.01	0.03	± 0.00
<i>Si L</i>	---	---	---	---
<i>S K</i>	0.03	± 0.01	0.02	± 0.00
<i>S L</i>	---	---	---	---
<i>Ti K</i>	23.97	± 0.09	8.29	± 0.03
<i>Ti L</i>	---	---	---	---
<i>Total</i>	100.00		100.00	



TECHNICAL UNIVERSITY OF CRETE (TUC)
SCHOOL OF ENVIRONMENTAL ENGINEERING
RENEWABLE AND SUSTAINABLE ENERGY
SYSTEMS LABORATORY